PHYSIK-DEPARTMENT

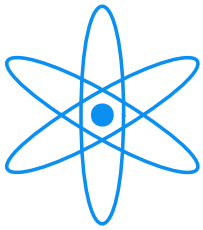

A Silicon Microstrip Detector for COMPASS
and
A First Measurement of the Transverse Polarization of Λ^0-Hyperons from Quasi-Real Photo-Production

Dissertation

von

Michael Wiesmann

TECHNISCHE UNIVERSITÄT
MÜNCHEN

Fakultät für Physik der Technischen Universität München
Physik Department E18

A Silicon Microstrip Detector for COMPASS
and
A First Measurement of the Transverse Polarization of Λ^0-Hyperons from Quasi-Real Photo-Production

Michael Wiesmann

Vollständiger Abdruck der von der Fakultät für Physik der Technischen Universität München zur Erlangung des akademischen Grades eines

Doktors der Naturwissenschaften (Dr. rer. nat.)

genehmigten Dissertation.

Vorsitzender: Univ.-Prof. Dr. A. J. Buras

Prüfer der Dissertation:

1. Univ.-Prof. Dr. St. Paul
2. Hon.-Prof. Dr. S. Bethke

Die Dissertation wurde am 27.01.2004 bei der Technischen Universität München eingreicht und durch die Fakultät für Physik am 13.02.2004 angenommen.

Contents

Introduction

Neutrons and protons are the basic building blocks of matter. They form the atomic nucleus (hence also the name *nucleons*) and are responsible for the major part of the atomic mass. In our current understanding they are composed of *quarks* bound by the strong *color force*.

Six different quarks, the *flavors*, are known. Sorted according to their mass they are (from lightest to heaviest): `Up` (`u`), `Down` (`d`), `Strange` (`s`), `Charm` (`c`), `Bottom` (`b`) and `Top` (`t`). In the naive *constituent quark model* nucleons are described as a combination of three *constituent quarks*. Together they define the properties of the nucleon like charge and mass. Different combinations of flavors result in different types of nucleons: protons consists of (`uud`), neutrons of (`udd`).

Besides an electrical charge, the quarks also carry a "strong" charge, the *color*: quarks can be "red" (`r`), "blue" (`b`) or "green" (`g`), anti-quarks carry the respective anti-colors "anti-red" ($\bar{\mathtt{r}}$), "anti-blue" ($\bar{\mathtt{b}}$) or "anti-green" ($\bar{\mathtt{g}}$). Since its introduction to particle physics, color has never been found with a free particle: quarks always appear as "white" clusters called *hadrons*. Two ways to get white hadrons have so far been observed: *mesons* are built of one quark and one anti-quark in such a way that their colors neutralize each other, *baryons* are made up of three quarks whose color combination (`rgb`), in the same way as in the optical analogon, also makes white. In this scheme the nucleons are only two hadrons out of many: they are the three-quark-systems consisting of `u`- and `d`-quarks only and are therefore the lightest baryons.

In the framework of *Quantum Chromodynamics* (QCD) the interaction of the quarks and their color fields is described in analogy to the very successful *Quantum Electrodynamics* (QED) by the exchange of field quanta, so-called *gluons*. The strength of the interaction between quarks and gluons is described in the *coupling constant* α_s. But while in QED the field quanta do not carry charge and therefore cannot interact among each other, in QCD gluons *are* colored and *do* show self-interaction, which leads to a much more complex interaction scheme than in QED.

It turned out that the interaction of quarks is rather weak when they come very close together, i.e. when their kinetic energies are high. It can then be nicely described assuming a one-gluon-exchange similar to the one-photon-exchange in the QED case. Due to a small coupling constant α_s, more-gluon-exchanges are said to be unlikely: at around 100 GeV, α_s was measured to be only of the order of $\sim 1/10$. It is therefore sufficient for many applications to calculate just the one-gluon exchange and add more gluons only as small disturbance. This is called *perturbative QCD*.

Surprisingly, in the case of large distances and, accordingly, small quark energies, the interaction gets *stronger*. To allow for more gluons in such interactions, the coupling constant α_s is said to be not constant but assumed to get larger for larger distances. Hence it is called a *running* coupling "constant". As a consequence this makes it impossible to separate two quarks, as the force field acquires so much energy that it finally bursts into a $\mathtt{q}\bar{\mathtt{q}}$-pair under conservation of the "white" color. The fact that quarks are not separable is called *confinement*.

At the nucleon's energy scale of 1 GeV, α_s is already more than 0.3. Consequently the behavior of quarks and gluons and therefore the structure of the nucleon cannot be described in the same perturbative way of a simple one-gluon-exchange anymore, but many-gluon-exchanges have to be taken into account as well. The method breaks down anyway at $\alpha_s \sim 1$ at the latest. In the last few years much effort has been spent on finding new ways of describing low-energy QCD. The most promising ones are *Lattice QCD* and *Chiral Perturbation Theory*. In Lattice QCD the field equations are solved exactly on a grid with a finite spacing, using a huge amount of computer power. *Chiral Perturbation Theory* uses the chiral symmetry of QCD at low quark momenta, which is approximately valid since the quark masses can be neglected because they are still much smaller than the quark momenta.

In the nucleon and in all baryons in general quarks move at distances for which the low-energy-models mentioned above are just starting to be applicable. In this region many peculiar features of QCD show up. Thus inside the nucleons a large number of so-called *sea quarks* were found, which have their origin in gluons fluctuating for short times into quark–anti-quark pairs. Furthermore, while in atoms the energy stored in the binding of the electrons to the protons with opposite electrical charge is very small [1], the "binding energy" is surprisingly large in the nucleon. Despite the large number of sea quarks, the contribution of quarks to the total momentum of the nucleon was measured to be only around 50%, the rest is contributed by the "binding", the gluons. These results helped considerably to advance the theoretical understanding of the nucleon: from a vacuum filled with three point-like quarks one moved to some kind of plum-pudding model where quarks are embedded into a background of gluons like raisins in the pudding. This background, however, transforms constantly back and forth into quarks and anti-quarks as well. The small excess of three valence quarks over the large number of quark–anti-quark-pairs in the sea defines the type of the nucleon. The constituent quark mentioned at the beginning finally became only an "effective" particle consisting of a valence quark with a large cloud of gluons and sea quarks around.

A very sensitive probe for the forces reigning the nucleon is another static property of quarks and nucleons, the *spin*. It seems that it plays a more important role in high-energy particle production than expected. Traditionally the spin of particles was considered little interesting as it was thought not to influence the particle production at all. At any rate in high-energy multi-particle production the particle's mass is small compared to its energy, and thus, it was assumed, its spin behavior should be as simple as that of massless particles. Surprisingly, experimental data did not confirm this assumption: more than 25 years ago in the collision of high energetic protons of 300 GeV with beryllium nuclei, scientists found Lambdas particles $\Lambda^0(\mathtt{uds})$ for which the spin direction was not distributed homogeneously, but mainly perpendicular (i.e. *transverse*) to the production plane spanned by proton and Λ^0, even though neither proton nor beryllium were polarized themselves [Bun76].

Since then such *spontaneous* polarization has been found with other interactions as well, exhibiting a regular pattern, which should help to uncover the underlying production mechanism. Yet the observed polarization still cannot be comprehensively described and is likely to originate from several sources, being related to either the structure of the baryon itself or to the production process. Measuring this quantity therefore gives an important insight into the world of the quarks and how they put themselves together to make up baryons.

While much data on transverse polarization phenomena have already been collected in proton-proton, kaon-proton or pion-proton collisions, no data is available from photo-production. COMPASS, a state–of–the–art experiment currently running at the high-energy particle physics

[1] Compare, for example, the binding energy of the electron of 13.6 eV with the hydrogen mass of 938 890 076.4 eV.

accelerator laboratory CERN[2] in Switzerland, has the unique chance to provide highly precise data on this topic, which will give a new view onto this subject and the possibility to check new models.

The work reported in this thesis was performed in the framework of the COMPASS experiment. In the first chapter this experiment is described: after an introduction to the general physics goals, an overview of the experimental setup is given. The chapter also provides some background information on transverse Λ^0 polarization.
Within this work a set of silicon detectors was developed, installed and brought into operation. After a short review of the principle of silicon detectors in particle physics with special emphasis on radiation-induced damages in Chapter 2, Chapter 3 presents the design and performance of the COMPASS detectors used since the beam time in the year 2002.
The analysis of the transverse Λ^0 polarization using first COMPASS data are then shown in the following three chapters: chapter 4 describes the procedures used to process the raw data to so-called *Data Summary Tapes* DSTs, and chapter 5 explains how the Λ^0 were extracted from the available data and analyzed for their polarization. In chapter 6 the results of the analysis are presented.

[2]Conseil Européen pour la Recherche Nucléaire, European Laboratory for Particle Physics

Chapter 1

The COMPASS Experiment

COMPASS is a fixed-target experiment at the CERN *Super Proton Synchrotron* (SPS). It uses both leptonic (muons (μ)) and hadronic probes (pions (π), protons (p), kaons (K)) on solid state targets to study the structure of the nucleon and to perform spectroscopy of hadrons. It continues a long tradition of predecessors as it has its roots in two different, originally separate projects:

Having worked together on a series of μ-scattering experiments at CERN in three collaborations (EMC, NMC and SMC: the *European*, the *New* and the *Spin Muon Collaboration*), a group of physicists proposed the *Hadron Muon Collaboration* HMC as follow-up to further investigate the spin structure of the nucleon via polarized μ-scattering off a polarized nucleon target.

On the hadronic side, the WA89 collaboration set the stage for investigating strange and charmed baryons with a Σ^- beam from the CERN/SPS at the Omega spectrometer. With Crystal Barrel at LEAR's low-energy anti-proton beam and WA91/WA102 central productions in 450 GeV pp-scattering, the road was paved for the discovery of exotic states and finally a good candidate for a glue ball, the $f_0(1500)$, was found. Together these groups proposed the CHEOPS (CHarm Experiment with Omni-Purpose Spectrometer) experiment.

Similar experimental requirements and financial limitations gave the trigger to combine efforts in a ***CO**mon **M**uon and **P**roton **A**pparatus for **S**tructure and **S**pectroscopy* = COMPASS in 1995. The collaboration today consists of 220 physicists from 26 institutes in 11 countries. The physics program was approved up to the year 2005, with good prospects for additional 5 years. Currently COMPASS is the biggest CERN experiment running between the LEP and the LHC[1] era.

After the approval of the program in 1997, the commissioning of the spectrometer took place in the year 2001, and first physics data were taken in 2002. Due to restrictions in finance and manpower, the complete installation is planned in two phases, so that currently COMPASS is running with an initial setup and a more specific physics program.

For the startup phase priority was given to the muon program because of the current strong interest in a measurement of the polarization of the gluon (see section 1.1.1). The hadron program (see section 1.1.2) may start with a first project in 2004, but its main physics program will commence only after 2005, when work with the SPS will be interrupted for a year for the preparation of the LHC.

[1] The *Large Hadron Collider* (LHC) is the successor of the *Large Electron Positron collider* (LEP) at CERN; both are the flagships of the CERN accelerator echelon, and with a circumference of 27 km the biggest accelerators of their kind worldwide. LEP was running from 08/1989 up to 11/2000, LHC will start in 2006.

This chapter will give an insight into both physics programs in section 1.1, with more emphasis on the hadronic sector as this is the author's field of involvement. The physics topic of this work, the transverse polarization of Λ^0, will be introduced in section 1.2. The last section 1.3 finally gives an overview of the experimental apparatus in 2002.

1.1 Physics Program of COMPASS

1.1.1 Physics with a Muon Beam

The main goal of the muon beam program is to find the origin of the spin of the nucleon. Naively one could expect it to be the sum of the spins of the three valence quarks. But it was shown by the EMC collaboration in 1989 [EMC89] that only 30% of the nucleon spin can be attributed to the quarks.

In general not only the valence quarks define the spin of the nucleon. Additionally one can also get contributions from the sea quarks, the gluons or from orbital momenta of quarks or gluons. One defines the spin contribution Δq for each quark flavor $q = u, d, s$ as the difference between the number of quarks, whose the spin is parallel $q^{\uparrow\uparrow}$ and those whose spin is anti-parallel $q^{\uparrow\downarrow}$ to the nucleon spin: $\Delta q = q^{\uparrow\uparrow} - q^{\uparrow\downarrow}$. ΔG, the gluons' spin distribution, is defined accordingly. The total spin of the hadrons of $\frac{1}{2}$ (in units of $\hbar$) can then be written as a sum of these components:

$$\frac{1}{2} = \frac{1}{2}\Delta\Sigma + \Delta G + L_q + L_G, \tag{1.1}$$

with $\Delta\Sigma = \Delta u + \Delta d + \Delta s + \Delta\bar{u} + \Delta\bar{d} + \Delta\bar{s}$ as the sum of the contributions from quarks and anti-quarks. $L_{q,G}$ denotes the orbital momentum of quarks and gluons respectively. While $\Delta\Sigma$ is already reasonably well known $(0.30 \pm 0.04 \pm 0.09)$ [Hermes99], the other terms are still untackled and need to be measured urgently.

The spin contributions of the quarks are experimentally accessible in *Deep Inelastic Scattering* (DIS), where one does not scatter on the complete nucleon, but on *partons* carrying only a fraction of the nucleon's momentum. In *inclusive* measurements only the scattered lepton is detected, including *all* possible reactions of the target nucleon. From the kinematics of the lepton alone the contributions of both quarks and anti-quarks to the spin could be extracted. The experiments of the next generation are hoped to find out more about the flavor-decomposed quark contributions or gluon polarization and orbital momenta. For this, more information on the scattered quark is needed. It is expected to hadronize into the hadron with the highest momentum (*leading* hadron), which has to be identified and its kinematics determined in *semi-inclusive* Deep Inelastic Scattering (SIDIS).

ΔG can be probed in so-called *Photon-Gluon-Fusion* (PGF), orbital momenta are accessible in *Deeply Virtual Compton Scattering* (DVCS). In recent years an additional, equally important spin distribution function, the so-called *transversity*, was found to be very interesting.

COMPASS will provide precise data on these topics. Both beam and target are polarized. While the spin direction of the μ is more or less fixed by the accelerators (see section 1.3.3), the target spin is rotated 3 times a day. To reduce systematic uncertainties, measurements with different target polarizations are compared in a way, that experimental biases cancel each other out. Gluon polarization is given priority here. It will be explained in the next section, a short overview of other spin-related measurements follows.

Gluon Polarization

The most promising candidate for a significant contribution to the spin of the nucleon not attributed to the quarks is the gluon. Similar to the missing momentum of the nucleon, one hopes to find a good fraction of the nucleon spin with these exchange bosons.
Unfortunately the spin of the gluons is not easy to probe: the clearest polarized probes are polarized photons, as e.g. in polarized muon scattering. But as gluons do not carry electric charge, they cannot interact with photons directly. One has to use a second order process, in which the photon interacts with the gluon via an intermediate quark line. Such a process is called *Photon–Gluon–Fusion* (PGF), the Feynman graph is depicted in fig. 1.1.
In order to enrich the data sample with PGF events, two ways are followed in COMPASS, namely *Open Charm Production* and events with *high* p_T.

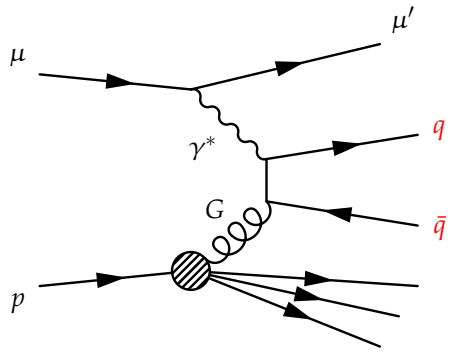

Figure 1.1: *Photon-Gluon-Fusion: The virtual photon in muon scattering cannot interact with the gluons in the hadrons directly. Instead an intermediate quark is needed as an adapter between color and electric charge.*

Open Charm Production. In leading order *heavy* quarks are produced via PGF, contributions from the sea quarks or the fragmentation process of light quarks are small. COMPASS will therefore measure the spin-dependent asymmetry A^{exp} for charm muo-production [CO96], which is given by the number $N_{c\bar{c}}$ of charm events for muon spin parallel and anti-parallel to the target spin.

$$A^{\text{exp}} = \frac{N_{c\bar{c}}^{\uparrow\downarrow} - N_{c\bar{c}}^{\uparrow\uparrow}}{N_{c\bar{c}}^{\uparrow\downarrow} + N_{c\bar{c}}^{\uparrow\uparrow}} \propto \frac{\Delta\sigma^{\gamma N \to c\bar{c}X}}{\sigma^{\gamma N \to c\bar{c}X}} = \frac{\Delta\sigma(\hat{s}) \otimes \Delta G(\eta, \hat{s})}{\sigma(\hat{s}) \otimes G(\eta, \hat{s})} \tag{1.2}$$

A^{exp} is related to the ratio of the helicity-dependent and helicity-averaged cross section for charm-photo-production $\Delta\sigma^{\gamma N \to c\bar{c}X}$ and $\sigma^{\gamma N \to c\bar{c}X}$, which in turn can be expressed as a convolution of the elementary photon-gluon cross sections $\Delta\sigma(\hat{s})$ and $\sigma(\hat{s})$ with the gluon distributions $\Delta G(\eta, \hat{s})$ and $G(\eta, \hat{s})$. Here, $\hat{s} = (q + k)^2$ is the invariant mass of the photon-gluon system, with q and k as the photon and gluon 4-momenta, $\eta = \hat{s}/2M_N E y$ is the gluon momentum fraction.

Typically around 60% of the charm quarks fragment into neutral D mesons ($D^0(\mathrm{c\bar{u}})$ and $\bar{D}^0(\mathrm{\bar{c}u})$), yielding an average of $N^{D^0}/N_{c\bar{c}} = 1.23$ D^0 mesons per charm event (including charge conjugates). The simplest way to detect the D^0 is via its decay into the two charged particles $D^0 \to K^- + \pi^+$ with a branching ratio of $3.8 \pm 0.9\%$.

About 33% of all D^0 come from the decay of D^{*+} into D^0 and a π with a very small energy of few MeV

$$D^{*+} \rightarrow D^0 + \pi^+{}_s \rightarrow (K^-\pi^+)\pi^+{}_s.$$

Thus the background for D^0 can be significantly reduced by requiring that the mass difference $\Delta M = m(K^-\pi^+\pi^+{}_s) - m(K^-\pi^+) - m(\pi)$ is small (D^{*+} tag).

COMPASS will set benchmarks in this exciting search for the gluon spin. In [CO96] ≈ 800 D^0 per day are expected inside the spectrometer acceptance, the total sensitivity for the whole run time is expected to be $\delta(\Delta G/G) \approx 0.14$.

High p_T events. An alternative to the limited cross sections of open charm production is looking for *all* possible quark types, which manifest themselves in the production of two jets with opposite azimuth [BvHK98]. In the case of the moderate energies of fixed-target experiments the "jets" shrink to only the two leading hadrons, which still reflect the original quark flavor and direction of the hard process. While the statistics situation is much better than in the charm–only case, the background situation is less favorable. Soft contributions can be suppressed by requiring the leading hadrons to have a high transverse momentum p_T: values of around $p_{T,\mathrm{min}} > 1.0 - 1.5\ GeV/c$ were shown to be sufficient by Bravar et al. [BvHK98]. But the main background process, the gluon radiation as shown in fig. 1.2a), stays. Both are same order in α_s and thus show a similar signature. As they cannot be separated experimentally, they have to be subtracted analytically. The crucial parameter is the ratio between the cross section $R = \sigma^{\mathrm{PGF}}/\sigma^{\mathrm{COMPT}}$ of these two processes in fig. 1.2a) and b) which cannot be measured directly, but has to be estimated from simulations. It will therefore introduce the largest uncertainty in the extraction of ΔG.

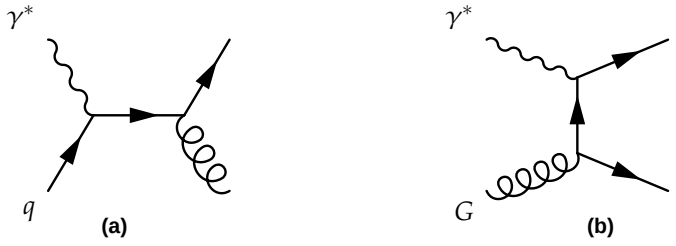

Figure 1.2: *Lowest order Feynman diagrams in α_s in DIS γN scattering: the virtual photon γ^* scatters either **a)** off a quark, which radiates a gluon later (Compton diagram), or **b)** via an intermediate quark off a gluon G from the nucleon (Photon-Gluon-Fusion PGF). Gluon radiation is the main background process for the measurement of $\Delta G/G$ with high p_T events.*

Currently only one point for ΔG has been measured worldwide [Hermes00]: the HERMES experiment measured an asymmetry of $A_\parallel = -0.28 \pm 0.12 \pm 0.02$ for the production of positive-negative hadrons with transverse momenta $p_T > 1\,\mathrm{GeV}$. The result is not very clear and tends to a positive value for the gluon polarization ($\Delta G/G = 0.41 \pm 0.18(\mathrm{stat}) \pm 0.03(\mathrm{exp.sys})$). Here only the known *experimental* systematic error is given, a final conclusion on the model-dependent systematic part, which is expected to be large in the HERMES energy range, is missing.

Other Spin-Related Measurements

Transversity. In leading order (Twist-2 [2]) three independent quark contribution functions are needed for the complete description of the nucleon. Besides the already mentioned q and Δq as the number density and the polarization of the quarks of flavor q, additionally the *transverse spin contribution* $\Delta_T q$ is necessary. It describes the quark distribution in a transversely polarized nucleon[3], in analogy to Δq as the difference between quark spin parallel and anti-parallel to the nucleon spin $\Delta_T q = q^{\uparrow}_{\uparrow} - q^{\uparrow}_{\downarrow}$. In the naive picture $\Delta_T q$ should be the same as Δq. But this is only valid in the non-relativistic regime, whereas for the quarks in the nucleons the two distributions are expected to differ from each other. Their discrepancy is a measure for the size of the relativistic effects and therefore interesting again.

Unfortunately, transversity cannot be directly probed in normal DIS, as the necessary process exhibits an inapt symmetry behavior: an involved spin flip changes the symmetry state from chiral-even to chiral-odd. Such processes have to be compensated with another chiral-odd effect (for more details see [Grü02] and the references therein), like in a sequence of two such processes (as in *Drell Yan Processes*) or when they are followed by an equally chiral-odd fragmentation process, the so-called *Collins Fragmentation*. This complication is the reason why transversity has not yet been measured and is now on the list of the physics goals of COMPASS. COMPASS wants to measure the azimuthal distributions of the leading π, which should — according to Collins — show an asymmetric behavior that can be related to $\Delta_T q$. Again SIDIS is the key to this topic.

In the context of this thesis it is especially interesting to note that [Ans02] proposes to measure the transversity in combination with the likewise chiral-odd transversity fragmentation function for transversely polarized Λ^0.

DVCS. As already mentioned, the orbital momentum of the quarks L_q is a very interesting quantity. This field has opened just recently, when a connection was found between the total angular momentum of the quarks $J = \frac{1}{2}\Delta\Sigma + L_q$ and the so-called *Generalized Parton Distribution Functions GPD* [Ji97].

It has been proposed to use *Deeply Virtual Compton Scattering* (DVCS) for the extraction of these GPDs in COMPASS. In DVCS the virtual photon emitted from the muon beam is scattered off the target nucleon and becomes real (see fig. 1.3).

The measurement of DVCS is not in the COMPASS proposal of 1996, but was proposed only much later. First feasibility studies and measurements already gave positive results. A measurement of DVCS is intended in the second phase of COMPASS after 2005.

1.1.2 Hadronic Physics Program

This part of the physics program continues the experimental efforts to learn more about the strong interaction inside the nucleon via spectroscopy of hadrons with different quark content (e.g. charmed baryons, see below) and non-$q\bar{q}$-systems (e.g. glueballs).

The need for very high statistics is common to all projects; it is due to small cross sections for charmed baryons or glueballs and high mass diffractive systems. Therefore high intensity beams are needed.

[2] The *Twist t* refers to the expansion of the hadronic part in DIS, the hadronic tensor $W^{\mu\nu}$, in powers of $[M/Q]^{t-2}$. The leading term is t=2, therefore the name Twist-2.

[3] with respect to the longitudinally polarized beam

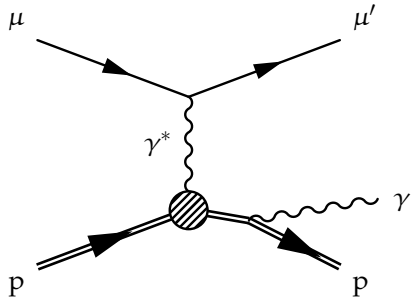

Figure 1.3: *Deeply Virtual Compton Scattering DVCS: the virtual photon emitted from the beam lepton just scatters off the target nucleon and can be found in the final state. Such events are thought to be sensitive of the orbital momenta of the quarks.*

The various beam energies between 100 - 300 GeV available at COMPASS permit very clear systematic studies, and different beam particles (π, K and p) open the possibility for studies in different environments with the same setup.

One of the key goals is the investigation of baryons with c-quark content, so-called *charmed* and *doubly-charmed baryons*. Such measurements require a highly optimized layout and are therefore not possible in the initial setup, but only later in phase 2 starting in the year 2006.

Many other hadronic topics, however, can be pursued earlier, for example the production of exotic states and the polarizability of the π.

Exotic States

Exotic states is the name for hadrons which cannot be described as ($q\bar{q}$) or (qqq) systems. Different scenarios are possible.

One of the most fascinating features of QCD is the fact that the transmitters of the color force, the gluons, carry color charge themselves and therefore should be able to form bound states among each other, so-called *glue balls*. An intermediate formation are *hybrids*, for which both valence quarks and exotic gluonic degrees of freedom are present.
Currently it is expected that even if these objects with gluonic degrees of freedom can be formed, they have a rather short lifetime and will be difficult to find in the background of other hadronic resonances. One can use the fact that objects with gluon content can form quantum states that cannot be reached with fermions alone, so-called *exotic* quantum numbers.

Additionally, it is interesting to look for hadronic structures which contain more than 3 quarks, like *Hexaquarks*, *Pentaquarks* and *Tetraquarks* with different combinations of heavy and light, quarks and anti-quarks.

From a theoretical point of view these objects are very interesting and several predictions are available. But experimentally their discovery is a very challenging task. The crucial point in this kind of measurements is that there are many hadronic resonances in the mass region between 1 and 2 GeV, which differ only in their arrangement of spins and the orbital momenta. They all contribute to the background and sometimes even mix among each other with systems of the same quantum numbers.

The data therefore have to be presented in several variables at the same time, which significantly lowers the statistics. In three- or more-body final states *Dalitz plots* provide a means to find cor-

relations between the different decay particles. The reconstructed invariant mass of a subset of particles is plotted versus another combination of these particles.

The Dalitz plot of $p\bar{p} \to \pi^0\pi^0\pi^0$ of the Crystal Barrel Experiment (fig. 1.4) attracted some attention. The invariant mass of pion 1 and 2 is plotted versus pion 2 and 3. Several resonances with characteristic orbital momenta can be identified, among them a state called $f_0(1\,500)$. From the decay pattern Crystal Barrel claims that this structure is a prime candidate for the ground state scalar glueball.

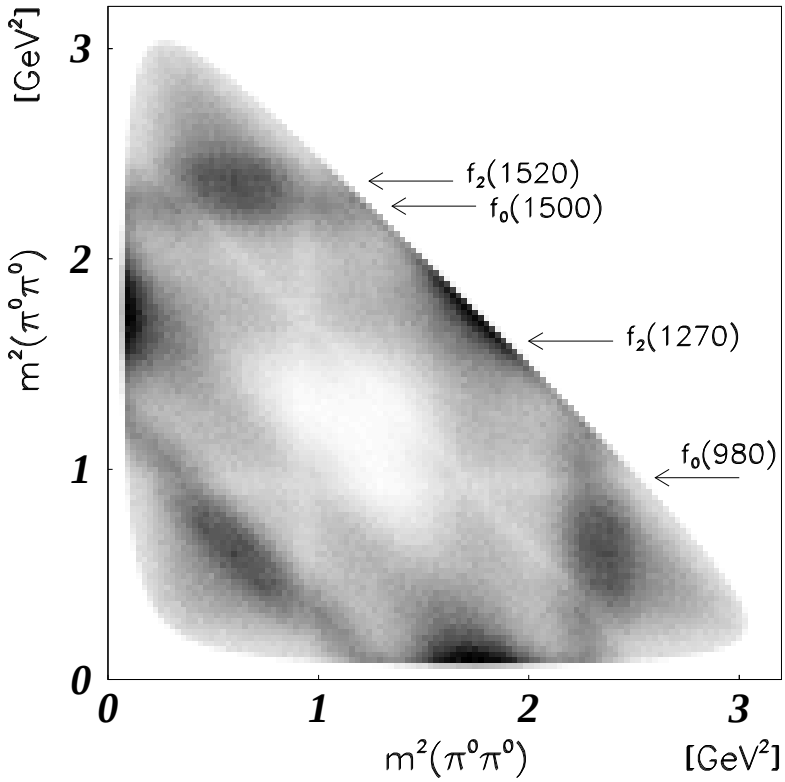

Figure 1.4: *Dalitz plot for $p\bar{p} \to \pi^0\pi^0\pi^0$. The resonance $f_0(1\,500)$ is claimed to be a glueball. (from [CB98])*

The *Partial Wave Analysis* (PWA) turned out to be an efficient way to separate different resonances: one makes use of the different orbital momenta of the resonances, which lead to a characteristic angular distribution in space. Sorted in such "partial waves", resonances can be identified more easily against the harsh background.

Both Dalitz plot and PWA require large statistics. For the clear identification of exotics it is important to map out the decay channels, including less prominent ones. COMPASS with its high rate of precise data will help to extract and identify these very interesting objects from the background.

Primakoff Scattering

The lightest and the simplest quark system is the π. It consists of one quark ($\mathtt{u}$ or $\mathtt{d}$) and one anti-quark ($\bar{\mathtt{u}}$ or $\bar{\mathtt{d}}$). As free quarks have not been observed yet, the π is the ball park for hadron physicists to learn about quarks and their interaction inside hadrons. The theoretical basis is quite

well understood: the π plays an important role in *chiral perturbation theory* (χPT), which has been very successful in the description of strong interacting systems at low energies in the last few years.

To find out more about the forces keeping the two quarks together one wants to see the influence of electromagnetic fields acting on the (electrically) charged quarks. The *polarizability* in particle physics follows an idea known from classical electrodynamics: a susceptibility χ is defined via the polarization $\vec{P}$ induced by an electric field $\vec{E}$, $\vec{P} = \chi\vec{E}$. It turns out that the π is a very stiff object and despite the fact that its components q and $\bar{q}$ have opposite electric charge it is very difficult to stretch it and induce an electric or magnetic dipole moment. In next-to-leading order calculations the current predictions differ from the experimental results by at least 2 standard deviations : whereas χPT predicts 2.4$\pm$0.5 and -2.1 $\pm$ 0.5$\times 10^{-4}$ fm^3 for the electric and the magnetic polarizability respectively [Bur96], the latest experimental results are 5.6$\pm$1.6 and -6.7$\pm$2.0$\times 10^{-4}$ fm^3 [Ant83, Ant85]. One therefore needs new experimental input with higher precision to either confirm or reject existing data or predictions.

As the π has a lifetime of only 10^{-8} s it is impossible to make a π target. One therefore has to turn to *inverse kinematics*, where a π-beam is scattered off the electric field of a high-Z nucleus, makes a so-called *inverse Compton* or *Primakoff reaction* and produces a real photon γ, see fig. 1.5.

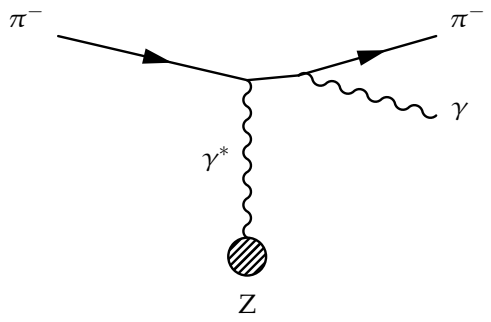

Figure 1.5: *Compton Scattering in inverse kinematics:* Primakoff Scattering. *The π is scattered off the electric field of a nucleus, a real photon is produced.*

The cross section has a strong dependence on the four-momentum transfer t from the incoming π to the target nucleus. In inverse kinematics it is convenient to go to the *projectile frame* (CMS of the π). The differential cross section then simplifies to:

$$\frac{\mathrm{d}^3\sigma}{\mathrm{d}t\,\mathrm{d}\omega\,\mathrm{d}\cos\theta} = \frac{\alpha}{\pi}\,\frac{Z^2}{\omega}\,\frac{t-t_0}{t^2}\,|F_A(t)|^2\,\frac{\mathrm{d}\sigma_{\mathrm{Comp}}(\omega,\theta)}{\mathrm{d}\cos\theta} \tag{1.3}$$

where α and Z are the electromagnetic coupling constant and the charge of the nucleus, θ and ω are the photon deflection and energy respectively. The minimum momentum transfer is $t_0 = {m_\pi\omega}/{p_{\mathrm{beam}}}$. F is the electromagnetic form factor of the nucleus and approximately 1 for the observed t range. The polarizabilities are hidden in the Compton cross section $\mathrm{d}\sigma_{\mathrm{Comp}}$.
The cross section increases for a target material with a high nuclear charge Z and for small momentum transfer t, with a maximum even for no momentum transfer at all (so-called *quasi-real photons*). While there are many processes leading to a π and a γ in the final state, only the single-photon exchange has a pole at t=0. A cut on small momentum transfers therefore reduces the background significantly. On the other hand such a cut also makes the measurement more difficult, as the scattered π is very close to the path of the non-scattered π.

Simulations have shown [Kuh01] that with its high event rate COMPASS will collect more Primakoff events in a few weeks than observed up to now. The experimental setup is rather "simple", thus the Primakoff program is already feasible with the initial-phase layout. Good tracking close to the beam and a highly precise electromagnetic calorimeter are needed. For 2004 a total of 4 weeks of π-beam is planned, which should be sufficient to decide on the current discrepancy between data and predictions.
COMPASS has the unique possibility to extend the measurement of polarizability to the next heavier hadron, the kaon.

Charmed Baryons

After the formulation of the SU(3) flavor group, which describes the similarities among u, d and s quarks, the scheme was soon extrapolated to additional, yet unobserved quark types. An even better motivation was provided by the GIM mechanism [GIM70], a theory in which the simple phenomenological model of weak interactions involving a single charged vector boson is considered as a quantum field theory. In higher orders of perturbation theory divergences show up, which the authors propose to absorb via the introduction of a 4^{th} "fundamental fermion", thereby revealing a suggestive lepton-quark symmetry. Following the rules of group theory, two baryonic (fig. 1.6) and two mesonic multiplets could be set up, predicting hadrons with c-content. In 1975 the c quark was finally found with the discovery of the J/ψ, consisting of $c\bar{c}$.

It turned out that while u, d and s have a rather similar mass of around 100 MeV, the c quark is much heavier (around 1 000 MeV). Consequently the symmetric behavior is less good when the c-quarks are included. On the other hand a larger mass results in a smaller binding distance, which can also be seen as an advantage: the c is already heavy enough for first perturbative methods of QCD to be applicable again, here in the framework of *Heavy Quark Effective Theories* HQET.

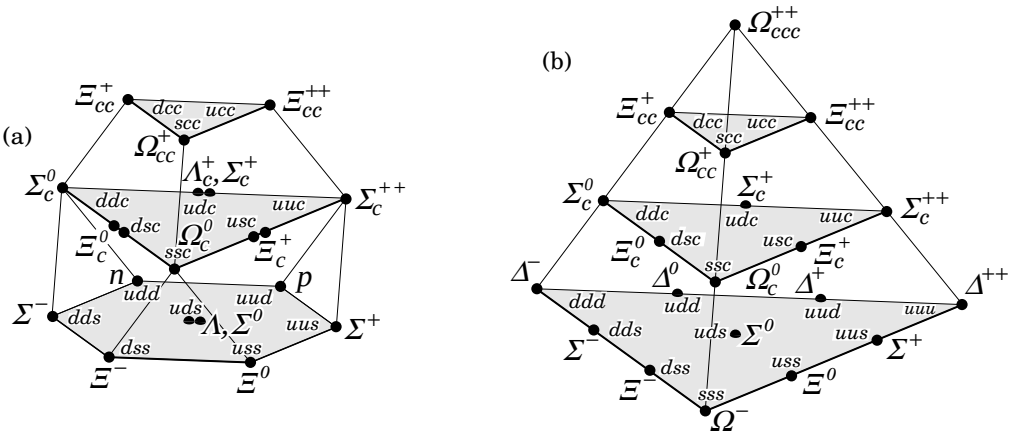

Figure 1.6: *SU(4) multiplets of baryons made of* u, d, s *and* c *quarks. The ground states have a total orbital momentum of* ***a)*** *J=1/2 or* ***b)*** *J=3/2. (pictures from [PDG00])*

While the knowledge about charmed mesons ($q\bar{q}$) is rather sound, most charmed baryons (qqq) are still an experimentally challenging subject: masses, lifetimes and decay widths still have rather large errors. In contrast to the singly charmed baryons, for which all ground states have at least been observed, basically nothing is known about doubly charmed baryons. Just recently the

first observation of Ξ_{cc}^{+} (ccd) was reported [Selex02], showing a lifetime significantly shorter than the predictions of 100 and 500 fs.

The charmed and doubly charmed baryons open a new field of investigation. First there seems to be a noticeable interference among the products of a weak decay: while the *spectator diagram* (similar to fig. 1.7a) is the main contribution to the decay width for mesons , in baryon decay the resulting s-quark might "feel" [Ric02] the presence of a second s, and strength is shifted to the less well understood internal W-exchange in fig. 1.7b) and c). For the description of the decay width all diagrams have to be taken into account.

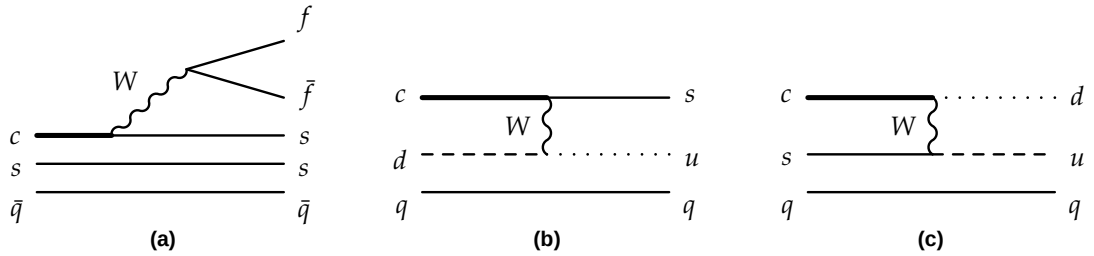

Figure 1.7: *Some decay diagrams of charmed baryons:* ***a)*** *spectator diagram with* ss*-interference,* ***b)*** *W-exchange for ordinary hadronic decay,* ***c)*** *W-exchange for suppressed decay.*

Second, baryons with two heavy quarks combine two extreme regimes in a single system: the relatively slow motion of two heavy quarks like in charmonium with the fast motion of a light quark, which might be even more relativistic than in the case of light meson. There are many theoretical predictions concerning doubly charmed baryons spectroscopy, but the question if the c is heavy enough for these effective theories to work remains.

Starting from a very high interaction rate of the order of 100 kHz, COMPASS will concentrate on high multiplicity events (as high as 10) and a large transverse energy in the calorimeter (> 5 GeV). Semi-leptonic decays are cleaner: when an additional μ is required in the final state, the background situation is a bit relaxed and the cut on the transverse energy can be reduced. An OR of both schemes is planned. A very high readout speed has to follow, combined with a second and third level trigger for track reconstruction and particle identification on the fly. First estimates range between 100 (pessimistic case) and 10 000 doubly charmed baryons in 100 days (to be compared with 15.9 Ξ_{cc}^{+} from [Selex02]).

The requirements for the setup are severe. Some optimizations have already started (e.g. the so-called *Online Filter* [4]), others still have to be developed, but are on solid grounding (e.g. updates of readout electronics). Doubly charmed baryons are therefore only on the list of long-range plans after 2006.

1.2 Transverse Λ^0 Polarization

Naively one would not expect polarization effects in a one-particle *inclusive* reaction like

$$a + b \rightarrow c + X, \tag{1.4}$$

[4] This is a software package developed for the 2003 run, which runs on the data acquisition computers and uses relatively simple methods to filter events which cannot be reconstructed. It is the ideal playground to gain experience in technical details and physical understanding for the Charm filters.

where only the particle of interest c is detected in the final state. When the available center-of-mass energy $\sqrt{s}$ is big enough, there are many different possibilities for X. As in *inclusive* reactions one sums over all available inelastic channels, which should have polarization of random magnitudes and signs, the sum should average to zero. Latest in high-energy collisions, the spin-flip amplitudes were thought to be too small compared to the involved energies to play an important role in production processes. The increasing multiplicity should further dilute a possible polarization signal.

But contrary to this anticipation, it seems that the particle spin *does* play an important role in the production of particles. In 1975 Λ^0 hyperons produced in pp collisions at low energy ($6\,\mathrm{GeV/c}$ in [Les75]) were found to be polarized and, even more surprisingly, this phenomenon remained at high energies: in 1976 polarized Λ^0s were found to emerge from unpolarized 300 GeV p scattering off a Be target with a polarization of up to $P_n = 0.28 \pm 0.08$ [Bun76].

The polarization found does not depend on the spin states of either beam or target particle and is therefore sometimes called *spontaneous* polarization. Due to the spin conservation in strong and electromagnetic interactions, it can only be directed normal to the production plane spanned by the incoming p-beam and the outgoing Λ^0. It is therefore called "transverse polarization" and receives the index "n" for "normal" in short notation, P_n. The geometry will be explained in more detail in section 5.2, especially in fig. 5.4. Transverse polarization should not be confused with so-called *spin transfer reactions*, where one wants to measure the spin distribution of s-quarks stemming from polarized targets nucleons, which *transfer* their spin from the target nucleon to the final state hyperon. In such cases spontaneous and transferred polarization adds up. For longitudinally polarized targets or beams, additionally *longitudinal* polarization pointing along the direction of motion of the hyperon is possible.

Since 1976 transverse polarization has been observed in further reactions, mainly in the production of (almost all) hyperons in various environments ranging from ordinary proton via meson to neutrino beams, but also in Z^0 decays at LEP. Yet it still cannot be comprehensively described. It is likely to originate from several sources, being related to either the structure of the nucleon itself or to the production process. Models range from simple constituent quarks to parameterizations based on QCD.

In this context it is interesting to mention the phenomenon of *transverse single spin asymmetry* A_N (analyzing power), which looks like an "inverse process": for a transversely polarized beam (particle a in eq. (1.4)) the particle produced (particle c) shows a non-uniform distribution with respect to the direction of the beam polarization. A third spin variable is the *polarization transfer* or *depolarization* D_{NN}, which can be defined, when both particles a and c are polarized. A_N and D_{NN} will not be treated further here, an overview can be found in [Bra98]. Doncel and Mendez have shown in 1972 [DM72] that polarization P_n, analyzing power A_N and polarization transfer D_{NN} should follow the relations $1 \pm D_{NN} \geq |P_n \pm A_N|$.

The spin has proven to be a very sensitive probe for the forces reigning the domain of hadrons. A closer investigation of the transverse polarization therefore could provide invaluable and completely new insight into the field of "spin physics" and the structure of the nucleon and its constituent quarks and might also yield a better understanding of the hadronization process. Since Bunce et al. [Bun76] much theoretical progress has been made and reviews of both the experimental [Fel97, Bra98, Abr01] and theoretical [Fel99, Sof99] situation are available.

While much data on Λ^0 production have been collected in the hadronic environment like pN-collisions, COMPASS has the unprecedented chance to look at this phenomenon from a different point of view, namely the *photo-production* of Λ^0. A first set of data was investigated, but not published, by the HERMES collaboration [Bru03]. In COMPASS the field opens to measure Λ^0 polar-

ization very precisely in leptonic reactions. The first measurement was carried out in this work. With [ABDM02] a first model based on the experience gained from pp data has been transferred to the production of Λ^0 in *semi-inclusive Deep Inelastic Scattering* (SIDIS) with leptonic probes and can be tested.

In this section more information on transverse Λ^0 polarization is presented. After a motivation of the Λ^0-channel and some general remarks in section 1.2.1, more details on the experimental phenomenology will be given in section 1.2.2, before in section 1.2.3 an overview of the different models follows. The actual measurements with COMPASS will then be presented later in this work in chapters 5 and 6.

1.2.1 General Remarks

Polarization and Quantization Axis

A sample of Λ^0 is called *polarized* when the average number of particle spins pointing along a certain *quantization axis* is different from zero, $P = <\vec{\sigma}\cdot\vec{n}>$, where $\vec{n}$ is the quantization axis and $\vec{\sigma}$ the spin operator. Being a spin-1/2 particle, the product can be simplified to

$$P = \frac{N^{\uparrow} - N^{\downarrow}}{N^{\uparrow} + N^{\downarrow}}, \tag{1.5}$$

where $N^{\uparrow}$ is the number of Λ^0 with spin pointing along the axis of quantization and $N^{\downarrow}$ the number of Λ^0 with spin pointing in the opposite direction.

A practical problem is to choose the quantization axis. As was already indicated above, the *production plane* spanned by the incoming beam and the outgoing Λ^0 is taken as reference. For transverse polarization the normal to this production plane $\vec{n} = (\vec{p}_{\text{beam}}\times\vec{p}_{\Lambda^0})/|\vec{p}_{\text{beam}}\times\vec{p}_{\Lambda^0}|$ is taken as quantization axis. Other possibilities are *longitudinal* and *sideways* polarization, where the quantization axes are chosen as $\vec{n}_l = \vec{p}_{\Lambda^0}/|\vec{p}_{\Lambda^0}|$ and $\vec{n}_s = (\vec{n}\times\vec{p}_{\Lambda^0})/|\vec{n}\times\vec{p}_{\Lambda^0}|$.

The Weak Decay of Hyperons

In general the measurement of polarization is rather difficult as the spin-distribution is not directly accessible in most cases. For most hyperons a rather elegant occasion arises: they can only decay via a weak process, in which the s-quark decays into a u-quark and an additional π^-, as depicted in fig. 1.8 for the Λ^0. In such processes parity is violated and the angular distribution of the decay particles in the hyperon rest frame can be distorted depending on the initial polarization according to:

$$\frac{\mathrm{d}N}{\mathrm{d}\cos\theta'} = A(1 + \alpha P\cos\theta'). \tag{1.6}$$

θ' is the angle between the direction of the decay particle and the quantization axis in the rest frame of Λ^0, and P is the polarization with respect to this axis. α is the decay asymmetry parameter specific for each particle and each decay channel. Some values of α can be found in table 1.1. A is the normalization. When one properly corrects for acceptance, a possible polarization can therefore be extracted as the slope in an otherwise flat distribution in $\cos\theta'$.

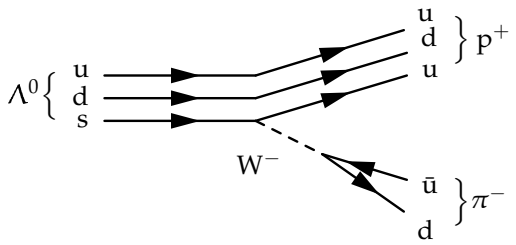

Figure 1.8: *Decay of Λ^0 into p and π^- via Intermediate W-Boson.*

hyperon	decay channel	BR (%)	α
Λ^0	$p\pi^-$	63.9±0.5	0.642±0.013
Λ^0	$n\pi^0$	35.8±0.5	0.648±0.047
Σ^+	$p\pi^0$	51.57±0.30	-0.980 $^{+0.017}_{-0.015}$
Σ^+	$n\pi^+$	48.31±0.30	0.068±0.013
Σ^-	$n\pi^-$	99.848±0.005	-0.068±0.008
Ξ^0	$\Lambda\pi^0$	99.54±0.05	-0.411±0.022
Ξ^-	$\Lambda\pi^-$	99.887±0.035	-0.293±0.007
Ω^-	ΛK^-	67.8±0.7	-0.026±0.026

Table 1.1: *Asymmetry parameter α for the decay of different hyperons into different channels. The branching ratios BR are given as well. (from [PDG00])*

The Λ^0 Hyperon

For the systematic study of polarization effects the Λ^0 is a very interesting particle for several reasons: it shows a rather high asymmetry α=0.64 for an experimentally easily accessible decay into the two charged particles p and π^- with a sufficiently high branching ratio of 64%. In 2-body decays the angular distributions of the daughters are strictly correlated. The polarization of the Λ^0 can therefore be extracted from the asymmetric distribution of either of the two daughters. For the definition of the sign of α the preferred direction of the leading baryon (here the p) is taken. The clear signature of this decay channel leads to the picture of the "self analyzing" Λ^0 decay [5].

Furthermore Λ^0 is the lightest hyperon and therefore produced in a comparatively large number. A small problem arises when Λ^0 is not produced in the primary interaction, but stems from the decay of heavier particles like $\Sigma^0 \rightarrow \Lambda^0\gamma$ or $\Xi \rightarrow \Lambda^0\pi$. Such Λ^0 will experience (if at all) a different polarization mechanism and therefore dilute the primary signal. If this cannot be excluded in the analysis by testing the vertex position(s) or the invariant mass of Λ^0 plus "something", it needs to be taken into account in theoretical descriptions. The fraction of Λ^0 stemming from the most important resonances can be estimated (as is done in e.g. Liu et al. [LXL01]).

In the constituent quark picture Λ^0 is the isospin singlet with quark content (uds). According to SU(6) symmetry, the spins of u and d are anti-parallel and compensate each other. The spin of the Λ^0 is therefore almost entirely carried by the s-quark. The cancellation of u- and d-spin facilitates the modeling of the Λ^0- spin as only the s-spin has to be taken into account.

[5] M. Anselmino, one of the leading theorists on spin physics, says the Λ^0 "reveals its polarization by itself" and calls it therefore a "nifty particle" [Ans03].

1.2.2 Experimental Phenomenology

A large amount of very significant data for hyperon- and anti-hyperon inclusive production with a rather broad energy spectrum of protons has been accumulated. Some of them exhibit a regular pattern, which may help to uncover the underlying production mechanism. In the following a summary of some commonly found features is given ([Bra98, Sof99]).

Direction: The polarization of hyperons is normal to the production plane.

Transverse Momentum: There is a strong dependence on the transverse momentum of the hyperon with respect to the incoming beam, p_T. For Λ^0 the magnitude of P_n increases linearly with p_T and reaches a plateau at around 0.7-1.0 $\mathrm{GeV/c}$, above which it remains constant.

Longitudinal Momentum: The second strong dependence is that on the longitudinal momentum of the hyperon with respect to the incoming beam in the center-of-mass (CMS) of the event, p'_z, or its reduced momentum *Feynman's* x_F[6]. P_n increases linearly with x_F.

Beam Energy: The Λ^0 polarization is (almost) independent of the beam energy over the measured interval of 10 - 2 000 $\mathrm{GeV/c}$. As will be shown below, this is not necessarily true for other hyperons.

Target Nucleon: There is a small dependence of the polarization on the nuclear mass of the target type (A-dependence).

Other Hyperons: Almost all hyperons are found to be polarized in the beam fragmentation region, but while the size is similar, the direction along the quantization axis can be different: $P_{\Sigma^0} \approx P_{\Sigma^+} \approx P_{\Sigma^-} \approx -P_{\Lambda^0} \approx -P_{\Xi^0}$, but $P_{\Omega^-} \approx 0$. A small overview[7] is plotted in fig. 1.9.

Anti-Hyperons: Some anti-hyperons produced by protons are also polarized: on the one hand $P_{\Lambda^0} \approx P_{\Xi^0} \neq 0$ and $P_{\bar{\Lambda}^0} \approx P_{\bar{\Xi}^0} \approx 0$, but on the other hand $P_{\bar{\Sigma}^-} \approx P_{\Sigma^+}$ and $P_{\bar{\Xi}^+} \approx P_{\Xi^-}$.

As the energy range increases and the variety and amount of data has increased as well, these features have become more striking. While the data on other hyperons are not as extensive as for Λ^0, they *basically* show a similar kinematic behavior, but with different signs and magnitudes of the polarization. In few cases, however, differences also show up in the *functional* dependence of the polarization with beam energy, p_T and x_F. According to Dureya et al. [D$^+$91] Ξ^- shows a different p_T/x_F pattern. The energy dependence of both Σ^+ and Ξ^- is unclear: while Bravar states [Bra98] an energy dependence for both particles, Soffer wants [Sof99] the Ξ^- to be constant with energy and Abramov traces the energy dependence of Σ^+back to different target materials (Be,Cu) and slightly different x_F for the used beam energies 400 and 800 $\mathrm{GeV/c}$ in the respective measurements [Abr01].

Felix emphasizes the importance of channels with specified final state [Fel96, Fel97, Fel99, Fel03]. The relevant parameter is the *diffractive mass* M_X, which is understood as the mass of the set of

[6] x_F is defined as the amount of momentum p_z carried by the hyperon with respect to the maximum momentum available from the interaction $p_{z\,\mathrm{max}}$ along the direction of the beam particle: $x_F := p_z/p_{z\,\mathrm{max}}$. Connecting only the momenta it cannot be Lorentz-invariant. Usually it is quoted for the center-of-mass system of beam and target particle, where the interpretation is very descriptive: everything moving forward is likely to be a modification of the beam particle and is called the *Current Fragmentation Region*, everything moving backward is labeled *Target Fragmentation Region* and understood to be mainly originating from the target nucleon. In this system x_F ranges from -1 for the target fragmentation region to +1 for the current fragmentation region. In the CMS it can be calculated $x_F = 2p'_z/\sqrt{s}$, where s is the squared total CMS energy.

[7] Bravar calls it an already "classic" plot in this field [Bra98].

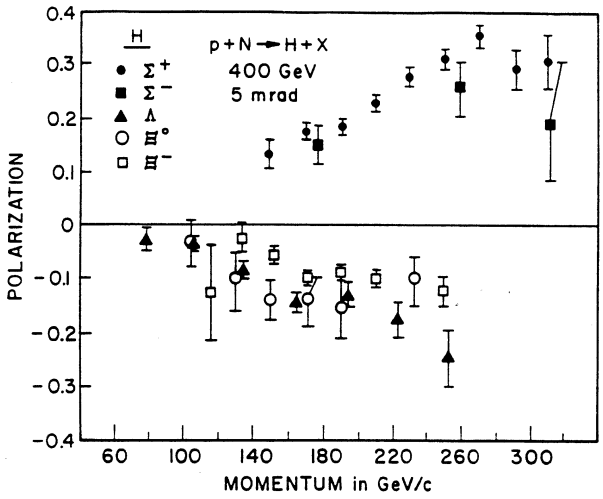

Figure 1.9: *Polarization of different hyperons H in $p + N \rightarrow H + X$ as a function of their momentum p_Y. The hyperons are produced at a fixed angle of about 5 mrad with a 400 GeV/c proton beam ($< x_F > \approx p_H/p_B$ and $< p_T > \approx p_H \times 0.005$). (from [Bra98])*

particles diffractively created or the mass of a subset of diffractively created particles [Fel97]. He points out that x_F, p_T and M_X are related to each other via $E^2 = {p_T}^2 + \frac{1}{4} s {x_F}^2 + M^2$ and that therefore P_n should show a similar dependence on M_X and p_T.

An extensive compilation of the latest experimental data is done by Abramov and can be found in [Abr01]. The author parametrizes the polarization of many different reactions (produced hyperons, beam particles, beam energies, target nuclei) as function of p_T and two scaling variables $x_{A\pm} = x_R \pm x_F/2$. Here, x_R is the analogon to x_F as defined above for the total momentum: $x_R := p'/p'_{\max}$ with p' as the total momentum of the produced hadron and $p'_{\max}$ its maximum possible value in the CMS. Abramov compares his parametrization with a large number of hyperon decays and gives thus a very good overview over the existing data. It is interesting to note in this context that Abramov implements the $x_{A\pm}$ dependence as a sine-function $\sin[\omega(x_{A\pm} - x_1)]$, which allows the reproduction of such features as an approximate linear dependence of P on x_F for Λ^0 and a non-linear, sometimes even oscillating behavior for other hyperons (e.g. $pA \rightarrow \Xi^- X$, see [Abr01] for more examples). The data seem to indicate that the oscillation frequency ω depends on the number and flavor of the involved quarks.

The features of Λ^0 polarization have led to the idea that polarization is primarily a leading particle effect, i.e. that the polarization is a consequence of the beam proton fragmentation mechanism. Thus there should be no polarization for particles that do not share any quarks with the incoming projectile, such as Ω^- and anti-hyperons. Indeed, it has been observed that Ω^- and $\bar{\Lambda}^0$ produced by p are not polarized. Against all expectations, however, large polarization has been found for $\bar{\Xi}^-$ and $\bar{\Sigma}^-$ produced with p.

Many interpretations of the polarization are based on quark parton models and especially on the effect of highly polarized s-quarks. For systematic reasons it is therefore interesting to extend the investigations to the production of *charmed* particles to see the influence of the larger mass of the c-quark [Bra98, Pau04].

1.2.3 Theoretical Ideas for Transverse Polarization

Many theories make an attempt to explain the transverse polarization of hyperons, but up to now none was able to comprehensively describe this effect. In this section some general ideas and some models are introduced to give a rough insight into the rich activity connected to this physics topic.

Spin-Flip Amplitudes

From the definition of polarization as given before as

$$P = \frac{\mathrm{d}\sigma^{\uparrow} - \mathrm{d}\sigma^{\downarrow}}{\mathrm{d}\sigma^{\uparrow} + \mathrm{d}\sigma^{\downarrow}}, \tag{1.7}$$

where the arrows at the cross-sections $\mathrm{d}\sigma$ indicate the different spin states of the Λ^0, one can already make a simple, but important conclusion. By using the generalized optical theorem, one can describe the unpolarized inclusive cross-section $\mathrm{d}\sigma = \mathrm{d}\sigma^{\uparrow} + \mathrm{d}\sigma^{\downarrow}$ by means of the forward, non-spin-flip (f_+) and spin-flip (f_-) amplitudes:

$$P\,\mathrm{d}\sigma = Im(f_+^* f_-). \tag{1.8}$$

For a non-vanishing polarization P, f_- has to be non-zero and furthermore should have a phase difference with f_+. For a real understanding of the polarization phenomena, such a phase shift should be taken into account. According to [Sof99] this is another way to say that a non-zero P corresponds to a non-trivial situation, reflecting a high coherence effect among different inelastic channels. While in low energetic exclusive reactions only few amplitudes participate and have to interfere constructively, the number of participating amplitudes in high-energy reactions is larger and makes such polarizing effects even more surprising.

Kinematical Regions

Soffer [Sof99] distinguishes between two different kinematical regions with respect to the relative longitudinal momentum x_F and the transverse momentum $x_T = {}^{2\cdot p_T}/\sqrt{s}$:

- In the **beam fragmentation region** Λ^0 carries a sizable fraction of the longitudinal momentum, e.g. $0.3 < x_F < 0.8$ and at the same time a small transverse momentum $0 \leq x_T < 0.15$. The **target fragmentation region** is similarly defined, but with opposite sign in x_F.

- In the **hard scattering region** the Λ^0 carries a large transverse momentum, say $x_T \geq 0.15$, with a negligible longitudinal momentum $x_F \sim 0$.

Rather different dynamical mechanisms are expected to be at work in these different kinematic regions. As the hard scattering region is difficult to access due to statistical reasons and not in the reach of COMPASS, only the first case, the fragmentation region with a limited transverse momentum, will be reviewed here in more detail.

Fragmentation Region

While the hard scattering region involves short-distance interactions and allows a treatment with perturbative QCD, the fragmentation region is essentially based on low energetic (*soft*) processes, where perturbative QCD is not applicable anymore.

Semi-classical models try to describe the hyperon polarization on the pure level of the parton model and fully ignore the relevance of the phase shift between the spin-flip and non-spin-flip amplitudes. Thus predictions going beyond a qualitative description of the effect cannot be expected. Nevertheless they give an intuitive picture of the production mechanism and two models will therefore be shortly mentioned here. Such models have in common that the s-quark provides spin, polarization and part of the transverse momentum of Λ^0. Their difference lies in the source of the s-quark and the way it gets its polarization.

In the *Lund model* [AGIS83] one assumes that Λ^0 is generated by replacing one u-quark in the p with an s-quark from the target sea. An incoming (ud)-diquark with spin $S = 0$ and isospin $I = 0$ scatters and stretches the confined color field of the target nucleon like a "string" until it breaks into an ($s\bar{s}$)-pair. The s-quark then combines with the (ud)-diquark and forms the Λ^0. If the ($s\bar{s}$)-string now has a transverse momentum, its stretching leads to an orbital momentum, which is assumed to be compensated by a polarization of the ($s\bar{s}$)-pair. As the s-quarks are expected to contribute partly to the transverse momentum of the Λ^0, the selection of high p_T of Λ^0 will also mean a selection of ($s\bar{s}$)-strings with large transverse momenta and therefore enhance the polarization. While this model is rather successful in deriving the *direction* of polarization for different hyperons from SU(6) symmetry, it is quite weak in the absolute magnitudes and the p_T-dependences. It does not suggest any dependence on x_F at all, nor does it give any hints on anti-hyperon polarization. Finally it "predicts" a correlation of the polarizations of the s- and the $\bar{s}$-quark which could not be confirmed in experiment (exclusive production of $\Lambda^0 K^+$ in [Fel96]).

In the *recombination model* [DMM85] a similar idea is pursued: again an s-quark has to be combined with a (ud)-diquark from the beam. But this time the different velocities of beam and target are stressed: the (slow) s-quark has to be accelerated to reach the (fast) beam diquark and thus its spin experiences a kind of *Thomas precession* $\vec{\omega}_T$ normal to the production plane. The energy stored in this precession is smallest when the spin $\vec{S}$ is anti-parallel to the precession $\vec{\omega}_T$, which makes this direction preferable. Although this approach is different from the Lund model, it seems to lead to similar observable effects. It is interesting to note that in the beam fragmentation region of the inclusive reaction $K^- p \to \Lambda^0 X$ the s-quark comes from the beam particle and has to be decelerated when joining the (ud)-diquark from the target. According to this model, the direction of polarization should therefore be inversed, in accordance with the data. But the magnitude of the polarization in $K^- p$ is roughly twice as large as in pp, a fact which the simplest version of this model fails to explain. The recombination model has further disadvantages. Firstly the polarization for anti-hyperons has to be 0, which is true for $\bar{\Lambda}^0$, but not in general for all anti-hyperons. Secondly the concept of Thomas precession is not per se excluded for the remaining diquark and thus should depend on its spin state as well. This leads to the unsatisfactory situation that more parameters have to be introduced to make relative predictions between several inclusive reactions.

In **Regge type models** the idea of the phase difference between f_+ and f_- is taken more seriously. The *Milano model* [BPR92] suggests that this phase might result from final state interactions, more precisely from the production of various baryon resonances, in general out of phase, which then decay into the observed Λ^0. For the Λ^0 production three mechanisms are considered: (a) direct, (b) intermediate baryon dissociation (Σ, $\Sigma^\star$) and (c) Σ^0 electromagnetic decay. Unlike others this model gives a reasonable description of the *unpolarized* cross section first and then modifies it

for the *polarized* case. The dependencies of P_n on p_T and x_F result from the different behavior of the production mechanism. While correct direction and magnitude can be achieved for low p_T, for higher p_T the unpolarized direct production starts to dominate and leads to a decrease of the polarization. This is, however, contradicted by experimental findings. Furthermore it seems to be difficult to extend this scheme to Σ and Ξ, as more and more resonances have to be included.

Another interesting approach is the *one-pion-exchange model* [ST92], in which the Λ^0 production in the fragmentation region is assumed to be dominated by *reggeized* one-pion-exchange. In such an approach an interaction is described as the exchange of a whole series of intermediate particles which are classified to be on the same Regge *trajectory*. But when quantum numbers allow, hadronic amplitudes have strong contributions from pure pion exchange anyway, and these contributions get even larger at small momentum transfers. In this model therefore the whole Regge trajectory is reduced to the binary reaction $p\pi \rightarrow K\Lambda^0$ as the leading contribution to the Λ^0-production process. The final $pp \rightarrow K\Lambda^0 X$ cross section is then obtained by integrating over the K phase space. All the basic features of the Λ^0 spectrum are predicted without additional parameters. The polarization of Λ^0 in πp reactions is essentially negative and thus leads to a negative Λ^0 polarization, which is compatible with the experimental values. While an extension to Σ looks promising, unfortunately it seems impossible to apply this idea on K-induced reactions like $K^-\mathrm{p} \rightarrow \Lambda^0 X$.

1.3 The COMPASS Spectrometer

1.3.1 General Remarks

The physics channels of interest have both small cross sections and small branching ratios and at the same time the data have to be accurate to distinguish among the different, existing models. The key feature of COMPASS is therefore the collection of a large amount of data with high resolution. These two points, *high statistics* and *high precision*, were the basis of all design decisions and had to be taken care of under many different aspects. Additionally the broad physics spectrum required a very flexible setup, which can be quickly adjusted to different measurements.

High Statistics

High Intensity Beams. The *Super Proton Synchrotron* (SPS) delivers up to 2×10^8 μ and 10^8 p,π and K to the COMPASS target every 16.8 s. The particles arrive randomly distributed within a so-called *spill* of 4.8 s.

High Trigger Rates. The trigger decision only ensures that a μ is separated from the non-scattered beam and points back to the target. In 2002 this resulted in a total trigger rate of approx. 22 000 events per spill (i.e. 4 kHz in-spill rate). For the hadron program the cross-sections are much higher and trigger rates up to 50 kHz are planned and needed.

High Readout Speed. COMPASS aims for a readout with the smallest dead-time possible: all stages of the readout system are designed to buffer the incoming data in local memories and thus block the readout process only for a minimum of time. Like this the collection of the data can be stretched over the full SPS cycle. As parts of the readout electronics were only available as prototypes, in 2002 the dead-time was fixed by the DAQ to $\sim$7%.

High Data Rate. With an event size of approx. 40 - 45 kBytes, the data per spill add up to approx. 900 MByte and approx. 4.4 TByte per day. In the 110-day-long running in 2002, $5 \cdot 10^9$ events were collected, resulting in a total of 260 TByte (see also fig. 5.1 in chapter 5).

Time Resolution. With an average time of 25 ns between two consecutive incoming beam particles, the detectors also have to be able to resolve the high beam rate and to attach all observations to the correct primary interaction. The region of the beam is equipped with very fast scintillating fibers with a time resolution of 350 ps. They are well suited to resolve every single beam particle. Silicon Microstrip detectors provide additional spatial resolution for the beam (14 μm with 3 ns time resolution).

Radiation Damage. The beam rate is so high that special precaution for all detectors is needed to make them stand several years of running. Most detectors have a hole in the beam region to avoid damaging of the active material directly by the beam. In addition radiation-hard materials were chosen (e.g. for the Scintillating Fibers). The Silicon detectors use the *Lazarus Effect*, which will be explained in more detail in chapter 2.

Reconstruction Time. Last but not least the data also have to be processed. An object-oriented software framework was developed within the COMPASS collaboration (CORAL, for more details see section 4.2). The reconstruction time is currently around 500 ms per event. It runs on the CERN batch computer pool on 500 Pentium type CPUs in parallel.

High Precision

Two Stage Spectrometer. One of the most pronounced features of the experimental setup is the structure as a double-stage spectrometer, for which two magnetic spectrometers are positioned behind each other. The first one has a relatively small integrated magnetic field of 1.0 Tm and is well suited for analyzing low momenta particles in the range of 5-50 GeV with large angles. It is therefore called *Large Angle Spectrometer* (LAS). The momentum resolution $\Delta p/p$ is 1 to 2 %. The calorimeters of the first spectrometer have a hole in the middle through which high momenta particles can pass to the second spectrometer without disturbance. The *Small Angle Spectrometer*, SAS, has a much stronger magnetic field integral of up to 5.2 Tm and has enough strength to give a measurable push to particles with momenta between 30 and 100 GeV. With a total spectrometer length of ~ 60 m even beam muons which experienced only a small energy loss in the target can be separated from the non-scattered beam.
Both spectrometers are designed with trackers before and after the magnet for the momentum measurement of charged particles, electromagnetic and hadronic calorimeters for neutral particles and separation between hadrons and electrons and photons, RICH detectors for $p/\pi/K$ separation and a μ detection system.

Staggered Tracking System. As the track density varies with the distance from the beam line, COMPASS uses a so-called *staggered tracking system*, for which detectors with different structure sizes are combined at one position along the beam. They cover different regions around the beam, so that they have similar occupancies: *Large Area Trackers* (LAT) with a large acceptance form a tracking station together with *Small Area Trackers* (SAT) with a smaller size, but a higher space resolution. In some regions additionally *Very Small Area Trackers* VSAT are added in the center with an even smaller size and a still higher space resolution. Examples are given in table 1.2.

Multiple Scattering. To measure tracks with high resolution not only precise detectors are needed, but the interference of the detector with the particles, here the multiple scattering,

has to be kept small as well. In COMPASS the mass inside the beam is carefully optimized: materials with high radiation lengths are chosen for the detector design, electronics and frames are mounted outside the acceptance, entry windows are kept as thin as possible, the RICH contains a separate gas volume with lower mass density for the beam passage (3.3 m of He).

Flexible Setup

Different beam particles and energies. A key feature of the wide physics spectrum is the usage of different types of beam particles (μ, p, π and K) and momenta (100 to 300 $\mathrm{GeV/c}$). For calibration purposes low intensity electron beams are also available.

Several Targets. The different physics programs require several targets. The most complicated one among them is the polarized target for the spin physics program. It is mounted on its separate platform and can be rotated out of the beam [8]. This target setup can already be filled with both ^{6}LiD and NH_3. Other target setups will be installed for e.g. Primakoff scattering (high Z material like Pb), production of exotics (proton target) and a specialized target for the Charm physics program.

Movable Parts. All big components like magnets, RICH and calorimeters are mounted on rails and can be shifted along the beam. For different bending powers and directions of the spectrometer magnets the calorimeters can be moved transversally to adapt the hole for the passage of the non-scattered beam.

1.3.2 Layout of the Spectrometer

In fig. 1.10 the general layout of the experiment is shown. The beam impinges on a fixed solid-state target and the produced particles are detected in a magnetic spectrometer with two stages (see also comment in section 1.3.1).

To measure the properties of the particles emerging from a reaction in the target, different detector systems have to be used.

The momentum of charged particles emerging from the target is analyzed via the deflection in the spectrometer magnets: position-sensitive detectors, so-called *trackers*, before and after the magnet measure the track segments; from the angle between them charge and momentum can be determined. Around the two COMPASS magnets a variety of trackers with different sizes, detection techniques and resolutions are installed. An overview is given in table 1.2.

Provided that the beam particles can be identified, their momentum alone is enough to determine the purely inclusive kinematics of the reaction. For semi-inclusive measurements, in which parts of the produced particles also have to be measured and identified, additional detectors are needed because for *Particle IDentification* (PID) the energy or velocity of the tracked particles has to be determined as well.

The total energy of particles is measured in calorimeters, where they are fully absorbed and deposit all their energy. Different techniques are used in electromagnetic calorimeters for e^-, e^+ and γ and in hadronic calorimeters for π, K and p. In contrast to the magnet-tracker-combination, calorimeters also detect neutral particles (n, γ, π^0). In the complete spectrometer each stage

[8] While the movements of other spectrometer parts are manageable within few days, dismounting the target takes approx. 2 weeks as it includes a long period of warming up from cryogenic temperatures before it can be moved.

will have both an electromagnetic and a hadronic calorimeter, but in 2002 only the two hadronic calorimeters were used.

The velocity of charged particles can be measured with Cherenkov detectors: if inside a medium particles travel faster than the light in this medium, they produce a cone of light. The opening angle of this cone is proportional to their speed. In COMPASS this information can be extracted in a *Ring Imaging Cherenkov* (RICH) detector. The complete setup contains two RICH detectors, in 2002 only RICH1 was installed.

For the identification of μ a much easier concept is applicable: one makes use of their interaction rate, which is very small compared to all other charged particles. Thus everything which can still be detected after a 1 m thick concrete absorber has to be a μ. Three thick walls of concrete and iron are therefore installed as muon filters in COMPASS.

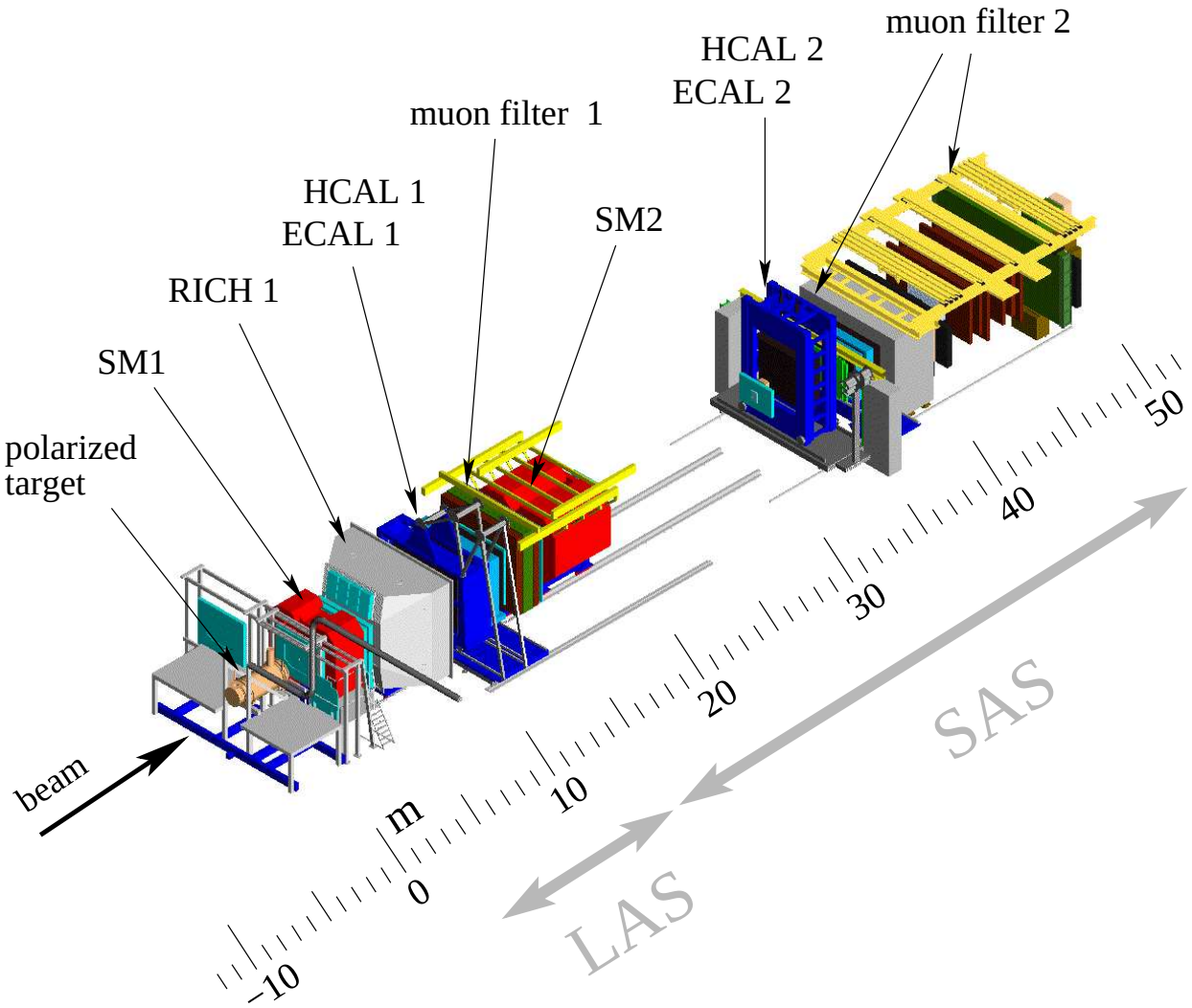

Figure 1.10: *Schematic view of the COMPASS Spectrometer. The two stages of the spectrometer, each with a red magnet in the middle and a blue calorimeter at the end, can be seen very well. (SM: spectrometer magnets, ECAL: electromagnetic calorimeter, HCAL: hadronic calorimeter)*

For the trigger decision in COMPASS the information of several sets of segmented scintillators placed at the back part of the spectrometer is used. With an elaborate coincidence system of the signals of μ in the different scintillator segments a rough target pointing is achieved and μ which interacted with the target can be distinguished from the non-scattered beam. Veto counters inhibit μ which were not inside the beam envelope leading to the target (so-called halo muons). In some classes of triggers hits in the hadronic calorimeters are additionally required to ensure the production of hadrons in the reaction.

In the rest of this section more details are given on the different components. The three types of beam available and the target will be presented in section 1.3.3 and 1.3.4. Section 1.3.5 gives a short overview over the various components along the beam line, trigger issues are summarized in section 1.3.6. The overview of the experimental setup closes with a description of the data acquisition system in section 1.3.7.

1.3.3 The COMPASS Beams

For the COMPASS experiment three different kinds of beam particles are available:

- a high-intensity muon beam in the energy range of 60 to 190 GeV with fluxes up to 2×10^8 muons per SPS cycle,
- a secondary hadron beam with energies between 40 and 280 GeV at a maximum allowed flux of 10^8 hadrons per SPS cycle,
- a low-intensity electron calibration beam (typically 10^3 to 10^4 electrons per SPS cycle) of energies up to 60 GeV.

The primary beam for the COMPASS beams is extracted from the *Super Proton Synchrotron* (SPS). The M2 beam line is 1 km long and serves both for the transport of particles from the SPS to the experimental area and for the production of secondary or even tertiary beams. Originally this line was optimized for the production and the transport of polarized muons for the preceding experiments. For COMPASS the beam line was modified for the additional transport of hadrons (p, π and K) and electrons.

A primary proton beam of up to 400 GeV is extracted from the SPS toward the North Experimental Area. A fraction of this beam of up to 1.2×10^{13} protons per SPS cycle (4.8 s extraction in a 16.8 s long cycle) is directed toward the primary target T6. From there a secondary beam (positive or negative) at zero production angle is derived.

A 600 m long decay channel follows, in which the different type of beam particles are selected before the beam is led from the underground SPS level up to the experimental hall by two groups of bending magnets. The double-bend-structure also serves as a momentum filter (e.g. μ of 160 ± 5 GeV). Before and after the upper bend two sets of scintillators called *Beam Momentum Station* (BMS) are placed to measure the momentum of each particle via its transverse position. At the end of the beam line a set of quadrupoles focuses the beam onto the COMPASS target. Typical spot sizes at the target are 8 mm RMS for μ, 3-5 mm RMS for hadrons and 8 mm RMS for e^-. A schematic layout of the M2 muon beam is shown in fig. 1.11.

The key zone of the M2 beam line is clearly the decay channel right after the T6 target, where the produced pions and kaons partly decay into muons. In case of the muon beam, the hadrons are removed by a 9.9 m long beryllium absorber at the end and only muons can pass to the double-bend upward. As the μ decay via a weak process, they come out polarized. The polarization in

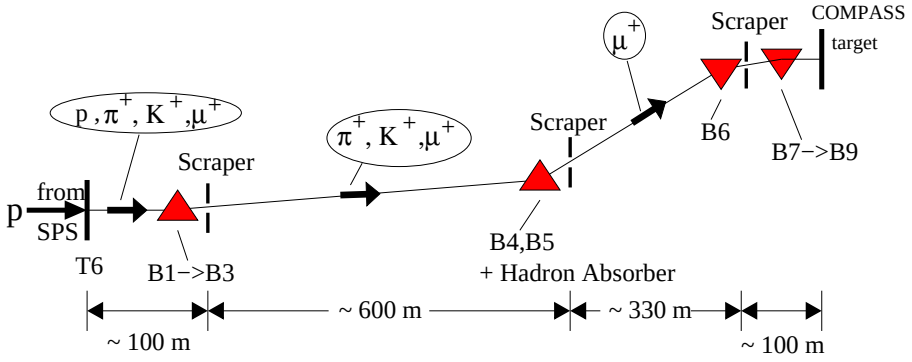

Figure 1.11: *Schematic of the M2 beam line, which guides the different types of beam particles from the SPS to the experimental hall, here the setup for the muon beam. (from [MvH02])*

the laboratory frame depends on the decay angle in the pion (kaon) rest frame with respect to its direction of motion in the lab frame. The value and the sign of the polarization can therefore be chosen by selecting a certain energy range of the μ. In order to optimize flux and energy positive muons moving forward in the pion (kaon) rest frame are chosen. They have an energy of 160 GeV and a negative polarization of -0.75 ± 0.04 [MvH02].

For the hadron beam the absorber in the decay channel is removed and the secondary hadron mixture is directly transported to the experiment. For this the beam guidance has to be retuned. In order to sort out the different particle types, additional Cherenkov counters of the CEDAR type are installed. They use an adjustable diaphragm to select only Cherenkov angles within a small range, thus allowing to positively identify particles of a preselected type. Two such counters can be used to provide tagging of two different particle species. Fig. 1.12 shows estimates of the composition of the hadron beam as a function of the primary proton energy.

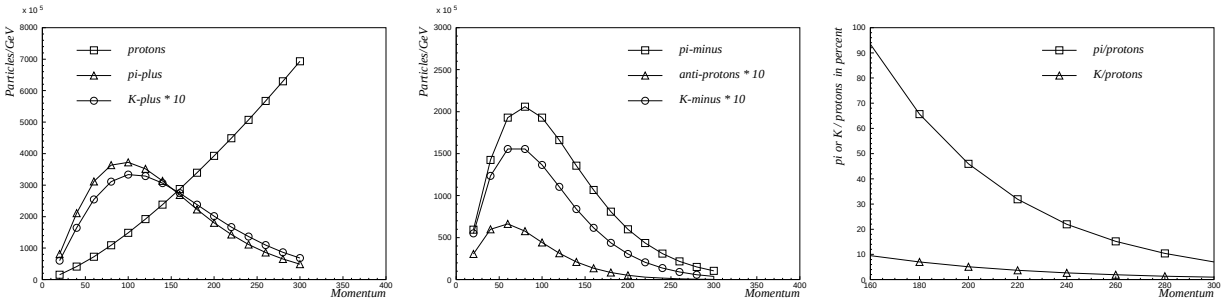

Figure 1.12: *Estimates on the composition of the hadron beam available at the M2 beam line as a function of momentum. Note that a momentum of 300 $^{GeV}/_{c}$ is the maximum that the beam line can transport. (from [CO96])*

Electron beams can only be provided as tertiary beams. A low-energy negative secondary beam (typically 100 or 120 GeV) is derived from the T6 target, transported down the decay channel and focused on a 5 mm lead converter. The converter serves as a secondary target, where secondary electrons are decelerated by Bremsstrahlung. Tertiary electrons in an energy range between some 30 and 60 GeV are selected and transported to the experiment.

1.3.4 The Polarized Target

For the muon program COMPASS uses thick, polarized solid state targets. NH_3 and ^{6}LiD [9] were chosen as target material for the measurement of the spin structure of the proton and the deuteron respectively. If the results from both materials are combined, the spin structure of the neutron can be extracted.

In 2002 ^{6}LiD was installed in COMPASS. While NH_3 is a rather well known target material, ^{6}LiD is a new development. It shows an excellent figure of merit F, which does not only reflect the density ρ and maximum polarization P_T of the material, but also the fraction of *polarizable* nucleons, the so-called dilution factor f: $F = \kappa\rho(Pf)^2$. κ is here just the packing factor of the target material; it is of the order of 0.6. With an F of 22.8 $\mathrm{kg/m^3}$ this is 2.3 times higher than for NH_3 (F=12.7 $\mathrm{kg/m^3}$). F in turn is directly connected to the precision of an asymmetry measurement as in eq. (1.2). The time t needed to measure an asymmetry A^{exp} with a precision δA^{exp} is $t \propto ((\delta A^{\mathrm{exp}})^2 F))^{-1}$ [Tak02].

The nucleons are polarized via *Dynamic Nucleon Polarization* (DNP): Irradiation with microwaves polarizes *paramagnetic centers* (= impurities with free electrons) in the material, which can then transfer their polarization to the nucleons. The polarization is measured with *Nuclear Magnetic Resonance* (NMR) probes glued to the target material. To avoid thermal relaxation the material is cooled down with a dilution refrigerator below 100 mK, where in the *frozen spin mode* the polarization has a lifetime in the order of 1000 h.

A superconducting solenoid with a magnetic field of 2.5 T defines the axis of polarization longitudinal to the beam. An additional dipole magnet also allows polarization transverse to the beam, which is needed for the measurement of transversity (see section 1.1.1). As the initially planned solenoid could not be completed in time, the magnet of the previous SMC experiment with a smaller opening was taken, which resulted in a reduction of the acceptance from 180 mrad down to 70 mrad.

For the measurement of asymmetries like in eq. (1.2), the relative alignment of target and beam spin has to be changed. As the direction of the beam polarization is more or less fixed (see also section 1.3.3), the target spin is reversed every 8 h by changing the field direction of the solenoid. To further reduce systematic influences, the target is shaped in two rods (60 cm long, 3 cm diameter) with opposite direction of polarization (both pointing either "inward" or "outward").

More details on the polarized target can be found in [PT].

1.3.5 Setup along the beam line

Up to now no real common description for all detector types included in COMPASS is published. The information presented on the following pages was therefore collected if not further specified from various Diploma- and PhD-theses [Kuh01, Wag01, Col02, Grü02, MvH02, Sch02] and the COMPASS webpage [COMPASS].

Magnets

COMPASS uses two conventional dipole magnets. The first one, **Spectrometer Magnet 1 (SM1)**, has a rather small integrated field strength of 1.0 Tm at 2 500 A. The gap is (length × width ×

[9] In a simple picture ^{6}Li is considered as being composed of a spin less α (^{4}He nucleus) and a spin 1 deuteron.

height) $110 \times 152.5 \times 172\,\mathrm{cm}^3$. The gap height is adjustable: for the muon program it was put to the maximum of 172 cm, for the hadron program a smaller gap height of 82 cm is preferable. The second magnet, **Spectrometer Magnet 2 (SM2)**, has a higher integrated field of a maximum of 5.2 Tm. In 2002 it was operated at 4 000 A, corresponding to an integrated field strength of 4.4 Tm. The gap is (length $\times$ width $\times$ height) $400 \times 200 \times 100\,\mathrm{cm}^3$.

Very Small Area Tracker (VSAT)

Three types of detectors are used for tracking directly in the beam:
About 100 m upstream the target the **Beam Momentum Station (BMS)** is placed between two bending magnets of the beam line. At this position different momenta lead to different transverse shifts. The BMS measures this shift with 5 mm wide slabs of scintillator. With a time resolution of 330 ps they are able to measure the momentum of each individual particle.
The **Scintillating Fiber Detectors (SciFi)** are similar from a technical point of view, but have a much finer granularity: here the scintillator is just a fiber with a diameter ranging from 0.5 to 1.0 mm, depending on the position inside the spectrometer. An especially radiation-hard material was chosen to ensure a long lifetime of these detectors in the harsh COMPASS environment. The SciFis have a time resolution in the order of 350 ps and are responsible for the time tag, which is attached to each event. In 2002 9 stations were installed throughout the whole spectrometer in different geometrical configurations.
The **Silicon Microstrip Detectors (Si)** are 300 µm thick wafers of silicon. The charge deposited by traversing particles is collected on 50 µm wide strips printed orthogonally on the front *and* back side. Thus one wafer delivers 2 projections with a spatial resolution of 14 µm. In 2002 2 stations with 2 wafers each were installed. A detailed description of these detectors will be given in chapter 3.

Small Area Tracker (SAT)

The Micro Mesh Gas detectors **MicroMegas (μM)** and the **Gas Electron Multipliers (GEM)** are bigger in size than the VSAT. Both use a gas volume for the primary ionization by particles. The charge is then amplified via an electric field and projected onto readout strips. The μMs use a micromesh of thin copper wires with a spacing of 51 µm at 100 µm above the readout board. With a potential of 410 V they reach an amplification of 6400. The GEMs use perforated double-sided copper-clad polymer foils with a thickness of 50 µm. A voltage of 328 to 410 V applied between the two layers of copper leads to an amplification between 8.5 and 50 inside the perforation [Ket03]. Three of these foils are staged behind each other to reach a total amplification of 8 000 to 10 000. In the case of the GEMs the charge clouds are projected on a printed circuit board with a *two*-dimensional readout pattern. One gas volume therefore provides two projections of the particle passage.
The μM are employed right behind the target (3 stations), the GEMs with their very light construction are distributed throughout the spectrometer (10 stations).

Large Area Tracker (LAT)

Large areas can usually only be covered sufficiently with gas amplification detectors, where a particle passage produces a small amount of primary ionization in a volume filled with specially chosen gas. The primary ionization then gets amplified in large electric fields. For the different regions of COMPASS, different designs are used.

3 stations of **Drift Chambers (DC)** are installed closely behind the target. Anode wires with a pitch of 7 mm are sandwiched between cathode planes. A potential of 1 750 V between anode wires and cathode planes leads to an amplification of factor 20 000 of the primary ionization. The charge is collected with readout wires interleaved with the anode wires. The drift time of the charge is used to measure the position between the readout wires.

The **Straw Chambers (ST)** are much bigger in size. To avoid a high dead-time due to charge clouds in the gas volume, they consist of 3 m long tubes. Close to the beam, where the particle density is higher, they have a diameter of only 6.14 mm, at larger distances from the beam they are 9.65 mm wide. The tubes are made of 60 µm thin carbon-loaded (inner side) and aluminum-coated (outer side) polymer foil, which serves as cathode. A wire in the center is the anode. A potential of 1 780 V and 1 950 V for the thin and thick straws respectively amplifies the primary ionization. Again the drift time is used to improve spatial resolution. In 2002 one complete station (6 planes) and one station with only 3 planes were installed right after SM1.

A heritage from the former OMEGA spectrometer of the WA89 experiment at CERN , the **Multi-Wire Proportional Chambers (MWPC)**, were refurbished for the COMPASS experiment. In much the same way as the DCs, anode wires are sandwiched between two cathode planes. But in contrast to the DCs, only the information on the fired wire is available from the particle passage and no further information on the drift time. The spacing of the wires is therefore smaller (2 mm) and the spacial resolution less good (0.5 mm). In total 15 stations were installed, which are partly different in their dimensions and the number of projections.

Another heritage — this time from the EMC experiment — are the **W45 Chambers (DW)** [Leb03]. They were installed during the 2002 run. They cover the huge surface of $5.2 \times 2.6\,\mathrm{m}^2$. The anode layer consists of interleaved potential (-800 V) and signal wires (+2 100 V) with a pitch of 2 cm. The cathode plane is built up of 0 V potential wires of 2 mm distance. Three cathode planes alternate with two anode layers to form one double layer. The amplification ranges between 70 000 and 80 000. In drift mode they reach a resolution of 2 mm.

Particle Identification (PID)

For the separation of π, K and p a **Ring Imaging Cherenkov Counter (RICH)** is used. The final goal is a RICH detector in both spectrometers, but up to now only RICH1 is installed and the second RICH is planned for COMPASS phase 2.
In the $100\,\mathrm{m}^3$ of C_4F_{10} of RICH1, traversing particles emit Cherenkov light, which is focused by $21.2\,\mathrm{m}^2$ of mirrors onto $5.3\,\mathrm{m}^2$ of photon detectors. In a layer of CsI the photons are converted to electrons and detected in an attached multi-wire chamber. 2-dimensional spacial information is achieved by segmenting the CsI photo cathode into 83 000 pads of $8 \times 8\,\mathrm{mm}^2$. The photon yield is 14 per ring.

After the tracking detectors in each spectrometer, calorimeters are installed, which fully stop most particles. The energy is deposited as a shower of low energy particles, which are then detected in scintillating material. The light is collected by photo-multipliers. From their signals the total energy of the particles can be determined. Two different systems are needed to stop the full range of particles: For photons and electrons, **Electromagnetic Calorimeters (ECal)** are needed. Again, two instantiations were planned, but not yet operational in 2002.
ECal1 will reuse lead glass blocks from the former experiments GAMS (2 840 pieces of $3.8 \times 3.8\,\mathrm{cm}^2$, close to the beam) and OLGA (320 pieces of $14.3 \times 14.3\,\mathrm{cm}^2$ at larger angles from the beam). For ECal2 the lead glass blocks from GAMS are used (2 044 pieces $3.8 \times 3.8\,\mathrm{cm}^2$) as well, this time in the outer region. For the inner part several options were available, but the issue

was undecided when this text was written. Resolution is an important issue for the ECals. The energy resolution quoted from GAMS is $\sigma/E = 5.8\%/\sqrt{E} \oplus 2.3\%$. For the detection of neutral pions $\pi^0 \rightarrow \gamma\gamma$ the minimum separation of the photons of 20 and 40 mm for ECal1 and ECal2 respectively has to be resolved.
The **Hadronic Calorimeters HCal** are optimized for hadron absorption and contain much more heavy nuclei than the ECals: they consist of iron with high absorption power sandwiched with slices of scintillator for the detection of the shower. The light is collected in wavelength shifters. The block sizes are $15\times15\times110\,\mathrm{cm}^3$ and $20\times20\times120\,\mathrm{cm}^3$, which corresponds to a radiation length of 5 and 6 for π and 7 and 9 for p for HCal1 and HCal2 respectively. As the hadronic showers are much wider than the electromagnetic ones, both spacial and time precision are less stringent than for the ECals.

The **Muon Filters (MF1** and **MF2)** constitute the end of each spectrometer. They are large trackers with thick absorbers (60 cm iron and 240 cm concrete) placed in between. Due to their high penetration power, μ are the only charged particles that pass the absorbers and give a signal in the chambers before *and* after the absorber. For MF1 plastic Iarocci tubes (squares of $1.2\times1.2\times400\,\mathrm{cm}^3$) are used: passing particles produce a discharge between an anode wire under very high potential and the surrounding plastic tube. As the plastic is electrically non-conductive, the discharge stays local and is quickly quenched. The charge recovery for subsequent particle passages is therefore rather fast. 8 planes were installed both before and after the absorber.
For MF2 aluminum drift tubes of $500\times3.4\,\mathrm{cm}^2$ are used. Again a high potential between a central wire and the aluminium tube leads to a amplification in the gas. 6 planes were installed.

Table 1.2: *(next page) List of target and detector components used in 2002, sorted in order of their appearance in the spectrometer. "*size*" is a characteristic number for the size of the active area, e.g. the diagonal. Projections are given as xyuv (x: horizontal axis, y: vertical axis, u: counter-clockwise rotated x axis, v: clock-wise rotated x axis. The angle of rotation depends on the detector type and ranges from 5 ° to 45 °.). One can nicely see the realization of the staggered tracking system, for which different-sized trackers are installed together.*

	Position [cm]	Name	type	size (cm)	Comment (Δx in μm, Δt in ns)
Beam	-10 000	BMS	VSAT	15-24	4 planes (y), Δx=5 000, Δt=0.25,
	-2 000	Veto BL	Trigger	39	segmented plane with hole
	-794 – -282	Veto I1, O1, I2	Trigger	32, 287, 71	3 segmented planes with hole
	-740 – -320	SciFi 1,2,15	VSAT	5.5	6 planes (xy), Δx=120, Δt=0.5
	-400 – -480	Si 1,2	VSAT	8.6	8 planes (xyuv), Δx=12, Δt=3
Target	-100 – 30	target	Target	3	2 rods ^{6}LiD, each 60 cm long
SAS	122 – 214	SciFi 3,4	VSAT	7.5	6 planes (xyu), Δx=120, Δt=0.3
	140 – 250	μM 1,2,3	SAT	56	12 planes (xyuv), Δx=50, Δt=10
	260	DC 1	LAT	170	8 planes (xyuv), Δx=170
	313 – 413	SM1	Magnet	230	1.0 Tm integrated field strength
	478 – 567	GEM 1,2,3	SAT	43	12 planes (xyuv), Δx=50, Δt=12
	462 – 511	DC 2,3	LAT	170	16 planes (xyuv), Δx=170
	534 – 558	Straw 3	LAT	405	6 planes (xyuv), Δx=250–300
	584	SciFi 5	VSAT	11.8	2 planes (xy), Δx=210, Δt=0.5
	600 – 950	RICH	PID	846	π/K separation up to 60 $^{\mathrm{GeV}/c}$
	960	GEM 4	SAT	43	4 planes (xyuv), Δx=50, Δt=12
	952	MWPC A*	LAT	214	4 planes (xyuv), Δx=700
	1 014 – 1 023	Straw 4	LAT	405	3 planes (xyv), Δx=250–300
	1 217 – 1 317	HCal 1	PID	516	Δx= 4 000–14 000, $\frac{\Delta E}{E} = \frac{0.59}{\sqrt{E}} \oplus 0.08$, $\frac{X}{X^0}$ = 5(π), 7(p)
	1 385 – 1 543	MF 1 + MW 1	PID	633	16 planes (xy), 60 cm iron in between, Δx=3 000
LAS	1 385 – 1 579	GEM 5,6	SAT	43	8 planes (xyuv), Δx=50, Δt=12
	1 375 – 1 570	MWPC A1,2	LAT	214	6 planes (uxv), Δx=700
	1 500	SciFi 6	VSAT	14	3 planes (xyv), Δx=290, Δt=0.5
	1 600 – 2 000	SM2	Magnet	224	4.4 Tm integrated field strength
	2 128 – 3 198	SciFi 7,8	VSAT	14,17	4 planes (xy), Δx=290, Δt=0.5
	2 021 – 3 139	GEM 7-10	SAT	43	16 planes (xyuv), Δx=50, Δt=12
	2 011 – 3 130	MWPC A4-6,11	LAT	214	12 planes (uxv), Δx=700
	2 100	HO 3	Trigger	256	2 planes ($y_u y_l$), pitch=7 cm
	3 034 – 3 071	W45	LAT	584	8 planes (xyuv), Δx=2 000
	3 174	HI 4	Trigger	36	1 plane (x), pitch=0.6 cm
	3 526 – 3 626	HCal 2	PID	483	$\frac{\Delta E}{E} = \frac{0.65}{\sqrt{E}} \oplus 0.04$
	3 700 – 3 940	MF2	PID	904	240 cm concrete
	4 005	HO 4	Trigger	677	1 plane (y) with hole, pitch=15 cm
	4 056	HL 4	Trigger	134	1 plane (x), pitch=2.2-6.7
	4 024	HM4	Trigger	125	4 planes ($x_u y_u x_l y_l$), pitch= 2.2, 2.5 (y), 6.2 cm (x)
	4 186 – 4 627	MWPC B1-6	LAT	195	9 planes (xuv), Δx=700
	4 244 – 4 524	MW 2	PID	600	6 planes (xyv), Δx=10 000
	4 650 – 4 690	MF 2'	PID	904	40 cm iron
	4 784	HM 5	Trigger	156	4 planes ($x_u y_u x_l y_l$), pitch= 2.5, 3.0 (y), 7.7 cm (x)
	4 808	HL 5	Trigger	175	1 plane (x), pitch=2.7-8.7
	4 905 – 5 065	MF3	PID	303	160 cm iron
	5100	HI 5	Trigger	62	1 plane (x), pitch=1.2 cm

1.3.6 The Muon Trigger

The task of the trigger setup is to select the events which should be read out. The maximum number of triggers is limited by the bandwidth of the data transmission from the COMPASS hall to the CERN mass storage system, which is 40 MByte/s. Without further reduction steps in 2002 this resulted in 25 000 triggers per spill (definition of spill see section 1.3.3). But as the expected rate of DIS events is already 10 000 per spill, a selectivity of the trigger as high as 50% is needed. The trigger latency is limited by the size of the data buffers available in the readout electronics. In COMPASS this boundary is given by the length of the delay cables of the calorimeters and is 600 ns. Such small times can only be reached with fast scintillators and custom-made coincidence logic.

For the muon program two different types of event classes are implemented: the PGF trigger and the DIS trigger [Leb02]. The specific detectors needed are displayed in fig. 1.13, the sizes and positions are included in table 1.2. The selected region in x_{Bj} and Q^2 is shown in fig. 1.14.

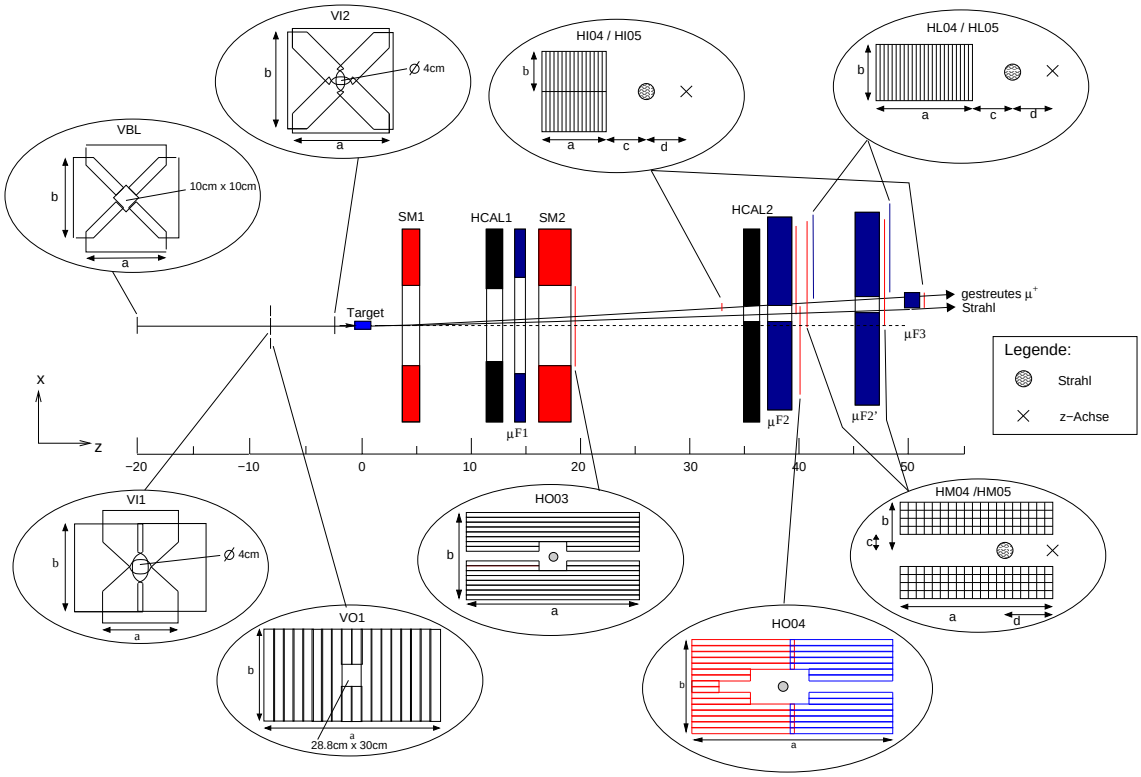

Figure 1.13: *Position and shape of all trigger hodoscopes. The sizes and positions can be found in table 1.2. (from [MvH02])*

PGF Trigger

For a high yield of PGF events, events for which the four-momentum Q^2 of the virtual photon is very small (so-called *quasi-real-photons*) should be selected. This goes along with a small scattering angle of the muon. At the same time it is required that the γ has a sizable fraction of the μ energy to ensure that it carries a reasonable longitudinal polarization, i.e. that the μ experienced an

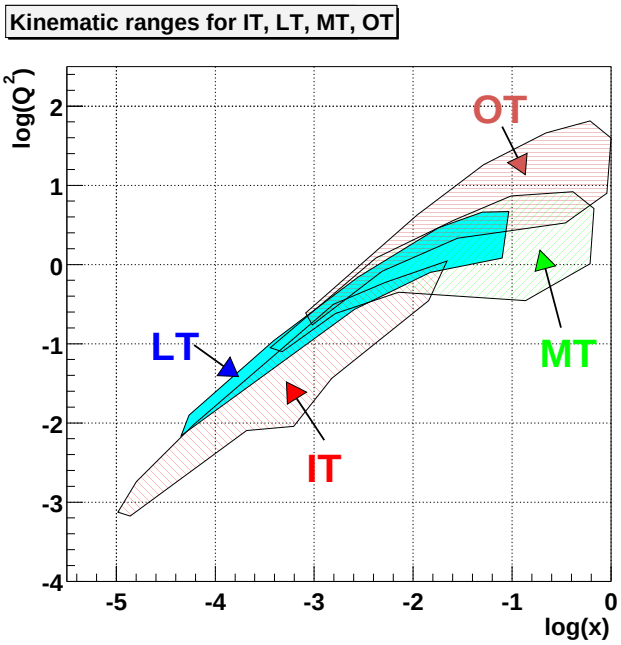

Figure 1.14: *Region in x_{Bj} and Q^2 selected by the trigger hodoscopes. (from [Leb02])*

energy loss. An additional handle to PGF is the necessary production of hadrons. Two detector subsystems are used for the μ and the hadron signature respectively.

The **energy loss trigger** uses the fact that a μ which experienced an energy loss gets separated from the non-scattered beam in the magnetic field. In order to distinguish between μ which were deflected in the magnetic field due to smaller momentum and μ which just had a bigger scattering angle, the separation from the non-scattered beam is measured at two different positions along the beam: two systems of vertical slabs of scintillator H4 and H5 are installed at $\sim$35 and $\sim$50 m after the target. A smaller sized set of hodoscopes, HI4 and HI5, is closer to the beam and forms the *inner trigger*; the hodoscopes HL4 and HL5 cover a region further away from the beam and define the *ladder trigger*. Requiring a coincidence of a certain combination of slabs of H4 and H5 one prefers μ with energy loss compared with μ with larger scattering angle.

To ensure that the measured energy loss took place in PGF and not in e.g. elastic μ-*e* scattering or Bremsstrahlung, an additional *calorimeter trigger* is set up. One requires the total energy deposition in either of the two HCal to be higher than twice the energy deposition of the μ of 2 GeV.

DIS Trigger

In order to ensure that the virtual photon made a *deep inelastic* reaction, one usually requires its four-momentum Q^2 to be more than $0.5\,\mathrm{GeV}^2/c^2$. For such events a *geometrical trigger* is implemented, which demands a minimum scattering angle and that the scattered μ points back to the target. Similar to the energy loss trigger two measurements of the transverse position of the μ are needed, but this time perpendicular to the bending plane. The hodoscopes HM4/HM5 and HO3/HO4 are therefore located above and below the bending plane and form the *middle* and *outer* trigger for medium and large Q^2 respectively. While the outer hodoscopes consist of horizontal scintillator slabs only, the middle hodoscopes have horizontal and vertical slabs and provide 2-dimensional space information. Again a coincidence between slabs of H4 and H5 is asked for, but

this time combinations are selected where the μ track points back to the target.

As this trigger is needed for *inclusive* measurements, no veto from the calorimeter is allowed.

Veto System

The big halo around the μ beam pollutes all trigger types. A veto system, which leaves only a small hole for the beam to pass, is therefore installed upstream of the target. A coincident detection inhibits the formation of a trigger signal. Four dedicated planes are installed. Additionally the SciFi upstream of the target are used to exclude tracks with big angles.

1.3.7 The Data Acquisition System

The COMPASS experiment has approx. 200 000 detector channels for readout, which are distributed over various subsystems and a 60 m long setup. Depending on the physics program the readout electronics has to cope with trigger rates from 5 kHz to a design maximum of 100 kHz. With an event size of around 40 kByte the accumulated data add up to 200 - 4 000 $^{\text{MByte}}/_{\text{s}}$. To read out such high data rates the duty cycle of the SPS accelerator is used, where particles can only be extracted for 4.8 s in 16.8 s (see also section 1.3.3). Pipelines and buffers quickly accept all data during the extraction. The actual collection of the data can then be stretched over the whole SPS cycle at a much slower speed. In the following a short overview of the readout chain is given. The schematic flow is shown in fig. 1.15, more details can be found in [Sch03].

The analogue detector information (this can be an amplitude or a time difference) is digitized in so-called *frontend electronics* as close to the detector as possible. *Analogue-to-Digital Converters* (ADC) and *Time-to-Digital Converters* (TDC) are used for amplitude and time measurement respectively.

The digitized data of several frontend devices are collected and formated in concentrator modules named *Catch* or *GeSiCA*: the event number and more information on the position of the detector (so-called *Geographic ID*) is added. Via optical link the data are then transferred to the DAQ computer where they are buffered on PCI cards called *spillbuffers*. The data of more than one spill can be stored on such devices and one benefits of the full duty cycle of the accelerators. Up to 4 spillbuffer cards can be installed in such *ReadOut Buffer* PCs (ROBs), from which the data are transmitted via Gigabit Ethernet to eventbuilder computers, where the sub-detector data are combined to complete event blocks and stored on local disks. Finished runs are continuously transferred to the CERN central data storage system, where they are temporarily stored on disk before they get migrated to the tapes of the *CERN Advanced STORage system* (CASTOR) [CASTOR].

While standard components could be used for ROBs and eventbuilders, most components upstream of the spillbuffers were custom-made for COMPASS.

To keep the data integrity in a pipelined readout, each trigger has to be identified with a unique event number to enable the event building of blocks collected on different ROBs. In COMPASS the synchronous transmission of the trigger and its identification to all detectors is done by means of optical signals distributed by the *Trigger Control System* (TCS) [Kon02]. It distributes a stable clock to the entire experiment, needed for precise time measurement, and provides additional means of control like artificial triggers for calibration and fixed and variable dead-time settings.

The DATE [DATE00] software package developed by the ALICE DAQ group and tailored to the COMPASS specific needs runs on ROBs and eventbuilders. It provides routines for eventbuilding, run control, information logging and event sampling for online monitoring purposes.

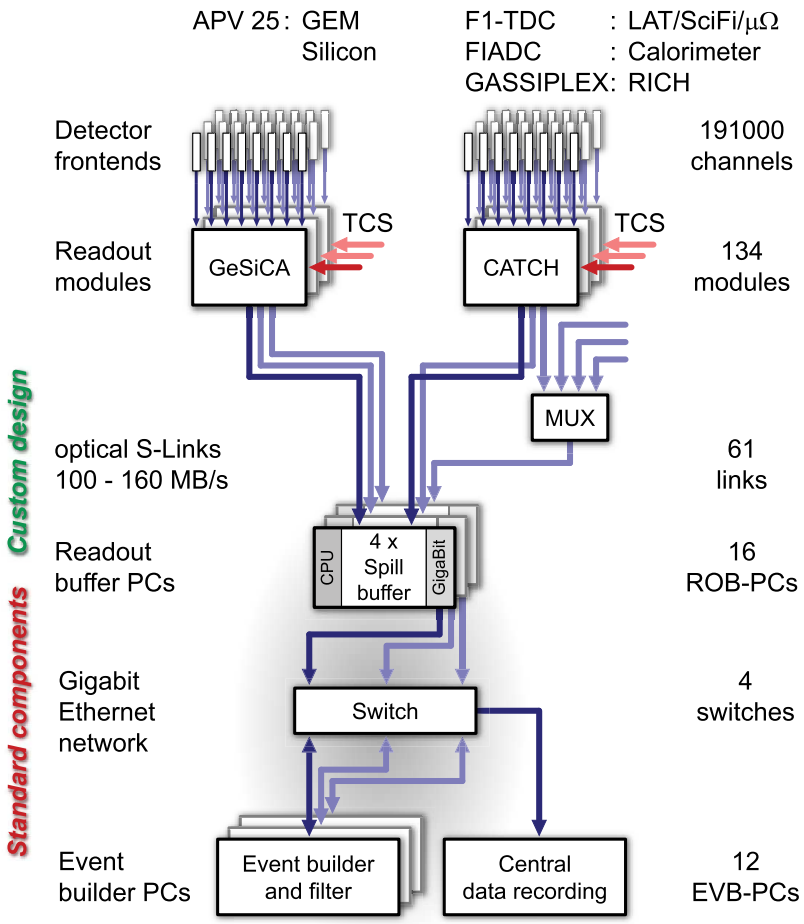

Figure 1.15: *Schematic flow of data in COMPASS (top to bottom): the analogue information from the detectors gets collected in the concentrator modules Catch and GeSiCA. Via optical link it is transferred to Readout Buffer PCs and finally assembled in the Event Builder PCs. The upper part was custom made for COMPASS, the lower half uses standard components. As can be seen, the system is easily scalable (picture from [Sch03]).*

A framework for the readout routines running on the ROBs is included. For the spillbuffer cards a special driver was developped within COMPASS.

As can be seen, the COMPASS DAQ provides a very high flexibility for adding and removing various components, be it detectors, readout modules or computers, which will allow a smooth upgrade to the complete setup in the second phase of COMPASS.

Chapter 2

Silicon Microstrip Detectors

Silicon detectors are nowadays widely used in high energy particle physics. The first devices were already favored in nuclear physics for their very good energy resolution in full absorption mode [Leo94]. With the introduction of the planar technology by J. Kemmer [Kem80] in 1980, the silicon surface could be segmented, which makes a position-sensitive readout possible. As low noise highly integrated readout electronics was further developed at the same time, silicon detectors have experienced a big boom in the particle physics sector since then.

This chapter gives an overview of the basic properties and operation principles of silicon diodes. For more details the reader is referred to more general text books like [Leo94], more specific high energy detector papers like [Pei92] or two closely related diploma theses [Wag01, Wie98]. Additionally the topics of radiation damage and annealing mechanism as well as the Lazarus Effect, which reduces the influence of radiation damage, are introduced before the next chapter describes the silicon detectors implemented in COMPASS in more detail.

2.1 Basic Operation of Silicon Detectors

In the picture of the statistical solid state physics the atomic electrons of semi-conductors are organized in so-called *bands*, a term which describes possible energy levels. The binding energy shows as a region of forbidden energy levels between the last bound band, the *valence band*, and the first free band, the *conduction band*. For excitation energies of more than the *band gap* energy, electrons can be lifted into the conduction band and then move freely through the lattice, contributing to the electrical current through the bulk. The remaining positive charge stays localized and can be treated as "particles" of their own, so-called *holes*, which can also move freely through the lattice. In semi-conductors, the band gap is relatively small (`Ge`: 0.67 eV, `Si`: 1.12 eV) and the thermal energy ($kT \approx 1/40$ eV) already contributes to the production of electron-hole pairs.

Traversing charged particles deposit energy in the crystal in the form of electron-hole pairs via inelastic scattering. With an electric field applied over the detector, the electrons and the holes can be extracted from the bulk material and collected on electrodes implanted on the surface. When connected to a low noise readout electronics, the particle detector is reliable and quite easy to handle.

A variety of silicon structures allows to tailor the properties to specific needs: silicon detectors can be optimized for very good energy, space or time resolution. They are comparatively small

and can be used where there is little space, they are operational under many conditions like warm or cold, in vacuum or in inert gases.

In the following the underlying physical processes and the basic geometry of a diode structure are shortly revisited before its behavior as a detector is explained.

2.1.1 Production of Signals

Charged Particle Interaction in Matter

Most charged particles interact in matter through inelastic scattering at the atomic electrons and elastic scattering at the atomic nuclei, except for electrons, for which Bremsstrahlung and Cherenkov radiation dominate. Nuclear reactions have only small influence as long as the ratio of the particle and the mass of the media nuclei stays small.

The deposition of energy via inelastic scattering is described in the Bethe-Bloch–formula [PDG00]. It is based on the idea that the traversing particle performs many interactions with only small energy transfers. Besides the kinematic variables like momentum and energy the key parameter is the *mean ionization energy* of such interactions, which characterizes the difference in the material. Its theoretical calculation being quite complicated, it is usually parametrized as a function of the nuclear charge Z.

The energy loss depends strongly on the actual energy of the particle. The Bethe-Bloch–formula therefore gives only the energy loss per step $\mathrm{d}E/\mathrm{d}x$, the so called *stopping power*, depicted in fig. 2.1a). The plot shows a minimum at $\beta \approx 0.96$, which is why particles with that velocity are called *Minimum Ionizing Particles* (MIPs). For slower particles the energy deposition increases rapidly, which leads to an accelerated stopping process and the main energy loss only on the last part of the trajectory, the so called *Bragg peak*. For faster particles the deposition increases again, but very slowly; they are therefore usually also treated as MIPs. The differential energy loss $\mathrm{d}E/\mathrm{d}x$ for MIPs is 1.66 MeV cm^2/g.

Energy Loss Distribution

The consequence of the statistical nature of the scattering processes is that the total number of interactions and therefore also the total energy loss in the material is not exact, but statistically smeared. The deposited energy is therefore distributed around the mean value calculated with the Bethe-Bloch–formula. For thick absorbers, where the number of interactions is large and the relative fluctuations are small, the distribution approaches the Gaussian limit. For thinner probes rare interactions with large energy losses get more important. The distribution gets asymmetric toward higher values and follows a Landau distribution:

$$L(\lambda) = \frac{1}{\sqrt{2\pi}} e^{-\frac{1}{2}(\lambda + e^{-\lambda})}, \qquad \lambda = \frac{\Delta E - \Delta E_{\mathrm{mp}}}{\xi}. \tag{2.1}$$

As can be seen in fig. 2.1b), the mean energy loss is now significantly higher than the most probable one. For MIPs the most probable energy loss is 26 keV in a 100 μm silicon layer, the mean energy loss is 39 keV, both scale within 10% between 20 and 300 μm.

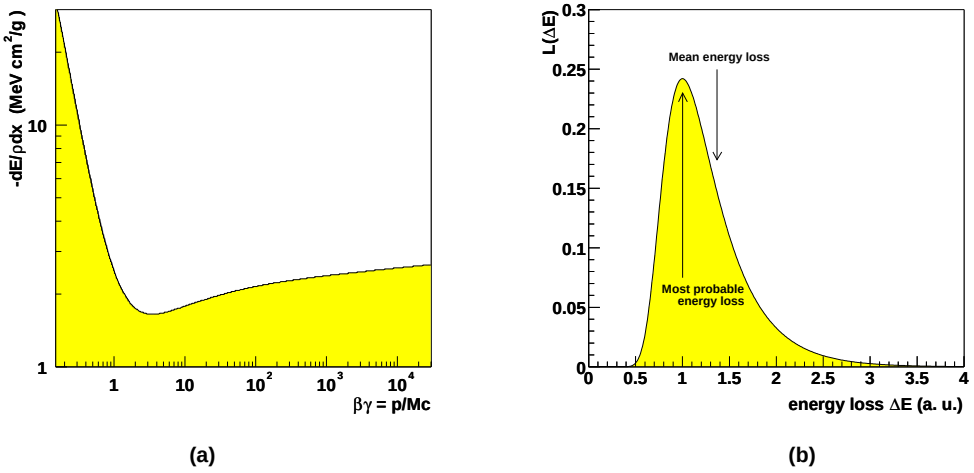

Figure 2.1: ***a)*** *Stopping power in silicon for muons, normalized on the density of the material. In this presentation the material dependence is reduced to the factor Z/A, which changes only slightly over a large region. The absolute values are therefore valid for nearly all materials.* ***b)*** *Energy loss distribution in thin absorbers: Landau distribution. The mean energy loss is shifted toward higher energies with respect to the most probable energy loss. (both pictures from [Wag01])*

Multiple Scattering

For the sake of completeness one has to mention that a particle traversing a medium not only suffers an energy loss, but also changes its direction of motion by many small-angle scatterings. Most of this is due to elastic Coulomb scattering from nuclei, and hence the effect is called *multiple Coulomb scattering* or simply *multiple scattering*. Both a shift and a change of direction occur. Usually both can be parametrized with a Gaussian distribution, where the width increases with the amount of material traversed and decreases with higher momentum of the particle. A characteristic number for the thickness of the material passed is the *radiation length* X_0. It is defined by [Tsa74] and interpreted as the mean distance over which a high-energetic electron loses all but $1/e$ of its energy by Bremsstrahlung. X_0 is thus the appropriate scale length for describing high-energetic electromagnetic cascades. A compact fit to the data is presented by

$$X_0 = \frac{716.4\, g/\mathrm{cm}^2 A}{Z(Z+1)\,\ln(287/\sqrt{Z})}. \tag{2.2}$$

For more details see [PDG00].

2.1.2 pn-Junctions

Silicon and semi-conductors in general make good detector material as the deposited energy produces electron-hole pairs with a rather low production threshold. In silicon the energy required for the production of one electron-hole pair is 3.6 eV — more than the 1.12 eV band gap between valence and conduction band, as silicon has an indirect band gap and needs additional phonon excitations.

The electron-hole pairs can be extracted with an electric field applied over the material, but due to the semi-conductivity no big fields build up. One therefore uses pn-diodes, biased in reverse direction. At the junction of p- and n-doted silicon the electrons of the donors of the n-side move into the holes of the acceptors of the p-side until their diffusion is compensated by the developing field. Around the junction the material gets *depleted* of free charge carriers and a so-called *space charge region* builds up. Electron-hole pairs produced by traversing particles in the depleted zone are now drawn off by the compensation voltage. For an additional externally applied bias voltage the polarity is important: in *forward bias*, i.e. p-side connected to "+" and n-side to "-", the junction has only a small resistance as the space charge region is "neutralized" from the bias current. But for *reverse bias*, i.e. p-side connected to "-" and n-side to "+", the space charge region is increased as the bias voltage depletes even more dopant atoms. In reverse bias therefore the active volume for electron-hole extraction and consequently the signal amplitude is much better than with the compensation voltage alone.

The depth d of the depletion zone can be calculated to be [Leo94]

$$d = 0.53\sqrt{\rho_n(V_0 + V_B)}, \tag{2.3}$$

where the specific resistance of the semi-conductor ρ_n is connected to the effective doping concentration $N_{\text{eff}} = N_D - N_A$ of the bulk via $1/\rho = eN_{\text{eff}}\mu$ and yields typically 2-20 $\text{k}\Omega/\text{cm}$. The intrinsic compensation voltage V_0 is in the order of 1 V, typical external bias voltages V_B are 50-100 V. To keep the bias voltage required for full depletion (*depletion voltage*) low and avoid the breakthrough of the junction, high resistivity material, i.e. very pure material, is preferred.

In order to optimize the size of the depletion zone, asymmetric dopant concentrations are also used: as the space charge region in total is electrically neutral, its size is defined by a balance of dopant atoms on both sides. One uses therefore highly doped p-sides (so-called p^+) and weakly doped n-sides so that the space charge region is mainly located in the n-zone. p-sides are accordingly made very shallow (few μm) in a bulk of n material (several 100 μm)[1].

Leakage current. Although the diode should be blocked when operated with reverse bias, nevertheless a small leakage current builds up from the thermal excitation of electron-hole pairs in the bulk material and on the surface. Such currents make up the noise of the detector and define the lower limit for the minimal energy deposition which still can be read out: the amount of charge has to be clearly higher than the leakage. The leakage current increases with the applied voltage like $I_{\text{leak}} \propto \sqrt{V_B}$ and saturates when the detector is fully depleted.

2.1.3 Silicon for Particle Detection

Altogether, silicon diodes are very suitable for particle detection. Special characteristics even make them superior compared to other detection techniques in some environments.

With 3.6 eV per electron-hole pair, the energy needed for charge carrier production is much smaller than in other techniques[2]. Thus the same deposited energy yields a larger number of charge carriers, which makes the fluctuation on the signal much smaller. This also implies that the probability of a particle passing without producing a signal at all is negligible. The intrinsic

[1] Usually n-doped material is taken as bulk. As the mobility of electrons is higher than that of holes (see also section 2.1.3 for the topic of mobilities) the space charge region and therefore the active volume is larger with the same bias voltage.

[2] A rule of thumb is: 3 eV in semi-conductors, 30 eV in gas, 300 eV with photo cathodes for charge carrier productions.

efficiency is therefore practically 100%. For the detection of non-MIPs, where one aims for total absorption, the small energy fluctuations lead to very good energy resolutions.

As explained in section 2.1.1, the produced charge for MIPs is only a function of the thickness of the detector, yielding about 390 $^{\mathrm{eV}}/_{\mu\mathrm{m}}$, corresponding to typically 108 electron-hole pairs per μm [Pei92]. Unlike gaseous detectors, intrinsic amplification of the primary charge in semi-conductor devices is neither possible nor necessary. Signal amplitudes from a relatively thin semi-conductor (100-300 μm) are already big enough (40-120 keV, corresponding to 10 000 to 30 000 electrons) to be read directly with low noise electronics in a comparatively simple setup.

Spatial Resolution. The main advantage of silicon devices for high-energy particle physics lies in their unique spatial resolution, which is connected to both localized charge clouds as well as in the very small structure sizes that are possible. Resolutions down to 2.6 μm can be reached [Pei92].
The transverse size of the charge cloud is relatively small, most charge is produced in a narrow tube of 1 μm around the particle trajectory. The charge drifts to the surfaces and forms a Gaussian distribution with a FWHM of around 10 μm. Main disruptions arise from rare excitation of high energetic (some keV) electrons (so-called δ-electrons) traveling parallel to the detector surface and depositing their energy outside the charge cloud. They can cause a shift of the center of the charge cloud by some micrometers.
From the technological point of view semi-conductor processing is rather well advanced (a beneficial effect of the micro-electronics industry's interest in this material), and it is possible to divide the p- and n-readout-"electrodes" into segments, usually strips and recently also pads, with structure sizes down to 10 μm. Aluminum layers deposited on the surface transfer the charge to the edges, where the possibility for the electrical contact is provided. The coupling to the dopant can be done either directly (*DC coupling*) or with a silicon oxide layer in between (*capacitive / AC coupling*). The main difference between the two methods is now the leakage current. For directly coupled diodes it gets drained off into the readout electronics and can thus be easily monitored. High leakage currents on the other hand introduce noise into the readout, for very sensitive electronics therefore capacitive coupling is preferred as a protection.
As long as the charge cloud is completely collected on one strip, the spatial information is simply the position of the strip center. In this case the uncertainty depends only on the the strip pitch δx according to $\sigma_x = {\delta x}/{\sqrt{12}}$, with the $\sqrt{12}$ being obtained by calculating the second moment of a homogeneous distribution of width δx. If the charge cloud is collected on several strips, the centroid of the cloud can be determined with much higher precision than ${\delta x}/{\sqrt{12}}$. For this purpose some wafer designs include additional strips which are *not* read out, but just distribute their collected charge via capacitive coupling to the neighboring strips. With this artificial "broadening of the charge cloud" the obtained spatial resolution for a certain number of readout channels can be increased significantly.

Timing Properties. Similarly to the spatial distribution, the time structure of the signal is also rather compact, as the mobility of electrons and holes $\mu_{e,h}$ (1350 and 480 $^{\mathrm{cm}^2}/_{\mathrm{Vs}}$ respectively) is surprisingly large [Leo94]. With a typical bias voltage of 100 V over D =300 μm the drift times $t_{\mathrm{drift}} = {D}/{\mu E}$ are 7 and 19 ns.

Charge Collection Efficiency. The ratio of collected charge and charge originally deposited in the silicon is called *Charge Collection Efficiency* (CCE). The CCE depends both on the semiconductor and the properties of the readout electronics. One argument concerning the CCE was

already given in section 2.1.2, where the size of the depletion zone was discussed: for not fully depleted bulk materials the charge which can be extracted is less than the charge which was deposited. The ratio follows the correlation in eq. (2.3). Another factor of influence is radiation damage, which will be discussed in section 2.2.

Noise. As no additional intrinsic amplification of the primary signal takes place, the signal-to-noise ratio in silicon detectors requires particular attention. This is especially true when the charge is distributed on several strips or the correlation between signals of p- and n-side is to be used. Since the signal from the detector appears as electric charge, electronic noise is usually quantified by giving its *equivalent noise charge* (ENC).
The noise of the preamplifier is particularly important as it ultimately affects the resolution of the detectors. For conventional charge-sensitive amplifiers the electronics noise depends on the capacitance of the readout strip, which acts like a load capacitance to the preamplifier:

$$\mathrm{ENC} = a + b \cdot C, \tag{2.4}$$

where a and b are amplifier-dependent constants and C the capacitance of the detector. The source of the capacitance is mainly the capacitance of the readout strips to its neighbors and to the backplane.
Besides the electronics contribution, additional contributions arise from the leakage current through the pn-junction ($\mathrm{ENC}_{\mathrm{leak}} \propto \sqrt{I_{\mathrm{leak}}}$) and from thermal noise in the bias resistor ($\mathrm{ENC}_{\mathrm{bias}} \propto \sqrt{T/R}$).
Typically, values for the total detector ENC are less than 1000. With the signal from a 300 μm thick silicon this results in signal-to-noise ratios of 30:1.

2.2 Radiation Damage

Heavy irradiation of silicon detectors creates defects in the bulk which lead to a considerable decrease in the efficiency of particle detection:

1. The effective doping concentration changes[3]. For larger N_{eff} a higher voltage is needed to fully deplete the bulk material.
2. A smaller resistivity results in an increase of the leakage current and consequently also the noise.
3. Additionally created energy levels in the band gap trap and possibly delay the signal charge until it is lost for the readout.

As the voltage is limited by the breakdown of the diode, at some point the detector can not be fully depleted anymore and part of the signal is lost. Signals get smaller (1,3) and noise higher (2) until finally the detectors are no longer usable.

The *fluence* Φ is taken as a measure for the amount of irradiation. It is simply the number of particles per area impinging on the diode and thus basically the time-integrated, better known *flux* (particles per area and time: the beam rate). Problems arise at fluences of the order of 10^{14} neutrons per cm^2.

[3] As will be shown later, N_{eff} first decreases with fluence; after type inversion, however, it increases again.

Non Ionizing Energy Loss

The underlying physical process is the *Non Ionizing Energy Loss* (NIEL), where lattice atoms are hit and displaced, producing a vacancy V and an interstitial atom (Frenkel pair). They constitute a so-called *point defect*. *Cluster defects* on the other hand are formed when the primary knock-on atom has enough energy to produce a trace of further Frenkel pairs, which stay closely together. Defects can also move through the lattice and form clusters by themselves. Common clusters are double vacancies like VV^- or interstitials captured by impurities like carbon C_i or oxygen O_i.

Defects in general form new energy levels in the band gap of silicon in addition to the levels of donors and acceptors. But while donor and acceptor levels are very close to conduction and valence band respectively (*shallow levels*), radiation-induced energy levels can be deep inside the band gap (so-called *deep levels*). For the silicon band gap of 1.12 eV the distance of shallow levels is in the order of 0.01 eV, the one of deep levels in the order of 0.4 eV.

To allow the comparison of radiation damage produced by different beam particles with various energies and finally to predict radiation damage acquired in an environment with particle and energy mixtures, the fluence is normalized to an *equivalent fluence* Φ_{eq}. For this one assumes that the effect scales with the displacement damage cross sections (NIEL scaling hypothesis). Partly for traditional reasons, normalization is done to the equivalent fluence of 1 MeV neutrons (i.e. fast neutrons). Much effort has been spent on getting the NIEL scaling factors, latest results can be found in [ROSE97, ROSE00b]. A summary plot of NIELs is shown in fig. 2.2, in which the muons relevant for the further work are also included.

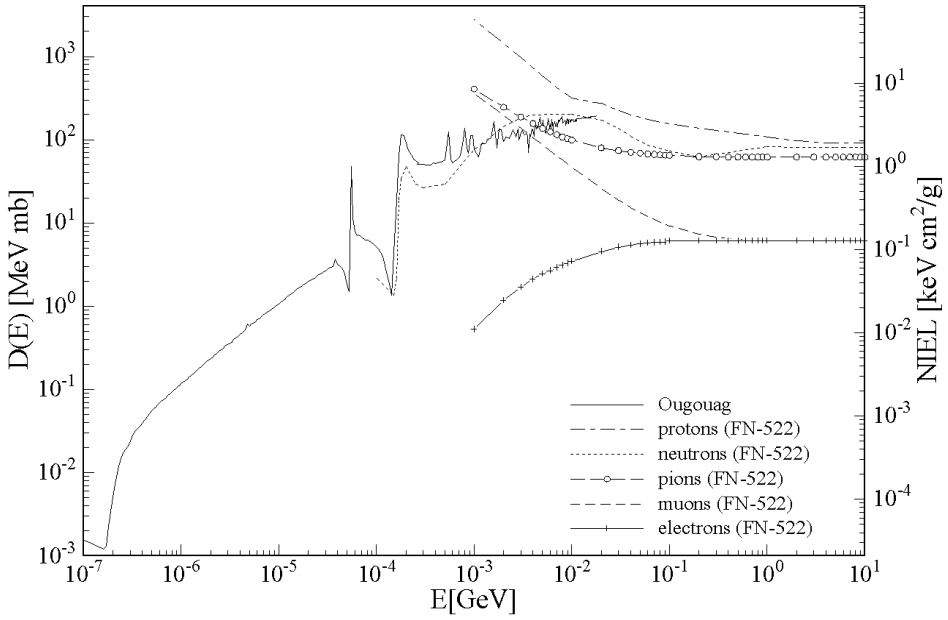

Figure 2.2: *NIEL scaling factors for the normalization of irradiation fluences to an equivalent fluence of 1 MeV neutrons (right axis) for different particles as a function of energy. The left axis shows the used damage cross sections. Note that this is one of the rare plots where not only the "classic" neutrons, protons and pions but also muons are included. (from [ROSE97])*

The NIEL scaling factors have proven to be an extremely useful tool to analyze the macroscopic

effects of irradiation. Latest results at CERN [ROSE00a, ROSE01], however, have shown that the microscopic damage produced by neutrons and charged hadrons differs: while the irradiation with neutrons produces mainly clusters via (hard) elastic scattering and high-energetic primary knock-on atoms, charged hadrons generate point-like defects via (soft) Coulomb scattering. Still, many macroscopic observables scale very well, among them the very important current-related damage rate α as explained below.

Leakage Current

The radiation-damage-induced increase of the reverse current I_{leak} is entirely due to the generation of electron-hole pairs in the silicon bulk. When measured at full depletion it is proportional to the volume of the bulk V and the equivalent fluence Φ_{eq} acquired by the probe:

$$I_{\text{leak}} = \alpha \, \Phi_{\text{eq}} \, V \tag{2.5}$$

When temperature-related effects are properly taken into account, the *current-related damage rate* α can be determined quite accurately to be $\alpha = (3.99 \pm 0.03) \times 10^{-17} A/cm$ [Mol99], corresponding to an increase in current in a standard 300 μm thick detector of δI = 120 μA per cm^2 detector and an equivalent fluence of 10^{14} NIEL. Inverting the argument, the leakage current is an accurate tool to measure the radiation damage already acquired by an installed detector. Note that the leakage also follows an additional simple exponential temperature dependence. Values are therefore usually normalized to 20°C.

Effective Doping Concentration and Type Inversion

In general irradiation introduces defects to the atomic lattice, which can have electronic energy levels in the band gap and thus behave like dopants. For the operation as diode the *effective doping concentration* $N_{\text{eff}} = N_d - N_a$ with N_d and N_a as the donor and the acceptor concentration respectively is important, as it is directly related to the size of the space charge region via the depletion voltage (see eq. (2.3) and the following explanation). Again, correcting for temperature-related effects, the voltage needed for full depletion is a good tool to measure the effective doping concentration. It turns out that irradiation changes the effective doping concentration preferably from donor-like to acceptor-like, both due to "donor removal" as well as to an enhanced generation of acceptor-like defects. As normally n-bulk material is used as detector material, *type inversion* occurs at a fluence of around 10^{13}-10^{14} NIEL and the pn-junction originally located at the p-side of the detector moves through the bulk to the n-side. The space charge region changes its sign correspondingly. After type inversion, N_{eff} and the related depletion voltage V_{dep} increase until the pn-junction breaks down.

Annealing and Reverse Annealing

The effective doping concentration N_{eff} nicely displays the behavior of irradiated silicon material *after* irradiation, when defects can move through the lattice due to their thermal energy. In fig. 2.3 the time dependence of N_{eff} is plotted. Three different processes are indicated: a short-term *beneficial annealing* N_A, a stable damage part N_C and the *reverse annealing* component N_Y. N_C can be described as an incomplete donor removal depending exponentially on the fluence and as a fluence-proportional introduction of stable acceptors. The time constants of the annealing

processes have been found to be independent of the irradiation fluence. Higher temperature accelerates the annealing processes, with the correlation between different temperatures being well measured.

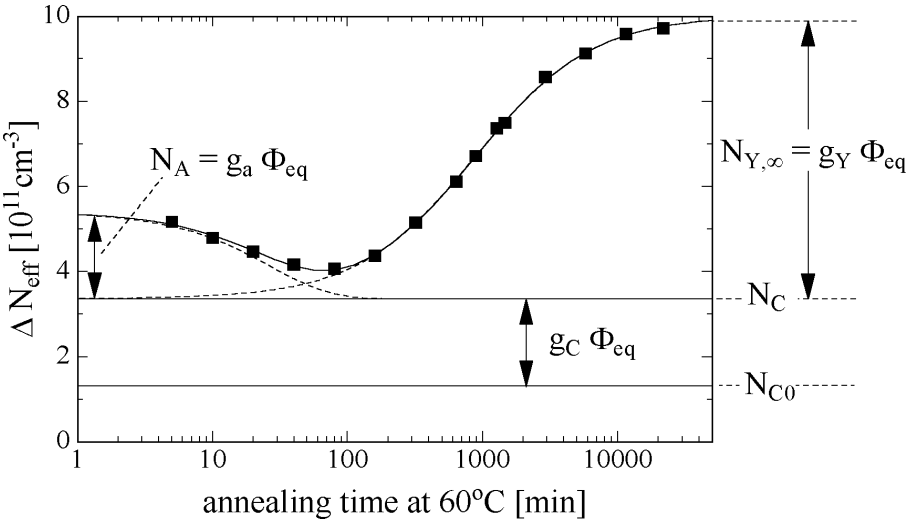

Figure 2.3: *Annealing processes for N_{eff}: the change of the effective doping concentration is plotted against time. Three different components can be distinguished: a stable damage part N_C, a short term beneficial annealing N_A and a long term reverse annealing N_Y. (from [Mol99])*

With the help of Deep Level Transient Spectroscopy (DLTS) the different processes could be correlated with the appearance and disappearance of certain defects via their behavior in the annealing process.

Radiation-Hard Silicon

In modern high-energy particle physics experiments, where powerful accelerators are available and high interaction rates needed, silicon detectors will be exposed to severe fluences. Scientists are therefore very interested in prolonging the lifetime of silicon devices in such harsh environments. Several ideas have been investigated: the HERA-*B* experiment at DESY optimized their diodes "geometrically", i.e. all structures were specially shaped to be less sensitive to irradiation-induced changes (see [Abt99] and section 3.1). The LHC experiments at CERN successfully pursued the strategy of "defect engineering", where the deliberate introduction of impurities improved the radiation hardness of irradiated detectors: additional oxygen was found to be very helpful [ROSE00a, ROSE01].

An unconventional, but very promising result was found by another CERN group [RD3900a, RD3900b]: the operation of silicon detectors at a temperature as low as 100 K leads to a "revival" of CCE even in heavily damaged silicon detectors exposed to fluences of up to 5×10^{14} NIEL. This "Lazarus Effect" was chosen for the COMPASS silicon detectors and will therefore be explained in more detail in the next section.

2.3 Lazarus Effect

In 1998 the RD39 group at CERN showed that the CCE of a heavily irradiated silicon detector recovers when operated at temperatures as low as 100 K. The effect was named *Lazarus effect* after the biblical tale. The first observation was reported in [RD3998], the respective measurement is shown in fig. 2.4: from a value too low for the detector to operate at RT, the CCE rises with decreasing temperature to up to 90% of the undamaged value at 130 K before it drops again for lower temperatures. Like this, detectors with damages of up to 5×10^{14} NIEL were successfully read out. The recovery is independent of the previous irradiation history and connected annealing phases, thus no special storage of the diodes is required. The Lazarus effect provides a highly efficient radiation resistance in a rather elegant way. The problems are shifted away from the silicon to the connected electronics and mounting, which have to be operational at these temperatures. Since the discovery much progress has been made in understanding the recovery and more experience has been gained in operating detectors at such temperatures. In the meantime first experiments are already running with cold silicon [Totem, NA50].

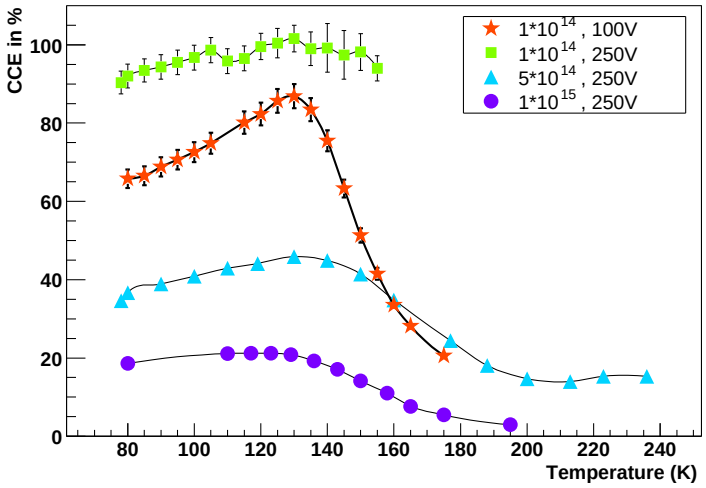

Figure 2.4: *The first observation of the Lazarus Effect [RD3900b] (CCE normalized to undamaged detectors). Three effects are illustrated. 1) The red stars show the CCE recovery for lower temperatures with the pronounced maximum at 130 K. 2) When one increases the bias voltage for the red stars, one gets full CCE again (green squares). 3) For a further increase in fluence the CCE finally breaks down at 10^{15} NIEL (from green squares over blue triangles to violet circles).(from [RD3900b])*

Low temperatures have other beneficial effects on the detector performance besides the Lazarus effect. For example the leakage currents from bulk or surface become negligible even with heavily damaged bulks and the edges get passivated, thus the diodes can be operated up to very high bias voltages. The small leakage even makes a successful operation of forward-biased diodes possible. The mobility of charge carriers also rises at low temperatures, leading to faster signals.

Model for the Lazarus Effect

According to recent results [RD3902], the Lazarus effect can be understood as the interplay of two concurrent processes with different temperature dependence, namely the trapping of signal charge and the change in resistivity of the silicon.

The primary loss of CCE at a constant bias voltage at room temperature is due to the reduction of the space charge region and an incomplete charge collection: as explained in section 2.2, irradiation leads to a higher effective doping concentration N_{eff} of the bulk material (i.e. smaller resistivity) due to the formation of deep levels, which in turn results in a smaller depletion depth (see eq. (2.3)). At some point the space charge region does not extend over the full depth of the bulk anymore and a neutral base is formed at the ohmic side of an originally fully depleted detector. The neutral region is not only deactivated (i.e. only a factor d/t of the deposited charge can be collected), but also acts as a capacitive charge divider (another factor d/t). The remaining CCE is therefore proportional to $(d/t)^2$ (d: depletion depth, t: thickness of the detector).

At lower temperatures the deep level part of N_{eff} gets less important for the current generation. At a certain temperature the most prominent deep levels even "freeze out", the resistivity rises and full depletion and CCE is regained again.

While negligible at room temperature, *trapping* gets stronger at low temperatures: charge deposited in irradiation-induced deep levels is trapped and released only with a small delay depending on the depth of the level. Thus part of the signal charge does not arrive in time at the preamplifier and might be lost for the readout. The resulting CCE is proportional to $e^{-t_{\text{drift}}/\tau_{\text{trap}}}$ with the charge drift time t_{drift} and the temperature dependent trapping time constant τ_{trap}. At low temperatures, however, the trapping time increases due to an enhanced absorption cross section, which leads to an increase in signal delay and thus a smaller CCE.

The effective CCE is a combination of both partial depletion and charge lost in traps: down to a temperature T_r the increase of active detector volume dominates and the CCE rises. When the detector is finally fully depleted at $T = T_r$, the trapping time takes over control and reduces the CCE again.

Polarization of the Bulk

The Lazarus effect is accompanied by an unpleasant feature: the CCE becomes smaller after some time of operation, see fig. 2.5. This behavior can be traced back to trapped charge in the bulk material. As more acceptor-like deep levels are produced in irradiation, positive charge collects at the ohmic side and leads to a polarization of the bulk material and correspondingly to an inhomogeneous electric field. At room temperature such polarization is quickly compensated by the normal leakage through the diode and usually not visible. In the case of low temperatures, for which basically no "natural" leakage is present, the polarization builds up to much higher values and leads to a reduction of the CCE. The time available for building up the polarization becomes longer at low temperatures due to longer trapping times and at higher irradiation rates, where charge is produced faster.

There are two obvious ways to eliminate the polarization effect: by optimizing the operation temperature to keep the value of the detector bulk generation current at a value equal to or higher than that generated by the incident radiation, or by injecting free carriers into the detector bulk, e.g. by illumination with an external light. In fig. 2.5 the easiest approach for higher leakage

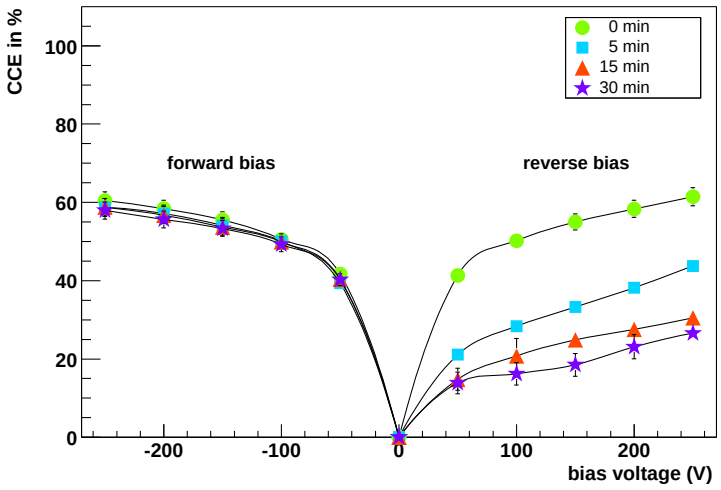

Figure 2.5: *Decay of CCE with time: CCE is measured at different times after the start of irradiation. For reverse bias the CCE drops down to approx. half of the immediate value. For forward bias, no time dependence shows. (from [RD3900b])*

current is shown as well: diodes operated in *forward* direction do not show a CCE decay at low temperatures.

Chapter 3

The COMPASS Silicon Detector

In COMPASS several stations of silicon microstrip detectors [Ang03] are installed. Their task is to provide spatial information with high resolution for precise tracks directly in the beam, which imposes hard requirements on the detector design.

To resolve close tracks a small structure size is needed. A microstrip design with structures sizes of 50 µm was therefore chosen. As a beam particle traverses the detector about every 25 ns, a good time resolution is helpful to disentangle hits from pile-up[1] and attach them to the right track. A low noise and fast readout electronics has to follow and preserve the intrinsically good resolution of silicon in space and time.

To reduce the radiation length (see section 2.1.1) of the detector system signals are read out on orthogonal strips on *both* sides of the silicon wafer. Thus one wafer provides 2-dimensional hit information.

A "side effect" of the intense beam is the radiation damage induced by the traversing particles as was explained in section 2.2. In the central beam area fluences of up to 10^{13} NIEL per cm^2 and year [Ang03] will be reached. To improve the radiation hardness and allow for several years of running, the Lazarus effect (see section 2.3) will be exploited. Thus the silicon detectors have to be operated at a temperature of 130 K. The need of a small radiation length put serious constraints on the design of both detector and cryogenic infrastructure.

In the COMPASS setup silicon detectors are needed for basically two different environments: Two stations of *beam silicon* are required standalone upstream of the target for the beam definition together with the Scintillating Fiber hodoscopes. *Spectrometer silicon* together with the GEM detectors is planned to form the small-area part of the staggered tracking stations. The main differences could be reduced to different mechanical mountings and an adapted electrical and cryogenic infrastructure, but the core will stay the same.

For the hadron beam program, for which much smaller targets than the polarized muon target (see section 1.3.4) are used, additional silicon detectors similar to the beam stations will be installed *downstream* of the target to measure the outgoing tracks with high precision.

For the starting muon beam period only beam silicon is required, which relaxes the conditions significantly: the need for small radiation length is limited to the zone directly in beam, as there are no scattering products around the beam yet. Second, as the radiation damage of muons is

[1] "pile-up" is the memory of the setup of a particle passages *before* the current event. Main sources of pile-up are a slow neutralizing of charge clouds and the shaping time of the preamplifier.

smaller than that of hadrons by a factor 10 (see fig. 2.2), the detectors could initially be operated at room temperature without employing the Lazarus effect. Consequently, in the 2002 run 2 stations of silicon microstrip detectors corresponding to 8 projections were installed upstream the target and operated successfully at room temperature. The first cold operation could then be performed in the 2003 run [RDM04, Fuc03]. More information on the commissioning phase in 2001 can be found in [Wag01].

This chapter describes the COMPASS silicon microstrip detectors and the considerations that lead to their design in more detail. In section 3.1 and 3.2 the silicon itself and the structure of one *module* including the frontend chip APV25 is described. Section 3.3 explains the readout chain, which our group especially developed for the readout of APVs (silicon and GEM detectors), featuring an ADC with zero suppression and a high speed optically linked readout module. In section 3.4 the integration into the COMPASS spectrometer is shown. The successful performance could be proven from the data of the 2002 run, characteristic properties are presented in section 3.5. The chapter concludes with a small summary and outlook.

3.1 Silicon Wafer Design

For COMPASS, double-sided silicon diodes originally designed for the HERA-*B* experiment are used [Abt99]. The design originated at the Halbleiterlabor (HLL) of the Max-Planck–Institute für Physik München and meets the requirements of COMPASS nicely. The MPI group put special effort into the design to reach a high level of radiation tolerance, which will be explained in more detail. The wafers used for the COMPASS detectors were produced for HERA-*B* by SINTEF, Oslo, Norway [Ber9797], and show slight technological differences to the original HLL design.

The detectors were produced on 280 μm thick 100mm wafers. The n-type silicon substrate had a resistivity of 2 to 3 kΩ cm. The active area of $50\times70\,\mathrm{mm}^2$ is rather large and provides a fine readout pitch of 54.667 μm on the n-side and 51.75 μm on the p-side. The expected depletion voltage is between 60 and 100 V.

Readout Strips. There are 1024 long and 1280 short readout strips on the p- and n-side respectively, realized as 15 μm wide implants of boron and phosphorus. To optimize the charge sharing between these strips, additional intermediate strips as explained in section 2.1.3 were included in the original HLL design. Due to technical problems the SINTEF design had to be modified on the n-side and has no intermediate strips anymore. The implanted strips are capacitively coupled to 14 μm wide aluminum strips via a SiO_2 layer (and a thin Si_3N_4 layer to avoid pinholes and reduce the chance of breakdown). Sizes can be taken from fig. 3.1.

The strips on the p- and n-side are orthogonal, but tilted by 2.5 $^\circ$ with respect to the borders of the wafer. Two such wafers mounted back-to-back as explained in fig. 3.2 provide 4 different projections with a stereo angle of 5 $^\circ$ (-2.5, 87.5, 2.5 and 92.5 $^\circ$) in a convenient way. The design has several advantages: mechanical complexity is limited, a large overlap of the counters is obtained and one detector design can be used for the whole system.

Bonding pads. At two edges of the detector the strips widen to bonding pads [2]. Due to their wider pitch of 60 μm, the pads are designed as four rows staggered behind each other. Fig. 3.3 shows more details of the layout.

[2] bonding: technique for fixing thin wires to the surface of small devices. The wires (down to 17 μm thickness) are heated with ultrasonic power and then pressed to the specially prepared target surface, the *bonding pads*.

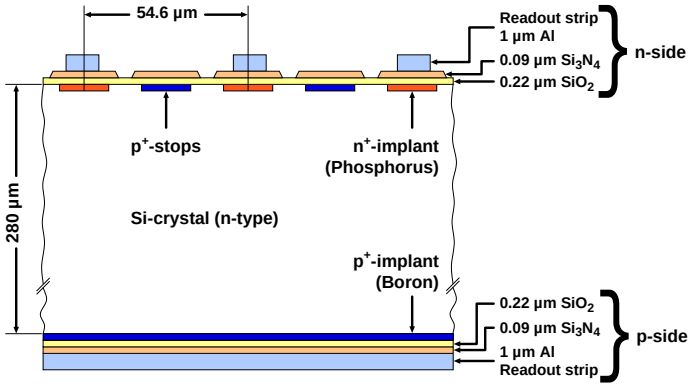

Figure 3.1: *Cross section of the silicon wafer with all implants and their sizes. Mind the replacement of the intermediate strips on the n-side by p-stops in the SINTEF design. (from [Wag01])*

Due to their tilt not all the strips extend to this edge of the detector and can be read out there.

As could already be seen in fig. 3.2, not all the strips of the (short) p-side end at the same edge of the wafer because of their tilt of 2.5°. For these strips the readout pads are implemented at the opposite edge of the wafer. In contrast to HERA-*B*, in COMPASS these strips are not read out in order to avoid the mechanical difficulties and left floating instead.

Separation between Strips. To avoid leakage between the strips, they have to be electrically insulated against each other. While this is trivially fulfilled on the p-side, where the strips are separated by the n-type bulk silicon in between, more effort is needed for the n^+ strips on n-side. The standard method puts additional p^+-strips, so-called p-stops, between the n^+ strips to separate them from each other. But as those p-stops were found to be sensitive to radiation damage, the HLL developed a so-called p-spray method, where p-implants are not localized in a strip, but realized as a layer of finely distributed p-material between the n^+-strips. Thus additional intermediate strips for charge sharing (see above) could be implemented as well. The new method, however, turned out to be difficult for mass production, which is why HERA-*B* fell back on a design using p-stops in the end. But in order to ensure a high production yield, a design with quasi individual p-stops was preferred. It has already proven to work in the HERA-*B* environment.

Bias Resistors. Traditionally the biasing infrastructure is realized in punch-through technique, requiring a relatively simple and short process. However, irradiation studies have shown that such contacts are sensitive to radiation damage. Traps are created on the bias lines and the resulting irregular charge flow leads to noise. The strip biasing in the HERA-*B* design is therefore realized with poly-silicon resistors of $\sim$1 MΩ, which are less sensitive to point defects.

Multi-guard-ring structure. With increasing radiation damage, the detectors are expected to require voltages as high as 300 to 500 V to reach full depletion of the silicon bulk. To allow the operation of such high bias voltage (there is, after all, an electric field of 15 $\mathrm{kV/cm}$), the entire sensitive area is surrounded by a multi-guard-ring structure consisting of up to 16 punch-through guard-rings on both sides of the detector. Via a resistor network they reach a gradual potential

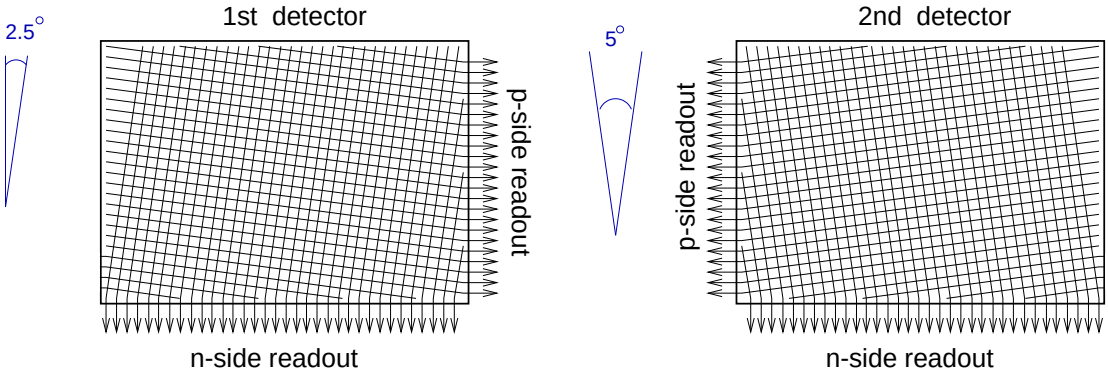

Figure 3.2: *Orientation of readout strips in back-to-back mounting. The strips on p- and n-side are orthogonal, but tilted by 2.5° with respect to the border of the detectors. Flipped around a short side, one gets a mirror image (left and right wafer). With the detectors mounted like this ("back-to-back") behind each other, a 5° stereo angle is obtained. (from [Abt99])*

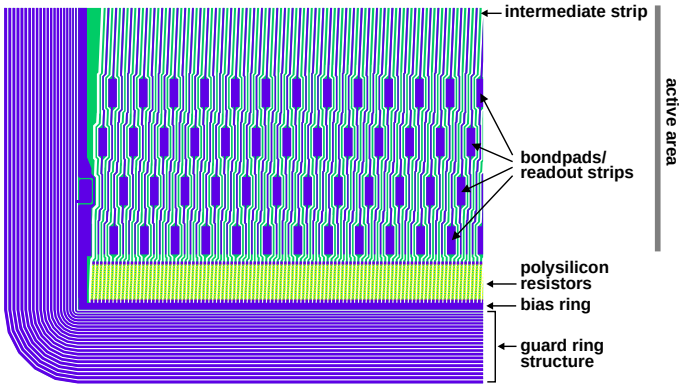

Figure 3.3: *Layout of one corner of the n-side of the silicon wafer. One can see the four staggered rows of bonding pads and again the tilt of the strips. (from [Abt99])*

drop from the high voltage part to the undepleted substrate without dangerous edges or corners. Additionally they shield the sensitive area from surface and edge leakage currents. They are also visible in fig. 3.3.

3.2 The Silicon Module

The basic unit of the silicon detector system is the *silicon module* (see fig. 3.4). It consists of one silicon wafer sandwiched between two Printed Circuit Boards (PCBs) named "L-boards". The L-boards (section 3.2.2) host the frontend chips including the electronic and cryogenic infrastructure and at the same time make a precise mounting of the module possible. A module is already fully operational and can be used standalone. It provides two projections of a particle passage.

The central part of the readout system is the frontend chip. The APV25 was chosen for this. The

features and requirements of this chip define the design of the following readout electronics; they are presented in section 3.2.1.

The first modules, including the modules used in the 2002 run, were produced in-house. For the further production an external company was employed [MIP]. In 2002 four modules were installed and successfully operated.

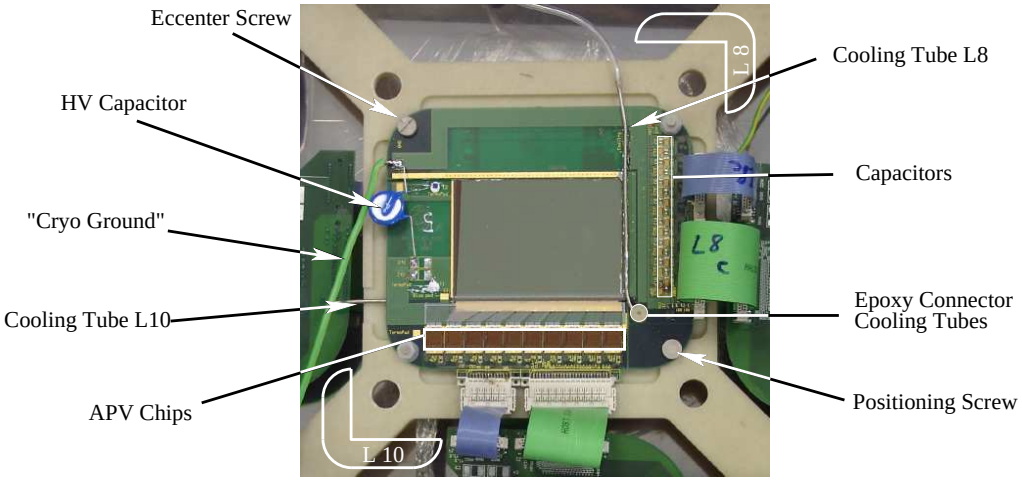

Figure 3.4: *One silicon module consists of the two* L*-boards (*L10 *and* L8 *as indicated) and one silicon wafer.*

3.2.1 The Frontend Chip APV25

The APV25[3] is a 128 channel analogue pipeline Application Specific Integrated Circuit (ASIC). It was developed for the readout of the silicon tracker of the CMS experiment at the LHC at CERN and combines the handling of the analogue signals with digital control functions. In COMPASS it is used for both GEM and silicon detectors in the versions APV25-S0 and APV25-S1. A detailed description including further references can be found in [APV99, APV00].

The chip has a total size of $8.2 \times 8.0\,\mathrm{mm}^2$ and is manufactured on 300 and 800 µm thick substrates in a deep sub-micron (0.25 µm) CMOS[4] process. Besides a low noise, low power consumption and a high circuit density, the CMOS process also shows a respectable radiation hardness.

The APV25 is biased with VSS=-1.25 V and VDD=+1.25 V and has a power consumption of 213 mW and 150 mW respectively.

Analogue Part

Each of the 128 channels is equipped with low noise 50 ns CR-RC-shaping amplifiers. The characteristic answer to a test pulse is shown in fig. 3.6. The CR-RC shape is sampled at 40 MHz, i.e. every 25 ns, and stored in consecutive cells of an analogue circular buffer. On the request of an external trigger signal, certain buffer cells are transferred to an intermediate buffer of FIFO[5] type

[3] APV: Analogue Pipeline, Voltage type; 25: 0.25 µm CMOS technology
[4] field-effect transistors made of Complementary-Metal-Oxide-Semiconductor (CMOS)
[5] First In, First Out

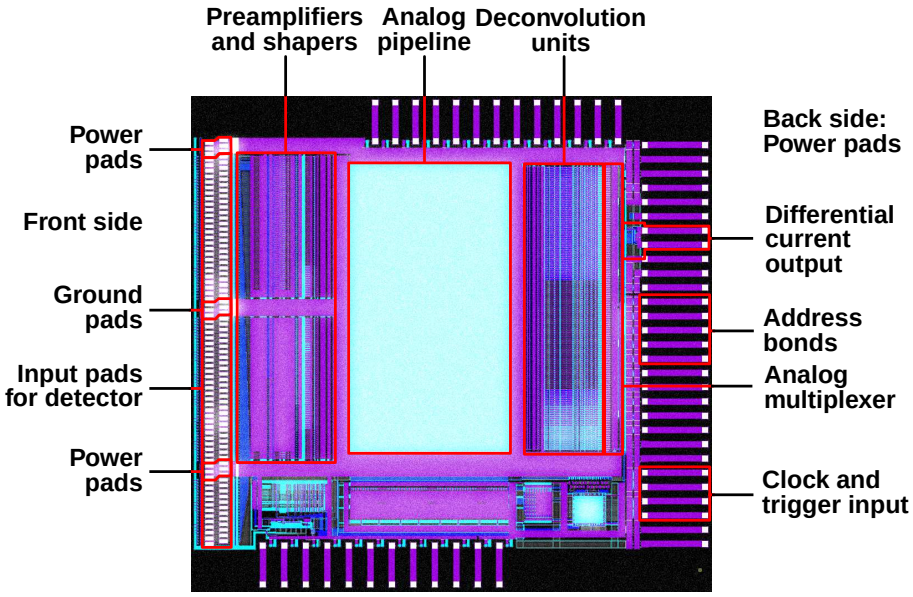

Figure 3.5: *Surface layout of the APV25, S0 version. At the front side (left) the chip can be bonded to the silicon wafer. The signals are shaped, preamplified and sampled in a 160 cells deep pipeline. The readout is done in an analogue multiplexer. At the back side (right) bonding pads provide connections for the output signal and control I/O. (from [APV00])*

for readout. The pipeline consists of 160 switched capacitor elements and accounts for the *latency* of the trigger signal: at 40 MHz sampling frequency the delay of the external trigger relative to the particle passage can be up to 4 µs before the buffer is overwritten again.

The chip can be operated in different modes: In *Peak* mode one sample is reserved in the pipeline for reading out. The signal corresponds to the peak voltage of the CR-RC shaped signal. Peak mode is generally used when data rates are sufficiently low, so that a pile-up of detector signals is not significant. At higher data rates however, where pile-up is more pronounced, the peak value alone is not enough as a later signal will sit on the tail of the previous one. For the CMS experiment an additional mode was therefore implemented: in *Deconvolution* mode the signals are processed in an Analogue Pulse Shape Processor (APSP), where the contents of three consecutive buffer cells are summed with optimized weights.

In COMPASS an intermediate mode is used: in *Multi* mode, three consecutive buffer cells per trigger are marked and read out unprocessed by the APSP in Peak mode. The reason for the changed procedure lies in the different experimental environments: while in CMS the very clear bunch structure of a colliding beam experiment limits the arrival time of the particles to only a short period, in COMPASS as a fixed target experiment the interactions are randomly distributed within a long spill of 5 s (see section 1.3.3) and are not connected to the 40 MHz bunch crossing rate of an LHC. In Peak or Deconvolution mode the arrival time is therefore homogeneously distributed within the 25 ns cycle and the sampling points of different events are thus at different positions on the CR-RC shape. In Peak mode alone this results in an amplitude fluctuation which can be estimated from fig. 3.6 to be approx. 10%. In COMPASS the correlation of the three consecutive samples is used to estimate the arrival time of the particle and to exclude pile-up events. The success of this method will be presented in section 3.5.3.

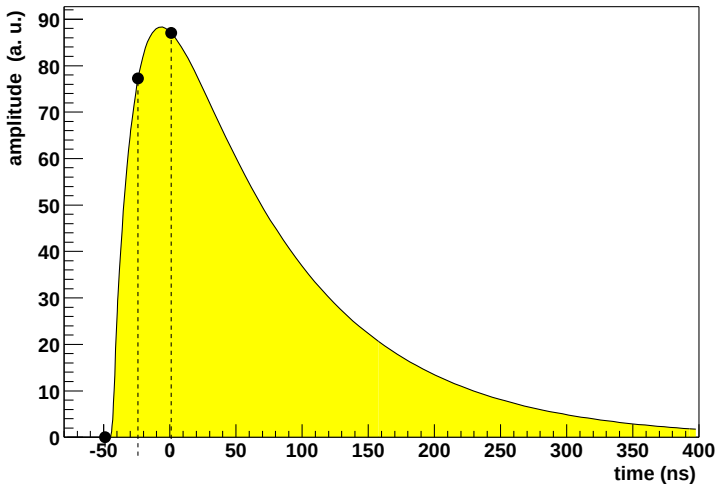

Figure 3.6: *Signal shape of the APV chip (result from a fit to data): the collected charge is proportional to the peak value after a rising time of approx. 50 ns. The decay time of the signal is in the order of 250 ns. The 3 points are an example of the position of the 3 sampling points in Multi mode as explained in the text.*

Up to 32 buffer cells can be stored simultaneously in the output FIFO, i.e. up to 10 events can be pipelined in Multi mode. An analogue multiplexer compresses the data of all 128 channels onto one single differential output line in three consecutive stages (8:1, 4:1, 4:1). Its frequency can be set independently of the sampling frequency to either 20 or 40 MHz[6]. For the 2002 run 20 MHz were chosen to simplify the electronics developments, for the hadron physic program the transition to 40 MHz is necessary. The final output of the multiplexer is $\pm$ 1 mA per MIP signal [APV99].

Output Format

During the absence of a trigger signal the APV sends out synchronization pulses ("ticks") every 875 ns. After the arrival of the trigger the raw data are sent out synchronously to such ticks. The full train of data is shown in fig. 3.7: one can see the three cycles of the Multi mode called *frames* consisting of the 128 analogue channels. Each frame is preceded by a 12 bit long digital header consisting of a start marker of 3 bits digital low, 8 bits with the Gray coded buffer cell address and an error bit indicating pipeline or latency errors. After the three frames, "ticks" can be seen. For the figure the trigger latency was set in a way that the first frame is close to the signal start, the second frame is on the rising edge and the third frame on top with a tendency toward the falling edge, similarly as shown in fig. 3.6.

Due to the internal multiplexing, neighboring strips on the front side of the chip do not come out one after the other, but are shuffled as indicated in the picture. The channel order therefore has to be rearranged later on.

[6] Actually, the clock is an external signal. For the multiplexer the scaling factors 1/1 or 1/2 can be chosen.

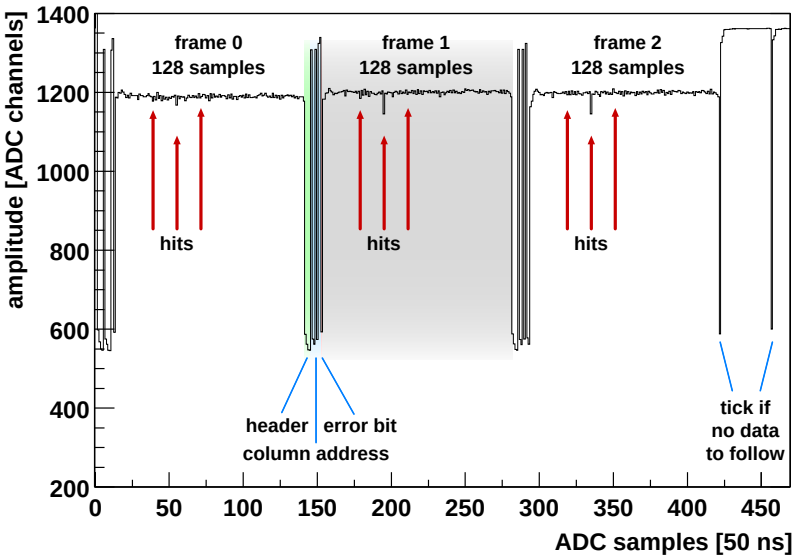

Figure 3.7: *APV raw data output format for the Multi mode. One can see the 3 frames with 128 channels starting with a 12 bit digital header (header (3), buffer address (8), error bit (1)). (from [Gru01])*

Digital part

Many settings of the APV can be configured by writing to special registers in the chip. For this a protocol compatible with the Philips I^2C standard is available [APV99]. Several slaves can be attached to one I^2C bus master simultaneously. Each chip has a 5 bit I^2C address for unique identification on this bus, which is defined by pulling the address pads on the chip to negative voltage VSS. The binary address 11111 is reserved for broadcast commands to all chips attached, the remaining 31 addresses can be used for APVs.

The configuration includes the setting of the mode (Peak, Deconvolution, Multi), the trigger latency and the bias voltages for adjusting the analogue circuit. For the reception of electrons and holes from p- and n-side the charge signals can be inverted, the zero line (baseline) can be adjusted to the amplitude of the signals.

The chip also provides a calibration circuit where a specific charge can be injected into the preamplifier for calibration purposes. Amplitude, polarity and channel pattern can be configured.

During data taking the APV is controlled by only one differential input line called TRIG. A pulse of one clock cycle length is interpreted as a trigger signal (“100”). A reset of the pipeline is sent on this line as well as two pulses with one empty clock cycle in between (“101”). Lastly two pulses directly behind each other (“110”) are a calibration request, which triggers charge injection into the preamplifiers one latency period later.

3.2.2 The Frontend Boards “L board”

The L-boards are 6-layer[7] Printed Circuit Boards (PCBs) of 1 mm thickness, produced by ILFA, Hannover [ILFA]. One set consists of two L-shaped pieces, see fig. 3.8. When glued together,

[7] 6-layer boards have 6 *conductive* layers between insulating layers, e.g. copper between glass fiber prepreg.

they form a rectangle of $11 \times 13\,\mathrm{cm}^2$ with a $5 \times 7\,\mathrm{cm}^2$ hole in the middle. At the corners position holes are drilled for the precise alignment of both boards relative to each other as well as for the following positioning of the module in the experiment: the small hole in the lower right corner defines a fixed position, the slit in the upper left corner allows rotation with an eccentric screw. The side diagonal is just used for fixing in the third dimension. The two Ls differ in the number of chips they host: the readout for the (long) n-side of the silicon hosts 10 chips and is labeled L10 (lower left L in the figure), the readout for the (short) p-side of the silicon hosts 8 chips and is therefore labeled L8 (upper right L in the figure).

The silicon wafer is sandwiched between the two Ls: the first layer is L10 with chips up, the second layer is silicon wafer with n-side up and the last layer is L8 with chips underneath. Silicon and L-boards are glued together on a 1.5 mm wide rim with a 50 µm thick layer of silicone glue [NEE]. The silicone glue was chosen for its very small electrical conductance [Abt98] and its flexibility at low temperatures. In the corners of the main diagonal the L-boards are fixed to each other with Epoxy-based two component glue [CIBA].

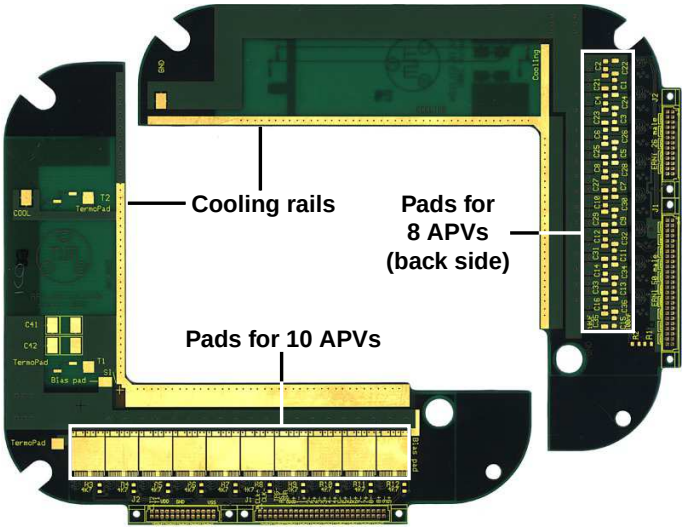

Figure 3.8: *The PCBs hosting the frontend chip APV:* L*-board. The silicon is sandwiched between the two boards. The boards have both electrical as well as mechanical and cryogenic functionality. (from [Wag01])*

Electronic Layout

The main function of the L-boards is to host the APV chips and provide the respective infrastructure, including analogue out, I^2C bus, fast clock and trigger signals and the power distribution.

The chips themselves are glued to a big VSS power pad with two component conductive glue [EPOXY]. As the chips are very sensitive to noise on the power- and grounding-lines and start to oscillate when a certain level is exceeded, special care was taken to provide very clean power connections. Capacitors (100 nF tantal, 10 μF electrolyte) were therefore mounted between the power lines directly under the chips on the backside of the PCB (see fig. 3.8 on L8).

Power lines and signal lines are led out on separate high density cables to avoid noise in the power lines. The space for the connectors can be seen in the figure. To avoid crosstalk on the

cable, the fast signal lines (clock, trigger and analogue out) are alternated with ground lines.

On the frontend side of the APV chips a pitch adapter is glued to match the output pattern of the APV and the silicon bonding pads. On the silicon side there are *four* staggered rows of pads behind each other with a pitch of 54.667 and 51.75 µm on n- and p-side respectively, on the APV side there are *two* staggered rows behind each other with a pitch of 44 µm. The layout is shown in fig. 3.9. Such small structures (both smallest wire and smallest distance in between are 9 µm) cannot be realized on PCB anymore and have to be produced on glass substrate. The pitch adapters for the silicon detectors were therefore made as aluminum wires on 300 µm thick glass.

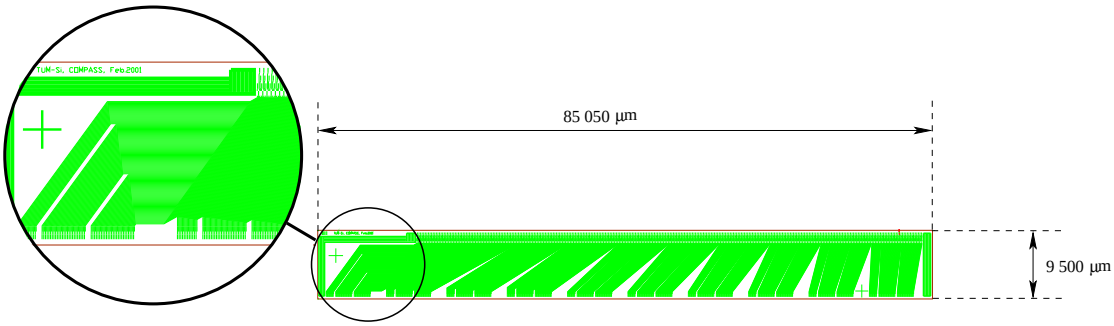

Figure 3.9: *Pitch Adapter for 10 APV chips, aluminum wires on glass. APV chips are connected to the two staggered rows of bonding pads on the bottom, the silicon is connected to the four staggered rows of pads on the top side. The smallest structures are 9* µm *wide.*

Cryogenic Layout

The cooling facilities for the silicon wafer are also incorporated into the L-boards. The silicon is glued on specially designed cooling rails with copper through all layers of the PCB and additional metalized holes. Thin Cu/Ni capillaries (diameters of d_{outer}=1.6 mm and d_{inner} =1.3 mm) which can be flushed with liquid nitrogen are soldered on the back side of the PCB. As the thermal conductivity of silicon is very good, it proved sufficient to cool the silicon only on two edges. The cooling tubes are thus installed only on the two readout sides, to thermally separate the cold silicon from the heat producing APV chips.

The cooling rails are separated from the "electrical" copper layers of the PCB and thus electrically and thermally decoupled. The thermal decoupling is convenient to reduce the thermal flow from the (heat producing) APVs to silicon and capillary and to make the cooling more efficient. The electrical decoupling is needed as the strips of the silicon side which is glued to the L-board have the opposite bias voltage as the L-board ground. The capillary of L10 is therefore capacitively coupled to the ground of L8 via the 50 µm thick silicone glue layer and vice versa. In addition the cooling rails have pads which can be connected to the ground of the other L-board for even better electrical coupling. To allow for only one cooling loop per module, the capillaries of L10 and L8 are joined via an electrically insulating connector cast of epoxy glue. A cross section of the L-board is shown in fig. 3.10, which shows the thermal coupling between the cooling tubes and the silicon wafer.

Two PT100 temperature sensors per L-board attached to the cooling rails complete the cryogenic installation.

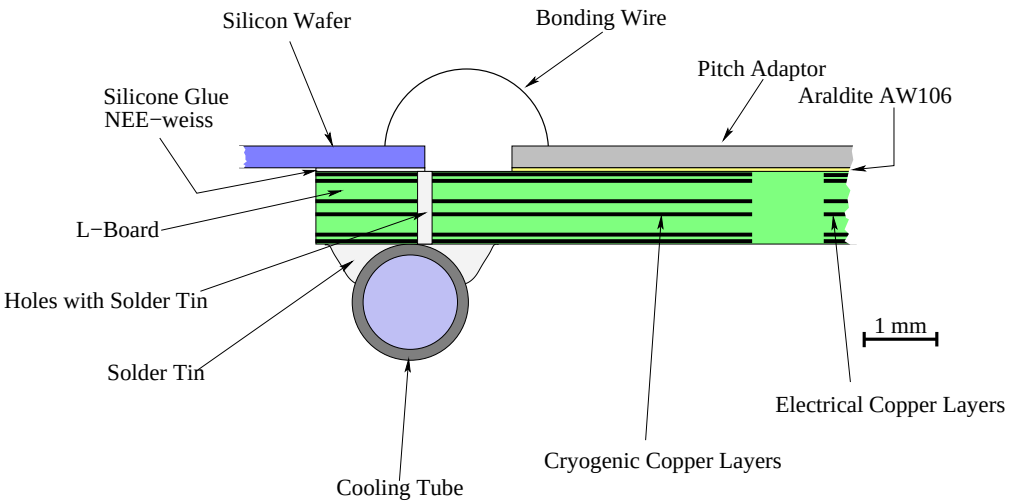

Figure 3.10: *Cross section of an* L*-board. One can see the cooling tube and the thermal coupling to the silicon wafer via the copper layers in the PCB and the silicon glue. Note also that the "cryogenic copper" is separated from the "electronic copper".*

3.3 The Readout Chain

For the APV signals of silicon and GEM a common readout system was developed at the TU Munich. The analogue signals go through a repeater card (section 3.3.1) to the ADC (`sg_adc`, see section 3.3.2) via flat cables. The ADC digitized the data, subtracts pedestals, performs a common-mode-noise correction and suppresses channels without signals.

To achieve optimal signal quality, repeater and `sg_adc` are on the same potential as the L-board to which they are connected and thus not necessarily on ground potential. As will be explained in section 3.3.4, repeater and `sg_adc` were designed as "floating" devices with no direct connection to ground.

The digitized data of four `sg_adcs` are transferred to the concentrator module GeSiCA (section 3.3.3) via optical connection, where the data are formatted and the header information is completed with a unique identifier, event number and time tag before it is sent to the Data AcQuisition computers (DAQ).

For an overview see also fig. 1.15. Details on the COMPASS readout system can be found in Schmitt et al. [Sch03], specific information on the GEM/silicon chain are given by Grube [Gru01].

3.3.1 The Repeater Card

Each L-board is connected to a *Repeater Card* with a high density flat cable of less than 50 cm length. The repeater basically refreshes all signals from and to the APVs: the fast clock and trigger signals get reshaped and the I^2C signals are regenerated. The analogue out signals receive a small preamplification which drives the transfer to the ADC. The ADCs therefore can be safely

positioned outside the beam and the acceptance of the spectrometer to avoid both damaging of the electronics and multiple scattering of the for the physics measurements relevant particles.

The repeater also provides the supply voltages for the APVs. As was explained in section 3.2.1, the APV is very sensitive to noise on the power lines. The voltages of $\pm 1.25\,\mathrm{V}$ are therefore formed with voltage regulators from $\pm 3.3\,\mathrm{V}$ and stabilized with additional capacitors of $12\,\mu\mathrm{F}$.

On the repeater cards the readout of the temperature sensors of the L-boards is also separated from the analogue data flow. From here on, the temperature signals are transferred to the DAQ in 4-wire technique to avoid signal losses in long cables.

3.3.2 The ADC Card `sg_adc`

The analogue data are now sent through another 100 cm of flat cable to the Analogue-to-Digital Converter `sg_adc`. As it was designed for both GEM and silicon detectors, the data of up to 12 APVs can be digitized simultaneously, which fits nicely for one complete GEM chamber (2 projections which each 6 APVs) or one projection of silicon (8 or 10 APVs). Digitization is done with 10 bit precision. A programmable FPGA[8] chip then performs an online data processing: it synchronizes with the data stream from the APV and extracts the signal amplitudes and the header information from all three samples (cf. fig. 3.7). Depending on the FPGA's configuration the channels are reordered to correct the shuffling of the APV multiplexer (see section 3.2.1).

The `sg_adc` can be operated in two major modes: in *Latch ALL mode* (LALL), the digitized values of *all* APV channels are transferred to the DAQ. As this results in a huge data rate of 2 kBytes per event, which also limits the maximum trigger rate of the complete readout system to 1 kHz, during normal running the ADC is operated in *zero suppressed mode* (Sparse): on-chip loaded values for the baseline of each individual channel, so-called *pedestals*, are subtracted and the remaining value of the third sample is compared with a level depending on the noise of each channel (e.g. 3 times the noise level, 3σ). Channels below this level are suppressed and not transferred to the DAQ.

It turned out that a big source of noise from the APVs can be easily corrected: small fluctuations in the supply voltages lead to a baseline shift in all 128 channels of one APV, called *common mode noise*. The size of such fluctuations can be extracted from an average value of the non-hit strips, which means that these values have to be acquired before zero suppression is carried out. The common-mode-noise correction is thus performed online in the FPGA as well. The details of the implementation of the common mode corrections into the FPGA despite heavy constraints on resources and time are explained in [Gru01]. For silicon such corrections can be as big as 10% of one MIP signal (sigma); when the APV is oscillating, fluctuations can go up to an equivalent of two MIPs [Wag01].

The data format in LALL and Sparse mode is different. For each APV channel which is written out a 32 bit word is available. As in LALL mode a channel identification is not necessary, all three samples are stored with 10 bit precision, leaving space for two more control bits. In Sparse mode, 7 bits are already needed for a unique channel number (0-127), which does not leave enough space for 3 times 10 bit. As the precision is limited by the noise level of the detector anyway, the analogue information was shortened to bits 1 to 9 for the last sample and bits 1 to 8 for the first and second sample. Bit 9 of the first and second sample can be reconstructed from the correlation of the three samples.

[8] Field-programmable Gate Array

A FIFO type memory after the FPGA provides a short term buffering before the data are sent to the GeSiCA module via an optical HOTLink connection. The optical fibers are a very convenient choice, as they provide an electrically decoupled connection without noise pick-up or ground loops and can reach over long distances (for silicon 30 m are sufficient) without significant signal loss. The bandwidth is 320 Mbit/s.

The FPGA can be controlled via an I^2C connection, where status registers can be read and the available functions like zero suppression or common mode correction can be switched on or off. Pedestals and noise levels are also loaded via the I^2C line.

3.3.3 The Data Concentrator GeSiCA

The Gem-Silicon-Controls-and-Acquisition unit GeSiCA is the link between frontend cards, DAQ system and user control. It is realized as a 9U VME module with programmable FPGAs.

GeSiCA receives the trigger signal and the system-wide clock through the COMPASS trigger module *TCS receiver* (cf. section 1.3.7 and [Kon02]) and distributes it to the frontend cards via optical HOTLink. It collects the data from up to four `sg_adcs`, adds header information like event number, time tag and its unique identification called *sourceID* and sends everything well formated through a buffer via the COMPASS S-Link card to the DAQ computer [Sch03]. From the TCS system-wide resets and run control signals are also received and processed.

For user control GeSiCA provides an interface to the VME bus. Programs for the FPGAs of GeSiCA, `sg_adc` and the TCS receiver are loaded via VME after power-up and in the rare case of a hiccough of the system. For further configuration of connected `sg_adc` and APVs, GeSiCA provides an I^2C master, which is also accessible via the VME interface.

3.3.4 A Word on the Grounding Scheme

The p- and n-side of the silicon wafers are pulled to different potentials by the applied bias voltage. The readout strips are capacitively coupled to the p- and n-implants to avoid that the leakage current through the silicon gets drained into the FE chips. Thus in principle the readout electronics could be on any potential. But in order to avoid problems connected with a breakthrough of one of the approx. 1000 strip capacitors on both p- and n-side, L-boards, repeater and `sg_adc` were put to the same potential as the respective implants. These devices were therefore designed "floating", i.e. without a connection to an external ground. GeSiCA is optically connected and thus already decoupled.

Two major problems arise from such a constellation, namely the need for power supplies, which provide a floating voltage and the noise pick-up in the floating electronics.

Noise Pick-up in Floating Electronics. As the long chains of electronics from the L-board via repeater and `sg_adc` cannot be properly grounded, they act like antennas and pick up noise. Via the capacitance of the silicon wafer the two readout sides are coupled together, thus the noise on one L-board will be passed to the input of the APV chips on the other L-board. Such fluctuations will lead to common-mode-noise and if a certain threshold is reached the chips will start to oscillate (see also section 3.2.2). In order to stabilize the potentials of the APVs, large capacitors were installed in parallel to the silicon, which act like a shortcut for high frequency noise. A 10 nF ceramic capacitor was thus installed directly on the L-boards (see fig. 3.4) and an additional 200 μF electrolyte capacitor outside the cryostat.

Power Supplies. From the design point of view there is no difference between the floating of the p- and the n-side. For the final installation one of the two sides could therefore connected to a reference ground and properly stabilized. This was done by connecting the p-side to the housing of the detector and defining the n-side as "high potential". As will be explained in more detail in the next section, the housing is a massive cryostat made from stainless steel, which makes a very good noise shield as well.

For the power supplies of bias voltage, APV and ADC floating devices had to be chosen and set up accordingly:

- For the bias voltage of the silicon cascaded 9 V batteries were used, which constitute the ideal case of a potential-free voltage. In 2003 the HV module EHQ 8006p_605-F from *iseg* [iseg] was used, which is floating in principle, but the negative voltage must not float more than 64 V against its housing. This finally pulls the potential of the cryostat close to the common ground in the hall.
- The power for APV and repeater is provided by the CAEN A525 (4 V, 3 A) module for the SY527 main frame, which is intrinsically floating according to the manufacturers [CAEN].
- For the `sg_adc` a system with DN35 modules (5 V, 7 A) from Deutronic [Deu] is set up. These modules are floating in principle, but turned out to have a 0.5 MΩ connection from the secondary circuit to their housing for safety reasons. Thus a "shortcut" of 1 MΩ was made when two ADCs with different potential were powered from the same crate. After changing these resistors to 10 MΩ, the leakage current sank to an acceptable level.

3.4 The Silicon Station

At COMPASS the silicon modules are installed in pairs as so-called *silicon stations*. In 2002 the two stations SI01 and SI02 were present. A view into the housing of SI01 is given in fig. 3.4.

The two modules are mounted back-to-back on a frame made from glass fiber (Stesalit) [Stesalit] resulting in four different projections as explained in fig. 3.2. The Stesalit frame is rotated by 2.5 ° so that the final strip directions are then +5, -85, 90 and 0 °, labeled as projections u,v,y and x. The distance between the two wafers is 10 mm. Glass fiber was chosen for its good mechanical stability and its small thermal expansion. At the same time it provides very good electrical and thermal insulation.

Cryostat

When operated at a temperature of 130 K, the modules have to be thermally well insulated to prevent icing on the surface of the structure. At the same time the material traversed by particles has to be kept low to avoid multiple scattering. Both requirements can be met using a vacuum vessel made of light material, which is still, however, a technically challenging project.

For the muon beam program silicon stations upstream the target, where the problem of radiation length is limited to the beam area, are sufficient. To get experience with the necessary techniques for vacuum stability and cryogenic operation the cryostat in fig. 3.11 was made from stainless steel. It has a surface of $240 \times 240\,\mathrm{mm}^2$ and extends 82 mm along the beam direction. It provides several feedthroughs for electric, cooling or vacuum needs.

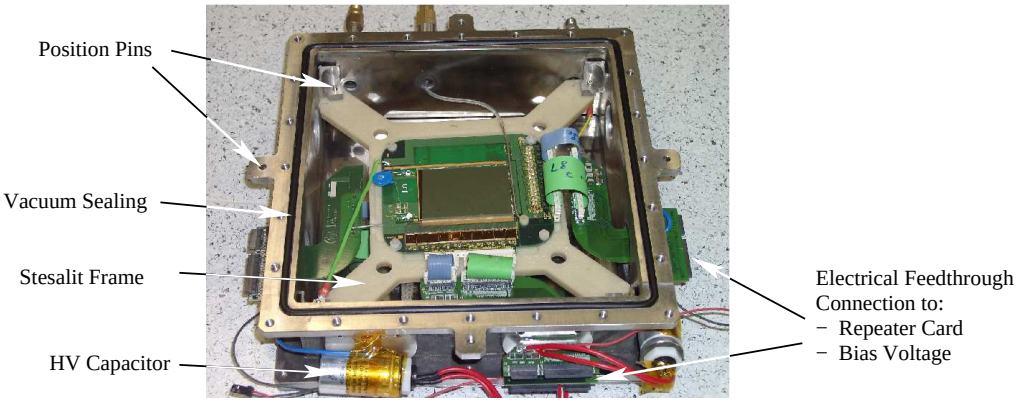

Figure 3.11: *View into the open cryostat of station SI01. One of the two modules mounted onto the Stesalit frame can be seen.*

The beam passes through two 80 mm large windows of 30 µm thick Mylar foil supported by Kevlar wires. An aluminum coating of ∼1 µm provides both electrical and optical shielding.

In 2002 both installed stations were operated at room temperature and the cryostat was therefore only used as mounting and electrical shielding. More information on the cryogenic operation of the setup can be found in [RDM04, Fuc03].

Optical Bench

Being installed standalone upstream of the target, the silicon stations need an extra mounting to reach the beam height of 3152 mm. Good thermal stability is important to avoid that temperature fluctuations in the hall influence through thermal expansion the position measurement of the particle tracks. Concrete blocks of 240 cm height are therefore used as a base. An optical bench made from highly braced iron bars is placed on top. It has two 120 cm long granite rails parallel to the beam direction, which allow a free placement of several cryostats. Concrete blocks, optical bench and the mounted cryostat can be seen in fig. 3.12.

3.5 Performance in the COMPASS beam

In 2002 the two silicon stations SI01 and SI02 with 8 projections in total were installed in the COMPASS experiment and successfully operated in standard data taking. After a short tuning period the detectors were running stably up to the end of the run. In total they were operated for 2 100 hours and observed 10^{14} muons corresponding to $\sim 10^{13}$ NIEL and a deposited energy of 1 kGy.

Both stations were installed upstream the target at -470.6 and -398.4 cm[9]. The size of the beam at this position can be seen in fig. 3.23. As the detectors were operated at room temperature, and thus no liquid nitrogen cooling was available, the power dissipated in the readout chips was removed by flushing the cooling capillaries with gaseous nitrogen instead. So the temperature on the board stayed below +45 °C.

[9]Origin of the COMPASS reference system is the middle of the upstream target cell.

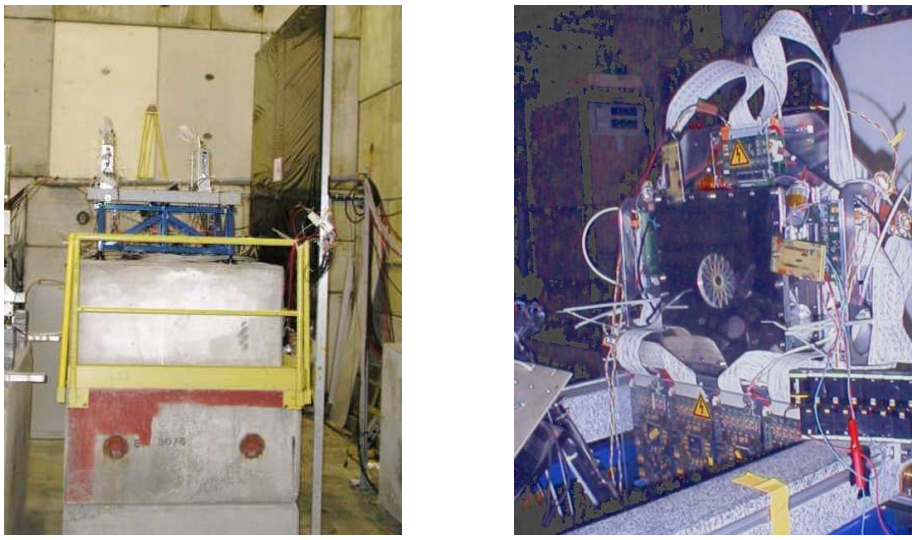

(a) (b)

Figure 3.12: *Installation in the hall:* ***a)*** *The optical bench is mounted on 240 cm high concrete blocks. On two stone rails on top two cryostats are mounted. The beam comes from the right side.* ***b)*** *A closer view of the second cryostat SI02 (beam from the left side).*

The startup trigger rate for the muon program in 2002 was 4.5 kHz, corresponding to 22 000 triggers per spill. The readout chain worked as expected and did not show any problems. After zero suppression the remaining data rate were 4.3 MByte per spill and projection.

The presented measurements were taken with activated zero suppression (see section 3.3.2). The threshold was set to 4 σ, i.e. the amplitude on every strip was tested against its own noise level (Gaussian sigma) and rejected when it was smaller than 4 times this level. The correct functioning of the suppression is shown in the following pictures. The data presented were taken from silicon station 1, projections xy (SI01XY), run 22486, except for fig. 3.19, which was taken from run 23224. If not otherwise stated, the left plots are from the p-side (SI01Y), the right plots from the n-side (SI01X).

3.5.1 Multiplicity and Occupancy

The number of strips above threshold is important both for the data acquisition, which has to digest the data, and for the track reconstruction procedure, where fewer hits mean less combinatorial background.

The total number of hit strips, the *multiplicity*, is shown in fig. 3.13. The peak value for the p-side (n-side) is 19 (19) out of 965 (1280) strips, corresponding to an average occupancy of 2.0 (1.5) % and to a suppression of data by a factor 33 per station, when headers are included.

These values are close to the expectation and can be explained with the pile-up in the detector readout caused by the high beam rate. From the beam intensity one estimates one beam muon every 25 ns. As can be seen in fig. 3.6, the signal shaped by the readout chips has a time over threshold of the order of 200 – 300 ns. One expects therefore 8 – 12 particles to be visible in the detector in the same readout gate – and only one of them correlated to the trigger signal. With a cluster size of 1.5 strips (see below) per particle, this results in 12 – 18 strips above threshold.

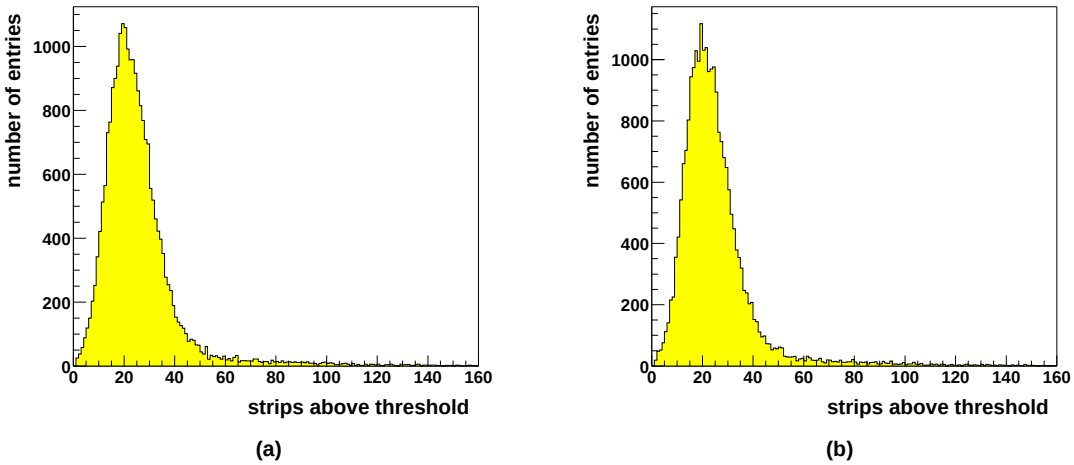

Figure 3.13: *Number of strips above threshold for p- and n-side* ***(a)*** *and* ***b)*** *respectively). The peak values are 19/965 and 19/1280 strips, corresponding to an occupancy of 2.0 and 1.5 %.*

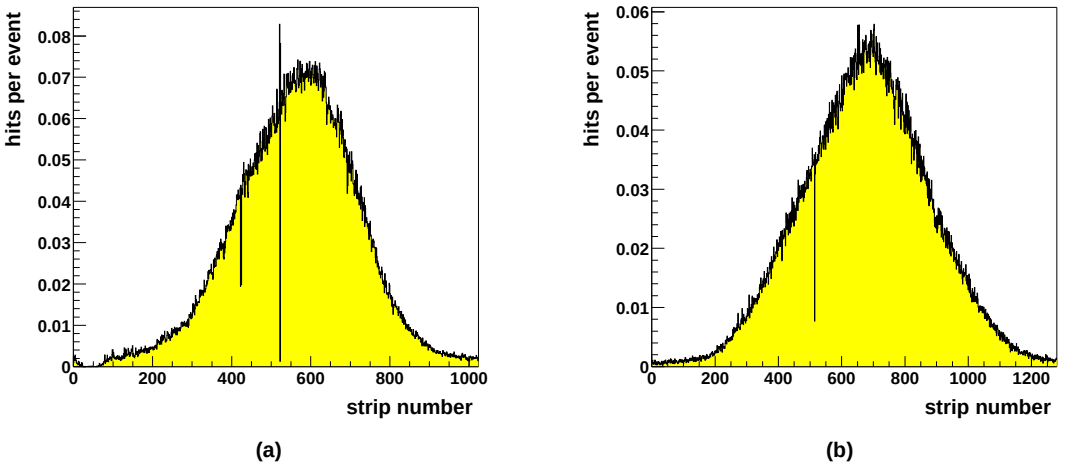

Figure 3.14: *Number of hits in each strip, normalized to the number of events, for p- and n-side: occupancy. The shape reflects the spatial distribution of the beam.*

Fig. 3.14 shows the number of hits for each strip, normalized to the total number of events. The maximum is at approx. 7 %. The shape reflects the spatial distribution of the beam. The width (RMS) can be extracted to be 7.9 mm vertical from the p-side and 10.9 mm horizontal from the n-side.

3.5.2 Pulse Height Information

The deposited charge of one particle can be distributed on several strips. For the full charge collection therefore the amplitudes of neighboring strips have to be added to form *clusters*. For the silicon detectors additionally the time information was used for the clusterization (see below) to

reduce wrong combinations due to pile-up. The number of strips per cluster is shown in fig. 3.15; it is on average 1.5 and 1.3 for the p- and n-side respectively. One should keep in mind that strips with very small signals are already cut by the zero suppression.

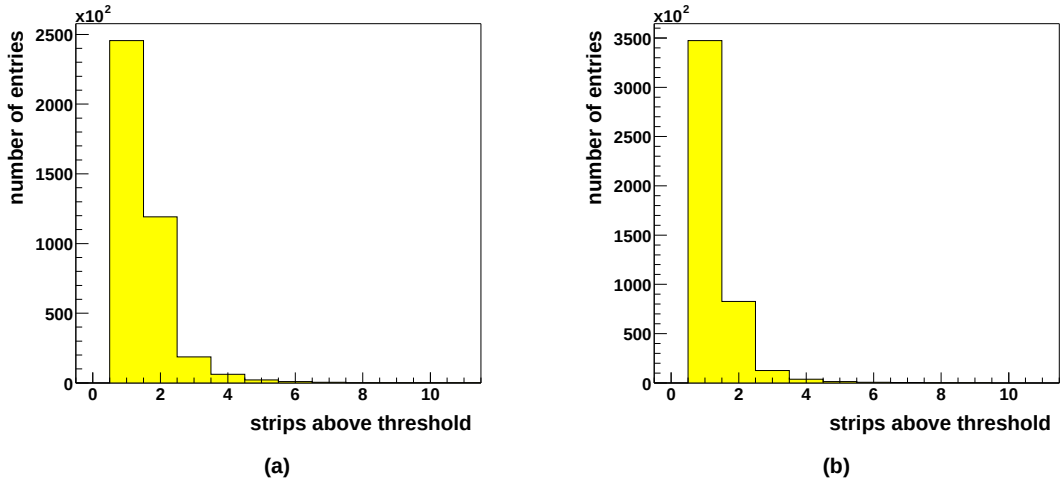

Figure 3.15: *Number of strips per cluster: the signals of neighboring strips with similar timing are taken to originate from the same charge cloud and to belong together.*

Fig. 3.16 shows the measured pulse height distribution of the beam muons in the clusters. On the left side the tail of the noise is visible, as well as the cut due to the sparsification. The signal peak is clearly separated from the noise. The most probable value is at 15 000 electron-hole pairs. The average noise level is 840 electrons ENC per strip, resulting in a ratio of cluster charge to noise in a single strip of 17.9.

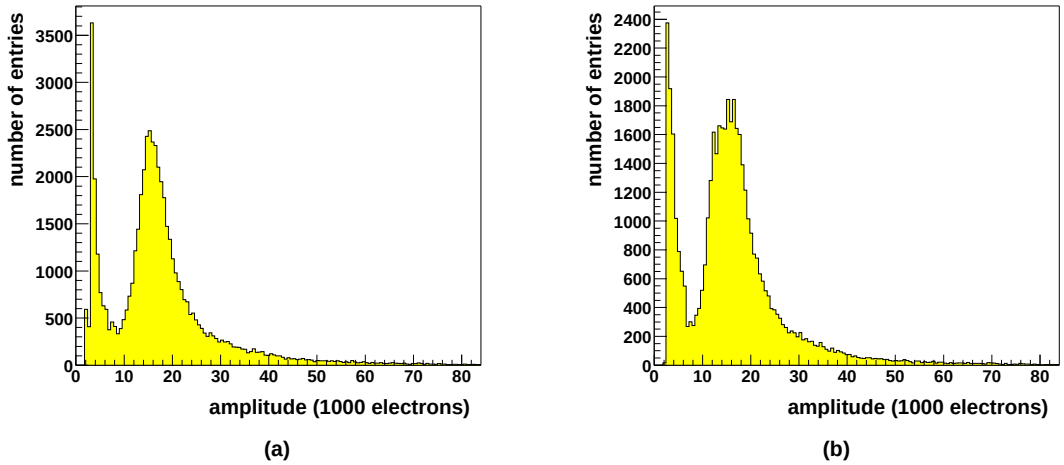

Figure 3.16: *Cluster charge collected for muons with 160 GeV on p- and n-side. A 4 σ cut on the amplitude of individual strips is applied. The separation of the signal from the noise can be clearly seen. The signal-to-noise ratio is 17.9.*

3.5.3 Time Resolution

In section 3.5.1 it was shown that due to the high beam intensity many pile-up hits are present in one readout gate. For good tracking results it is necessary to reduce the pile-up significantly. As explained in section 3.2.1 the silicon signal is sampled synchronously to the COMPASS-wide 40 MHz clock. Using the amplitudes at three consecutive sampling points $a_0 = A(t_{\text{tr}} - 50\,\text{ns})$, $a_1 = A(t_{\text{tr}} - 25\,\text{ns})$ and $a_2 = A(t_{\text{tr}})$, it is possible to improve the time resolution below the sampling time of 25 ns.

Fig. 3.6 on page 55 was the result of a fit to the response of the APV to a δ-function-like signal. A combination of two exponentials motivated by the general behavior of capacitor-resistor networks was used as fit function:

$$A(t) = A_0 \cdot e^{-(t-t_0)/\tau_{\text{fall}}} \cdot (1 - e^{-(t-t_0)/\tau_{\text{rise}}}), \tag{3.1}$$

where τ_{rise} and τ_{fall} are the time constants of the shaping circuit of the rising and the falling edge, A_0 is the amplitude and t_0 the (real) arrival time of the signal. The fit is shown in fig. 3.17 and yielded the time constants $\tau_{\text{rise}} = 22\,\text{ns}$ and $\tau_{\text{fall}} = 100\,\text{ns}$.

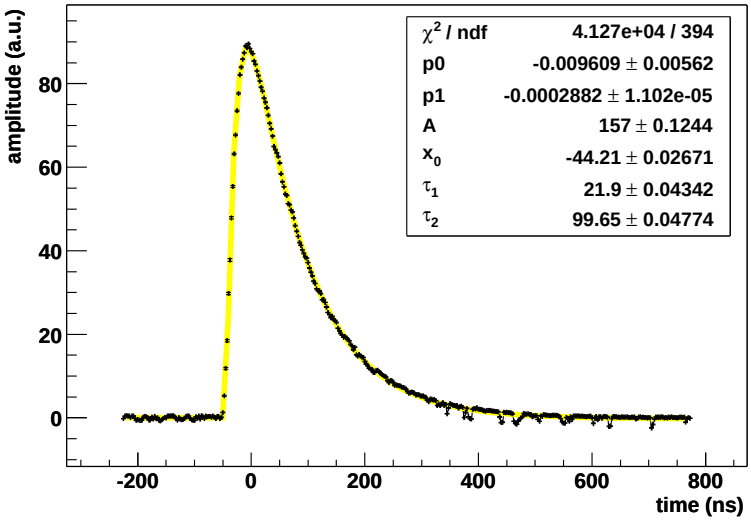

Figure 3.17: *Response function of the frontend chip APV25 to a δ-function like input. Eq.* (3.1) *and additional background (first order polynomial) was used as fit function.*

It is convenient to use the ratios $r_0 = a_0/a_2$ and $r_1 = a_1/a_2$ for the extraction of t_0, because then in the picture of eq. (3.1) the amplitude A_0[10] drops out. For fig. 3.18 r_0 and r_1 are calculated from eq. (3.1) and plotted together with the APV shape as a function of the trigger time t_{tr}: for small values of t_{tr} the nominators of the ratios and therefore the ratios themselves are small[11]. As soon as the signal starts to show in a_1, r_1 rises and converges to $e^{25\,\text{ns}/100\,\text{ns}} = 1.3$, displaying the constant decay time τ_{fall} of the exponential. r_0 rises later and to a higher value of $e^{50\,\text{ns}/100\,\text{ns}} = 1.6$.

[10] Note that A_0 basically follows a Landau distribution introduced with eq. (2.1).

[11] As both nominator and denominator see only noise, the ratios should rise again and stabilize around ≈ 1. In experimental data, however, an activated zero suppression requires a_2 to be above threshold and therefore the collection of ratios with $r_0 \approx r_1 \approx 0$ is preferred.

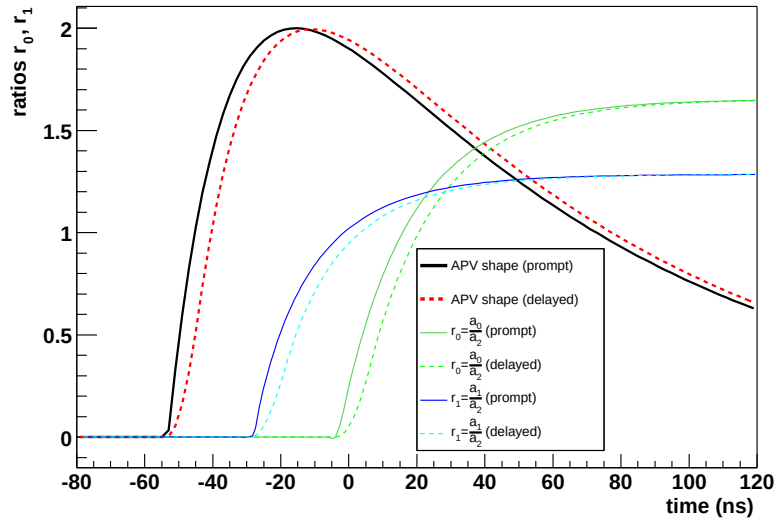

Figure 3.18: *Amplitude ratios r_0 and r_1: from the three sampling points on the APV shape (black and red line, in a.u.) the ratios $r_0 = a_0/a_2$ (green lines) and $r_1 = a_1/a_2$ (blue lines) can be defined and used to estimate the position of the APV shape within the 25 ns sampling window. The curves were calculated from eq.* (3.1) *for immediate charge arrival (solid lines) and convoluted with a delayed charge distribution (dashed lines).*

Eq. (3.1) describes only the shaping process of the readout chip. When connected to a detector, the shape of the charge distribution also has to be taken into account. According to [Leo94] the pulse shape resulting from a particle passage in general is rather complicated to calculate, but should basically have a fast rising time of the order of a nanosecond. For the proof of principle therefore a simple rectangular charge distribution was here assumed to describe a non-prompt, but delayed arrival of charge, and convoluted with the APV shape. For a 10 ns-long distribution corresponding to the order of the drift time of electrons or holes through the whole of the detector thickness (see also section 2.1.3), the effect is already clearly visible: the slope of the ratios decreases and gets softer corners.

From the values of r_0 and r_1 the position of the APV shape within the 25 ns sampling windows can be extracted with remarkable accuracy. Obviously, best results are achieved when the two ratios are between their upper and lower limit. For the absolute time additionally the relative phase between the 40 MHz sampling clock and the asynchronous trigger signal t_{tr} are needed and have to be measured externally.

Extraction from the data

In 2002 the ratios r_0 and r_1 were extracted from the data and the region between the two limits described in a first approach with a straight line. In fig. 3.19 the difference between the trigger time and the time calculated from the three silicon samples and the phase between trigger and clock is plotted. A clear correlation can be seen, which proves that the method works very well. The width of the peak is of the order of 2 – 4 ns. For the pronounced peak in fig. 3.19 a special data set was chosen. Firstly the beam intensity was reduced by a factor 5 compared to nominal.

Secondly, a very tight time cut was used for the hits in the SciFi hodoscopes to reduce their multiplicities and exclude ambiguous hits. And finally a decent silicon cluster amplitude of more than 5 500 electrons was required. For nominal conditions the peak stays the same, but the background rises significantly. The validity of the time information is not touched.

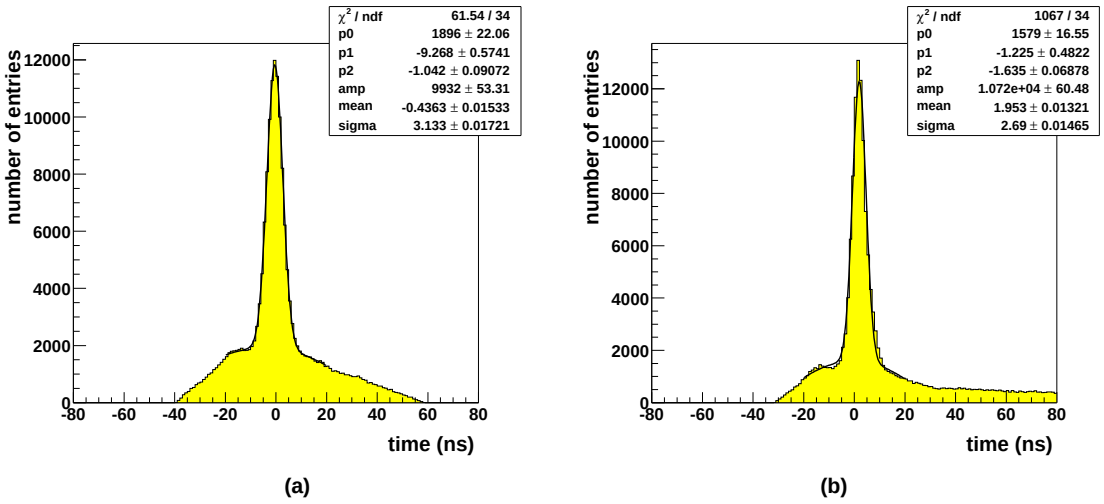

Figure 3.19: *Difference of the trigger time and time extracted from silicon data. A simple straight line fit was used to describe the correlation between r_0/r_1 and the trigger time.*

For the reconstruction of the 2002 data a rather conservative "ratio cut" was applied to the silicon hits, i.e. the hits are excluded only when $r_1 < 0.45$ and $r_0 > 1.1$. As the tails of the time distribution are non-Gaussian and relatively wide, such a cut is preferred to a "sigma cut" around the peak value.

Calculation of the Time Resolution

An estimate for the lower limit of the time resolution can be extracted from the known APV shape. The main restriction for the resolution arises from the finite signal-to-noise ratio, for which the accuracy of the amplitudes and consequently also of the ratios is limited. The important number is the signal-to-noise ratio S/N.

With the error δr_i of $r_i = a_i/a_2$ defined like (i=0,1):

$$(\frac{\delta r_i(t_{\mathrm{tr}})}{r_i(t_{\mathrm{tr}})})^2 = (\frac{\delta a}{a_i(t_{\mathrm{tr}})})^2 + (\frac{\delta a}{a_2(t_{\mathrm{tr}})})^2, \tag{3.2}$$

where δa is the noise level of the detector of 840 electrons as explained in section 3.5.2, the uncertainty in the time is

$$\delta t_i(t_{\mathrm{tr}}) = \delta r_i(t_{\mathrm{tr}}) \cdot (\frac{\mathrm{d}r}{\mathrm{d}t}(t_{\mathrm{tr}}))^{-1}. \tag{3.3}$$

Fig. 3.20 shows the results of the numerical differentiation for r_0 and r_1 separately and when both ratios are combined like

$$(\frac{1}{\delta t(t_{\mathrm{tr}})})^2 = (\frac{1}{\delta t_0(t_{\mathrm{tr}})})^2 + (\frac{1}{\delta t_1(t_{\mathrm{tr}})})^2 \tag{3.4}$$

for the three signal-to-noise ratios 14, 18 and 22. According to this estimation resolutions down to 1 ns can be achieved. When one takes into account that with the present hardware it was not

possible to optimize the position of the 25 ns readout window relative to the trigger time, this is in accordance with the values extracted from the data.

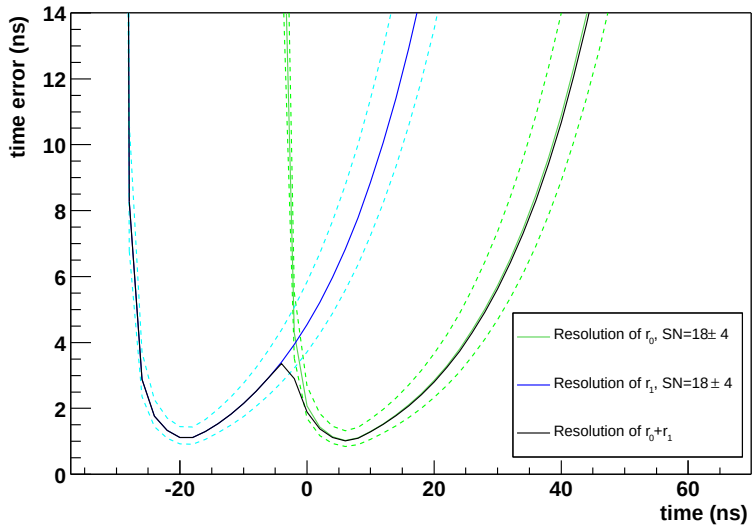

Figure 3.20: *The error on the time information extracted from the ratios of the amplitude is limited by the finite signal-to-noise ratio. The plot shows the dependence of the error on the trigger time for the two ratio separately and a combined value for the signal-to-noise ratios 18±4. (blue lines: r_1, green lines: r_0, black line: r_1 and r_0 combined, solid lines: SN=18)*

3.5.4 Efficiency

As explained in section 2.1.3 one expects a very high efficiency for a solid state detector. For the final efficiency, however, the complete readout chain has to be included.

In order to avoid a bias of the efficiency against silicon-specific problems, test tracks were reconstructed from the SciFi hodoscopes alone. As only 2 x- and 2 y-projections SciFi were installed upstream of the target, combinatorial background had to be suppressed by applying a very tight cut on the time correlation of the hits in the SciFi of ± 1 ns. A "road" of ± 200 µm width defined by the SciFi resolution was then searched for silicon hits. Random coincidences were corrected with information collected from tracks far away from the road.

Without any further cuts on the silicon data, efficiencies above 99% were reached (fig. 3.21). When the time cut as described in section 3.5.3 is applied, the efficiency is reduced by 0.5% to the satisfactory value of around 99%.

3.5.5 Correlation between p– and n–Side

The p– and the n–side of a silicon detector see charge clouds originating from the same particle with opposite polarity but same amplitude. It is possible to use this information to correlate the clusters from the two projections and to improve tracking efficiency in regions with high multiplicity.

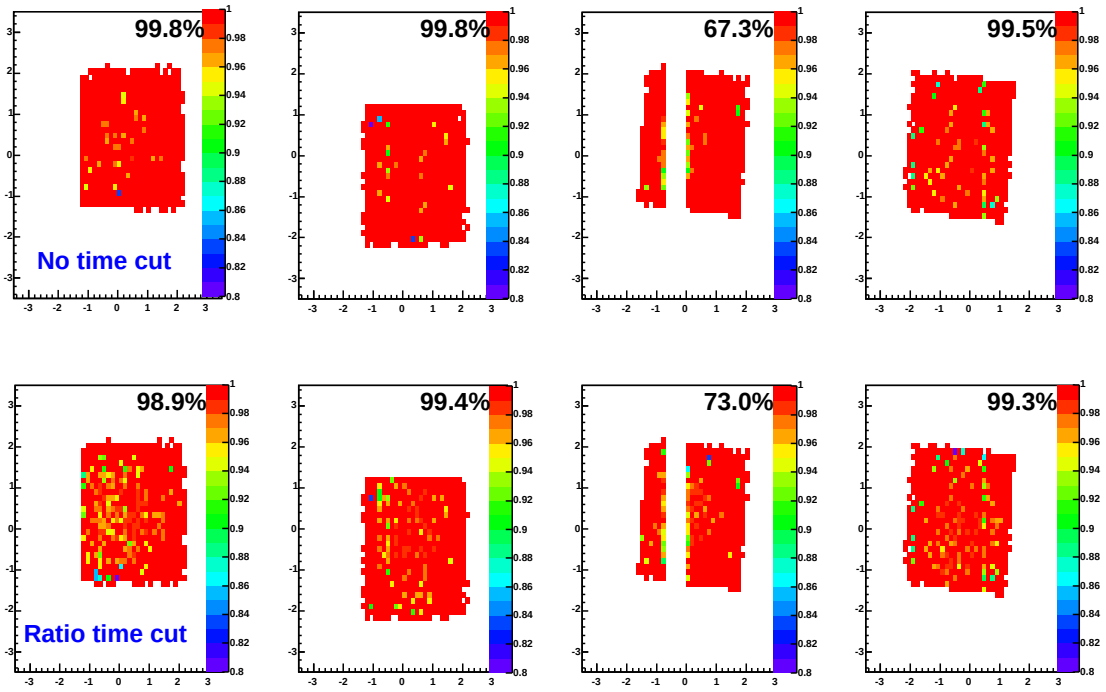

Figure 3.21: *Efficiency for silicon detectors, here SI01, in 2002 with and without a cut on the time information extracted from the amplitude spectrum. Due to the limited size of the SciFis only the inner $4\times4\,cm^2$ could be characterized. In projection SI01U one readout chip was broken.*

In fig. 3.22 the correlation of the signal amplitudes is shown. The two signals were joined by means of their timing behavior as explained above. The amplitudes on both sides are very similar, the ratio is close to 1 (compare with the bisecting line).

Both pieces of information, amplitude *and* time correlation, together can be used to make a hit profile which gives a 2-dimensional view of the beam (fig. 3.23) from the silicon alone. Such a plot is already available online in the COMPASS control room and provides a means for monitoring the beam position.

3.6 Summary and Outlook

In 2002 8 projections of silicon detectors were installed in the COMPASS environment and successfully operated.

A good signal-to-noise ratio of 18 is reached in double-sided readout. The extracted time resolution in the order of 3 ns provides a powerful handle for the track reconstruction.

For the full functionality the detectors have to be operated at 130 K. The first successful operation took place in the 2003 run and will be reported in [RDM04, Fuc03].

In 2004 a 4-week period of hadron beam is planned. For the measurement of the Primakoff reaction (see section 1.1.2) the precise knowledge of the tracks leaving the target is essential. Up to

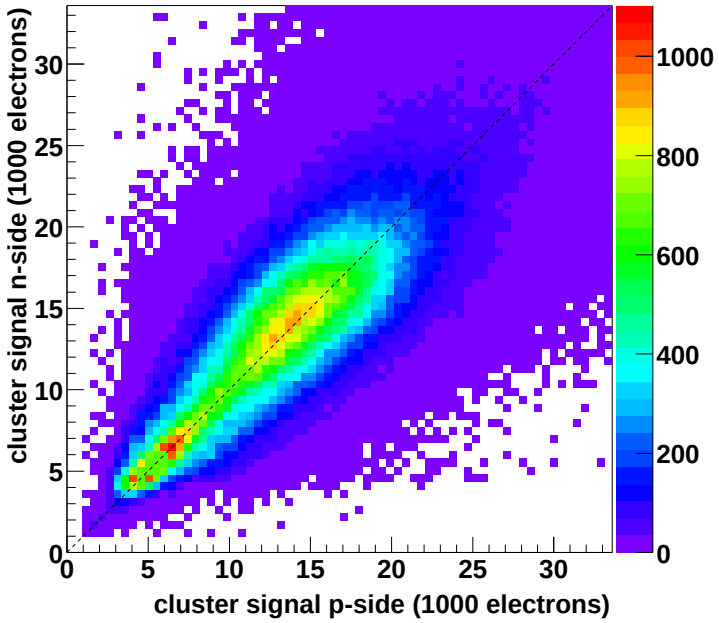

Figure 3.22: *Correlation of hits in p– and n–side. The structure in the center is created by real particles, the structure in the lower left corner is noise (see also fig. 3.16).*

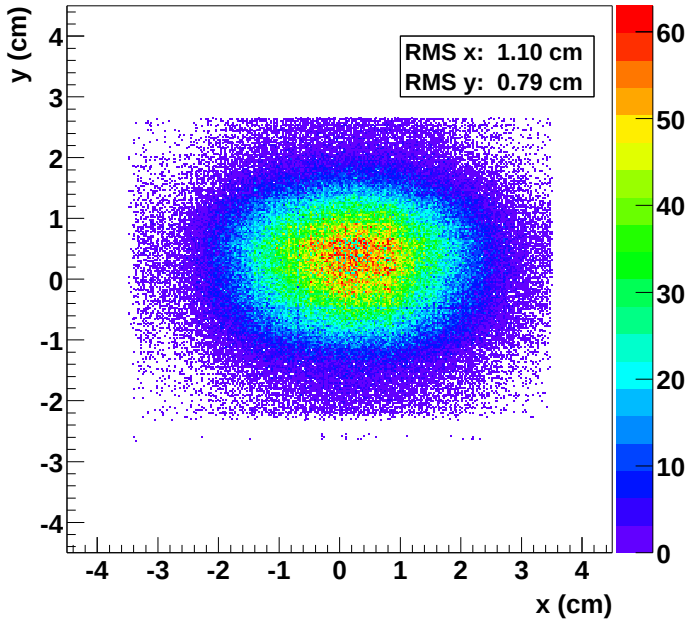

Figure 3.23: *Hits correlated between p– and n–side show the spatial extension of the beam at the position of silicon station SI01XY at 471.15 cm upstream the target.*

three silicon stations are planned at this position, preferably operated at 130 K.

For COMPASS phase 2, the electronics need to be upgraded for higher data rates. It is planned to increase the readout speed of the APV chips from currently 20 to 40 MHz, thus making trigger rates up to 90 kHz possible. The synchronization between readout chip and ADC has to be carefully tuned and the performance thoroughly checked.
For the `sg_adc` the possibility to apply a simple time cut already at this level to further reduce the occupancy is investigated.

The operation at 130 K changes the timing and shaping of the APV chip. In the offline reconstruction therefore adaptation is necessary. Ideas for the optimization of the time resolution are already being developed [Fri04].

Chapter 4

Event Reconstruction and Related Tools

In modern high-energy physics experiments the analysis become more and more complex, partly connected to the continuously increasing amount of highly precise data. Consequently, a fast software is needed as well, which is easy to maintain and to scale.

In general commercial software is only available for few standard tasks and large parts of the analysis tools have to be developed by the collaboration or at least within the HEP community. Such projects are usually updated very frequently. On the one hand this makes them very flexible as new features can be made available and debugged quickly. On the other hand the user has to follow the project status carefully and continuously adjust his own code to the environment.

For the analysis described in chapter 5 three main packages were used and thus have to be explained here in more detail, so the later description of the extraction methods can concentrate on the essential points.

After the data were taken and properly written to tape, the raw detector information and its hardware identifiers had to be transformed into the physically relevant objects of particles with a charge and a momentum. Within the COMPASS collaboration the framework CORAL was developed for this purpose. It will be described in more detail in section 4.2.

For the physics analysis on a more natural level a simpler package called PHAST was developed. It already operates on rather moderate sized data summary files and can easily be operated at the home institute. Section 4.3 gives an overview over its functionality.

The software package ROOT was developed at CERN for high energy physics and is a powerful tool for standard analysis tasks. ROOT provides entities for accessing, modifying, displaying and storing complex data structures in a very general way. As both CORAL and PHAST are linked to its libraries, it is described first in section 4.1.

4.1 The ROOT Analysis Framework

ROOT [BR97, ROOT] is an object-oriented framework aimed at solving the data analysis tasks of high-energy physics. It has been developed at CERN since the mid-1990s and emerged as the

successor of the famous *PAW* package, when it became obvious that PAW could not meet the challenges of modern high intensity accelerators.

Being developed by high energy physicists, it is especially tailored to their needs. In a set of libraries it provides functionalities like a command line interpreter for interactive working, histograming and fitting routines as the standard tools of analysis, graphics user interface widgets for the convenient access to the data, 2-dimensional graphics, I/O procedures optimized for the amount of data of modern high energy physics, collection classes to ease data management and a script processor for fast developing.

It is written in C++ and supported on many different platforms (several Unix/Linux derivatives, but also MacOS and Windows systems).

It can be used — and is also used within this thesis — in several different ways. The libraries can be simply linked to standalone programs so that data containers and functions can be called. Alternatively the specially developed interpreter CINT permits the use C++ commands directly on the command line and provides access to all library facilities as well as an online help. One can either collect commands in separate files called macros, which can even easily be compiled to optimize for speed and executed, or work interactively with the mouse through click-able objects. The mixture of user-written code, which starts an interactive ROOT window is also possible.

The main ROOT entities are histograms (`class TH1`) for storing, displaying and analyzing one, two or three parameter or trees (`class TTree`). While `TH1` has no memory of the filling process of the data points, a `TTree` stores objects on an event-by-event basis. In contrast to PAW's `ntuple`, objects are here not only simple built-ins like float or integer numbers, but also more complicated structures like tracks or vertices. The data are structured in instantiations of `TBranch` which can be individually activated or deactivated for a faster access to parts of the data or for a data-size-driven writing procedure. `TTree` provides a simple interface for data selection via cuts on various parameters as well as data-displaying facilities; even a browser with mouse control is provided.

ROOT was chosen to be the official analysis software for COMPASS and is linked to the two main COMPASS offline packages CORAL and PHAST (see the following sections) as well as to the online monitoring program COOOL (COmpass Object oriented OnLine).

4.2 Reconstruction and Analysis with CORAL

4.2.1 General Layout

As explained at the end of section 1.3.7, the data *taking* ends when the raw data files are saved on tape. *Raw data files* contain the pure detector information, i.e. a collection of hardware channel identifiers and digitized values (signal amplitudes, time differences or scaler values). The organizational structure of these files is provided by the readout program DATE [DATE00], the format of the hardware information depends on the actual type of frontend chip read out. The data are divided into so-called *runs* of typically 100 spills, which correspond to roughly half an hour of beam time. DATE writes the data to disk in *chunks* with a file size of not more than 1 GByte. An example of a typical physics run is run number 22217 from Monday 19 August 2002, 01:40:15, which consists of 2.3 million events, in total 101.4 GByte, divided into 110 chunks. The raw files and all subsequent transformations are stored on the *CERN Advanced STORage system* (CASTOR), a Hierarchical Storage Manager (HSM) developed at CERN, where the data are ultimately stored on tapes, but made available in a transparent way to the user on the disks of data server PCs (cf.

[CASTOR]). The logistic administration is taken care of by a database software, which keeps track of where the different runs and all their corresponding chunks can be found. In March 2003 the data base software was changed from *Objectivity/DB* to *Oracle 9i*.

Before a physics analysis can be done, the raw data have to be converted to 3-dimensional tracks with a momentum calculated and possibly a particle identification attached. For this purpose the software package *COmpass Reconstruction and AnaLysis project* (CORAL) was developed within the COMPASS collaboration. It is organized as a set of object-oriented class libraries, implemented in C++. As the object-oriented design enforces the definition of concrete interfaces between the different tasks, one can provide alternative modules which can be combined at run time depending on which type of job is wanted. Important consequences are that e.g the input data can have different formats, like "real data" raw files or data from Monte Carlo simulations, which are treated with the same procedures after the reading. For tracking three alternative algorithms were implemented, which are loaded dynamically at run time and allow a user to make systematic studies.

CORALs functionality is controlled with a so-called *option file*, which is read by the main executable and interpreted at run time. It defines the job that CORAL should do, e.g. processing of real data, decoding and clustering or the kind of tracking to use. Depending on the settings in the option file, the respective modules are loaded and executed. Also many "variable" pieces of information like type and name of input and output data file, the verbosity of logging information, the mapping, geometry and calibration files to use and even optimization of parameters for e.g. tracking or clusterization are given here.

The standard output of CORAL is a so-called *Data Summary Tape* (DST), which is not a "tape" in the original meaning anymore but just a normal file. It contains all fully reconstructed events, i.e. all tracks and vertices including error matrices, momenta and particle ID, all calorimeter objects plus some event-wise numbers such as the incident beam flux. Compared to the raw data the file size is reduced to about 6% (from 101.4 GByte to 6.5 GByte for run 22217). In addition a ROOT file can be written, where user defined histograms and trees can be stored and used later for further analysis. Such histograms are also used to check the success and quality of the data processing: for each data file meaningful parameters like the number of tracks with momentum per event or the value of the reconstructed K^0 mass are plotted and can be compared with other productions.

The content of the DSTs is a rather delicate subject. On the one hand one wants to have as much information as possible from the reconstructed raw data. But on the other hand the huge number of events makes it necessary to keep the data size per event as small as possible: parameters which can be easily calculated from standard values later cannot be included, no redundancy is allowed. This analysis is based on DST version 4.

The DST production is done at CERN. For this, CORAL runs on the CERN batch computing system of CERN `lxbatch`. Currently $\sim$ 500 PCs are available. In average CORAL needs 0.5 s [Mar03] per event, adding up to $\sim$ 20 000 events per spill-equivalent time, which roughly matches the speed of data taking.

The physics analysis is done in the home institutes of the collaboration. At TUM a small cluster of 32 CPUs was available for further processing. The last analysis steps were finally carried out on the local desktop PC.

4.2.2 Selected Steps of the Reconstruction

In the following some steps of the reconstruction are explained in more details.

Decoding. The *DAQ Data Decoding* library is used to extract the detector information from the raw data file. It is a standalone package, which is not only used in CORAL, but also in the online monitoring program COOOL. It scans raw data files and sorts the information into a hierarchy of "chip classes": the data format of the different frontend chips used at COMPASS is checked and dynamically cast onto the data at run time. Like this the hardware identifiers (e.g. GeSiCA 640, ADC 1, chip 5, channel 50; a strip in the middle of the first silicon projection) and the analogue values (in this case three amplitudes, for explanation see chap. 2) are extracted from the raw data file without any additional testing overhead. The correspondence between these hardware identifiers and the logical identification is read from *mapping files* and resolved. The logic address is the information needed for the tracking: a projection name containing the detector type, a positional parameter and the orientation of this projection (here: SI01V: Silicon station 1, horizontal strips inclined by 5°). The channel number is combined with the chip number to a channel-number-in-this-projection (wire 333; in CORAL the channels of all detectors, independent of the hardware type, are called *wire*).
The DAQ data decoding library also decodes the information about errors in the DAQ system, which are available in dedicated error words.

Clustering, Geometry and Calibration. This functionality is provided directly inside CORAL. A cluster no longer carries the information about the hits in terms of channel numbers, but in spatial coordinates in the COMPASS Main Reference System. Neighboring wires originating from the same particle passage are combined to one hit information and the "mean" wire number is transformed into 3-dimensional space coordinates This is done for each detector type individually. The correlation between wire number and space information is kept in a file, typically called "detectors.dat". The so-called *alignment* is a result of surveyors' information supplemented by corrections obtained from further analysis of particle tracks (*software alignment*).
In many cases a calibration of the raw detector data is needed. For calculating drift velocities in drift detectors, for example, a systematic offset, the "zero time", has to be subtracted: for the Silicon detectors the time information has to be calculated from the amplitudes with a parametrization. For this additional, detector-specific calibration files have to be read in and applied to the data.

Tracking. The main package for the track reconstruction is called *TRAck Finding and FItting in COMPASS* (TRAFFIC). The procedure is divided into three steps. During the *pre-pattern step* the spectrometer is divided into 5 zones, in which the tracks are assumed to be straight. Such zones are naturally defined by particular spectrometer parts: upstream of the target, from target to SM1, from SM1 to SM2, from SM2 to MF2, after MF2. Track pieces are searched for separately in every zone and for each available projection. For this, all recorded hits are combined in pairs to define straight-line candidates. If one or more additional hits are found to coincide within $5\,\sigma$ with this line, it is accepted as a candidate for a track segment. The candidates from the various projections are then combined to a track segment in space, if at least three projections match geometrically. Thus so-called ghost tracks are suppressed. In the *bridging step* the track pieces found in the different zones are combined by extrapolation into the next zone, taking into account the magnetic field and multiple scattering in MF2. In the third step a *global fit* to the actual hit positions is performed, which leads to the final track parameters.

Apart from the TRAFFIC package, two additional packages are available, whose approach is slightly different.
TRAFDIC is a TRAFFIC derivative, in which an alternative bridging step is used: instead of extrapolating the track pieces through the magnetic fields between the different zones, a dictionary of possible hit combinations on both sides of the magnets, which was obtained from Monte Carlo simulations, is used. The pre-pattern method is somewhat modified as well. In a first step strict cuts on the hits are applied to simplify track finding, in a second step the cuts are relaxed to collect the remaining associated hits. For the DST production in 2002, TRAFDIC was used as it yields a slightly higher number of tracks per event and is significantly faster.
RECON as the third tracking package is specially tailored for large angle tracking after SM1. Because of the fringe field of SM1, the straight-track-assumption in this zone is no longer valid for slow particles. RECON uses an iterative procedure to allow for bended tracks: tracks are at first only searched in a subsample of detector planes. In the subsamples the straight tracks are found first by applying strict cuts to the hits. In the following iterations the cuts are relaxed and tracks with larger curvature can be found. In a last step the subsamples are combined to full tracks. The fine tuning of RECON, for which the data of 2002 are used is still ongoing.

Vertexing. The reconstruction of primary and possibly secondary interaction points is done in the vertex package. In a pre-filtering step tracks are selected according to geometrical and kinematical criteria to originate from one vertex. A first estimate of the vertex position is the average of the points of closest approach. In a second step the method of the inverse Kalman filter is used, in which all track candidates obtained from the pre-filter are included in a global fit. The filter advances from one detector plane to the next along the tracks and optimizes the difference between an extrapolation and the measured hit position in this plane. Individual tracks are excluded if their contribution to the total χ^2 of the fit exceeds a certain value. After each step the global fit is repeated. The output of the vertex procedure are the vertex coordinates and the refitted parameters of the tracks associated to the vertex.

4.3 Physics Analysis with PHAST

For the physics analysis the software package *PHysics Analysis Software Tools* (PHAST) was written [Ger]. It is completely built on top of ROOT and therefore contains all its functionality for data analysis. PHAST provides both a specific data format, the so-called *Mini Data Summary Tape* (mDST), and an executable with a specific user section, where an easy access to all reconstructed data is possible. At the time of this work PHAST was constantly being developed, as more and more features were needed, and sometimes there were update periods of only a few days. But as not all new features influenced the topic analyzed here, the PHAST version 5.97 and mDST version 5 were finally used for the complete analysis.

4.3.1 mDST Files

The mDSTs are written by the PHAST module of CORAL. They are either produced from raw data directly or converted from DST files. The 2002 mass production was written in parallel with the DST production. For the mDSTs only *analyzable* events are selected, for which at least one vertex was reconstructed. For the 2002 data this lead to a selection of about 1/3 of all DST events. For a typical run[1] this means 0.8 out of 2.3 million events are selected, resulting in a file size

[1] run 22217 as above

reduction to 15% (from 6 514.7 to 992.3 MByte); compared to the raw file, the mDST are reduced to 0.9% of the data volume.

The mDST consists of two types of PHAST objects. For each event a `PaEvent` object is present, which contains information like reconstructed particles, vertices and tracks, and in the case of Monte Carlo events also the generated particles, vertices and tracks. A `PaSetup` object, which contains information on magnetic field maps, material maps or detector geometrical information is instantiated for each run contributing to an mDST file. The basic idea of the mDST format was that a "PHAST file contains everything that is needed for analysis" [Ger].

4.3.2 UserEvent Function

The recommended way to read mDSTs is via the `phast` executable, which provides a loop over the collection of `PaEvents`. For each `PaEvent` up to 10 different `UserEvent`N`()` functions can be called, in which the user has now full access to all reconstructed data. These functions are the place where user code should be put it. Here the events can be selected according to their characteristics and analyzed.

`phast` allows two different types of output files: usually the user wants to write a ROOT file, which contains histograms or trees of particular parameters defined in the `UserEvent`N`()` functions, like e.g. the kinematic variables x_B and Q^2 of a deep inelastic reaction or even reconstructed invariant masses of Λ^0 particles (see chapter 5 for more details). Such files can then be easily analyzed further within the standard ROOT frame.

Additionally `phast` can write out its own format. This is useful for either merging several mDST files to one or for making an mDST with specially selected events, a so-called micro-DST (μDST).

Chapter 5

Reconstruction of Λ^0 in COMPASS

The spin distribution of Λ^0 is analyzed with the help of its parity-violating weak decay $\Lambda^0 \rightarrow p\pi^-$, which features a non-uniform distribution of the decay p for polarized Λ^0. The angular distribution of the decay proton in the rest frame of Λ^0 is given in eq. (1.6). Simply speaking, one therefore just compares the number of p going in one direction with the number of p going in the other direction. The directions will be precisely defined in section 5.2.

Being a neutral particle, the Λ^0 cannot be seen in the spectrometer directly. Thus in a first step (section 5.5) Λ^0 have to be identified via their (charged and therefore visible) decay products p and π. In principle the identification of p and π can be nicely done with a Cherenkov detector. But in 2002 the COMPASS RICH was not yet fully operational: while a good p / π separation could be proven, it did not yet cover the full acceptance. As this analysis aims for an asymmetry measurement, no RICH information is used. Instead the Λ^0 selection is based on pure kinematical arguments and the invariant mass of the decay products (see section 5.3). The purity of the Λ^0 sample is important as the main background process $K^0 \rightarrow \pi^+\pi^-$ is unpolarized and will dilute a possible Λ^0 polarization signal. A series of cuts is therefore needed to reduce such background events and enrich the sample with Λ^0.

In a second step the angular distribution of the decay particles is extracted and used for a polarization measurement. To avoid systematic effects of an imperfect experimental setup on the measurement, the *bias-canceling method* as explained in section 5.7 is used for acceptance correction.

In 2002 the beam time was 114 days long (May 27 to September 17), of which 52 days were used for data taking with a longitudinal and 19 for a transverse polarized target. At the time when this work was written, the production of mDSTs, version 5, from raw data at CERN had just started and therefore the data of only 21 days were included in this analysis (periods P2D, P2E and P2F from August 14 to September 4). Still this resulted in 400 M reconstructed events, yielding 155 000 Λ^0. Fig. 5.1 gives an impression of the fraction of the acquired data that were used.

This chapter describes the techniques used to extract the polarization from the mDSTs, including the applied cuts, and presents more details on the Λ^0 sample the analysis is based on. In sections 5.1-5.4 some general information is given, section 5.5 describes the selection of Λ^0 from the mDSTs and the treatment of background. The extraction of the polarization from the remaining sample is then thoroughly explained in sections 5.7 and 5.8.

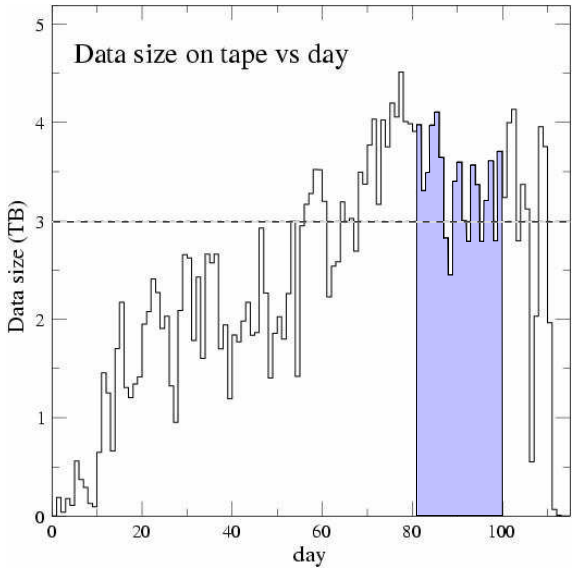

Figure 5.1: *Acquired data in the year 2002 in terabyte (TB) per day. The shaded area shows the period which was used in this analysis. The dashed line indicates the design value of the data storage system.*

5.1 Event Topology V^0

The Λ^0 is a neutral particle and cannot be tracked in the spectrometer directly. Instead one has to find its decay particles and reconstruct its decay vertex. The Λ^0 decays into the two charged particles proton and pion $\Lambda^0 \rightarrow p\pi^-$ with a branching ratio of 64% [1]. Thus one looks for two tracks with different charge which meet at one point in space (called *vertex*) without an incoming track. The V-shaped geometry is the reason why this kind of decay is called V^0 (see fig. 5.2).

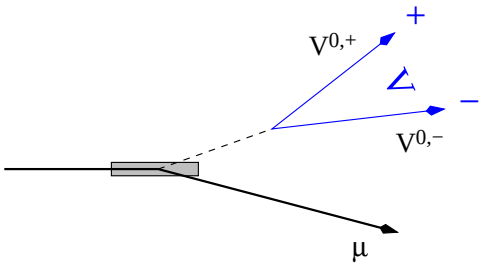

Figure 5.2: *V^0 geometry: μs impinge on a target from the left side and produce a neutral (=invisible) particle, which decays at some distance into two charged (=visible) particles $V^{0,+}$ and $V^{0,-}$. The resulting picture leads to the name "V^0" for this kind of event.*

The Λ^0 is not the only particle with a V^0 topology. Neutral kaons K^0 ($K^0 \rightarrow \pi^+\pi^-$) and photons γ ($\gamma \rightarrow e^+e^-$, $\gamma \rightarrow \mu^+\mu^-$ and rarely also $\gamma \rightarrow q\bar{q}$) show a V^0 behavior as well. While γ can be cut out by relatively simple kinematical arguments, K^0 is more difficult to suppress as will be

[1] The next probable decay is $\Lambda^0 \rightarrow n\pi^0$ – two neutral particles, which is rather difficult to detect.

explained later. On the other hand, being produced in much higher number than Λ^0, K^0 provides a good opportunity for making checks of the data quality and systematic studies of the analysis methods.

Armenteros Plot

The different V^0 particles can be distinguished in an *Armenteros plot* by the momenta of the decay particles and their charge alone, without any further assumptions on the particle identities. The key point is that these particles can only acquire momentum transverse to the direction of the V^0 from the mass difference between mother and decay particles, the *phase space* of the decay. In an Armenteros plot (fig. 5.3) the longitudinal and the transverse momenta with respect to the V^0 momentum p_L and p_T of a combination of decay particles are compared. Daughters originating from the decay of a V^0 collect on arcs: decays in two particles with the same mass are symmetrical around $p_L^+ - p_L^-/p_L^+ + p_L^- = 0$ (e.g. $K^0 \rightarrow \pi^+\pi^-$ are distributed on the big arc in fig. 5.3), for daughters with different masses (e.g. $\Lambda^0 \rightarrow p^+\pi^-$, $\bar{\Lambda}^0 \rightarrow p^-\pi^+$) the arcs are shifted (left arc for $\bar{\Lambda}^0$, right arc for Λ^0). The "radius" of the arc is a measure for the phase space: for K^0 p_T^{max} is 206.1 MeV/c, for Λ^0 100.8 MeV/c are available. The highly pronounced structure at the bottom of fig. 5.3 corresponds to photon conversion in material $\gamma \rightarrow e^+e^-$ with a very small phase space.

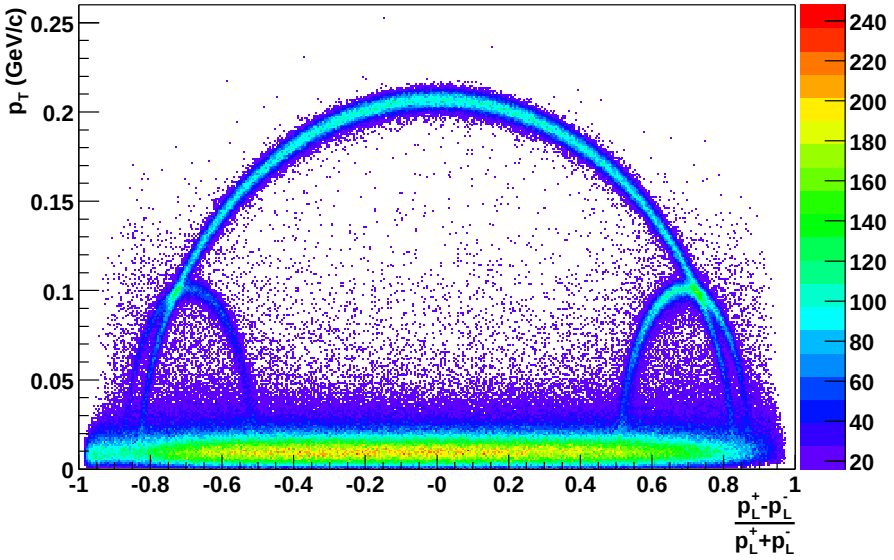

Figure 5.3: *Armenteros plot for COMPASS V^0: the transverse and longitudinal momenta (p_T, p_L) of the daughters are compared. The structures in the plot correspond to different V^0: big arc: K^0, small arc right: Λ^0, small arc left: $\bar{\Lambda}^0$, "arc" on the bottom: γ. Note that for the plot a minimum of 16 entries per cell was required to clean up the background.*

In one section in the Armenteros plot K^0 and Λ^0 overlap and show the same kinematical signature, thus they cannot be separated completely with geometrical arguments alone.

5.2 Definition of Coordinate System

Fig. 5.4 depicts the coordinate systems which will be used throughout this analysis. In fig. 5.4a) the production of V^0 in the *laboratory system* is shown as the collision of a virtual photon γ^* with a target nucleon p, n.

For the determination of the polarization kinematical variables have to be extracted from the *rest frame* of the V^0 ($\vec{x}'$ $\vec{y}'$ $\vec{z}'$) as shown in fig. 5.4b). Now the key feature is the *production plane* spanned by the momentum vector of the γ^* and the V^0. For *transverse polarization* the quantization axis $\vec{n}'$ is chosen normal to this *production plane* $\vec{\gamma^*} \times \vec{V^0}$, which is also taken as $\vec{y}'$ axis. The direction of the V^0 is kept as the $\vec{z}'$ axis. For the completion of the right handed coordinate system $\vec{x}'$ is chosen to be $\vec{y}' \times \vec{z}'$.

A possible polarization is then extracted from the angle between the direction of the positive decay particles in this coordinate system and $\vec{n}'$ and evaluated according to formula (1.6).

Other directions of polarization are possible and interesting, but not covered in this analysis: for *longitudinal* polarization $\vec{z}'$ is taken as quantization axis, for "sideways" polarization $\vec{x}'$.

Fig. 5.4 also illustrates the two different definitions of *transverse momentum* used in this work: a V^0 acquires a p_T with respect to γ^*. This momentum is important for the measurement of polarization. When the V^0 decays, the daughter particles acquire a transverse momentum p_T from the phase space of the decay with respect to the direction of V^0. This momentum is used in connection with the Armenteros plot introduced in fig. 5.3.

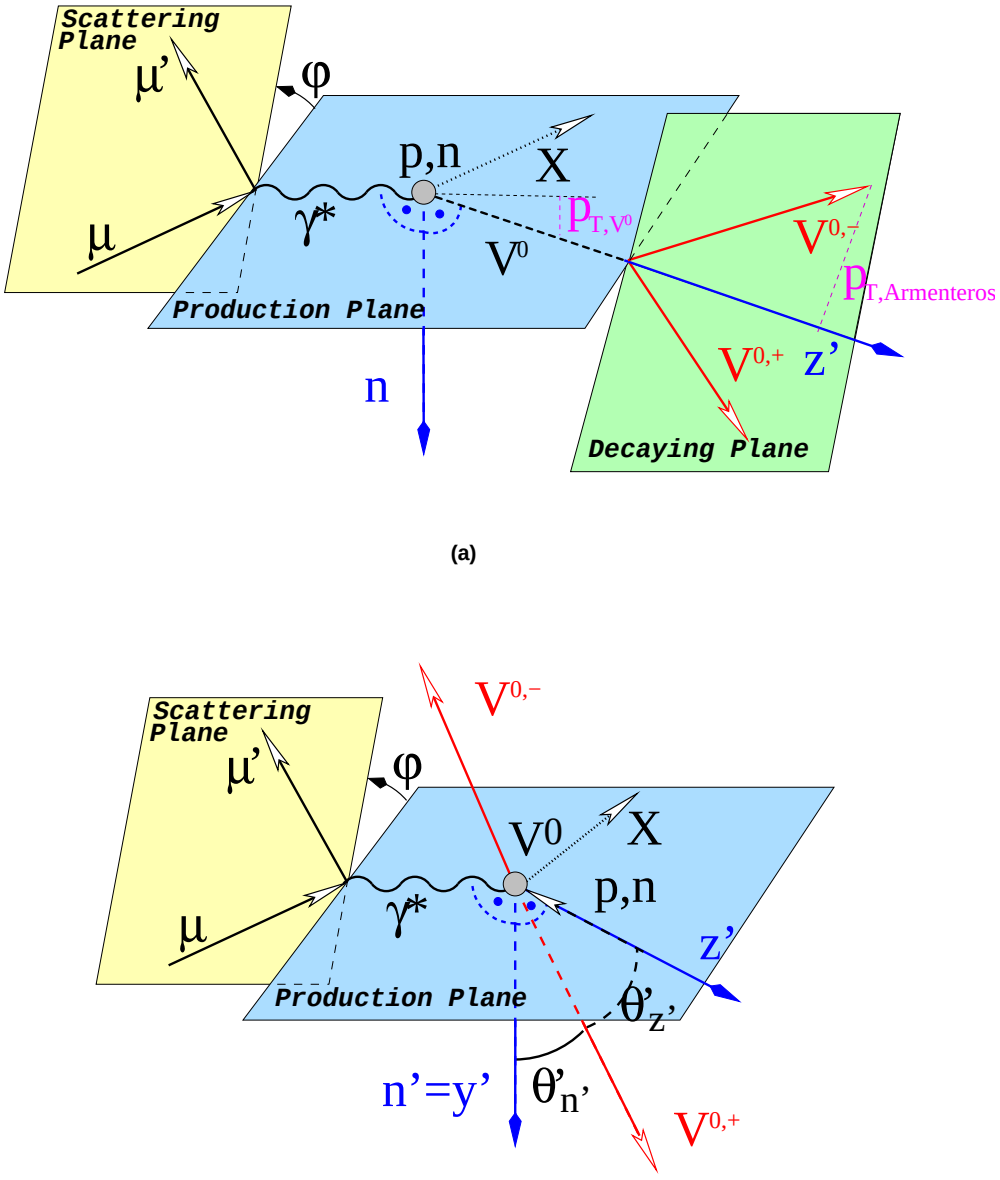

Figure 5.4: *Definition of V^0 Coordinate Systems for* ***a)*** *laboratory and* ***b)*** *V^0 rest frame: The V^0 is produced in the scattering of a virtual photon γ^* emitted by the beam muon μ off the target nucleon (p,n) together with an unidentified rest X. After its lifetime, V^0 decays into two charged particles $V^{0,+}$, $V^{0,-}$. A possible polarization has to be measured with respect to the production plane spanned by the virtual photon γ^* and V^0/ target nucleon for laboratory or rest frame respectively (normal vector $\vec{n} = \vec{\gamma^*} \times \vec{V}$). From the direction of the (positive) decay particle in the rest frame the polarization can be extracted: $\theta'_{n'}$ for transverse and $\theta'_{z'}$ for longitudinal polarization (see eq. (1.6)). For the measurement of the transverse polarization the rest frame system of the V^0 was therefore defined by $\vec{n}'$ and the former direction of the V^0, $\vec{z}'$.*

5.3 Invariant Mass Spectra and Side Band Correction

Having no further handle on the V^0 identity, one is left to calculate the invariant mass of the mother particle by making a mass *assumption* for the daughters. Track combinations for which the assumption is correct will pile up in a peak close to the V^0 mass. The minimum width of the peak depends on the lifetime of the particle (2.5 μeV for Λ^0), but is smeared out by the resolution of the spectrometer (~ 3 MeV for Λ^0).

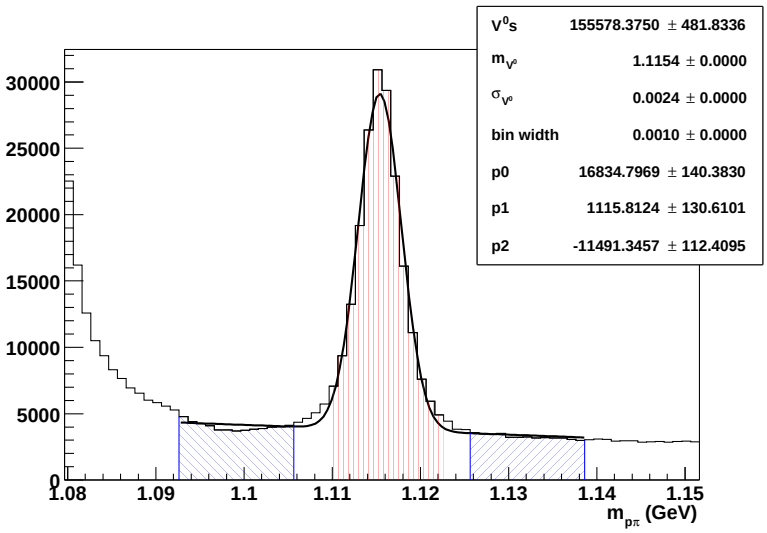

Figure 5.5: *Invariant mass spectrum of two daughters under the assumption $p^+ + \pi^-$: one clearly sees the accumulation close to the Λ^0 mass of 1.1157 GeV. The Gaussian width is 2.4 MeV and corresponds to the resolution of the spectrometer. The definition of signal and side bands, which can be used for background correction, is also shown. The plot was produced with the final cuts plus a cut to reduce the influence of the K^0 (see section 5.5.2).*

In fig. 5.5 one can see the invariant mass spectrum under the assumption that the daughters were p^+ and π^-. The peak at 1.1154 GeV is clearly visible, and within the resolution of the spectrometer it is close enough to the PDG mass of 1.1157 GeV [PDG00]. A first geometrical estimate of the area under the peak yields roughly 155 000 Λ^0.

Usually the mass peak sits on a background, which one needs to correct for. As shown in fig. 5.5 one defines samples of events which are under the peak and in bands left and right of the peak. Under the assumption that the events in the side bands have similar characteristics as the background under the peak, one can correct properties of the "peak" events with events in the side bands on a statistical basis. For this the histograms of the needed property of the two side bands is subtracted from the respective histograms of the peak band. While this works fine for the K^0, the same method is not directly applicable for the Λ^0 as will be explained later in section 5.5.2. For fig. 5.5 bands of $2\sigma_{\text{Gauss}}$ width were chosen, the middle of the side bands is $5.5\sigma_{\text{Gauss}}$ away from the peak.

5.4 Kaon Mass Resolution

When the invariant mass of the K^0 was reconstructed, it turned out that the resulting mass peak was shifted by 1.5 MeV to higher values. After systematic studies it emerged that the description of the fields of the spectrometer magnets in the reconstruction was not up-to-date. Therefore a correction was developed within this analysis. It scales the measured momentum of the particles with respect to the amount of magnetic field that they traversed in each magnet as

$$p_{\mathrm{cor}} = p_{\mathrm{orig}}(r \cdot c_1 + (1 - r) \cdot c_2), \tag{5.1}$$

with p_{orig} and p_{cor} as the original and the corrected reconstructed momentum and c_1 and c_2 the correction factors for SM1 and SM2 respectively. r is the contribution from SM1 to the total magnetic field that the particle passed: $r = 1.0$ for short tracks in the LAS, $r \approx 0.2$ for long tracks in both LAS and SAS and $r = 0.0$ for tracks starting after SM1 and traversing SAS only (see section 1.3 for LAS and SAS). The best values found were c_1=0.991 and c_2=1.010.

A comparison of plots with and without the correction is shown in fig. 5.6. In the mass spectra in plots a) and b) it can be seen that the shift is reduced by a factor 10 to 100 keV, which also leads to a width, reduced by 10%.

Plots c) and d) show the position of the mass peak (full lines) and its width (dashed lines, open symbols) for different track lengths (**s**: **s**hort, only SM1 was traversed; **l**: **l**ong, both magnets were traversed). The absolute shift is plotted over the π^+ direction in the K^0 rest frame [2], which is a measure for tracks going to the inner part of the spectrometer ($\cos \approx \pm 1$) and to the outer one ($\cos \approx 0$). The dependence on this angle was a first hint on problems with the field maps of the spectrometer magnets. The different mass shifts for different track lengths can be seen clearly, as well as the effect of the correction.

Plots e) and f) finally show an effect which could not be fully corrected: a left-right asymmetry of the K^0 mass. The mass shift is here plotted over the angle of the particle momenta to the horizontal plane (0 is the left side, $\pm\pi$ is the right side of the beam). The direction of the asymmetry depends on the charge sign of the particles. Such an effect can be explained with an additional momentum kick from the magnetic field in the horizontal plane [Sie03]. Indeed it was found that an interference between the target solenoid and SM1 leads to a saturation of the magnetic fields and is not well described by the linear summation of the separated fields used in the event reconstruction.

[2] Alternatively the absolute distribution in space could have been taken, but as will be explained in section 5.5.2, this angle has a high relevance for the analysis and the effect was first found here.

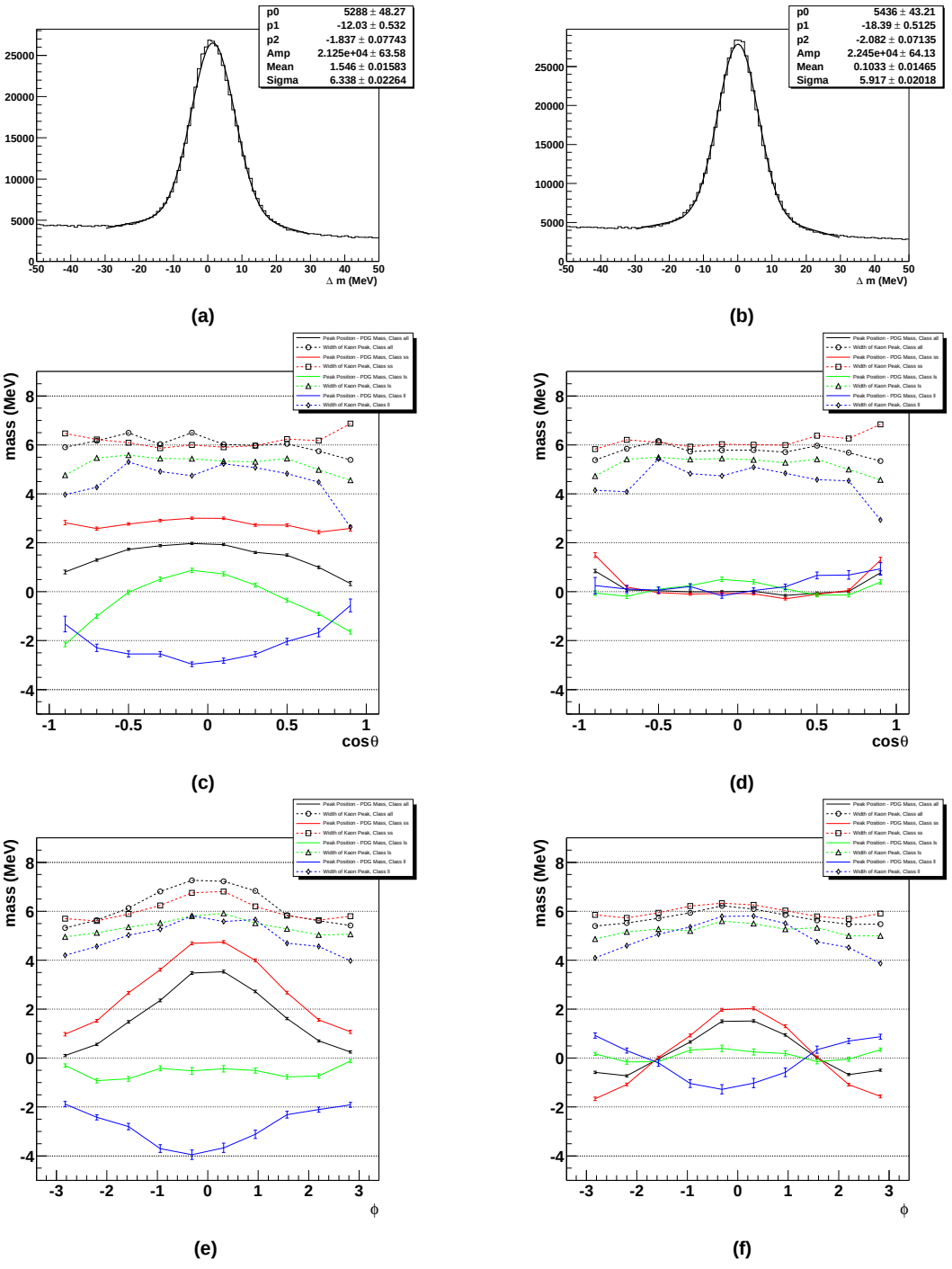

Figure 5.6: ***a)*** *The descriptions of the fields of the spectrometer magnets used in the reconstruction led to a 1.5 MeV higher K^0 mass.* ***b)*** *With the correction as explained in the text, the shift could be reduced to few hundred keV. Plots* ***c)*** *and* ***d)*** *show an inner-outer asymmetry, plots* ***e)*** *and* ***f)*** *a left-right asymmetry (uncorrected left, corrected right). The solid lines show the shift from the nominal position, the dashed lines the width of the peak. The effect gets worse if one distinguishes between the influence of the two magnets (red line: only SM1 involved (ss tracks); blue line: both magnets involved (ll tracks); green line: one daughter both magnets, the other daughter only SM1 (ls tracks); black line: all cases).*

5.5 Selection Criteria for V^0 and Background Suppression

For the measurement of polarization Λ^0 are collected in certain classes and their numbers compared. For their identification as Λ^0 several conditions have to be fulfilled. In a first step events with the proper topology as described in section 5.1 were selected and written to μDSTs (section 5.5.1). Then the Λ^0 candidates were chosen and written vertex-wise into a `TTree` (`TTree`, see section 4.1). As many background events like e.g. γ still remained, further cuts were applied in order to enhance the number of Λ^0 with respect to this background (section 5.5.2). The K^0 was finally suppressed with a specially developed background subtraction.

5.5.1 Event Selection

For the definition of the production plane via γ^* and Λ^0 as explained in section 5.2 the complete kinematics of the primary interaction is needed. Events for which beam and scattered muon could not be fully reconstructed and uniquely identified were therefore dropped. The position of the primary vertex was requested to be inside the target material within its uncertainty. Starting with a batch of 400 M events, 167 M primary vertices (41.9%) were found. The following list gives the remainder with respect to the full sample after each of the two cuts:

- unique primary vertex with completely reconstructed beam and scattered muon track (64%)
- primary vertex within errors inside the target volume (42%)
  $(-100\,\text{cm} - 1\sigma_{z_{\text{prim}}}) < z_{\text{prim}} < (30\,\text{cm} + 1\sigma_{z_{\text{prim}}})$
  $r_{\text{prim}} < (1.5\,\text{cm} + \sqrt{\sigma^2_{x_{\text{prim}}} + \sigma^2_{y_{\text{prim}}}})$

For the V^0 vertices two outgoing tracks with opposite charge and again fully reconstructed kinematics were required. Tracks which passed more than 50 radiation lengths of material were identified as muons and rejected. The longitudinal position of the secondary vertex was required to lie not more than $2\sigma_z$ upstream of the primary vertex. In order to exclude events where a wrong scattered μ was taken, the total momentum of the scattered μ and the two daughter particles was asked to be less than the momentum of the primary μ. These cuts reduced the number of events to 69 M (17.3%). 210 M out of 276 M two-track-vertices (76.3%) could be selected. The results were written as μDSTs on an event base, i.e. all events where at least one V^0 candidate was found were selected.

- V^0 vertex downstream of the primary vertex (87%)
  $z_{V^0} - z_{\text{prim}} > -2\sqrt{\sigma^2_{z_{\text{prim}}} + \sigma^2_{z_{V^0}}}$
- exclusion of V^0 daughters identified as $\mu^+\mu^-$ (79%)
- tracked momentum conserved (76%)
  $p_{\mu_{\text{prim}}} \geq p_{\mu_{\text{scatt}}} + p_{V^{0,+}} + p_{V^{0,-}}$

Λ^0, $\bar{\Lambda}^0$ and K^0 Selection

In this step each selected V^0 was written as its own entry into a `TTree`. As the μDSTs is organized event-wise, the V^0 cuts mentioned above therefore had to be checked again for each V^0 vertex

beforehand. The momentum is usually calculated by the deflection in the magnets SM1 and SM2. In rare cases it is possible to calculate the momentum for slow particles as well, which do not pass SM1 and are already deflected by its fringe field. While such tracks might be useful for specific physics channels, their low momentum resolution make them less suitable for V^0 reconstruction and they were therefore excluded. The reconstructed invariant mass of the two daughter particles under the respective V^0 assumption was chosen as a window of $\pm 100\,\mathrm{MeV}$ around the PDG mass. The sum of the energy of scattered μ and the two V^0 daughters was required to be less than the energy of the beam μ. These cuts reduced the sample in the Λ^0 case from 260 M V^0 candidates down to 33 M vertices (12.8%).

- V^0 cuts from above (81%)
- end of tracks $V^{0,+}$, $V^{0,-} > 360\,\mathrm{cm}$ (70%)
- selection of invariant mass (13%)
  $|m_{V^0} - m_{\Lambda,\mathrm{PDG}}| < 100\,\mathrm{MeV}$
- tracked energy conserved (13%)
  $E_{\mu_{\mathrm{prim}}} \geq E_{\mu_{\mathrm{scatt}}} + E_{V^{0,+}} + E_{V^{0,-}}$

5.5.2 Enriching of Λ^0

From the Λ^0 sample reached above one could in principle already extract the number of Λ^0 with a side-band background correction as explained in fig. 5.5. As a possible polarization of Λ^0 manifests itself in a small excess of decay daughters in one direction, a high sensitivity is needed. It is therefore essential to keep the background correction small enough to reach small errors and to enrich the sample with Λ^0 even if the absolute number of Λ^0 is reduced. In the following additional cuts are described, which exclude more background than good events and at the same time leave the Λ^0 sample unbiased in its kinematic characteristics. The influence of the cuts on the various parameters of Λ^0 therefore has to be checked thoroughly. After the description of the applied cuts on the following pages, these parameters are plotted in fig. 5.9 on page 94. All cuts are shown after a background correction with the side-band method. Without further cuts the background correction yielded 480 122 Λ^0 from the 33 M V^0 candidates.

Geometrical Cuts for the Target Region

The lifetime $c\tau$ of Λ^0 is 7.89 cm [PDG00], in COMPASS they travel 2 m in average before they decay. The expected exponential decrease of events as a function of the decay position is smeared out with the very long COMPASS target of 130 cm. Instead one gets a distribution with a clear maximum at around the end of the target cell (see fig. 5.7)). It turned out that the signal-to-background ratio for Λ^0 decaying inside the target gets worse the deeper they lie inside the target, both because of worse background conditions and because of reduced reconstruction quality due to the higher radiation length the V^0 daughters have to pass. The simple condition that the decay position of the Λ^0 lies outside the target cleans the spectrum, but also reduces the statistics dramatically.

Fig. 5.7 shows some properties of the Λ^0 sample as a function of the decay position along the beam. For reference, the two target cells are drawn as black lines from -100 cm to -40 cm and -30 cm to +30 cm. The solid line gives the purity of the sample, namely the ratio between the number of Λ^0 (=S, Signal) and the number of background events (=B, Background) as defined in

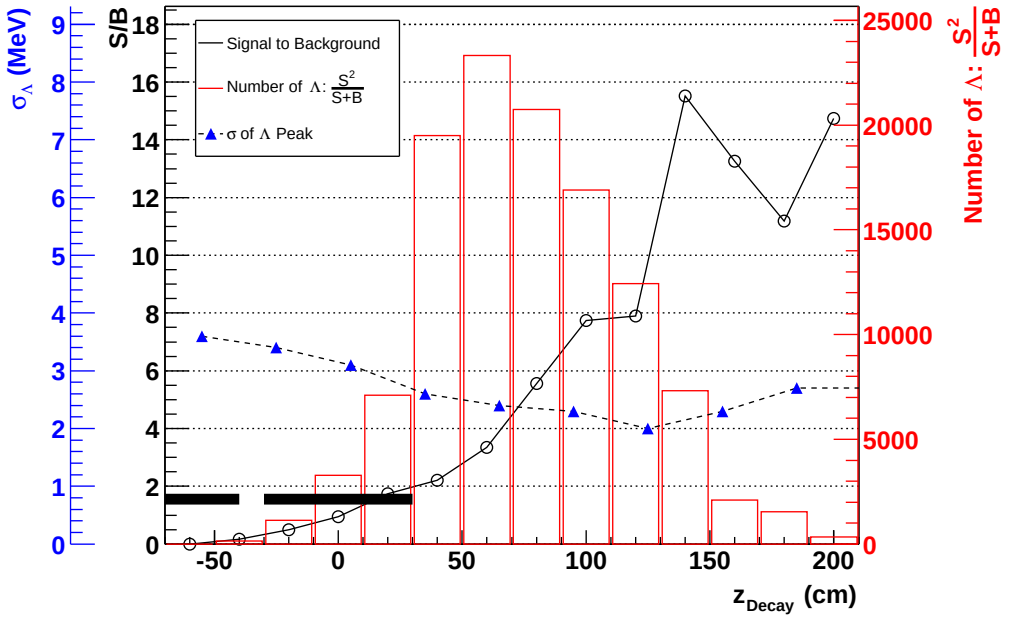

Figure 5.7: *Decay Position of Λ^0: The figure shows the dependence of the signal-to-background S/B on the decay position (solid line). Additionally $S^2/S+B$ as a measure of the absolute number of Λ^0 (histogram, right axis) and the width of the Λ^0 peak in the invariant mass spectrum (dashed line, left axis) is drawn. The position of the two target cells is sketched for reference as black lines between -100 cm and 30 cm. The plot was produced with the final cuts applied, except for a cut on the longitudinal position of the decay vertex.*

fig. 5.5, and exhibits a strong increase after the end of the target up to a maximum at around 10 before it breaks down due to statistics. But it is no good, if a high purity leads to a very small number of Λ^0. In addition to the S/B thus one uses the relative signal $S/S+B$, weighted with the absolute number of Λ^0, $S^2/S+B$, shown in fig. 5.7 as the red histogram with the right axis. One sees that the main "source" of Λ^0 is the region shortly after the target, and *not* the region with maximum purity.

The dashed line in fig. 5.7 shows the width σ_{Λ^0} of the Λ^0 invariant mass peak (labels on the left-most axis). Together with the amplitude information from the S/B it demonstrates the decreasing reconstruction quality for decays inside the target mentioned above: the invariant mass peak gets wider and lower until it finally disappears.

For the target region therefore three specific cuts were used. First the decay position of the Λ^0 could be relaxed and was chosen to be not entirely downstream of the target, but after the center of the second target cell. As can be seen in fig. 5.7 at least a small fraction of Λ^0 decaying inside the target survived all cuts.
Additionally the reconstructed Λ^0-momentum vector was required to point back to the primary vertex. For this the angle α between the momentum direction and the straight line connecting primary and Λ^0-vertex was chosen to be small.
In order to avoid wrong track combinations within the spatial resolution of the tracks a longitudinal separation between primary and Λ^0-vertex was required. In total the background corrected

sample size goes down to 227 000 Λ^0 (47.3%). The explicit numbers are given in the following list:

zCut: decay position of Λ^0 not upstream of the center of the second target cell $z_{V^0} > 0\,\text{cm}$ (69%)

aCut: angle α between Λ^0-direction and connection primary-secondary (58%):
$-100 < z_{V^0} < 40\,\text{cm} : \alpha < 15\,\text{mRad}$
$z_{V^0} > 40\,\text{cm} : \alpha < 40\,\text{mRad}$

Sep: separation between primary and Λ^0-vertex (47%):
$-100 < z_{V^0} < 20\,\text{cm} : (z_{V^0} - z_{\text{prim}}) > 40\,\text{cm}$
$20 < z_{V^0} < 30\,\text{cm} : (z_{V^0} - z_{\text{prim}}) > 30\,\text{cm}$
$30 < z_{V^0} < 40\,\text{cm} : (z_{V^0} - z_{\text{prim}}) > 20\,\text{cm}$

Suppression of V^0 background

In the Armenteros plot in fig. 5.3 one can already see that the Λ^0 sample is diluted with different types of V^0 background events. Apart from the K^0, which heavily interferes with the Λ^0 line, γ is most pronounced. Both types of background are unpolarized and will therefore dilute a possible Λ^0 polarization. It is therefore essential to exclude them from the measurement. A common method to reduce the γ-contribution is a cut on the Armenteros variable $p_T > 0.025$. However, as will be explained below, this variable does not remove the background sufficiently.

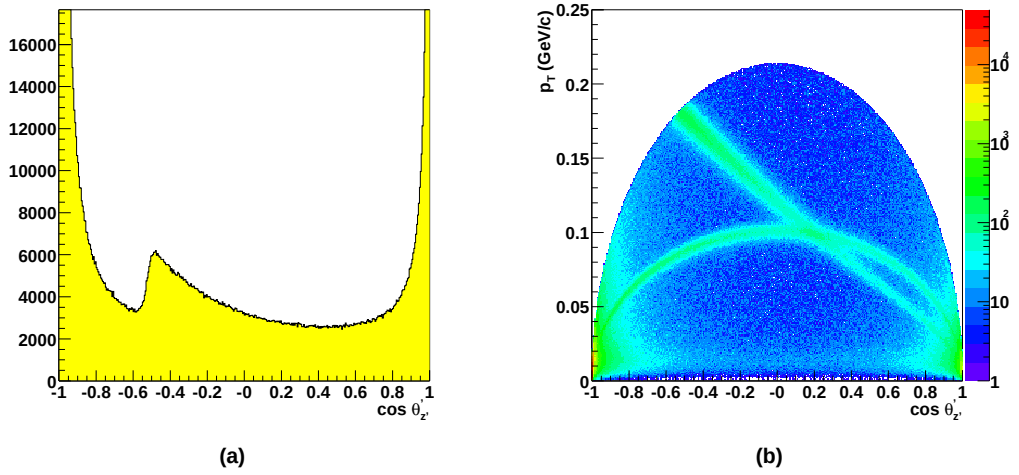

Figure 5.8: *Angular distribution $\cos\theta'_{z'}$ of Λ^0 daughters in the rest frame of the Λ^0: as explained in the text, one expects a flat distribution in plot **a)**. Expanded with the Armenteros variable p_T in **b)** one gets a kind of zoom of the Armenteros plot: Λ^0 lie on the big arc in the middle, K^0 are on the line from top left to bottom right, γ collect on the left and right margins. The shape of the plot is a result of a cut on the reconstructed Λ^0 mass to be $\pm 100\,\text{MeV}$ around the PDG Λ^0 mass. A cut on $\cos\theta'_{z'}$ clearly reduces the number of photons even better than a cut on p_T. Note that plot **b)** is logarithmic in z.*

A clearer way is displayed in fig. 5.8. As Λ^0 is a particle without further orbital momentum the spacial distribution of its decay particles in its rest frame has to be uniform. The same is true for the K^0. Plot a) shows the angle $\theta'_{z'}$ of the proton in the Λ^0 rest frame with respect to the Λ^0-direction (forward–backward, see fig. 5.4 for further explanations). Obviously, this distribution

is not as flat as one would expect. In plot b) $\cos\theta'_{z'}$ is plotted versus the Armenteros variable p_T, which produces a kind of zoom of the Armenteros plot itself [3]. In this picture Λ^0 are evenly distributed on the arc in the middle. The K^0 line comes in from top left to bottom right. The structure in the middle of plot a) is the projection of the K^0 line.
γ collect on the extreme $\cos\theta'_{z'}$ bins left and right and can be removed easily with a cut on $\cos\theta'_{z'}$. In contrast to a cut on Armenteros p_T, this cut is nearly *orthogonal* to a cut on the reconstructed invariant mass of Λ^0, which cuts parallel to the Λ^0 arc in fig. 5.8b). A cut on $\cos\theta'_{z'}$ of around ± 0.7 removes an additional 30% of good Λ^0 events, but it also reduces the influence of the unpolarized γ on the background correction as will prove to be important in the next section.

A straightforward solution to remove K^0 from the sample is to exclude events for which the $\pi^+\pi^-$ mass hypothesis is close to the PDG K^0 mass. The cut is good enough to estimate the total number of Λ^0 and the efficiency of the various cuts as well as signal-to-background ratios, but it has two disadvantages. For one thing it influences the left and right side bands differently as can be seen in fig. 5.8b). Second, it removes Λ^0 in an unsystematic way and will leave a strange hole in the $\cos\theta'_{z'}$ spectrum. For a later measurement of the polarization angular distributions will become important and such a cut might have a crucial influence. A specific procedure was therefore developed within this work to remove K^0 influence in a "softer" way. It will be explained on page 95.

The explicit values for $\cos\theta'_{z'}$ and K^0 cut can be found in the list below. The effect of the cut is given as the reduction after the geometrical cuts explained above.

Cos: angular distribution of daughters in the Λ^0 rest frame (77%):
$$-100 < z_{V^0} < 30\,\text{cm} : -0.65 < \cos\theta'_{z'} < 0.70$$
$$z_{V^0} \geq 30\,\text{cm} : -0.70 < \cos\theta'_{z'} < 0.80$$

K0: $\pi^+\pi^-$ mass hypothesis for Λ^0 candidate (68%):
$$|m_{\pi^+\pi^-} - m_{K^0,\text{PDG}}| < 10\,\text{MeV}$$

A summary of the influence of the different cuts for some characteristic parameters is given in fig. 5.9. One can nicely see that while the number of Λ^0 is reduced, the basic shape of the kinematic variables p_{V^0}, p_T and x_F is conserved.

[3] Actually it is the Λ^0 arc in the Armenteros plot seen from the center of the arc.

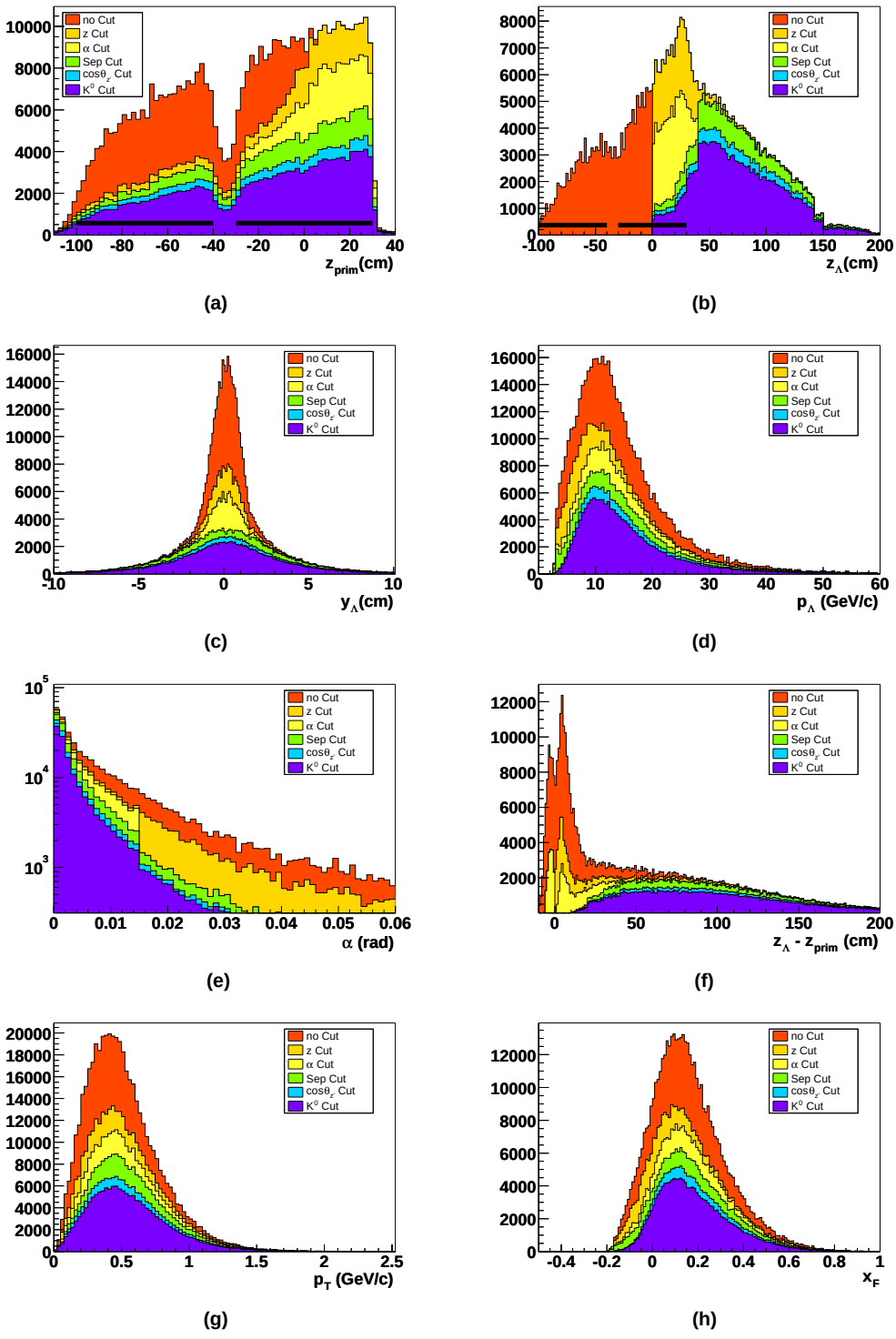

Figure 5.9: *Remaining Λ^0 after the cuts applied as explained above. All plots are background-corrected with the side band method. In plots* ***a)*** *and* ***b)*** *the position of the target cell is sketched.*
a) *position of primary vertex z_{prim};* ***b)*** *longitudinal position of Λ^0 decay z_Λ;* ***c)*** *vertical position of Λ^0 decay y_Λ;* ***d)*** *momentum p_Λ of Λ^0;* ***e)*** *target pointing α of Λ^0 track;* ***f)*** *separation of primary and Λ^0 vertex $z_\Lambda - z_{\mathrm{prim}}$;* ***g)*** *transverse momentum p_T of Λ^0;* ***h)*** *Feynman's x_F of Λ^0.*

2-dimensional K^0 Subtraction

Instead of simply cutting events for which the $\pi^+\pi^-$ mass hypothesis $m_{\pi\pi}$ is close to the PDG K^0 mass and absorbing the resulting hole in a side-band correction, one can use the known properties of K^0 and make a specialized background subtraction.

In fig. 5.10a) the invariant mass under the $p\pi$ assumption $m_{p\pi}$ is plotted versus the $\pi^+\pi^-$ invariant mass $m_{\pi\pi}$. The two arcs of Λ^0 and K^0 from the Armenteros plot in fig. 5.3 now appear as straight lines: Λ^0 goes from front to back at $m_{p\pi} = 1.115\,GeV/c^2$ and K^0 from left to right at $m_{\pi\pi} = 0.494\,GeV/c^2$.

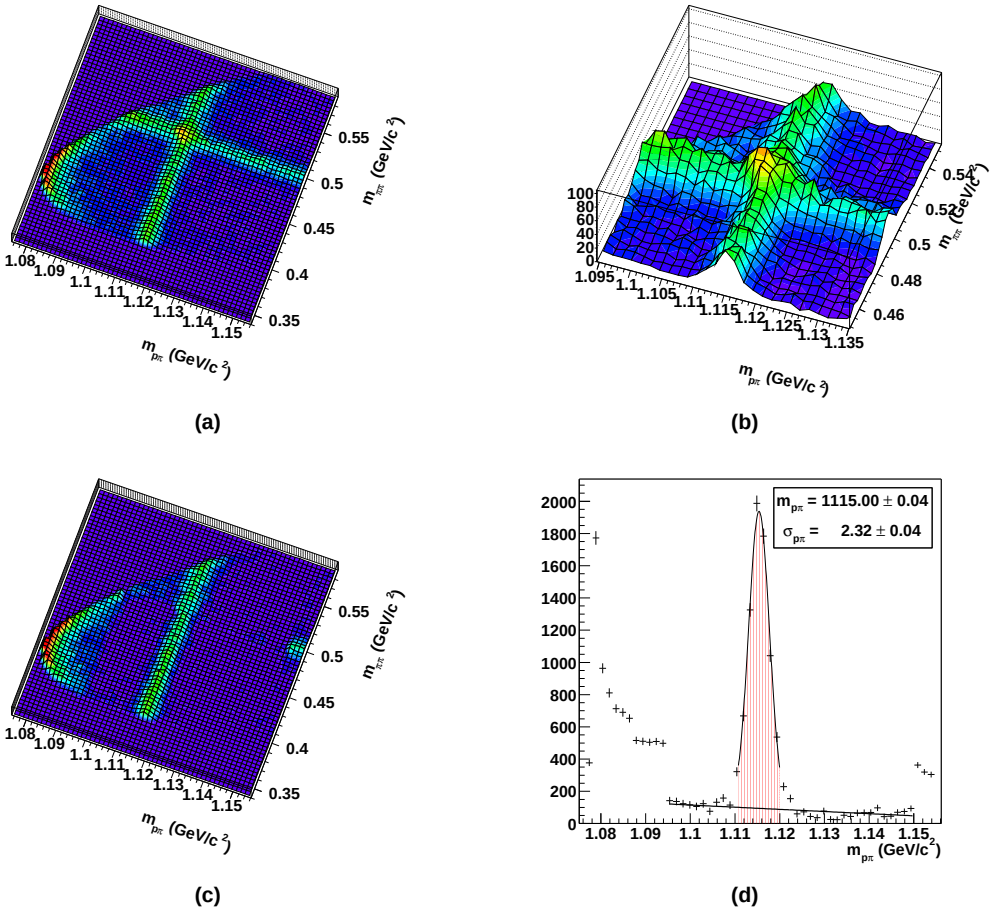

Figure 5.10: *K^0 background subtraction.* ***a)*** *$m_{\pi\pi}$ is plotted versus $m_{p\pi}$: the Λ^0 line goes from front to back and the K^0 line from left to right;* ***b)*** *shows a zoom of the overlap region of Λ^0 and K^0;* ***c)*** *plot a) after the background subtraction: one can clearly see the region where the correction was applied;* ***d)*** *projecting back onto the $m_{p\pi}$ axis, the homogeneous background can be subtracted with a 1st order polynomial fit.*

The shape of the plot in fig. 5.10a) is dominated by the kinematics of the reaction: not all combinations of $m_{p\pi}$ and $m_{\pi\pi}$ are possible. The border for low $m_{p\pi}$ and $m_{\pi\pi}$ is produced by the cut on $\cos\theta'_{z'}$: the positive border of the $\cos\theta'_{z'}$-cut removes γ with $m_{\pi\pi}$ larger than $0.4\,\mathrm{GeV/c^2}$, the negative border of the $\cos\theta'_{z'}$-cut removes γ with $m_{\pi\pi}$ smaller than $0.4\,\mathrm{GeV/c^2}$. As already mentioned

above, the lines of constant Armenteros p_T run parallel to the Λ^0 mass region: a cut thus removes the peak at $m_{p\pi} \approx 1.08\,^{GeV}/_{c^2}$, but it does merely influences the regions closer to the Λ^0 line.

In plot b) one can clearly see the overlap of K^0 and Λ^0 line and how they sum up in this region. The aim is to describe the background *including* the K^0 structure. For this, the 2-dimensional surface was fitted with a 2-dimensional, 12 parameter function, Λ^0 region excluded:

$$f(m_{p\pi}, m_{\pi\pi}) = \mathrm{BG}(m_{p\pi}, m_{\pi\pi}) + A(m_{p\pi}) \cdot \mathrm{Gauss}(m_{\pi\pi}, \mu(m_{p\pi}), \sigma(m_{p\pi})), \tag{5.2}$$

where BG(...) is a background distribution (polynomial 2^{nd} order in $m_{p\pi}$ and $m_{\pi\pi}$) and Gauss(...) a Gaussian distribution at the mean value $\mu(m_{p\pi})$ with Amplitude $A(m_{p\pi})$ and width $\sigma(m_{p\pi})$ as 2^{nd} order polynomials in $m_{p\pi}$:

$$\begin{aligned}
\mathrm{BG}(m_{p\pi}, m_{\pi\pi}) &= c_0 + (c_1 \cdot m_{p\pi} + c_2 \cdot m_{p\pi}^2) + (c_3 \cdot m_{\pi\pi} + c_4 \cdot m_{\pi\pi}^2) \\
A(m_{p\pi}) &= c_5 + c_6 \cdot m_{p\pi} + c_7 \cdot m_{p\pi}^2 \\
\mu(m_{p\pi}) &= c_8 + c_9 \cdot m_{p\pi} \\
\sigma(m_{p\pi}) &= c_{10} + c_{11} \cdot m_{p\pi}
\end{aligned}$$

The result is then subtracted from histogram a) yielding plot c) and projected back onto the $m_{p\pi}$ axis. A nice peak is formed, whose remaining background can now easily be subtracted with a straight line fit (plot d)). Plot c) shows the success of this method: the Λ^0 line now sits on a nearly flat background, the K^0 line is completely removed.

This procedure is not a cut in the usual sense, where events are rejected according to their value in a certain variable. The method described here can only be used to estimate the number background events in a given sample more accurately and produces only the *number* of "good" events. It does not provide a handle on which event is "good" or "bad".

The 2-dimensional fit has to be done separately for every bin of every variable which has to be corrected for its K^0 contribution. The available events therefore have to be divided into many subsamples, where finally each one has a relatively small size (in this thesis the Λ^0 sample was divided into 16 histograms (including the bias-canceling method as will be described later) with 54×62 bins ($1.5 \times 4.0\,\mathrm{MeV}^2$) each). The 2-dimensional background subtraction was therefore only used to extract the distributions of the very sensitive polarization variables, for other variables like position of primary vertex or momentum of Λ^0, the K^0 was suppressed via a cut on $m_{\pi\pi}$ as explained above.

5.5.3 $\bar{\Lambda}^0$ Sample

For the $\bar{\Lambda}^0$ sample basically the same cuts were applied as for the Λ^0, i.e. the cut on the decay position of the $\bar{\Lambda}^0$ **zCut**, the cuts on the target pointing **aCut** and on the separation between primary and secondary vertex **Sep** and the cut for γ suppression **Cos**. Again for the sake of simplicity the K^0 suppression cut **K0** was applied to all measurements except for the polarization, where the 2-dimensional background subtraction was used. The invariant mass plot after all cuts can be seen in fig. 5.11. It yields a total of $\approx$78 000 $\bar{\Lambda}^0$.

To demonstrate the suppression of γ via a cut on $\cos\theta'_{z'}$ (**Cos**), the corresponding $\cos\theta'_{z'}$ distributions are shown in fig. 5.12. Referring to the π^+, it is a mirror image of fig. 5.8, but consistent with the Armenteros plot in fig. 5.3.

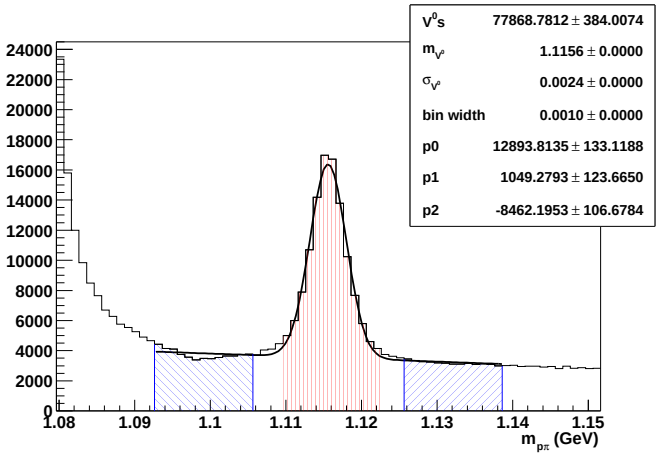

Figure 5.11: *Invariant mass spectrum for the $\bar{\Lambda}^0$ sample with cuts mentioned in the text under the assumption that the daughter particles were $\bar{p}\pi^+$. The peak value of 1.1156 GeV/c² is within the error close enough to the PDG $\bar{\Lambda}^0$ mass of 1.1157 GeV/c², the resolution of 2.4 MeV/c² is the same as for the Λ^0. According to the fit, the sample contains ≈78 000 $\bar{\Lambda}^0$.*

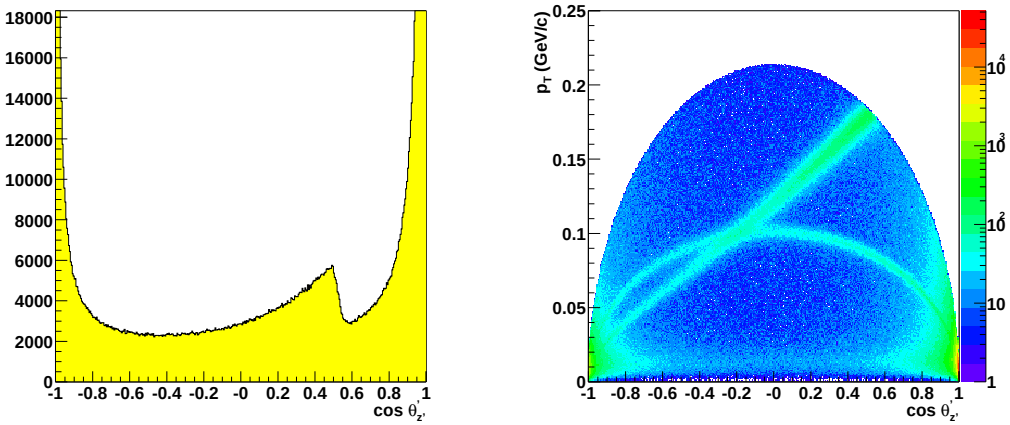

Figure 5.12: $\cos\theta'_{z'}$ *spectrum for $\bar{\Lambda}^0$ after geometrical cuts* **zCut**, **aCut** *and* **Sep**. *Equivalent to fig. 5.8, the left plot* ***a)*** *shows the distribution directly and in* ***b)*** $\cos\theta'_{z'}$ *versus the Armenteros p_T. One can see the contaminations from the different V^0: left and right structures come from γ, the structure in the middle from K^0. Again, the γ can be removed easily by cutting on $\cos\theta'_{z'}$. The spectrum shows $\cos\theta'_{z'}$ of the* positive *daughter particle and is therefore a mirror image of fig. 5.8.*

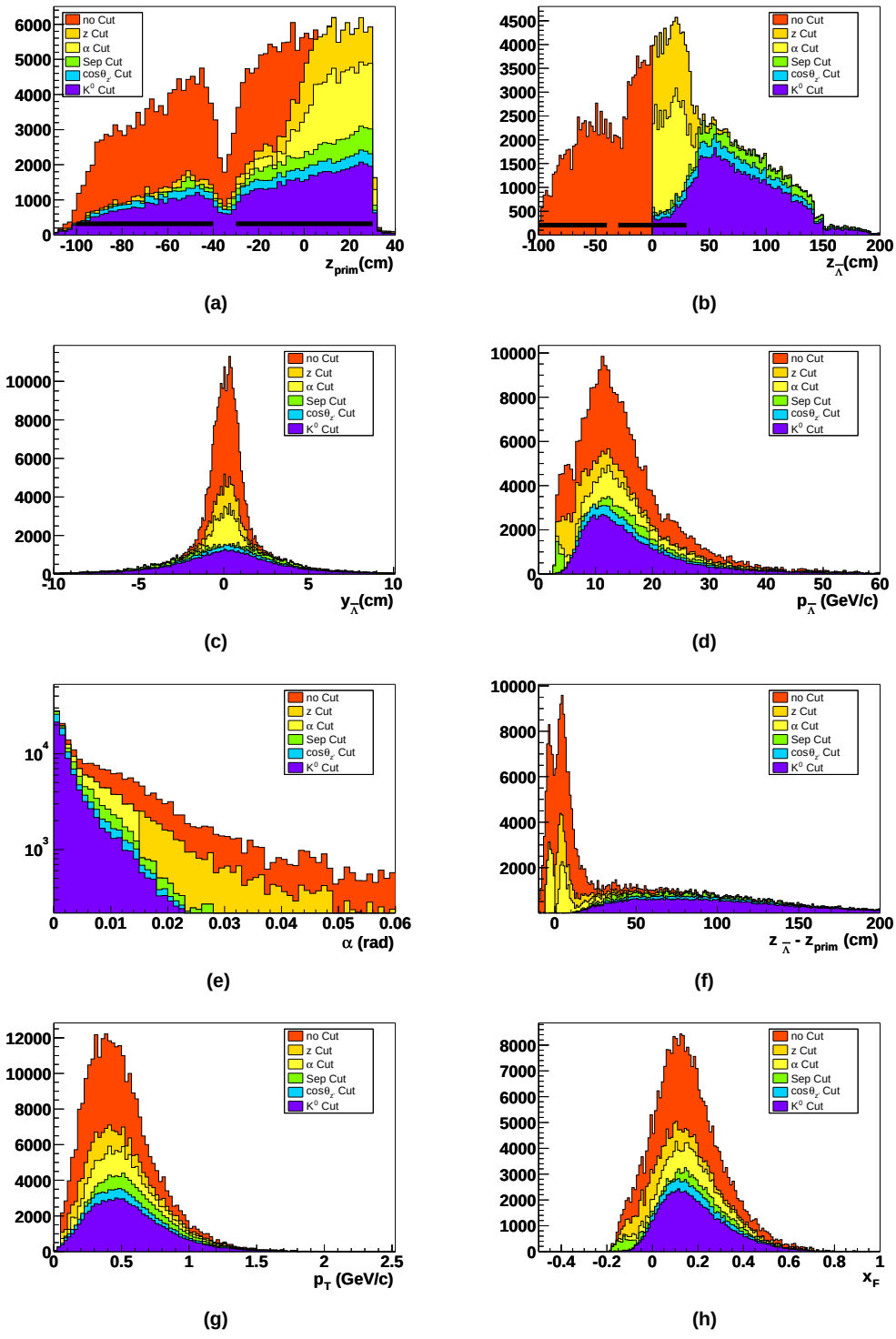

Figure 5.13: *Remaining $\bar{\Lambda}^0$ after the cuts applied as explained above. All plots are background-corrected with the side band method. In plots* ***a)*** *and* ***b)*** *the position of the target cell is sketched.*
a) *longitudinal position of primary vertex z_{prim};* ***b)*** *longitudinal position of $\bar{\Lambda}^0$ decay $z_{\bar{\Lambda}}$;* ***c)*** *vertical position of $\bar{\Lambda}^0$ decay $y_{\bar{\Lambda}}$;* ***d)*** *momentum $p_{\bar{\Lambda}}$ of $\bar{\Lambda}^0$;* ***e)*** *target pointing α of $\bar{\Lambda}^0$ track;* ***f)*** *separation of primary and $\bar{\Lambda}^0$ vertex $z_{\bar{\Lambda}} - z_{\mathrm{prim}}$;* ***g)*** *transverse momentum p_T of $\bar{\Lambda}^0$;* ***h)*** *Feynman's x_F of $\bar{\Lambda}^0$.*

As a summary for the $\bar{\Lambda}^0$ sample, the same characteristic parameters as for the Λ^0 sample in fig. 5.9 are shown in fig. 5.13.

The samples of Λ^0 and $\bar{\Lambda}^0$ differ in a small technical detail. Per convention, the sign of the polarization is defined by the direction of the involved baryon, i.e. the p for Λ^0 and the $\bar{p}$ for $\bar{\Lambda}^0$. But in this analysis for both cases the *positive* decay daughter of the V^0 was taken as the reference for the angular distributions. i.e. the p for Λ^0 and the π^+ for $\bar{\Lambda}^0$. As the two daughters have opposite direction in the V^0 rest frame this results in a sign flip of the asymmetry between Λ^0 and $\bar{\Lambda}^0$. This effect is properly taken into account, when going from the asymmetry to a polarization.

5.5.4 K^0 Sample

The selection of K^0 is less stringent than that of Λ^0 or $\bar{\Lambda}^0$. As can already be seen in the Armenteros plot (fig. 5.3) and even more clearly in the $\cos\theta'_{z'}$ plots in fig. 5.16, both γ, Λ^0 and $\bar{\Lambda}^0$ touch the K^0 area only on the margins of its phase space. Especially fig. 5.16a) shows that the restriction that $\cos\theta'_{z'}$ must be within [-0.75,0.75] is sufficient to remove *all* V^0 background in one go. The remaining region exhibits a nice flat distribution as expected. The standard cuts defined above could therefore be relaxed a little bit. The exact numbers are listed below. Obviously, no additional cut on the invariant masses of Λ^0or $\bar{\Lambda}^0$ were needed. The invariant mass plot after all cuts is shown in fig. 5.14 and yields 1 070 000 K^0. Fig. 5.15 shows the influence of the cuts on the characteristic parameters again.

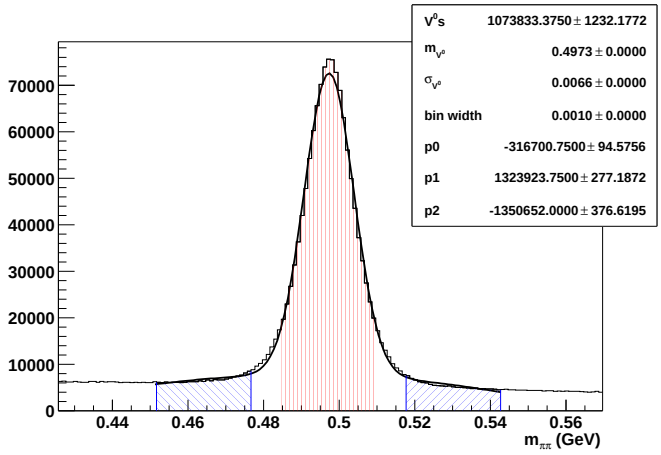

Figure 5.14: *Invariant mass spectrum for the K^0 sample with the cuts mentioned in the text under the assumption that the daughter particles were $\pi^+\pi^-$. As explained in section 5.4, the magnetic fields were adjusted in such a way that the peak value of 0.4973 GeV/c² is close to the PDG value of 0.4977 GeV/c². The fit yields 1 070 000 K^0.*

zCut: decay position of K^0 not upstream of the second target cell: $z_{V^0} > 0\,\text{cm}$

aCut: angle α between K^0-direction and connection primary-secondary vertex: $\alpha < 30\,\text{mRad}$

Sep: separation between primary and K^0-vertex: $-100 < z_{V^0} < 40\,\text{cm} : (z_{V^0} - z_{\text{prim}}) > 10\,\text{cm}$

Cos: angular distribution of daughters in the K^0 rest frame: $-0.75 < \cos\theta'_{z'} < 0.75$

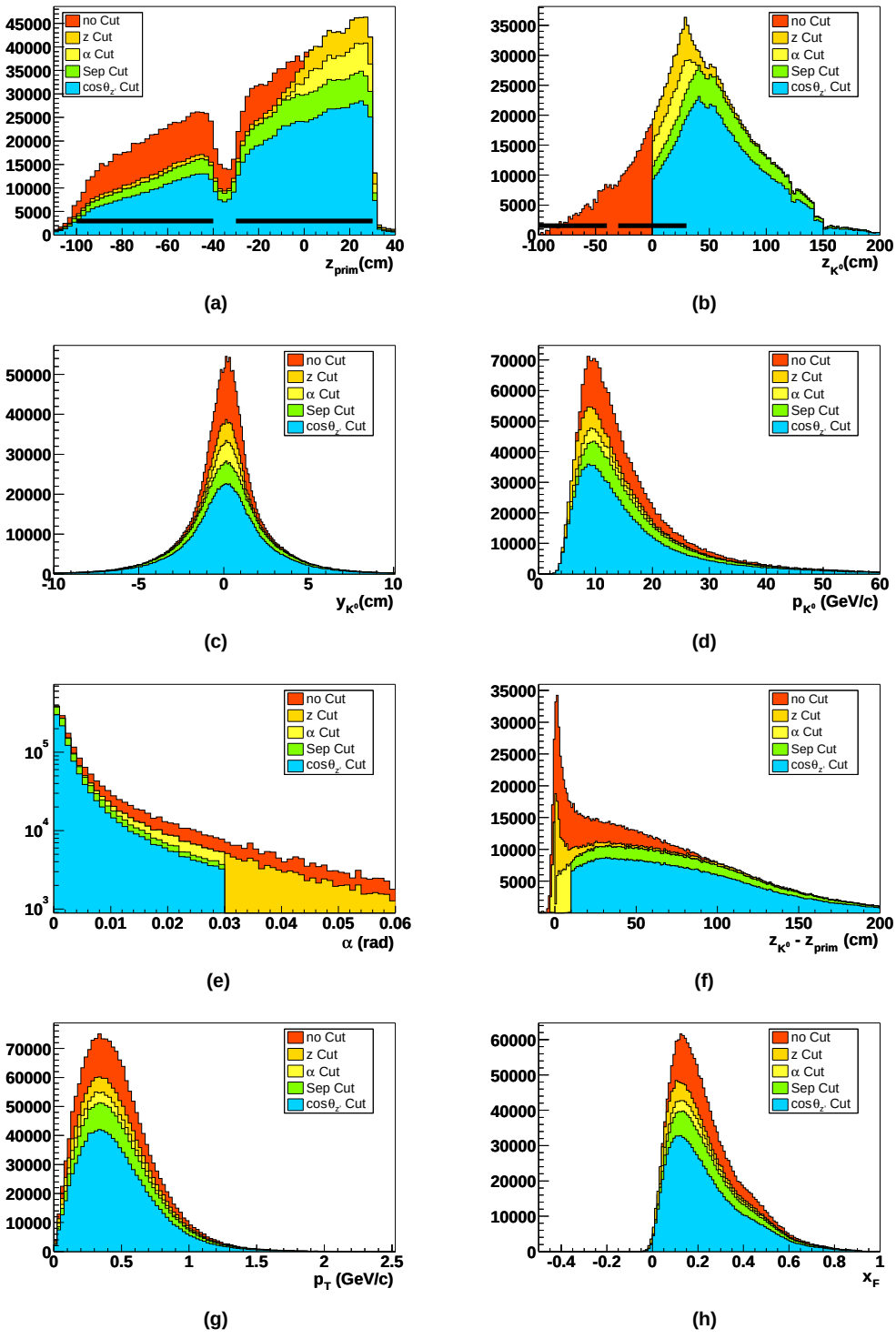

Figure 5.15: *Remaining K^0 after the cuts applied as explained above. All plots are background-corrected with the side band method. In plots* ***a)*** *and* ***b)*** *the position of the target cell is sketched.*
a) *position of primary vertex z_{prim};* ***b)*** *longitudinal position of K^0 decay z_{K^0};* ***c)*** *vertical position of K^0 decay y_{K^0};* ***d)*** *momentum p_{K^0} of K^0;* ***e)*** *target pointing α of K^0 track;* ***f)*** *separation of primary and K^0 vertex $z_{K^0} - z_{\text{prim}}$;* ***g)*** *transverse momentum p_T of K^0;* ***h)*** *Feynman's x_F of K^0.*

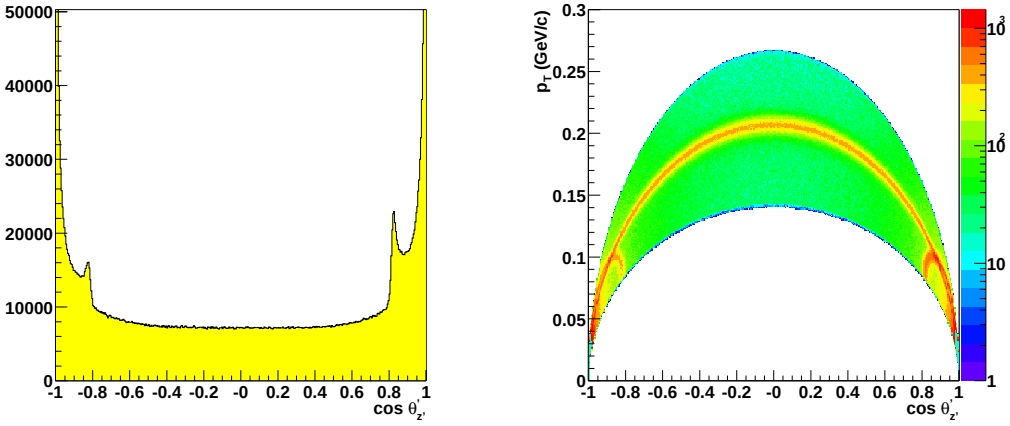

Figure 5.16: $\cos\theta'_{z'}$ *spectrum for* K^0 *after the geometrical cuts* **zCut**, **aCut** *and* **Sep**. *Equivalent to fig. 5.8 and fig. 5.12, the left plot* ***a)*** *shows the distribution directly and in* ***b)*** $\cos\theta'_{z'}$ *is expanded with the Armenteros* p_T. *It is clearly visible that* γ, Λ^0 *and* $\bar{\Lambda}^0$ *touch the strong* K^0 *line only on the margin of its phase space and can be easily removed in one common cut on* $\cos\theta'_{z'}$. *The remaining region is basically flat as it should be. Note also that in plot* ***a)*** *one can nicely see that there are roughly twice as many* Λ^0 *than* $\bar{\Lambda}^0$.

5.6 Properties of the Virtual Photon Beam

The yield of PGF events is higher for events for which both the 4-momentum Q^2 of the γ^* is small and the energy ν is large. As was explained in section 1.3.6, the trigger system of COMPASS was especially designed to select γ^* with small Q^2, so-called *quasi-real photons*. The characteristic parameters Q^2 and ν of the γ^* for the selected Λ^0 sample are shown in fig. 5.17. In analogy to the properties of the Λ^0-particles themselves, the spectra are displayed after the cuts described in the last section. The Q^2 of the γ^* peaks at around $0.05\,\mathrm{GeV}^2/c^2$ and demonstrates the quasi-realness. The mean photon energy is $\approx 70\,\mathrm{GeV}$.

In fig. 5.18 the correlation between Q^2 and ν is plotted. The ratio between Q^2 and ν is a measure for the in-elasticity of the scattering process. It is convenient to use the definition by Bjorken (see any particle physics book, e.g. Povh et al. [PRSZ94]) $x_{\mathrm{Bj}} := Q^2/2M\nu$, where this ratio is normalized with the target nucleon mass M. For elastic scattering is $x_{\mathrm{Bj}} = 1$, for inelastic scattering is $x_{\mathrm{Bj}} < 1$. In fig. 5.18 the lines for some selected x_{Bj}-values are drawn as well. The limit for the low Q^2 values comes from the finite mass of the muon. It corresponds to events where the scattering angle of the μ was zero and the μ experienced a pure energy loss ν.

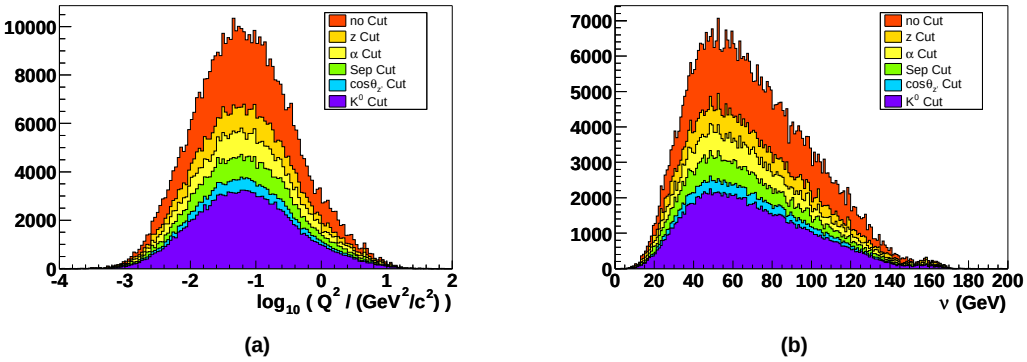

Figure 5.17: *The COMPASS Λ^0 are mainly produced from quasi-real photons with very small Q^2. Plot* ***a)*** *shows the Q^2 distribution of γ^* for the selected Λ^0 sample with the different cuts applied as described in the previous section. Plot* ***b)*** *shows the energy spectrum ν of γ^*.*

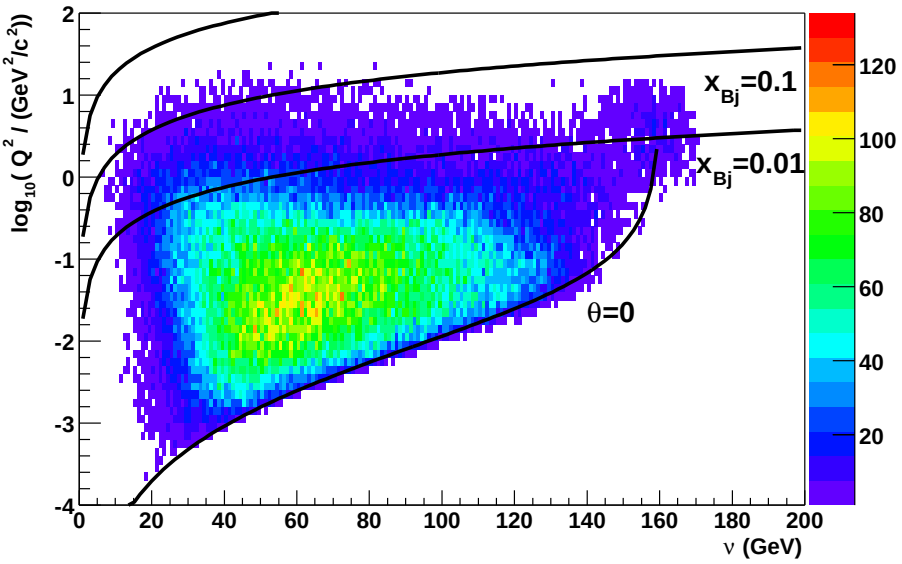

Figure 5.18: *The correlation between the 4-momentum Q^2 and the energy ν of γ^* used for Λ^0 photo-production. The upper lines are regions with constant x_{Bj}, the lowest line is the kinematical limit of zero scattering angle θ.*

5.7 Bias-Canceling Method

As explained in section 1.2 a possible transverse Λ^0-polarization P_n is reflected in the angular distribution of the decay particles of Λ^0 according to

$$\frac{\mathrm{d}N}{\mathrm{d}\cos\theta'_{n'}} = A(1 + \alpha\, P_n \cos\theta'_{n'}), \tag{5.3}$$

where $\theta'_{n'}$ is the angle between the normal of the production plane $\vec{n'}$ and the direction of the decay proton in the Λ^0 rest frame (see fig. 5.4 for the geometry). α is the decay asymmetry parameter as listed in table 1.1. A possible polarization thus shows up as a slope in the distribution of the events with $\cos\theta'_{n'}$.

The *acceptance* A, however, is not necessarily independent of $\cos\theta'_{n'}$ and might lead to results which cannot easily be distinguished from polarization-induced effects. In fig. 5.19 the number of Λ^0 for different $\cos\theta'_{n'}$ bins is shown. A rather significant discrepancy from a flat distribution illustrates the problem. There are many sources for such a behavior, examples are geometrical acceptance edges of the spectrometer and regions of local inefficiencies, but also the application of cuts to the data in the process of analysis.

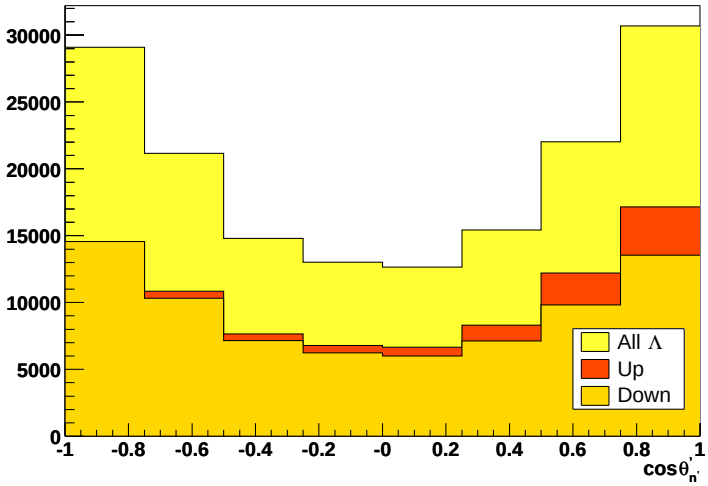

Figure 5.19: *Angular distribution of the decay p in the Λ^0 rest frame. The plot shows a clear discrepancy from a flat distribution due to acceptance distortions. For the further analysis the data were divided into two subsamples as explained in the text. As can be seen in the plot as well the two samples do not share the total statistics equally among each other.*

A commonly used method to unfold again such irregularities is to extract correction functions from Monte Carlo simulations. But besides a good knowledge of the systematics of the spectrometer a high confidence into its description is needed. *Bias-canceling techniques* can be used to avoid the introduction of such systematical uncertainties. In these methods correction functions are extracted from the experimental data directly. When comparing two subsamples of the data with each other, certain acceptance effects drop out. The method applied in this analysis was already used in the EXCHARM experiment [Ale00] and originally developed by Ohlsen and Keaton [OK73].

Left-right Asymmetry

The key point for acceptance problems is the orientation of the production plane spanned by the virtual photon γ^* and the Λ^0 track $\vec{n} = \vec{\gamma^*} \times \Lambda^0$. If this plane is not arbitrarily oriented in space, possible irregularities in the spectrometer acceptance might be mistaken as polarization. As was explained before, the photons are mostly quasi-real with a very small Q^2 and thus have

a very small angle with respect to the incoming beam. The orientation of the production plane is therefore dominated by the direction of the Λ^0 track: for Λ^0 tracks going upward with the vertical momentum component $p_{y,V^0} > 0\,{}^{GeV}/_{c}$ the normal vector $\vec{n}$ points to the right side of the spectrometer $n_x < 0\,\text{cm}$, for Λ^0 tracks going downward $p_{y,V^0} < 0\,{}^{GeV}/_{c}$, $\vec{n}$ points to the left side $n_x > 0\,\text{cm}$. Fig. 5.20 shows the correlation between p_{y,V^0} and n_x.

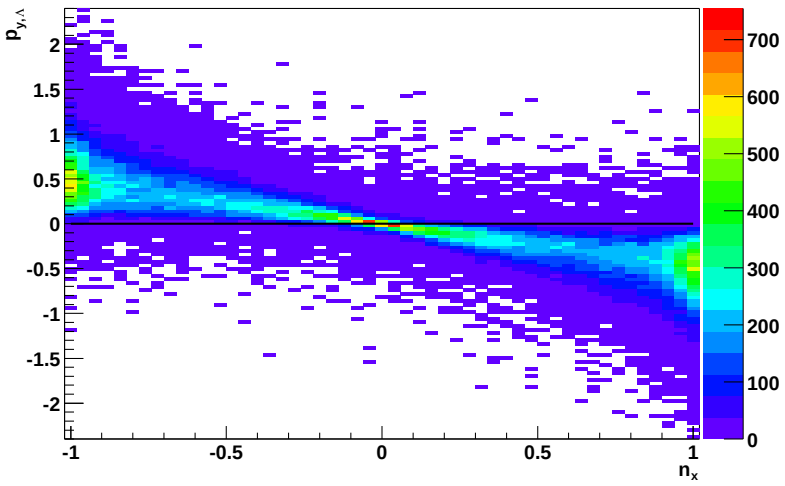

Figure 5.20: *Correlation between the direction of the Λ^0-track and the orientation of the production plane $\vec{n}$. The y component of the Λ^0-momentum (up-down) and the x-component of $\vec{n}$ (left-right) is plotted. One can see that basically all Λ^0 going upward ($p_{y,V^0} > 0$) are connected to a normal vector pointing to the right ($n_x < 0$).*

A possible polarization manifests itself in a difference of protons going along and against $\vec{n}$. For positive polarized Λ^0 one expects therefore that the Λ^0 going upward emit their protons preferably to the right side of the spectrometer and the Λ^0 going downward to the left side.

Due to the COMPASS magnets, however, the acceptance on the left side of the spectrometer differs from the acceptance on the right side and is in particular charge dependent. If the proton is emitted to the right side, it is bent back into the spectrometer and away from its edges; if it is emitted to the left side, it is bent closer to the spectrometer edges or even out of the acceptance at all. The effect of a bending magnet on the two charged tracks of V^0 decays, which go to the different sides of the spectrometer, is sometimes referred to as the *cowboy-and-sailor* effect: if both particles are bent back into the spectrometer, their trajectories remind strongly of a cowboy's legs, if both particles are bent out of the spectrometer their trajectories remind more of a sailor's legs. In fig. 5.21 one can see that the acceptance for "cowboy" tracks is obviously larger than for "sailor" tracks. Thus *upward* Λ^0 have a *larger* acceptance (cowboy) if they are *positively* polarized, *downward* Λ^0 have a *larger* acceptance if they are *negatively* polarized. In conclusion, the left-right asymmetry prefers positive $\cos\theta'_{n'}$ in the case of Λ^0 going upward and negative $\cos\theta'_{n'}$ for Λ^0 going downward.

As long as the number of events for Λ^0 going up- and downward is exactly the same, the left-right asymmetry prefers positive and negative $\cos\theta'_{n'}$ in the same way and drops out. But for a different number of Λ^0 going upward and downward the left-right asymmetry is propagated to the angular distribution in $\cos\theta'_{n'}$ and is superimposed onto a possible polarization.

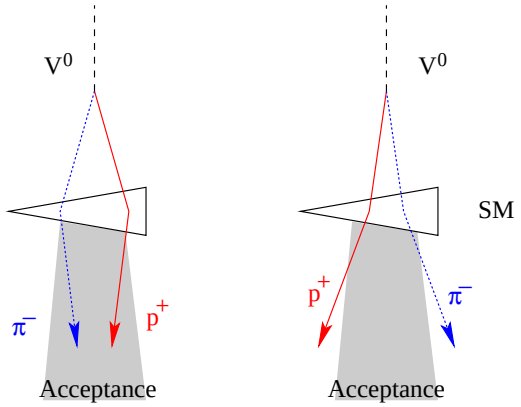

Figure 5.21: *The geometrical acceptance of V^0-decay particles depends on whether the positive particle was emitted in the opposite or in the same direction as the bending direction of the spectrometer magnet SM. The resulting picture reminds of the legs of a "cowboy" (left) or a "sailor" (right).*

Double Bias-Canceling

Bias-canceling techniques can be used to correct left-right asymmetries. One uses the fact that the spectrometer is in principle symmetric with respect to the central plane of the magnets, or more precisely, that the *geometrical* acceptance, i.e. size and angular coverage of the spectrometer and possible local inefficiencies, is the same in the upper and the lower hemisphere.

The full sample of Λ^0 is now divided into two subsamples with Λ^0 tracks going upward (U) and downward (D) respectively. Eq. (5.3) is valid for both samples separately:

$$\begin{aligned} U(\cos\theta'_{n'}) &\equiv \frac{\mathrm{d}N_U}{\mathrm{d}\cos\theta'_{n'}} = A_U(\cos\theta'_{n'})\ (1+\alpha P\cos\theta'_{n'}) \\ D(\cos\theta'_{n'}) &\equiv \frac{\mathrm{d}N_D}{\mathrm{d}\cos\theta'_{n'}} = A_D(\cos\theta'_{n'})\,(1+\alpha P\cos\theta'_{n'}). \end{aligned} \tag{5.4}$$

Note that the acceptance A from eq. (5.3) is now written as a function of $\theta'_{n'}$ to show the explicit acceptance dependence. For the two samples the normal of the production plane $\vec{n}$ now points preferably to the right (U) or the left side (D) of the spectrometer.

The acceptances A_U and A_D can be related to each other via the symmetry of the spectrometer. Fig. 5.22 shows as an example the extreme case of two vertical production planes, for which the Λ^0 tracks have no further x-component. The normal vectors $\vec{n}$ then point to opposite directions. For the two Λ^0 decays, the two indicated proton tracks should have the same acceptance in a symmetric spectrometer, but the opposite sign in $\cos\theta'_{n'}$:

$$A_D^{\mathrm{geo}}(\cos\theta'_{n'}) = A_U^{\mathrm{geo}}(-\cos\theta'_{n'}). \tag{5.5}$$

Even for the extreme case, for which the acceptance is zero on the left side of the spectrometer and 100% on the right side, a polarization can still be extracted by comparing the number of upward

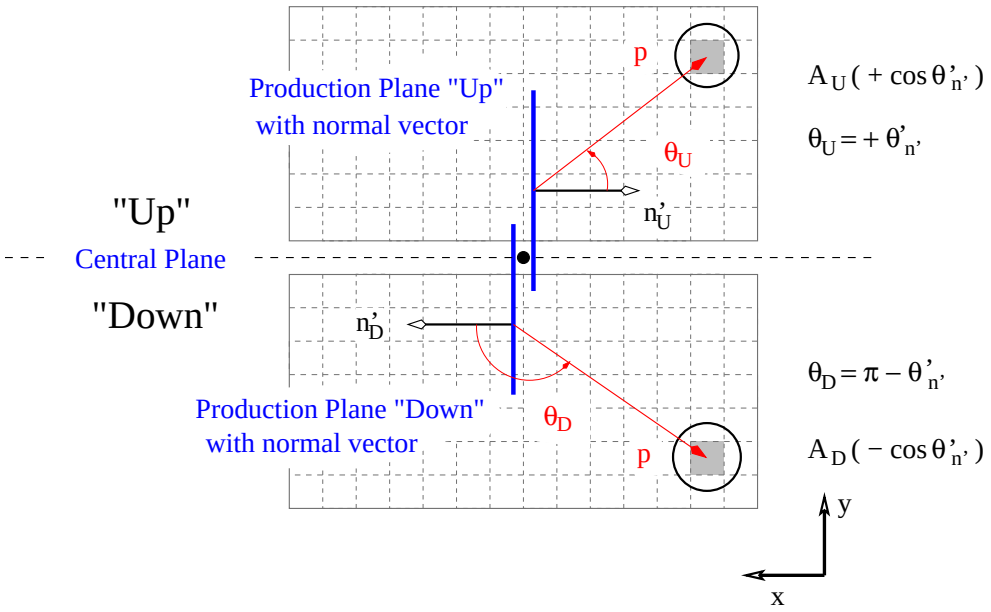

Figure 5.22: *Downstream view of the spectrometer, the beam passes through the center of the picture. Two production planes are drawn for a Λ^0 going upward and a Λ^0 going downward. The normal vectors then point either to the right or to the left side. If the spectrometer is symmetric with respect to the central plane of the magnet, the two indicated protons have the same acceptance, but with the opposite sign in $\cos\theta'_{n'}$.*

events with positive $\cos\theta'_{n'}$ with the number of downward events with negative $\cos\theta'_{n'}$. This method fails if the absolute number of upward and downward Λ^0 are not correctly normalized.

The symmetry of the spectrometer is included in a cleaner way if the division into the two subsamples is made in such a way that the *decay position* of the Λ^0 y_{V^0} is in the upper ($y_{V^0} > 0\,\text{cm}$) or the lower hemisphere ($y_{V^0} < 0\,\text{cm}$), as the charged tracks emerge from this point and are tracked in the spectrometer thereafter. Due to the small divergence of the virtual photon and its negligible path in space, the correlation between y_{V^0} and n_x is only marginally wider than for the direction of the Λ^0 p_{y,V^0}. It is shown in fig. 5.23.

Fig. 5.19 shows the angular distribution in $\cos\theta'_{n'}$ for the total Λ^0 sample and the two subsamples for $y_{V^0} > 0\,\text{cm}$ and $y_{V^0} < 0\,\text{cm}$. The lower half of the spectrometer has less entries than the upper half. This can partly be related to an asymmetric trigger setup and an asymmetric position of the target cell. For a mere statistical difference in the two hemispheres, the acceptances can be connected via a simple factor $f(\cos\theta'_{n'})$. If now the ratio of the acceptances in the upper and lower hemisphere is taken, the factor f cancels again:

$$\frac{A_U(+\cos\theta'_{n'})}{A_D(-\cos\theta'_{n'})} = f = \frac{A_U(-\cos\theta'_{n'})}{A_D(+\cos\theta'_{n'})} \tag{5.6}$$

This symmetry condition can be used when the polarization is calculated from the difference between positive and negative $\cos\theta'_{n'}$ for the *geometric mean* of the number of Λ^0 decaying in the upper and lower hemisphere:

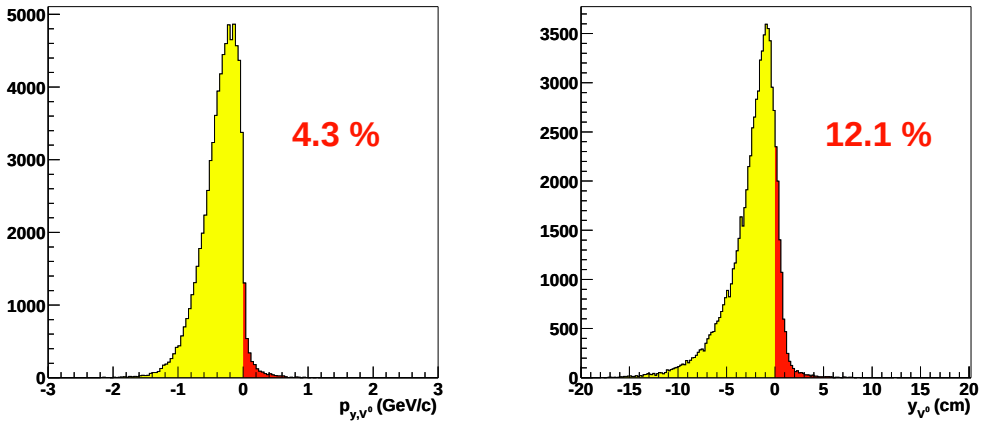

Figure 5.23: ***a)*** p_{y,V^0} *and* ***b)*** y_{V^0} *for* $n_x > 0$. *Both variables have the opposite sign as* n_x *to a large extent. The small leakage to positive values is a result of the divergence of* γ^* *and the finite size of the target.*

$$R \equiv \frac{\sqrt{U(\cos\theta'_{n'})D(\cos\theta'_{n'})} - \sqrt{U(-\cos\theta'_{n'})D(-\cos\theta'_{n'})}}{\sqrt{U(\cos\theta'_{n'})D(\cos\theta'_{n'})} + \sqrt{U(-\cos\theta'_{n'})D(-\cos\theta'_{n'})}}, \tag{5.7}$$

for $\cos\theta'_{n'} > 0$. Each square root now averages over the left-right asymmetry by taking the product of a preferred and a disfavored region and is at the same time properly normalized with respect to the other square roots by averaging over an upper and a lower region. With eq. (5.6) finally the acceptance effects cancel and R can be simplified to:

$$R = \alpha\, P \cos\theta'_{n'}. \tag{5.8}$$

Statistical Effect of Bias-Canceling

R as stated in eq. (5.8) is a convenient choice for the extraction of the polarization as it has a simple linear dependence on both $\cos\theta'_{n'}$ and P_n. But due to the division into the two subsamples of the upper and lower hemisphere, the statistical error of P_n increases by a factor of $\approx \sqrt{2}$. A simple example illustrates this:

- The polarization can be calculated from the number of Λ^0 with positive $\cos\theta'_{n'}$, N^+, and negative $\cos\theta'_{n'}$, N^-, as $P_n = \frac{N^+ - N^-}{N^+ + N^-}$. Assuming a small polarization, both N^+ and N^- are approximately half of the total number N of Λ^0: $N^+ \approx N^- \approx N/2 \pm \sqrt{N/2}$. Propagating the error of N^+ and N^- to P_n one gets $\Delta P_n = 1/\sqrt{N}$.

- For an additional division into two hemispheres, one has now $N^\pm = \sqrt{N_U^\pm \cdot N_D^\pm}$. Assuming again for the sake of simplicity a factor of $1/2$ in statistics for the subsamples of "Up" and "Down", one gets $N^+ \approx N^- \approx \sqrt{N/4 \cdot N/4} = N/4$ with an error of $\pm\sqrt{N/4}$. The total error in P_n is now $\Delta P_n = \sqrt{2}/\sqrt{N}$.

Thus on the one hand bias-canceling reduces the systematic uncertainty, but on the other hand it increases the statistical error.

Influence of Cuts on $\cos\theta'_{n'}$

Apart from the shape of the spectrometer cuts can also influence the shape of the acceptance function $A(\cos\theta'_{n'})$. In fig. 5.24 the correlation of $\cos\theta'_{n'}$ and the cut on $\cos\theta'_{z'}$ introduced earlier is shown: the cut is stronger on bins of $\cos\theta'_{n'} \approx 0$. This cut is the origin of the hole in the middle of fig. 5.19. It is important, however, that cuts are symmetric in $\cos\theta'_{n'}$, as this was assumed for eq. (5.7).

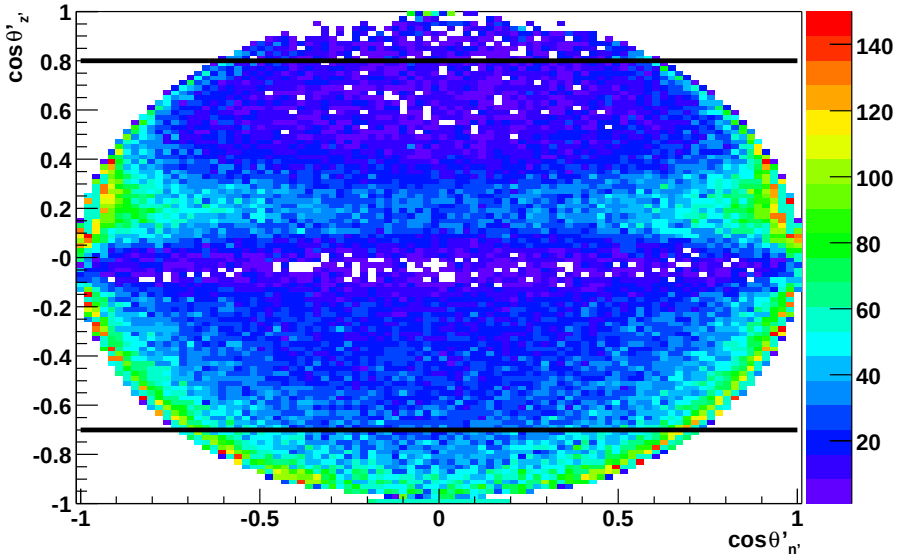

Figure 5.24: *Correlation between the* **Cos** *cut on $\theta'_{z'}$ introduced in section 5.5.2 and the angle $\theta'_{n'}$ needed for the measurement of the polarization. The cut on $\cos\theta'_{z'}$ is indicated with the two lines and is symmetric in $\cos\theta'_{n'}$, but stronger for $\cos\theta'_{n'} \approx 0$. The structure at $\cos\theta'_{z'} \approx 0.2$ are K^0 events.*

Conclusions on Bias-Canceling

Unfortunately, in this work the systematic effect of the bias-canceling on the data could not be investigated in more detail. Especially simulations would be helpful to determine more closely which kind of asymmetries are removed under which conditions or if false asymmetries are introduced. It was made plausible that bias-canceling can remove a left-right asymmetry in the acceptance. No hints were found that bias-canceling introduces false asymmetries, but it was shown that the application of bias-canceling techniques increases the statistical error. Thus even if a positive effect could not yet be proven, a negative effect (except of the known statistical one) on the measurement of polarization seems to be unlikely. As will be shown later in chap. 6 the absence of false asymmetries for the K^0 sample indicates that the method is basically working. Consequently, bias-canceling was used in this analysis.

5.8 Extraction of Polarization

For the extraction of the polarization, the V^0 were sorted into 4 bins of negative and 4 bins of positive $\cos\theta'_{n'}$ for both the "Up" and "Down" spectrometer part. A V^0 was treated as "Up" when its decay position y_{V^0} was positive and as "Down" for negative y_{V^0}.

For Λ^0 and $\bar{\Lambda}^0$ the 2-dimensional $m_{p\pi}$-$m_{\pi\pi}$-surface correction from fig. 5.10 was applied in each of the 16 subsamples. The remaining background was estimated with a 1st order polynomial fit. For the K^0 no 2-dimensional background subtraction was needed and a 1st order polynomial was fitted to the invariant mass plot directly. In both cases the resulting signal peak was fitted with a Gaussian function. The number of "good" entries was calculated as the sum of the number of entries for the bins in $m_{p\pi}$ (or $m_{\pi\pi}$ for the K^0) within $2\,\sigma$ around the fitted maximum. As the bin width was relatively large (1.5 MeV) and thus the number of bins comparatively small (7 to 8), the number of V^0 was systematically estimated too large. The contributions of the lowest and highest bins in $m_{p\pi}$ ($m_{\pi\pi}$) to the sum of "good" entries were therefore weighted according to their contribution to the $2\,\sigma$ region.

y_{V^0}	$\cos\theta'_{n'}$	N_{V^0}	- 2D BG	- 1st order pol	n_{V^0}
+	+0.00 - +0.25	11 408±106	-3 515	-1 248	6 643±99
+	-0.00 - -0.25	11 659±107	-3 590	-1 279	6 789±101
-	+0.00 - +0.25	10 168±100	-2 938	-1 221	6 007±95
-	-0.00 - -0.25	10 336±101	-2 995	-1 105	6 235±95
+	+0.25 - +0.50	13 259±115	-3 691	-1 258	8 309±107
+	-0.25 - -0.50	12 787±113	-3 629	-1 503	7 653±106
-	+0.25 - +0.50	11 559±107	-3 042	-1 392	7 123±101
-	-0.25 - -0.50	11 524±107	-3 223	-1 155	7 145±100
+	+0.50 - +0.75	18 622±136	-4 606	-1 804	12 211±128
+	-0.50 - -0.75	17 317±131	-4 450	-2 024	10 842±124
-	+0.50 - +0.75	15 422±124	-3 814	-1 786	9 821±117
-	-0.50 - -0.75	16 034±126	-3 783	-1 940	10 310±120
+	+0.75 - +1.00	25 121±158	-5 810	-2 164	17 146±150
+	-0.75 - -1.00	22 823±151	-6 159	-2 125	14 537±142
-	+0.75 - +1.00	20 446±142	-4 841	-2 070	13 533±135
-	-0.75 - -1.00	21 325±146	-5 292	-1 472	14 560±139

Table 5.1: *The Λ^0 sample was divided into 8 bins in $\cos\theta'_{n'}$ for the "Up" (+) and the "Down" (-) spectrometer separately and background-corrected as explained in the text. N_{V^0} is the number of entries in a $2\,\sigma$ wide area under the peak before, n_{V^0} the respective number after background correction.*

In table 5.1 this procedure is demonstrated with the full Λ^0 sample. For every sample the number of entries within the 2σ area under the peak before (N_{V^0}) and after all corrections (n_{V^0}) is given, as well as the reduction of the two steps. The total error is assumed to be dominated by the *statistical* error $\propto \sqrt{N_{\Lambda^0}}$. Errors from the functions used for the background subtraction were therefore omitted. The errors of N_{V^0} and n_{V^0} are consequently nearly the same. A small difference arises as the corrected peak is narrower than the original one (the K^0 running perpendicular are removed)

and thus the definition of the 2σ area changes as well.

For each group of 4 bins with the same $|\cos\theta'_{n'}|$ the ratio R was calculated according to eq. (5.7). These values can be found in table 5.2 for the Λ^0 sample and are plotted in fig. 5.25. For $\bar{\Lambda}^0$ and K^0 the plots are shown in fig. 6.1. Errors were propagated according to the standard rules of statistics (i denotes the different $\cos\theta'_{n'}$-bins):

$$\Delta R_i = \sqrt{(\frac{\mathrm{d}R}{\mathrm{d}U_{+i}} \cdot \Delta U_{+i})^2 + (\frac{\mathrm{d}R}{\mathrm{d}U_{-i}} \Delta U_{-i})^2 + (\frac{\mathrm{d}R}{\mathrm{d}D_{+i}} \cdot \Delta D_{+i})^2 + (\frac{\mathrm{d}R}{\mathrm{d}D_{-i}} \cdot \Delta D_{-i})^2}. \qquad (5.9)$$

According to eq. (5.8) the slope of R is proportional to the polarization. R was therefore fitted with a straight line $R = c_1 \cdot x$. For systematic checks, a 1^{st} order polynomial $R = c_{11} \cdot x + c_{10}$ was also fitted with a free value c_{10} at the origin, but basically c_{10} was within the error compatible with 0.

$\cos\theta'_{n'}$	U(+$\cos\theta'_{n'}$)	D(+$\cos\theta'_{n'}$)	U(-$\cos\theta'_{n'}$)	D(-$\cos\theta'_{n'}$)	R
0.00 - 0.25	6 643±99	6 007±95	6 789±101	6 235±95	-0.015±0.008
0.25 - 0.50	8 309±107	7 123±101	7 653±106	7 145±100	0.020±0.007
0.50 - 0.75	12 211±128	9 821±117	10 842±124	10 310±120	0.018±0.006
0.75 - 1.00	17 146±150	13 533±135	14 537±142	14 560±139	0.023±0.005

Table 5.2: *The bias-canceled ratio R as defined in eq.* (5.7) *is constructed from the number of Λ^0 (n_{Λ^0} from table 5.1) in 4 bins of $\cos\theta'_{n'}$ for "Up" and "Down" spectrometer and positive and negative $\cos\theta'_{n'}$.*

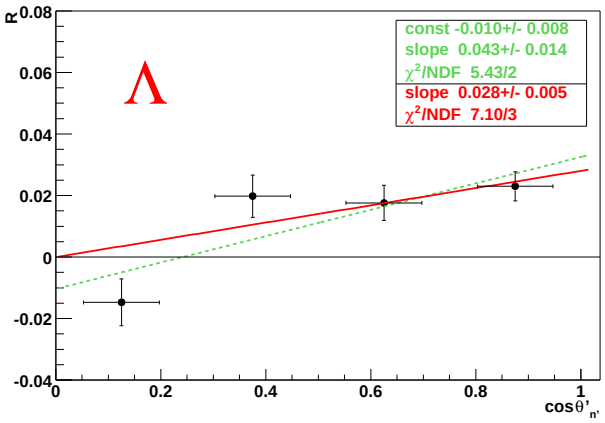

Figure 5.25: *Acceptance-corrected angular distribution R: according to* (5.8)*, R is linear in $\cos\theta'_{n'}$ with the slope $\propto P_n$. The points were therefore fitted with a straight line (red line and values). For systematic checks a 1^{st} order polynomial fit was done as well (green, dashed line and values).*

Chapter 6

Transverse Λ^0 Polarization

While in the previous chapter the selection criteria for Λ^0 were introduced and the method of extraction explained, in the following sections the results of the measurement of the polarization of Λ^0 and $\bar{\Lambda}^0$ are presented. They are accompanied by the respective data for the K^0 sample, on which the same method of extraction was performed. Being a spin 0 particle, the K^0 *cannot* be polarized. But since it is produced in a high number, the K^0 can be used to make an estimate of the systematic error of this analysis: any polarization extracted for the K^0 has to be treated as an artifact created by the analysis and included into the systematic error.

After the presentation of the values extracted from the full data sample in section 6.1, the dependence on the key parameters x_F and p_T is further investigated in section 6.2. In section 6.3 the results are interpreted and compared with other measurements.

6.1 Average Transverse Polarization of Λ^0, $\bar{\Lambda}^0$ and K^0

In a first step, the bias-canceled ratio $R(\cos\theta'_{n'})$ was extracted in four bins of $\cos\theta'_{n'}$ for the *full* samples of Λ^0, $\bar{\Lambda}^0$ and K^0 as explained in section 5.8.

The plots for the three V^0-channels are shown in fig. 6.1. R is always extracted from the angular distribution of the *positive* decay particle, i.e. p^+ for Λ^0 and π^+ for $\bar{\Lambda}^0$. In principle this would result in an inverted slope for the $\bar{\Lambda}^0$, but as the asymmetry parameter α for Λ^0 and $\bar{\Lambda}^0$ have opposite sign, this effect drops out again when going from ratio R to polarization P_n. While the polarization for $\bar{\Lambda}^0$ is compatible with zero, the Λ^0 values show a clear discrepancy from the horizontal line. A straight line fit $R = c_1 \cdot \cos\theta'_{n'}$ (red color in the figure) yields a slope of 0.028±0.005 and -0.009±0.007, corresponding to a polarization of 4.4±0.8 % and -1.4±1.1 % for Λ^0 and $\bar{\Lambda}^0$ respectively.

In addition to the straight line fit a 1$^{\text{st}}$ order polynomial $R = c_{11} \cdot \cos\theta'_{n'} + c_{10}$ was also fitted to the data to check for a systematic behavior. The fit was performed in several kinematical regions, and in most cases c_{10} was slightly negative, but within its error compatible with zero.

The K^0 sample in fig. 6.1c) shows a perfectly unpolarized distribution. With a value of -0.003±0.002, a systematic effect of the extraction method is small compared to the error emerging from the fit of the Λ^0 and $\bar{\Lambda}^0$ points.

Table 6.2 summarizes the values of the three V^0 samples and their polarizations.

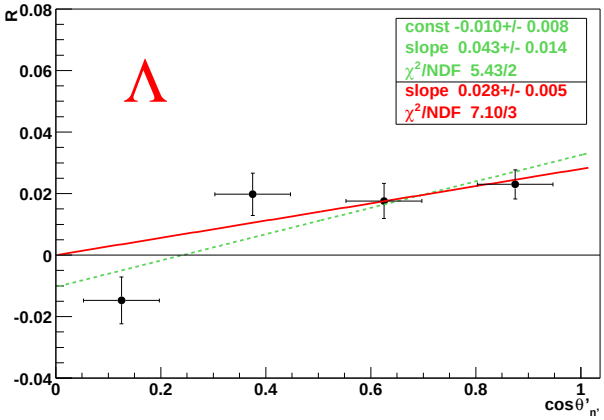

(a)

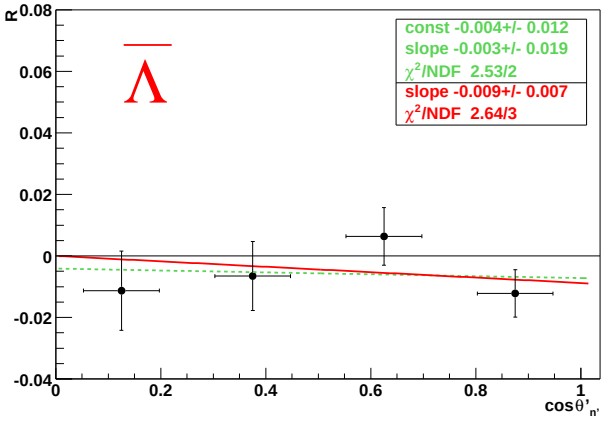

(b)

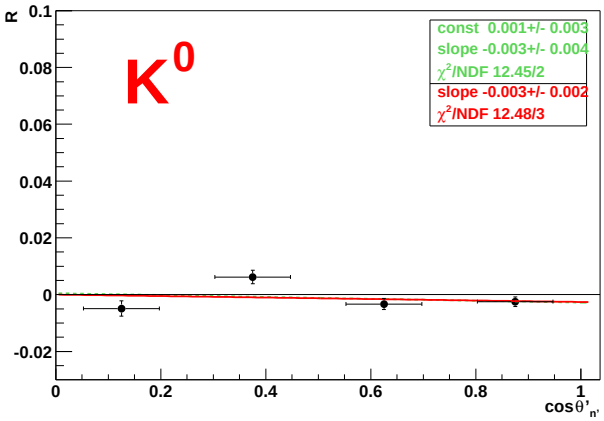

(c)

Figure 6.1: *Bias-canceled angular distributions R for* ***a)*** *Λ^0,* ***b)*** *$\bar{\Lambda}^0$ and* ***c)*** *K^0. According to* (5.8) *the slope of R is proportional to the polarization P.*

V^0	c_1	χ^2/NDF	c_{10}	c_{11}	χ^2/NDF
Λ^0	0.028±0.005	7.10/2	-0.010±0.008	0.043±0.014	5.43/1
$\bar{\Lambda}^0$	-0.009±0.007	2.64/2	-0.004±0.012	-0.003±0.019	2.53/1
K^0	-0.003±0.002	12.48/3	0.001±0.003	-0.003±0.004	12.45/2

Table 6.1: *Results of the straight line fit $R = c_1 \cdot \cos\theta'_{n'}$ and 1st order polynomial $R = c_{11} \cdot \cos\theta'_{n'} + c_{10}$ to the full samples of Λ^0, $\bar{\Lambda}^0$ and K^0.*

V^0	n_{V^0}	$< x_F >$	$< p_T >$ (GeV/c)	P_n (%)
Λ^0	155 173	$0.18^{+0.17}_{-0.16}$	$0.55^{+0.29}_{-0.30}$	4.4±0.8
$\bar{\Lambda}^0$	77 853	$0.19^{+0.16}_{-0.15}$	$0.55^{+0.29}_{-0.29}$	-1.4±1.1
K^0	1 038 706	$0.24^{+0.18}_{-0.16}$	$0.47^{+0.28}_{-0.28}$	-0.5±0.3

Table 6.2: *Polarization of Λ^0, $\bar{\Lambda}^0$ and K^0 as extracted from the full samples introduced in section 5.5 and plotted in fig. 6.1. The mean values for Feynman's x_F and the transverse momenta p_T of the samples are also included. For K^0 the same α as for Λ^0 was taken for proper comparison. (Errors are statistical errors only.)*

6.2 Dependence of $P_n^{V^0}$ on x_F and p_T

In section 1.2 it was explained that the polarization is expected to show a strong dependence on p_T and x_F. The polarization was therefore extracted for four different bins in one of these variables, without constraint on the other variable. The background-corrected p_T-x_F distribution for Λ^0 is given in fig. 6.2 and shows only a small correlation between x_F and p_T. The bin positions and widths were optimized for the Λ^0 sample to have roughly the same number of events per bin. They are indicated with the dashed white lines in fig. 6.2.

The extraction of the polarization for these subsamples was performed in analogy to the extraction for the full samples described in the previous section. The resulting polarizations are plotted in fig. 6.3 and listed in table 6.3 together with the corresponding numbers for the selections in p_T and x_F.

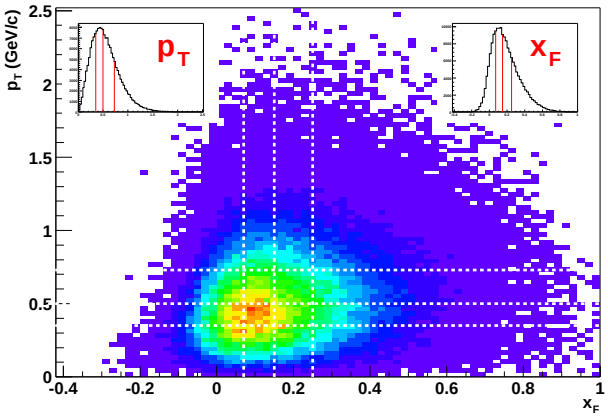

Figure 6.2: *Background-corrected distribution p_T versus x_F for Λ^0. The inserts show the projection on the respective axes. p_T and x_F are only weakly correlated. The dashed white lines indicate the binning applied for the polarization measurement. Mean values and widths for each bin are given in table 6.3.*

Polarization Correlations for x_F and p_T

An attempt was made to extract the polarizations in the previously introduced four bins in x_F and p_T, and at the same time to keep the other variable high or low. As large statistics were needed for this, it was only performed for Λ^0 and K^0 samples. The plots are shown in fig. 6.4 and fig. 6.5 for Λ^0 and K^0 respectively, the values for polarization and values for x_F and p_T are given in table 6.4 and table 6.5.

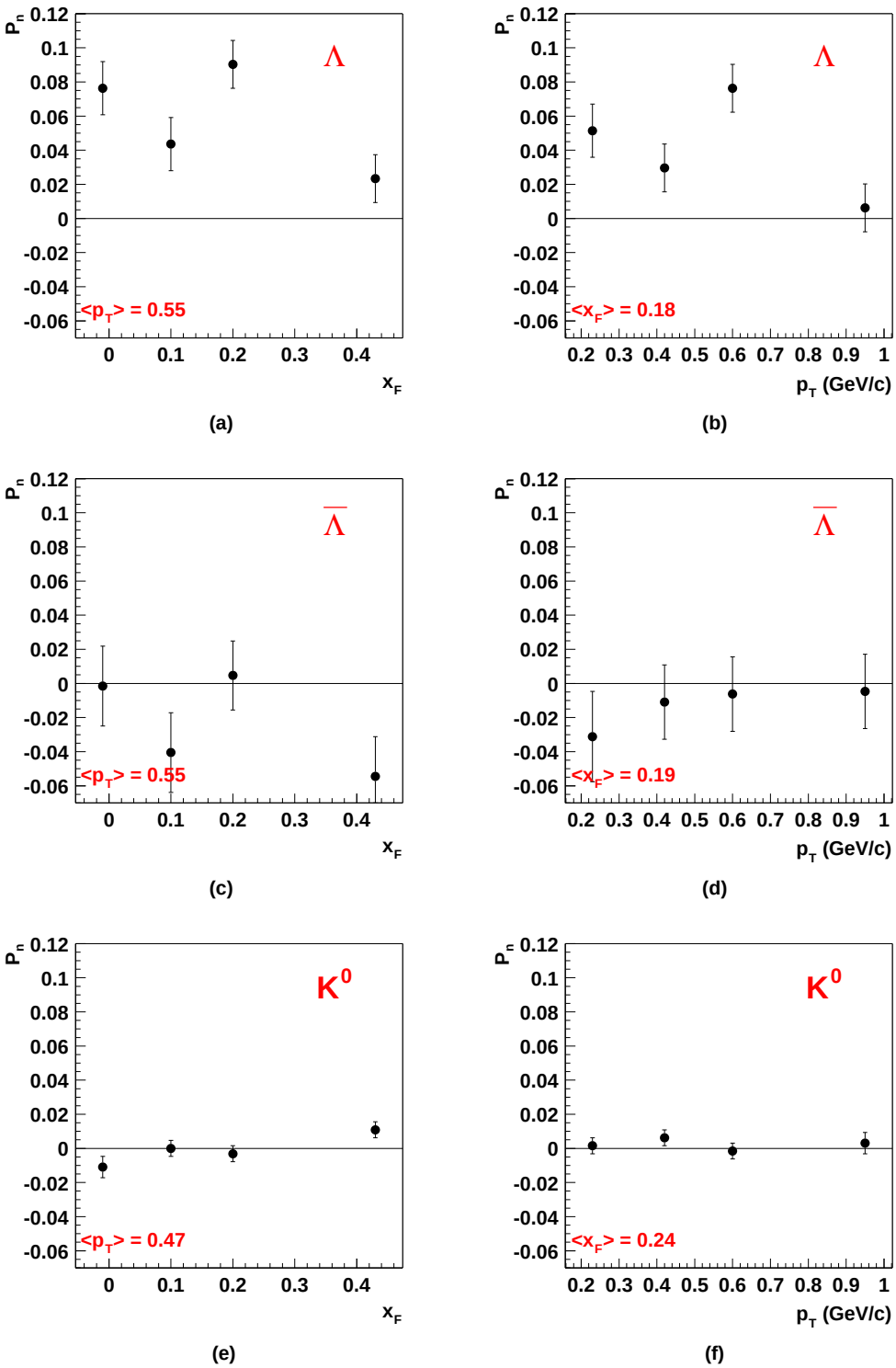

Figure 6.3: *Dependence of P_{V^0} on x_F and p_T for Λ^0, $\bar{\Lambda}^0$ and K^0. For K^0 the same asymmetry parameter α as for Λ^0 was assumed. The values are listed in table 6.3.*

V^0	x_F	$\overline{x}_F$	p_T (GeV/c)	$\overline{p}_T$ (GeV/c)	n_{V^0}	n_{V^0}/N_{V^0}	P_{V^0} (%)	χ^2/NDF
all Λ^0	-1.00 - 1.00	$0.18^{+0.17}_{-0.16}$	0.00 - 7.00	$0.55^{+0.29}_{-0.30}$	155 173	1.00	4.4±0.8	7.10/2
$P_{\Lambda^0}(x_F)$	-1.00 - 0.08	$0.00^{+0.05}_{-0.05}$	0.00 - 7.00	$0.49^{+0.26}_{-0.26}$	35 434	0.23	9.7±1.6	16.34/2
	0.08 - 0.16	$0.10^{+0.04}_{-0.04}$	0.00 - 7.00	$0.55^{+0.28}_{-0.29}$	34 904	0.22	4.0±1.6	5.58/2
	0.16 - 0.28	$0.20^{+0.06}_{-0.06}$	0.00 - 7.00	$0.57^{+0.30}_{-0.30}$	47 244	0.30	6.4±1.4	1.09/2
	0.28 - 1.00	$0.41^{+0.12}_{-0.11}$	0.00 - 7.00	$0.61^{+0.31}_{-0.31}$	37 590	0.24	3.1±1.4	6.17/2
$P_{\Lambda^0}(p_T)$	-1.00 - 1.00	$0.16^{+0.16}_{-0.15}$	0.00 - 0.33	$0.22^{+0.09}_{-0.10}$	36 000	0.23	5.3±1.6	8.39/2
	-1.00 - 1.00	$0.17^{+0.16}_{-0.16}$	0.33 - 0.51	$0.41^{+0.07}_{-0.07}$	34 476	0.22	1.1±1.4	1.39/2
	-1.00 - 1.00	$0.19^{+0.17}_{-0.16}$	0.51 - 0.72	$0.59^{+0.10}_{-0.09}$	46 323	0.30	7.9±1.4	2.59/2
	-1.00 - 1.00	$0.22^{+0.17}_{-0.17}$	0.72 - 7.00	$0.95^{+0.20}_{-0.20}$	38 373	0.25	1.1±1.4	7.30/2
all $\bar{\Lambda}^0$	-1.00 - 1.00	$0.19^{+0.16}_{-0.15}$	0.00 - 7.00	$0.55^{+0.29}_{-0.29}$	77 853	1.00	-1.4±1.1	2.64/2
$P_{\bar{\Lambda}^0}(x_F)$	-1.00 - 0.08	$0.01^{+0.05}_{-0.05}$	0.00 - 7.00	$0.50^{+0.26}_{-0.27}$	15 323	0.20	-4.4±2.3	1.23/2
	0.08 - 0.16	$0.10^{+0.04}_{-0.04}$	0.00 - 7.00	$0.53^{+0.28}_{-0.28}$	18 411	0.24	-1.9±2.3	8.64/2
	0.16 - 0.28	$0.20^{+0.06}_{-0.06}$	0.00 - 7.00	$0.56^{+0.29}_{-0.29}$	25 827	0.33	0.9±2.0	5.19/2
	0.28 - 1.00	$0.39^{+0.11}_{-0.10}$	0.00 - 7.00	$0.61^{+0.31}_{-0.31}$	18 291	0.23	-2.8±2.3	3.36/2
$P_{\bar{\Lambda}^0}(p_T)$	-1.00 - 1.00	$0.16^{+0.15}_{-0.14}$	0.00 - 0.33	$0.23^{+0.09}_{-0.10}$	17 827	0.23	-0.3±2.6	3.47/2
	-1.00 - 1.00	$0.18^{+0.15}_{-0.15}$	0.33 - 0.51	$0.41^{+0.07}_{-0.07}$	17 231	0.22	-1.9±2.2	6.58/2
	-1.00 - 1.00	$0.19^{+0.15}_{-0.15}$	0.51 - 0.72	$0.59^{+0.10}_{-0.09}$	23 796	0.31	-5.6±2.2	3.22/2
	-1.00 - 1.00	$0.21^{+0.17}_{-0.16}$	0.72 - 7.00	$0.95^{+0.20}_{-0.20}$	18 998	0.24	-2.3±2.2	4.30/2
all K^0	-1.00 - 1.00	$0.24^{+0.18}_{-0.16}$	0.00 - 7.00	$0.47^{+0.28}_{-0.28}$	1038 706	1.00	-0.5±0.3	12.48/3
$P_{K^0}(x_F)$	-1.00 - 0.08	$0.04^{+0.03}_{-0.03}$	0.00 - 7.00	$0.39^{+0.23}_{-0.24}$	89 356	0.09	-1.1±0.6	8.38/3
	0.08 - 0.16	$0.10^{+0.04}_{-0.04}$	0.00 - 7.00	$0.43^{+0.25}_{-0.25}$	250 529	0.24	0.0±0.5	8.89/3
	0.16 - 0.28	$0.20^{+0.06}_{-0.06}$	0.00 - 7.00	$0.48^{+0.27}_{-0.27}$	360 737	0.35	-0.3±0.5	5.61/3
	0.28 - 1.00	$0.43^{+0.13}_{-0.13}$	0.00 - 7.00	$0.53^{+0.30}_{-0.31}$	338 083	0.33	1.1±0.5	0.77/3
$P_{K^0}(p_T)$	-1.00 - 1.00	$0.21^{+0.17}_{-0.15}$	0.00 - 0.33	$0.21^{+0.10}_{-0.10}$	358 860	0.35	0.2±0.5	4.21/3
	-1.00 - 1.00	$0.22^{+0.16}_{-0.15}$	0.33 - 0.51	$0.40^{+0.07}_{-0.07}$	241 035	0.23	0.6±0.5	3.69/3
	-1.00 - 1.00	$0.25^{+0.17}_{-0.16}$	0.51 - 0.72	$0.59^{+0.10}_{-0.09}$	262 980	0.25	-0.2±0.5	2.42/3
	-1.00 - 1.00	$0.29^{+0.19}_{-0.18}$	0.72 - 7.00	$0.94^{+0.20}_{-0.20}$	175 831	0.17	0.3±0.6	3.48/3

Table 6.3: *Dependence of P_{V^0} for Λ^0, $\bar{\Lambda}^0$ and K^0 on x_F and p_T. Each group of four corresponds to one plot in fig. 6.3. Additionally the numbers for the full samples are given for comparison. Both the binning and the mean value of x_F and p_T are given.*

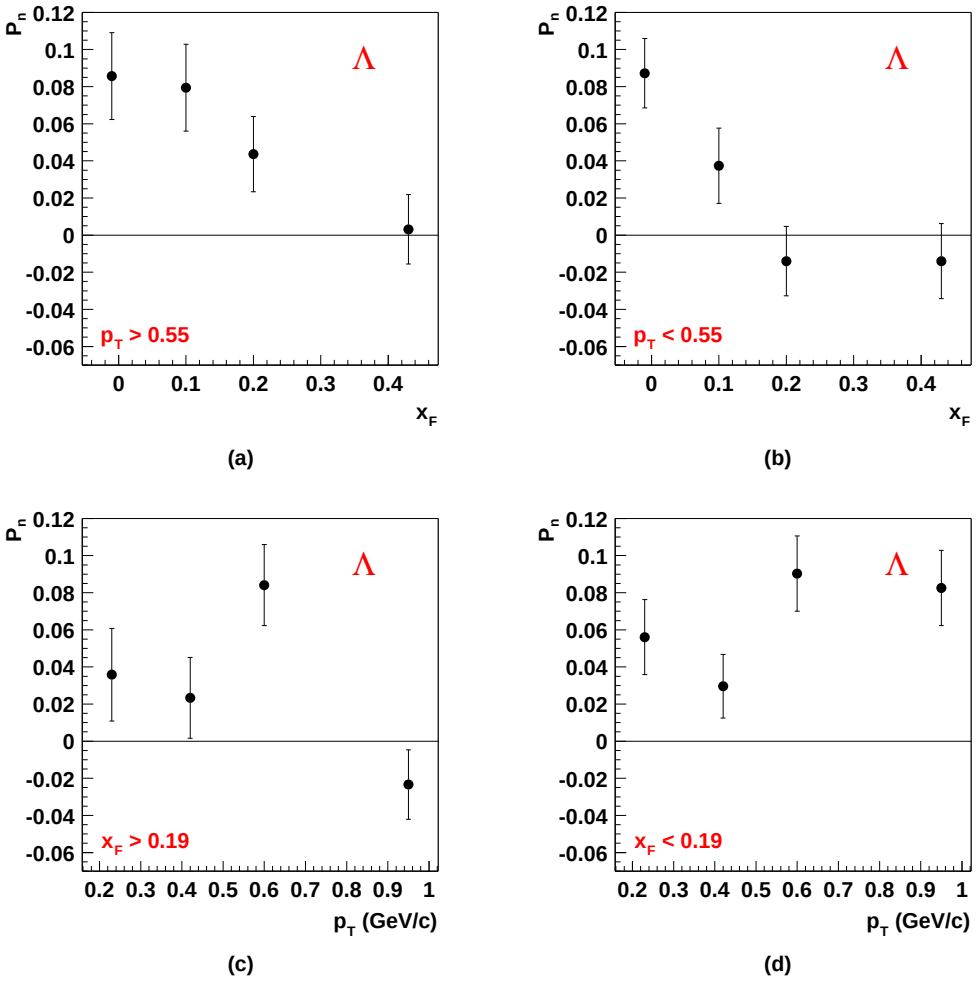

Figure 6.4: *Polarization for Λ^0 as function of x_F (top) and p_T (bottom). On the right side the other variable was chosen to be high, on the left side low. The values are given in table 6.4.*

V^0	x_F	$\overline{x}_F$	p_T (GeV/c)	$\overline{p}_T$ (GeV/c)	n_{V^0}	n_{V^0}/N_{V^0}	P_{V^0} (%)	χ^2/NDF
all Λ^0	-1.00 - 1.00	$0.18^{+0.17}_{-0.16}$	0.00 - 7.00	$0.55^{+0.29}_{-0.30}$	155173	1.00	4.4±0.8	7.10/2
$x_{F,\Lambda^0}, p_T > 0.55$	-1.00 - 0.08	$0.01^{+0.05}_{-0.05}$	0.55 - 7.00	$0.76^{+0.19}_{-0.19}$	12859	0.08	6.1±2.3	7.41/2
	0.08 - 0.16	$0.10^{+0.04}_{-0.04}$	0.55 - 7.00	$0.79^{+0.22}_{-0.22}$	15650	0.10	6.4±2.2	3.58/2
	0.16 - 0.28	$0.20^{+0.06}_{-0.06}$	0.55 - 7.00	$0.81^{+0.23}_{-0.23}$	22640	0.15	4.7±2.0	1.04/2
	0.28 - 1.00	$0.41^{+0.12}_{-0.12}$	0.55 - 7.00	$0.82^{+0.23}_{-0.24}$	20163	0.13	0.8±1.9	2.15/2
$x_{F,\Lambda^0}, p_T < 0.55$	-1.00 - 0.08	$-0.00^{+0.06}_{-0.06}$	0.00 - 0.55	$0.33^{+0.15}_{-0.16}$	22575	0.15	10.3±1.9	4.32/2
	0.08 - 0.16	$0.10^{+0.04}_{-0.04}$	0.00 - 0.55	$0.34^{+0.15}_{-0.15}$	19254	0.12	0.3±2.0	14.29/2
	0.16 - 0.28	$0.20^{+0.06}_{-0.06}$	0.00 - 0.55	$0.35^{+0.15}_{-0.15}$	24603	0.16	-1.2±1.9	2.86/2
	0.28 - 1.00	$0.40^{+0.11}_{-0.11}$	0.00 - 0.55	$0.35^{+0.15}_{-0.15}$	17427	0.11	-0.9±2.0	0.97/2
$p_{T,\Lambda^0}, x_F > 0.19$	0.19 - 1.00	$0.31^{+0.12}_{-0.12}$	0.00 - 0.33	$0.22^{+0.09}_{-0.10}$	13544	0.09	3.3±2.5	1.81/2
	0.19 - 1.00	$0.32^{+0.12}_{-0.12}$	0.33 - 0.51	$0.41^{+0.07}_{-0.07}$	14113	0.09	2.8±2.2	5.33/2
	0.19 - 1.00	$0.33^{+0.13}_{-0.12}$	0.51 - 0.72	$0.59^{+0.10}_{-0.09}$	21241	0.14	6.9±2.0	0.17/2
	0.19 - 1.00	$0.34^{+0.14}_{-0.13}$	0.72 - 7.00	$0.97^{+0.21}_{-0.21}$	20028	0.13	-2.5±1.9	0.59/2
$p_{T,\Lambda^0}, x_F < 0.19$	-1.00 - 0.19	$0.06^{+0.09}_{-0.09}$	0.00 - 0.33	$0.22^{+0.09}_{-0.10}$	22456	0.14	6.5±2.0	12.85/2
	-1.00 - 0.19	$0.07^{+0.09}_{-0.09}$	0.33 - 0.51	$0.41^{+0.07}_{-0.07}$	20363	0.13	2.3±1.7	1.07/2
	-1.00 - 0.19	$0.07^{+0.08}_{-0.08}$	0.51 - 0.72	$0.59^{+0.10}_{-0.09}$	25081	0.16	7.0±1.9	3.21/2
	-1.00 - 0.19	$0.09^{+0.08}_{-0.08}$	0.72 - 7.00	$0.94^{+0.20}_{-0.19}$	18345	0.12	7.2±2.0	11.22/2

Table 6.4: *Polarization of Λ^0, as function of x_F and p_T for two bins in the free variable p_T and x_F respectively. The plots can be found in fig. 6.4.*

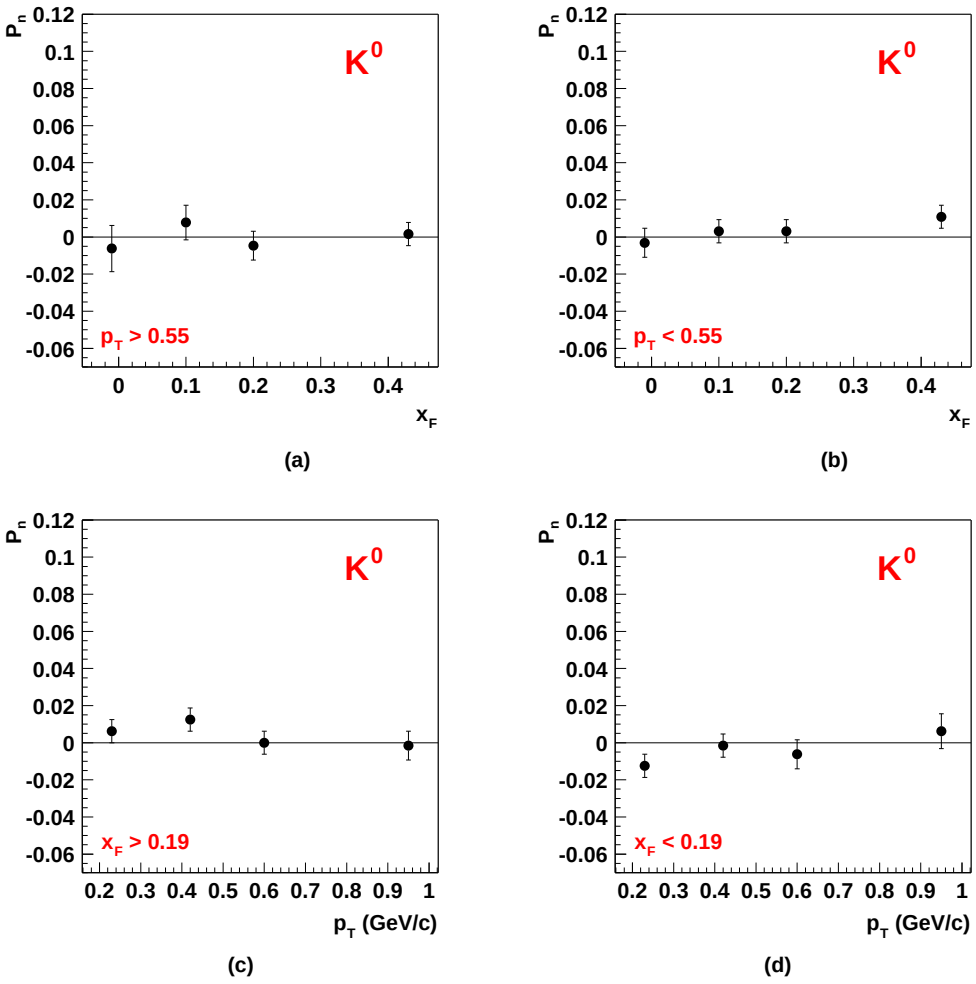

Figure 6.5: *Polarization of K^0 as function of x_F and p_T for two bins in the free variable p_T and x_F respectively. On the right side the other variable was chosen to be high, on the left side low. The values can be found in table 6.5.*

V^0	x_F	$\overline{x}_F$	p_T (GeV/c)	$\overline{p}_T$ (GeV/c)	n_{V^0}	n_{V^0}/N_{V^0}	P_{V^0} (%)	χ^2/NDF
all K^0	-1.00 - 1.00	$0.24^{+0.18}_{-0.16}$	0.00 - 7.00	$0.47^{+0.28}_{-0.28}$	1038706	1.00	-0.5±0.3	12.48/3
$x_{F,K^0}, p_T > 0.55$	-1.00 - 0.08	$0.04^{+0.03}_{-0.03}$	0.55 - 7.00	$0.74^{+0.19}_{-0.18}$	19097	0.02	-0.6±1.2	1.74/3
	0.08 - 0.16	$0.10^{+0.04}_{-0.04}$	0.55 - 7.00	$0.75^{+0.18}_{-0.18}$	67680	0.07	0.8±0.9	0.72/3
	0.16 - 0.28	$0.21^{+0.06}_{-0.06}$	0.55 - 7.00	$0.77^{+0.20}_{-0.20}$	123742	0.12	-0.5±0.8	5.82/3
	0.28 - 1.00	$0.44^{+0.15}_{-0.14}$	0.55 - 7.00	$0.81^{+0.23}_{-0.23}$	146086	0.14	0.2±0.6	2.66/3
$x_{F,K^0}, p_T < 0.55$	-1.00 - 0.08	$0.04^{+0.03}_{-0.03}$	0.00 - 0.55	$0.29^{+0.17}_{-0.16}$	70258	0.07	-0.3±0.8	5.66/3
	0.08 - 0.16	$0.10^{+0.04}_{-0.04}$	0.00 - 0.55	$0.31^{+0.16}_{-0.16}$	182849	0.18	0.3±0.6	8.51/3
	0.16 - 0.28	$0.20^{+0.06}_{-0.06}$	0.00 - 0.55	$0.32^{+0.16}_{-0.16}$	236995	0.23	0.3±0.6	4.87/3
	0.28 - 1.00	$0.42^{+0.12}_{-0.12}$	0.00 - 0.55	$0.32^{+0.17}_{-0.17}$	191997	0.18	1.1±0.6	1.44/3
$p_{T,K^0}, x_F > 0.19$	0.19 - 1.00	$0.34^{+0.15}_{-0.14}$	0.00 - 0.33	$0.21^{+0.10}_{-0.11}$	170875	0.16	0.6±0.6	3.14/3
	0.19 - 1.00	$0.33^{+0.14}_{-0.13}$	0.33 - 0.51	$0.40^{+0.07}_{-0.07}$	126829	0.12	1.2±0.6	3.30/3
	0.19 - 1.00	$0.35^{+0.15}_{-0.14}$	0.51 - 0.72	$0.59^{+0.10}_{-0.09}$	157380	0.15	0.0±0.6	5.81/3
	0.19 - 1.00	$0.37^{+0.17}_{-0.16}$	0.72 - 7.00	$0.95^{+0.20}_{-0.20}$	120736	0.12	-0.2±0.8	4.28/3
$p_{T,K^0}, x_F < 0.19$	-1.00 - 0.19	$0.10^{+0.06}_{-0.06}$	0.00 - 0.33	$0.21^{+0.10}_{-0.10}$	187984	0.18	-1.2±0.6	2.58/3
	-1.00 - 0.19	$0.10^{+0.06}_{-0.06}$	0.33 - 0.51	$0.40^{+0.07}_{-0.07}$	114205	0.11	-0.2±0.6	9.95/3
	-1.00 - 0.19	$0.11^{+0.06}_{-0.06}$	0.51 - 0.72	$0.58^{+0.10}_{-0.09}$	105600	0.10	-0.6±0.8	3.45/3
	-1.00 - 0.19	$0.11^{+0.06}_{-0.06}$	0.72 - 7.00	$0.92^{+0.18}_{-0.18}$	55094	0.05	0.6±0.9	1.15/3

Table 6.5: *Polarization of K^0 as function of x_F and p_T for two bins in the free variable p_T and x_F respectively. As asymmetry parameter α the same as for Λ^0 was taken. The plots can be found in fig. 6.5.*

6.3 Interpretation of the Results and Comparison with other Experiments

The results presented above are strongly affected by low statistics and limited systematic studies. Nevertheless within the errors some observations can be made. The negligible polarization values extracted for the unpolarized K^0 in all subsamples indicates that the analysis method used is basically functional. A systematic error on the Λ^0 polarization can be estimated from the false K^0 polarization to be of the order of $\Delta P_{n,\mathrm{sys}} = 0.5\%$ and has thus a similar size as the statistical one for the full Λ^0 sample.

- The data suggest that Λ^0 from quasi real photo production in general show a positive polarization of $P_n^{\Lambda^0} = +4.4 \pm 0.8(\mathrm{stat.}) \pm 0.5(\mathrm{sys.})\%$ at $< x_F >$=0.18 and $< p_T >= 0.55\,^{GeV}/_{\mathrm{c}}$ (fig. 6.1a)).
- The magnitude seems to be highest for $x_F \approx 0$ (see fig. 6.4a) and b)), where the influence of the target nucleons is strongest. P_n reaches values of around 10%. Fig. 6.4d) indicates that this value is independent of p_T in this region.
- In the current fragmentation region for large x_F, the polarization is very small or even compatible with zero, see fig. 6.3a).
- In general the dependence on p_T is weak, and in the observed range of 0 - 1 $^{\mathrm{GeV}}/_{\mathrm{c}}$ it is difficult to extract even a trend (see fig. 6.4c) and d)). If at all in fig. 6.3b) the polarization seems to get smaller with higher p_T.
- The total polarization of $\bar{\Lambda}^0$ is, within the error, compatible with zero $P_n^{\bar{\Lambda}^0} = -1.4 \pm 1.1(\mathrm{stat.}) \pm 0.5(\mathrm{sys.})\%$ for $< x_F >= 0.19$ and $< p_T >= 0.55\,^{GeV}/_{\mathrm{c}}$ (fig. 6.1b)). A scan in x_F and p_T does not show any further trends either (fig. 6.3c) and d)).

Comparison with Measurements from HERMES

The data can be compared with measurements from HERMES, the only other experiment performing such measurements in photo-production. Their plots where presented at several conferences (see e.g. the latest from A. Brüll [Bru03]), but not yet published. HERMES provides a similar environment with a charged lepton beam, namely positrons. With 27.5 GeV HERMES has a lower beam energy than COMPASS. This poses sometimes problems in the application of QCD or strong interaction models, as these are usually optimized for higher energies. The positrons are scattered off an internal gas target of various gases (e.g. hydrogen, deuterium, neon), which offers a larger acceptance in the target fragmentation region and allows for a scan on different targets. For the measurement of the transverse Λ^0 polarization the *inclusive* reaction $\gamma^\star N \to \Lambda^0 X$ is used, where the positrons are scattered at very small angles and cannot be observed by the HERMES spectrometer. The virtual photons are quasi-real with a $Q^2 \approx 0$.

Average Magnitudes. In [Bru03] Brüll gives a positive polarization for Λ^0 with a similar size of $P_n = +5.5 \pm 0.6(\mathrm{stat}) \pm 1.6(\mathrm{sys})\%$. The data differ in the case of $\bar{\Lambda}^0$, where HERMES states a similar size, but the opposite direction: $P_n^{\bar{\Lambda}} = -4.3 \pm 1.3(\mathrm{stat}) \pm 1.2(\mathrm{sys})\%$. The systematic error was estimated by the measurement of the false transverse polarization of K^0 and hadron-hadron pairs which did not originate from $\Lambda^0(\bar{\Lambda}^0)$ decay. This has to be compared with the measurement of the polarization of K^0 of about 0.5% in this work.

Target and Beam Fragmentation. As the scattered positron is not detected, no x_F and p_T can be calculated for the interactions. To estimate whether the hyperons were produced in the forward or the backward region in the CMS of $\gamma^* N$, the *light cone momentum fraction* of the beam positron carried by the outgoing hyperon $\zeta \equiv {}^{(E_{\Lambda^0}+p_{z,\Lambda^0})}/_{(E_B+p_B)}$ was taken. According to their Monte-Carlo studies, ζ has been found to be correlated with x_F. Particularly $\zeta \geq 0.25$ points to the forward hemisphere with $x_F > 0$. In accordance with the present analysis the polarization seems to be higher in the region around $x_F \approx 0$ with a similar value of approx. 10%. Fig. 6.6 shows the correlation of ζ and x_F and the polarization of Λ^0 and $\bar{\Lambda}^0$ versus ζ.

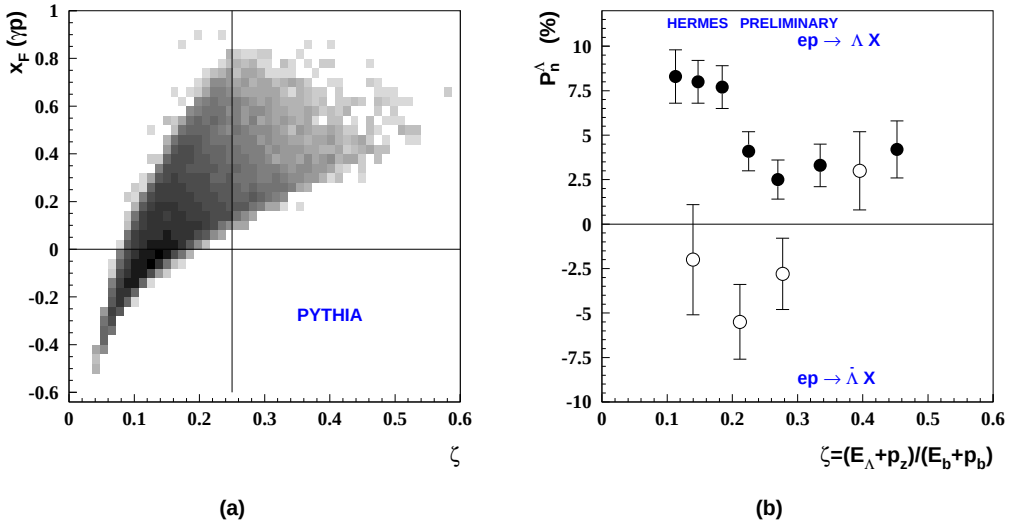

Figure 6.6: ***a)*** *Light cone momentum ζ as defined in the text and its correlation with x_F. For $\zeta > 0.25$ the interaction can be related to the beam fragmentation. Plot* ***b)*** *shows the polarization of Λ^0 and $\bar{\Lambda}^0$ as function of ζ. This plot should be compared with fig. 6.4a) and c). (from [Bru03])*

The negative polarization of $\bar{\Lambda}^0$ clearly originates from the target region. HERMES points out that while the polarization of Λ^0 and $\bar{\Lambda}^0$ are similar at high ζ, they are of opposite sign for low values of ζ. This can neither be confirmed nor disproved from this analysis.

Dependence on p_T. The transverse momentum of Λ^0 with respect to γ^* cannot be measured directly either by HERMES. Instead the transverse momentum of Λ^0 with respect to the beam positron was taken. Contrary to this analysis HERMES *does* see a dependence of the polarization on their p_T in fig. 6.7: in both target and beam fragmentation region polarization increases, while in this analysis the polarization in the target region is roughly independent of p_T and – if at all – decreases for larger $p_T$in the beam fragmentation region.

Comparison with Hadro-Production

As stated above, in the current fragmentation region, which has been studied for the first time in this analysis, the polarization seems to be very small. The target fragmentation region now can be compared to data taken with hadron beams. Data from meson beams (πp,$K^- p$) show positive polarization for negative x_F as well (fig. 6.8). For K^- beam additional kaons were required in the final state to ensure s-quark production. Note that the polarization rises again with p_T.

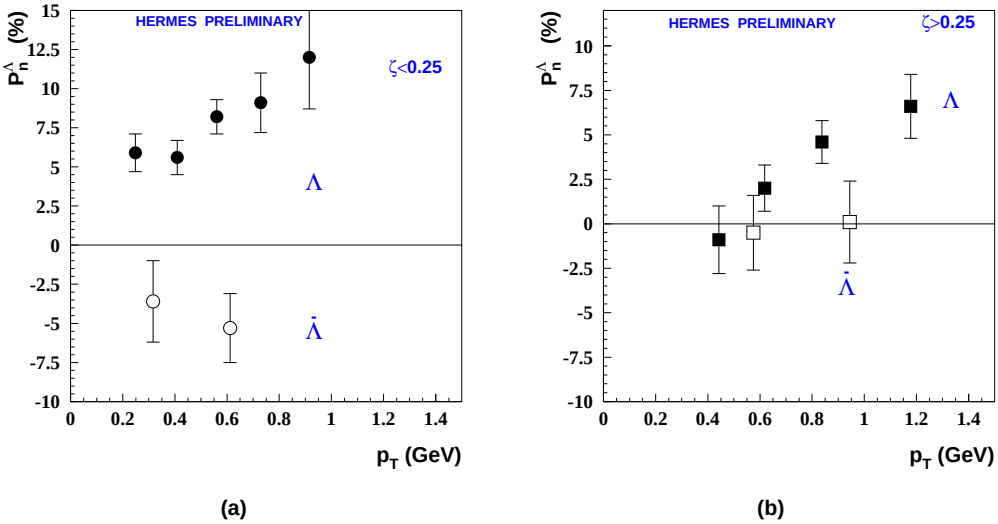

Figure 6.7: *Dependence of the polarization of Λ^0 and $\bar{\Lambda}^0$ on p_T for* ***a)*** *target and* ***b)*** *beam fragmentation region. Note that the p_T used by HERMES is not the same as the p_T used in this analysis, see text. (from [Bru03])*

Comparison with Model

With Anselmino et al. [ABDM01b, ABDM02] a first attempt was made to transfer a transverse Λ^0 polarization mechanism from pp interaction [ABDM01a] to semi-inclusive DIS. The authors see the origin of this polarization phenomenon solely in the *fragmentation* of quarks produced *unpolarized* in a reaction, as long as the final hyperon has a non-zero transverse momentum *with respect to the quark direction*, labeled $k_\perp$. The fragmentation is then described in a newly introduced *polarizing fragmentation function* (FF), which employs perturbative QCD and its factorization theorems *and in addition* polarization and intrinsic transverse momentum $k_\perp$ effects.

The parameters of the polarizing FF have to be extracted from measurements before they can be used for the prediction of other reactions. Based on their experience from pp interactions, the authors adapted the model from hadro-production to photo-production. They use the usual DIS variables $x = Q^2/2p\cdot q$, $y = p\cdot q/p\cdot l$ and $z_h = p\cdot p_h/p\cdot q$, where l, p, q and p_h are the 4-momenta of the initial lepton, the proton, the virtual boson and the observed hadron respectively. z_h is a variable coming close to the x_F used in this analysis. In fig. 6.9 the polarization is plotted as function of the longitudinal momentum fraction z_h and averaged over p_T for several production processes of different experiments. In the case of HERMES, which is closest to the case of COMPASS, a kinematic region of $0.023 < x < 0.4$, $y < 0.85$, $1 < Q^2 < 10\,GeV^2/c^2$ and $E_{\Lambda^0} > 4.5\,\text{GeV}$ was assumed. Unfortunately this does not fit to the region measured in both HERMES and COMPASS, where the production by quasi-real photons dominates the data sample. Nevertheless it is interesting to see that this model yields *negative* values for P_n. In small z_h, where the target fragmentation should dominate, the model predicts no polarization.

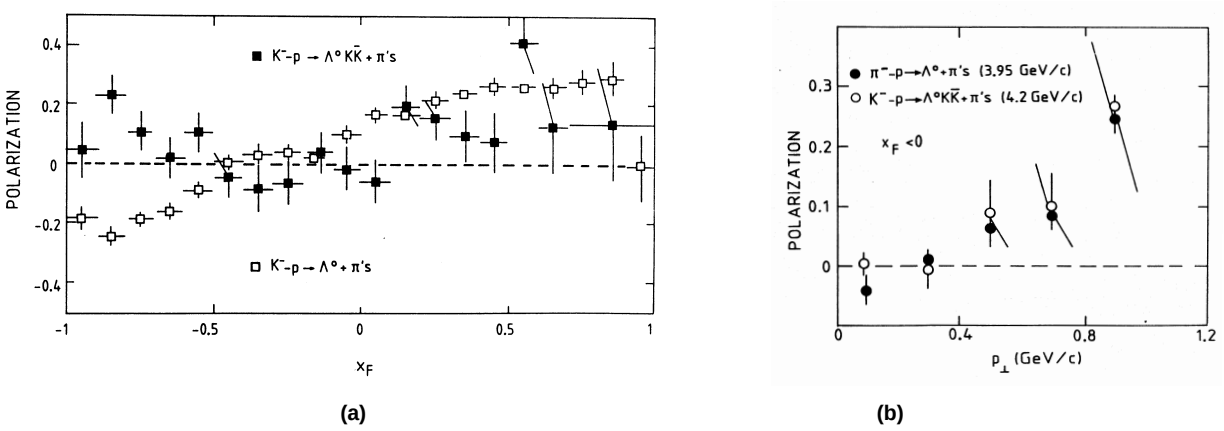

Figure 6.8: *Comparison of Λ^0 production in Kp and πp reactions. In both cases the polarization is positive in the target fragmentation region (if* s*-quark production is required).* ***a)*** *shows the x_F dependence of Kp,* ***b)*** *shows the p_T dependence of both Kp and πp for negative x_F. (from [Pau04])*

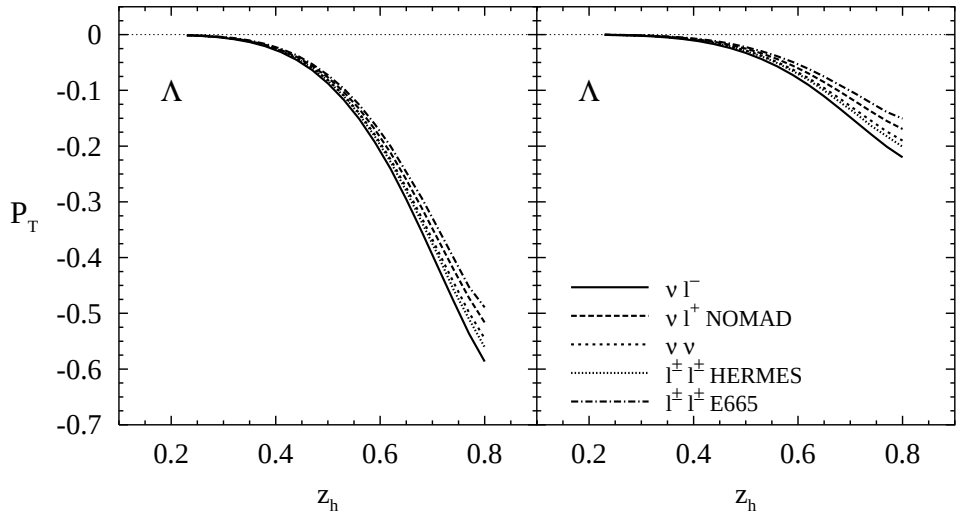

Figure 6.9: *Λ^0 polarization in SIDIS calculated via polarizing FFs. The left and right plot differ in the assumptions on the weights from* u*,* d *against* s*-quarks in the polarizing FFs. (from [ABDM02])*

Summary and Outlook

This work was done in the framework of COMPASS, a fixed-target experiment at the CERN/SPS.

In the first part the design and the performance of the silicon microstrip detector system developed for COMPASS was presented. The detectors take part in the definition of the beam upstream of the target. A system of two stations, providing 8 projections, was installed for the beam time 2002 and successfully operated at room temperature.

High beam intensities as in COMPASS can induce radiation damage in silicon detectors. To avoid a major degradation of the performance the silicon detector was designed from the beginning for an operation at a temperature of 130 K to deploy the Lazarus effect.

Despite the technically very challenging double-sided readout scheme, the data taken in the 2002 beam-time show that the detector delivers clear signals at a very low noise level. The good signal-to-noise ratio of around 18 can certainly be related to the specially developed readout electronics and the consequent floating powering scheme.

The detector proved to be well suited to resolve the huge particle fluxes both in space and time. The time resolution is important in a fixed-target experiment, as no time-structure of the beam can be used to correlate an external trigger to the correct signal. The time resolution has been improved by comparing the analogue information sampled in three consecutive 25 ns intervals. Values of the order of 3 ns or better could be achieved. Efficiency measurements yielded values of around 99%.

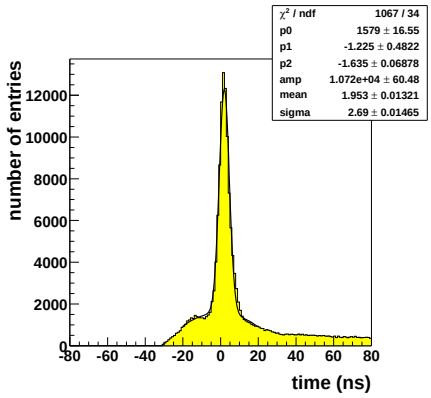

The time resolution extracted from the analogue signals of the silicon is of the order of 3 ns. Here the difference between trigger time and "silicon" time is shown.

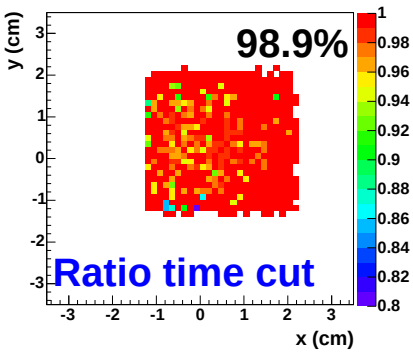

The tracking efficiency of the silicon detectors are of the order of 99%. Here the percentage of tracks is shown, which where found by the SciFi detectors.

In 2003 one detector was at times operated at cryogenic temperatures. The performance below 145 K was investigated in [Fuc03] and found to be promising. For 2004 it is planned to further develop the cryogenic infrastructure and to operate one detector at low temperatures for the whole run.

In the second part of this work the transverse polarization of Λ^0-hyperons was investigated. While much data have been collected on this phenomenon in hadro-production, the measurement in COMPASS provides the first data from photo-production of Λ^0 with quasi-real photons.

The data show a transverse polarization of $P_n^{\Lambda^0} = +4.4 \pm 0.8(\text{stat.}) \pm 0.5(\text{sys.})\%$ at $< x_F >$=0.18 and $< p_T >= 0.55^{GeV/c}$, which even increases up to $\sim 8\,\%$ at $x_F \sim 0$. While the sign and absolute magnitude is similar to a preliminary measurement by HERMES, the p_T dependence measured by HERMES cannot be confirmed by the current analysis.

A comparison with data from meson-production of Λ^0 with π and K beams indicates a similar behavior in the target fragmentation region at $x_F \approx 0$. In both cases the polarization is positive and of the same order of magnitude.

In accordance with the hadron data the polarization of $\bar{\Lambda}^0$ is compatible with zero in basically all kinematical regions. For the total sample a value of $P_n^{\bar{\Lambda}^0} = -1.4 \pm 1.1(\text{stat.}) \pm 0.5(\text{sys.})\%$ at $< x_F >= 0.19$ and $< p_T >= 0.55$ was found.

For an estimate of the systematic uncertainties the transverse polarization of K^0 was determined. In all kinematical regions, the result was compatible with zero; for the total sample a value of $P_n^{K^0} = -0.5 \pm 0.3(\text{stat.})\%$ was extracted.

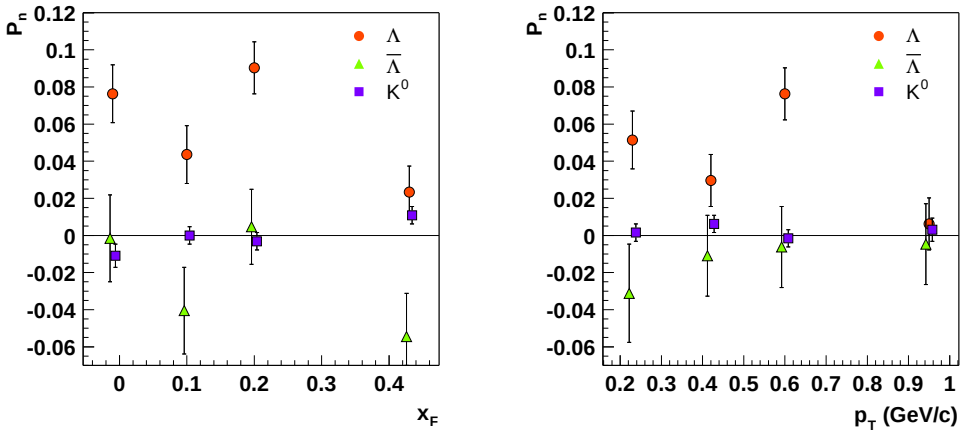

Transverse Polarization for Λ^0, $\bar{\Lambda}^0$ and K^0 for different bins in x_F (left) and p_T(right). While both $\bar{\Lambda}^0$ and K^0 are compatible with zero, Λ^0 shows a positive polarization of few percent.

This analysis gives a first insight into this very exciting topic of spontaneous transverse polarization in photo-production at COMPASS. Clearly, more work is needed to put the results on a more solid basis. While this work was writing further data from COMPASS became available and can now be included into this analysis. The systematic studies have to be intensified. Especially a thorough check with Monte-Carlo simulation is needed. Additional tests include the measurement of the sideways polarization, which should be compatible with zero, and a closer look into the acceptance correction.

With a continuously increasing data volume it will become interesting to look at exclusive channels, and to extend the analysis to deep inelastic scattering, for which a new trigger has recently been installed.

List of Figures

List of Tables

Bibliography

[ABDM01a] M. Anselmino, D. Boer, U. D'Alesio, and F. Murgia. Lambda polarization from unpolarized quark fragmentation. *Phys. Rev.* **D63**, 054029 (2001).

[ABDM01b] M. Anselmino, D. Boer, U. D'Alesio, and F. Murgia. Transverse Λ polarization in unpolarized semi-inclusive DIS. In *IX International Workshop on Deep Inelastic Scattering (DIS2001)*. Bologna, Apr 2001.

[ABDM02] M. Anselmino, D. Boer, U. D'Alesio, and F. Murgia. Transverse Λ polarization in semi-inclusive DIS. *Phys. Rev.* **D65**, 114014 (2002).

[Abr01] Victor V. Abramov. Universal scaling behaviour of the transverse polarization for inclusively produced hyperons in hadron hadron collisions. *hep-ph/0111128* (2001).

[Abt98] I. Abt et al. Gluing silicon with silicone. *Nucl. Instrum. Meth.* **A411**, 191–196 (1998).

[Abt99] I. Abt et al. Double sided microstrip detectors for the high radiation environment in the HERA-B experiment. *MPI-PhE* **99-05** (1999).

[AGIS83] B. Andersson, G. Gustafson, G. Ingelman, and T. Sjostrand. Parton fragmentation and string dynamics. *Phys. Rept.* **97**, 31 (1983).

[Ale00] A. N. Aleev et al. A measurement of the transverse polarization of Λ hyperons produced in nC reactions in the EXCHARM experiment. *Eur. Phys. J.* **C13**, 427–432 (2000).

[Ang03] H. Angerer et al. Present status of silicon detectors in COMPASS. *Nucl. Instrum. Meth.* **A512**, 229–238 (2003).

[Ans02] M. Anselmino. Transversity and Λ polarization. In *Workshop on Future Physics @ COMPASS*, Sep 2002.

[Ans03] M. Anselmino. Λ polarization in pp and lp inclusive processes. In *Seminar at the Physics Department of the TU Munich*. TU Munich, 2 Jun 2003.

[Ant83] Yu. M. Antipov et al. Measurement of π-meson polarizability in π compton effect. *Phys. Lett.* **B121**, 445 (1983).

[Ant85] Yu. M. Antipov et al. Experimental evaluation of the sum of the electric and magnetic polarizabilities of pions. *Z. Phys.* **C26**, 495 (1985).

[APV99] L. L. Jones et al. The APV25 deep submicron readout chip for CMS detectors. *CERN* **99-09** (1999).

[APV00] L. L. Jones. APV25-S0 User Guide version 2.1, `http://www.te.rl.ac.uk/med/`.

[Ber9797] R. W. Bernstein and T. Westgaard. Technical and test specifications for MPI HERA-B doublesided silicon. Technical report, SINTEF Electronics & Cybernetics, 1997.

[BPR92] R. Barni, G. Preparata, and P. G. Ratcliffe. A Simple explanation of hyperon polarization at high p(T). *Phys. Lett.* **B296**, 251–255 (1992).

[BR97] R. Brun and F. Rademakers. ROOT: An object oriented data analysis framework. *Nucl. Instrum. Meth.* **A389**, 81 (1997).

[Bra98] A. Bravar. Experimental overview of spin effects in hadronic interactions at high energies. In *13th International Symposium on High-Energy Spin Physics (SPIN 98)*. Protvino, Russia, Sep 1998.

[Bru03] A. Brull. Transverse polarisation of Λ and $\bar{\Lambda}$ hyperons in quasi-real photon nucleon scattering. *AIP Conf. Proc.* **675**, 548–552 (2003).

[Bun76] G. Bunce et al. Λ^0 hyperon polarization in inclusive production by 300 GeV protons on beryllium. *Phys. Rev. Lett.* **36**, 1113–1116 (1976).

[Bur96] Urs Burgi. Charged Pion Polarizabilities to two Loops. *Phys. Lett.* **B377**, 147–152 (1996).

[BvHK98] A. Bravar, D. v. Harrach, and A. Kotzinian. Large gluon polarization from correlated high-p(T) hadron pairs in polarized electro-production. *Phys. Lett.* **B421**, 349–359 (1998).

[CAEN] C.A.E.N Costruzioni Apparecchiature Elettroniche Nucleari. A525 - SY527, `http://www.caen.it`.

[CASTOR] CASTOR: The CERN Advanced STORage Manager, `http://castor.web.cern.ch/castor/`.

[CB98] The Crystal Barrel Collaboration. The Dalitz plot for $p\bar{p}$ at rest goes to three π^0, `http://www.phys.cmu.edu/cb/pi03.html`.

[CIBA] Ciba-Geigy. *Araldite AW 106 / HV953U*. also known as Araldite 2011.

[CO96] The COMPASS Collaboration. A proposal for a Common Muon and Proton Apparatus for Structure and Spectroscopy. *CERN* **SPSLC 96-14** (1996).

[Col02] M. L. Colantoni. *Performance of COMPASS spectrometer for the muon and hadron physics*. PhD Thesis, Università degli Studi di Torino, 2002.

[COMPASS] The COMPASS Collaboration. `http://wwwcompass.cern.ch`.

[D$^+$91] J. Duryea et al. Polarization of Ξ- hyperons produced by 800 GeV protons. *Phys. Rev. Lett.* **67**, 1193–1196 (1991).

[DATE00] CERN ALICE DAQ Group. ALICE DATE User's Guide. *ALICE-INT-2000-31 v.2* (2000).

[Deu] Deutronic Electronic GmbH. *DN35W-5*. Deutronicstraße 5, 84166 Adlkofen, Germany. `http://www.deutronic.com`.

[DM72] M. G. Doncel and A. Mendez. Spin rotation parameters for inclusive reactions. *Phys. Lett.* **B41**, 83–86 (1972).

[DMM85] T. A. Degrand, J. Markkanen, and H. I. Miettinen. Hyperon polarization asymmetry: polarized beams and Ω-production. *Phys. Rev.* **D32**, 2445–2448 (1985).

[EMC89] J. Ashman et al. An investigation of the spin structure of the proton in deep inelastic scattering of polarized muons on polarized protons. *Nucl. Phys.* **B328**, 1 (1989).

[EPOXY] EPOXY Produkte GmbH + Co. Vertr. KG. *Silber-Leitkleber 3025*. Postfach 1207, 64658 Fürth/Odw., Germany.

[Fel96] J. Felix et al. Study of Λ^0 polarization in $pp \rightarrow p\Lambda^0 K^+\pi^+\pi^-\pi^+\pi^-$ at 27.5 GeV. *Phys. Rev. Lett.* **76**, 22–25 (1996).

[Fel97] J. Felix. On experimental studies of Λ^0 polarization. *Mod. Phys. Lett.* **A12**, 363–370 (1997).

[Fel99] J. Felix. On theoretical studies of Λ^0 polarization. *Mod. Phys. Lett.* **A14**, 827–842 (1999).

[Fel03] J. Felix et al. Resonances and Λ^0 polarization in 800 GeV/c $pp \rightarrow p_{\text{diffracted}}\Lambda^0 K^+$. *Nucl. Phys.* **A721**, 805–808 (2003).

[Fri04] J. M. Friedrich et al. Publication in preparation, 2004.

[Fuc03] A. Fuchs. *Setup of low Temperature Silicon Detector for the COMPASS Experiment*. Diploma Thesis, Technische Universität München, December 2003.

[Ger] S. Gerassimov. PHAST: PHysics Analysis Software Tool, `http://ges.home.cern.ch/ges/phast/`. especially the link *PHAST for beginners*.

[GIM70] S. L. Glashow, J. Iliopoulos, and L. Maiani. Weak interactions with lepton - hadron symmetry. *Phys. Rev.* **D2**, 1285–1292 (1970).

[Gru01] B. Grube. *The trigger control system and the common GEM and Silicon readout for the COMPASS experiment*. Diploma Thesis, Technische Universität München, December 2001.

[Grü02] A. Grünemaier. *Eine universelle Ausleseschnittstelle für das COMPASS-Experiment*. PhD Thesis, Universität Freiburg, 2002.

[Hermes99] K. Ackerstaff et al. Flavor decomposition of the polarized quark distributions in the nucleon from inclusive and semi-inclusive deep- inelastic scattering. *Phys. Lett.* **B464**, 123–134 (1999).

[Hermes00] A. Airapetian et al. Measurement of the spin asymmetry in the photoproduction of pairs of high p(T) hadrons at HERMES. *Phys. Rev. Lett.* **84**, 2584–2588 (2000).

[ILFA] ILFA Feinstleitertechnik GmbH. *6M 10 FR4 I20 K35*. Lohweg 3, 30559 Hannover, Deutschland. `http://www.ilfa.de/multilayer_bautypen/mlbt_6m10fr4i20k35.pdf`.

[iseg] iseg Spezialelektronik GmbH. *EHQ 8006p_605-F*. Bautzner Landstraße 23, 01454 Radeberg, Germany. `http://www.iseg-hv.de/`.

[Ji97] Xiang-Dong Ji. Deeply-virtual Compton scattering. *Phys. Rev.* **D55**, 7114–7125 (1997).

[Kem80] J. Kemmer. Fabrication of low noise Silicon radiation detectors by the planar process. *Nucl. Instr. and Meth. in Phys. Res.* **169**, 499 (1980).

[Ket03] B. Ketzer, `Bernhard.Ketzer@ph.tum.de`. Private communication, 2003.

[Kon02] I. Konorov et al. The Trigger Control System for the COMPASS Experiment. In *IEEE Nuclear Science Symposium (2001)*, San Diego, 2002.

[Kuh01] R. Kuhn. *Simulations for the Measurement of the Polarizabilities of the Pion at COMPASS*. Diploma Thesis, Technische Universität München, November 2001.

[Leb02] M. Leberig. *Das COMPASS–Triggersystem zur Messung des Gluonbeitrags ΔG zum Protonspin*. PhD Thesis, Universität Mainz, 2002.

[Leb03] M. Leberig, `Mario.Leberig@cern.ch`. Private communication, 2003.

[Leo94] W. R. Leo. *Techniques for Nuclear and Particle Physics Experiments*. Springer, 2nd revised edition, 1994.

[Les75] A. Lesnik et al. Observation of a difference between polarization and analyzing power in Λ^0 production with 6 GeV/c polarized protons. *Phys. Rev. Lett.* **35**, 770 (1975).

[LXL01] Ch. Liu, Q. Xu, and Z. Liang. Hyperon polarization in semi-inclusive deeply inelastic lepton nucleon scattering at high energy. *Phys. Rev.* **D64**, 073004 (2001).

[Mar03] C. Marchand. Email to coral-weekly@listbox4.cern.ch, Subj: Re: time profile (fwd). 14 Mar 2003.

[MIP] MIPOT. Via Corona, 5 (zon ind.), 34071 Cormons, Italy. `http://www.mipot.com`.

[Mol99] M. Moll. *Radiation Damage in Silicon Particle Detectors - microscopic defects and macroscopic properties*. PhD Thesis, Universität Hamburg, 1999.

[MvH02] M. Frhr. v. Hodenberg. *A First Reconstruction of COMPASS Data*. Diploma Thesis, Universität Freiburg, 2002.

[NA50] `http://na50.web.cern.ch/na50/`.

[NEE] Dr. Neumann Peltier Technik. *NEE-001-weiß*. Am Mossgraben 25, 86919 Utting/Ammersee, Germany.

[OK73] G. Ohlsen and P. W. Keaton. Techniques for measurement of spin-$\frac{1}{2}$ and spin-1 polarization analyzing tensors. *Nucl. Inst. and Meth.* **109**, 41 (1973).

[Pau04] S. Paul. Polarization of strange and charmed hadrons. Publication in preparation, 2004.

[PDG00] D. E. Groom et al. Review of particle physics. *Eur. Phys. J.* **C15**, 1–878 (2000).

[Pei92] A. Peisert. Silicon microstrip detectors. *Adv. Ser. Direct. High Energy Phys.* **9**, 1–79 (1992).

[PRSZ94] B. Povh, K. Rith, C. Scholz, and F. Zetsche. *Teilchen und Kerne*. Springer, Berlin, 2. Auflage, 1994.

[PT] COMPASS Polarized Target, `http://wwwcompass.cern.ch/compass/detector/target/PT.html`.

[RD3998] V. Palmieri et al. Evidence for charge collection efficiency recovery in heavily irradiated Silicon detectors operated at cryogenic temperatures. *Nucl. Instr. and Meth. in Phys. Res.* **A 413**, 475–478 (1998).

[RD3900a] K. Borer et al. Charge collection efficiency and resolution of an irradiated double sided silicon microstrip detector operated at cryogenic temperatures. *Nucl. Instrum. Meth.* **A440**, 17–37 (2000).

[RD3900b] K. Borer et al. Charge collection efficiency of irradiated silicon detectors operated at cryogenic temperatures. *Nucl. Instrum. Meth.* **A440**, 5–16 (2000).

[RD3902] K. Borer et al. RD39 Status Report 2002. *CERN/LHCC* **2002-004** (2002). `http://rd39.web.cern.ch/RD39`.

[RDM04] R. De Masi. *COMPASS Silicon Detectors*. PhD Thesis in preparation, Technische Universität München, 2004.

[Ric02] J. Richard. Double charm physics. In *Workshop on Future Physics @ COMPASS*, Sep 2002.

[ROOT] R. Brun, F. Rademakers, et al. `http://root.cern.ch/`.

[ROSE97] A. Vasilescu. The NIEL scaling hypothesis applied to neutron spectra of irradiation facilities in the ATLAS and CMS SCT, `http://cern.ch/rd48`. ROSE/TN/97-2.

[ROSE00a] G. Lindstrom et al. Developments for radiation hard silicon detectors by defect engineering - Results by the CERN RD48 (ROSE) Collaboration. *Nucl. Instrum. Meth.* **A465**, 60–69 (2000).

[ROSE00b] A. Vasilescu and G. Lindstroem. Notes on the fluence normalisation based on the NIEL scaling hypothesis, `http://cern.ch/rd48`. ROSE/TN/2000-02.

[ROSE01] G. Lindstrom et al. Radiation hard silicon detectors developments by the RD48 (ROSE) Collaboration. *Nucl. Instrum. Meth.* **A466**, 308–326 (2001).

[Sch02] T. Schmidt. *A Common Readout Driver for the COMPASS Experiment*. PhD Thesis, Universität Freiburg, 2002.

[Sch03] L. Schmitt et al. The DAQ of the COMPASS Experiment. In *13th IEEE Real Time Conference 2003*, Montreal, May 2003.

[Selex02] M. Mattson et al. First observation of the doubly charmed baryon Ξ_{cc}^{+}. *Phys. Rev. Lett.* **89**, 112001 (2002).

[Sie03] H. W. Siebert, `Hans-Wolfgang.Siebert@cern.ch`. Private communication, 2003.

[Sof99] J. Soffer. Is the riddle of the hyperon polarizations solved? In *Batavia 1999, Hyperon physics (Hyperon99)*, pages 121–126, Sep 1999.

[ST92] Jacques Soffer and Nils A. Tornqvist. Origin of the polarization for inclusive Λ production in pp collisions. *Phys. Rev. Lett.* **68**, 907–910 (1992).

[Stesalit] Stesalit AG. Fabrikweg 54, 4234 Zullwil, Switzerland.

[Tak02] N. Takabayashi. *Polarized target for the measurement of the gluon contribution of the nucleon spin in the COMPASS experiment*. PhD Thesis, Nagoya University, 2002.

[Totem] Totem: Total Cross Section, Elastic Scattering and Diffraction Dissociation at the LHC, `http://totem.web.cern.ch/Totem`.

[Tsa74] Y. Tsai. Pair production and bremsstrahlung of charged leptons. *Rev. Mod. Phys.* **46**, 815 (1974).

[Wag01] R. Wagner. *Commissioning of Silicon Detectors for the COMPASS Experiment at CERN*. Diploma Thesis, Technische Universität München, 2001.

[Wie98] M. Wiesmann. *Messungen an einem Siliziumdetektor für das HERMES–Experiment*. Diploma Thesis, Universität Erlangen-Nürnberg, 1998.

Acknowledgments

In the first place I would like to thank Prof. Stephan Paul for the very interesting work I was involved in, for his confidence in my doings and his continuous support, especially for his commitment and the friendly atmosphere.

I would like to thank my three tutors, who guided me along my work in the last years. I. Konorov I would like to thank for the invaluable advice in debugging everything. Additional thanks for teaching me to laugh in good and in hard times. For the continuous help in the Λ^0-analysis I would like to thank J. Friedrich. Extra thanks for showing me the fun in physics. L. Schmitt deserves thanks for helping "in the background", for answering silly questions on general physics topics and sometimes just for listening.

A big hug to the silicon group. Despite being a small group, it was always a very active group and full of motivation. Thanks to R. De Masi and R. Wagner for the fruitful and harmonic cooperation, but also to A. Esposito, A.-M. Fuchs, M. Becker. He was only a "secret" member of the silicon group: B. Ketzer. Thanks for all the support at CERN and with software business. Thanks also to A. Lounkov for his help to the "grosses bavarisches Wissenschaftler".

A deep thanks to the remaining COMPASS group in München for their continuous help in so many things and making the work enjoyable: H. Angerer, B Grube, R Kuhn and Q. Weitzel. And finally the many people from the institute in München for the very nice atmosphere and the cooperation across the different physics topics, among them Frau Frank and Herr Hartmann and of course D. Tortorella for being a likeable office-mate.

Thanks to the numerous colleagues from the COMPASS group at CERN, from which I will only shortly mention S. Gerassimov and G. Mallot. It was an exciting adventure to see this experiment coming to life!

I got help from many technical students, thanks to all of them.

Mein herzlicher Dank geht natürlich auch an die Werkstätten des Physik Departments, die für den experimentellen Teil unverzichtbar waren und hervorragende Arbeit geleistet haben. Allen voran Martin Aigner, der mir mit viel Geduld beigebracht hat, welche Anforderungen der Physik auch in die Realität umsetzbar sind. Aber natürlich auch die anderen der "Putzer Werkstatt" waren stets aufmerksam und halfen aus, wenn gerade mal wieder nichts mehr ging. Die Zentalwerkstatt muss hier noch erwähnt werden, wo nie das Gefühl aufkam, dass irgendetwas "unmöglich" ist und zu Zeiten sogar die "Kuh flog". Stellvertretend für die vielen hilfreichen Hände geht hier der Dank and die Herren Pfaller und Reiter. Auch an die Elektronikwerkstatt ergeht herzlicher Dank, hier wieder nur stellvertretend an Herrn Franz.

Own Contributions

The dominant part of my time for this thesis was spent on the design, development, construction and installation of the silicon detectors. Within a small group of around 3 people, I was basically involved in every part of the work on the detector. My main responsibility was the preparation of all mechanical parts of the detector, which included the design, choice and allocation of material, contact to the work-shop, assembly and installation of the optical bench, cryostat and modules.
At the assembly of the silicon modules my responsibility was the gluing of silicon wafers.
Furthermore I was involved in the debugging of the frontend electronics whenever APVs or silicons were attached. This includes the optimization of detector noise. Partly I also provided software for the VME readout in the start-up phase and for monitoring of detector performance.
I participated in several test-beams carried out at CERN.

I supervised technical and diploma students contributing to the silicon detectors. I was involved in the financial planing and scheduling of the silicon detector project and presented its status to the collaboration.

In the middle years I organized the commissioning of the detectors at CERN, which includes the actual setup in the hall and the organization of the appropriate infrastructure as well as the incorporation into the COMPASS DAQ and data base systems.
I was involved in the analysis for the evaluation of the performance of the silicon detectors.
During the beam time 2002 I participated in the COMPASS shift business, partly as shift leader.

After the beam time 2002 I started the data analysis based on mDSTs and PHAST in Munich. Software had to be installed and correctly set up on the cluster of the institute and the data had to be transfered from CERN before I could start with the actual writing of `UserEvent` functions. Under the supervision of Prof. S. Paul and Dr. J. Friedrich I developed a procedure for the measurement of the transverse polarization of Λ^0.